

**Development of fast track finding algorithms
for densely packed straw tube trackers and its
application to $\Xi(1820)$ hyperon
reconstruction for the PANDA experiment**

DISSERTATION

zur

Erlangung des Grades eines
Doktors der Naturwissenschaften
in der Fakultät für Physik und Astronomie der
Ruhr-Universität Bochum

von

Anna Alicke
geb. Scholl

aus

Euskirchen

Bochum (2023)

Versicherung gemäß §7 Abs. 2 Nr. 6 PromO 2011

Hiermit versichere ich, dass ich meine Dissertation selbstständig und ohne unerlaubte fremde Hilfen angefertigt und verfasst habe und keine anderen als die angegebenen Hilfsmittel und Hilfen benutzt habe. Meine Dissertation habe ich in dieser oder ähnlicher Form noch bei keiner anderen Fakultät der Ruhr-Universität Bochum oder bei einer anderen Hochschule eingereicht.

- | | |
|---------------|---------------------------|
| 1. Gutachter: | Prof. James Ritman, Ph.D. |
| 2. Gutachter: | Prof. Dr. Ulrich Wiedner |

Datum der Disputation:

Abstract

The future [PANDA](#) experiment located at [FAIR](#) in Darmstadt will utilize a cooled antiproton beam incident on a proton target to study features of [QCD](#) accessible at low and medium energies. Of particular interest is the study of baryons containing at least one strange quark, so-called hyperons. Hyperons have a mass excess in the confinement domain, which makes them an excellent probe to study the transition region between perturbative and non-perturbative [QCD](#). Ground state hyperons have a very distinct signature in the detector because they have a mean flight path of a couple of centimeters before they decay. Therefore, the detection of charged particle tracks not coming from the primary interaction point by several centimeters is a strong indication of a hyperon. Consequently, [PANDA](#) must have a good track finding efficiency for final state particles with a displaced secondary vertex. In addition, unlike most older experiments [PANDA](#) will use a full detector online event filter to reduce the data stream before storage. The event filter will perform an online pre-analysis based on the complete detector data to decide whether an event is of physical interest. The basis for nearly all physics analyses is track reconstruction. This thesis deals with the development of track finding algorithms for [PANDA](#)'s target spectrometer. The main topics of the thesis focus on the development of a primary track finder and its online capability, as well as the development of a secondary track finder. The primary track finder achieves an efficiency for primary tracks of about 90 %, which is comparable to the currently existing standard track finder. Additionally, the number of wrongly found tracks is reduced by a factor of two compared to the standard tracker. Porting the algorithm on a GPU improves the speed of the newly developed algorithm by a factor of five. To reach an online capability further research is needed. In combination with growing capacities of [GPUs](#) the approach is promising. The secondary track finder is able to find particles with a displaced secondary vertex and improves the finding rate of secondary particles by 20 %-points compared to the standard tracker. The secondary tracker therefore significantly improves the reconstruction efficiency of hyperon decays. Applying the developed algorithms to a typical hyperon reaction $p\bar{p} \rightarrow \Xi^+ \Xi(1820)^-$ improves the full event reconstruction efficiency including the detector acceptance by a factor of four compared to the currently existing algorithms from a full event reconstruction rate of only 0.3 % with the currently existing track finder to 1.2 % by adding the secondary track finder.

Kurzfassung

Bei dem zukünftige **PANDA**-Experiment bei **FAIR** in Darmstadt trifft ein gekühlter Antiprotonenstrahl auf ein Protonentarget, um die Eigenschaften der **QCD** bei niedrigen und mittleren Energien zu untersuchen. Von besonderem Interesse ist hierbei die Untersuchung von Baryonen, die mindestens ein Strange-Quark enthalten, sogenannte Hyperonen. Hyperonen haben einen Massenüberschuss im Bereich des *Confinements*, was sie zu einem ausgezeichneten Forschungsobjekt für die Untersuchung des Übergangsbereichs zwischen störungstheoretisch lösbarer und nicht lösbarer **QCD** macht. Hyperonen im Grundzustand haben im Detektor eine sehr deutliche Signatur, da sie eine mittlere Flugbahn von einigen Zentimetern haben, bevor sie in andere Teilchen zerfallen. Daher ist die Entdeckung von Spuren geladener Teilchen, die mehrere Zentimeter vom primären Wechselwirkungspunkt entfernt sind, ein starker Hinweis für ein Hyperon. Folglich muss **PANDA** eine gute Effizienz für Endzustandsteilchen mit verzögertem sekundären Vertex aufweisen. Im Gegensatz zu den meisten älteren Experimenten wird **PANDA** zudem einen Online-Eventfilter für den gesamten Detektor verwenden, um den Datenstrom vor der Speicherung zu reduzieren. Der Eventfilter führt eine Online-Voranalyse auf der Grundlage der vollständigen Detektordaten durch, um zu entscheiden, ob ein Ereignis von physikalischem Interesse ist. Die Grundlage für fast alle physikalischen Analysen ist die Spurrekonstruktion. Diese Arbeit befasst sich mit der Entwicklung von Algorithmen zur Spurrekonstruktion für das Targetspektrometer von **PANDA**. Die Hauptthemen der Arbeit konzentrieren sich auf die Entwicklung eines primären Spurrekonstruktionsalgorithmus und dessen Online-Fähigkeit, sowie die Entwicklung eines sekundären Spurrekonstruktionsalgorithmus. Der Primärspurfinder erreicht eine Effizienz für Primärspuren von ca. 90 %, was mit dem derzeit existierenden Standardspurfinder vergleichbar ist. Zusätzlich wird die Anzahl der falsch gefundenen Tracks im Vergleich zum Standard-Tracker halbiert. Die Portierung des Algorithmus auf einen Grafikprozessor verbessert die Geschwindigkeit des neu entwickelten Algorithmus um einen Faktor von fünf. Um eine Online-Fähigkeit zu erreichen, sind weitere Entwicklungen erforderlich. In Kombination mit den wachsenden Kapazitäten von **GPUs** ist der Ansatz vielversprechend. Der sekundäre Trackfinder ist in der Lage Teilchen mit verschobenem Vertex zu finden und verbessert die Effizienz von sekundären Teilchen im Vergleich zum Standardtracker um 20 %-Punkte. Der sekundäre Tracker verbessert daher die Effizienz der Rekonstruktion von Hyperonenzerfällen erheblich. Die Anwendung der entwickelten Algorithmen auf eine typische Hyperonreaktion $p\bar{p} \rightarrow \Xi^+\Xi(1820)^-$ verbessert die Rekonstruktionseffizienz des gesamten Ereignisses im Vergleich zu den gegenwärtig existierenden Algorithmen um einen Faktor von vier, von einer Rekonstruktionsrate des gesamten Ereignisses einschließlich der Detektorakzeptanz von nur 0.3 % mit dem gegenwärtig existierenden Spurfinder auf 1.2 % durch Hinzufügen des sekundären Spurfinders.

Contents

1	Introduction	1
2	Motivation	5
2.1	The Standard Model of Particle Physics	5
2.1.1	Elementary Particles	5
2.1.2	The Fundamental Forces	6
2.2	Hadron Physics	11
2.3	State of the Art in Hyperon Spectroscopy	13
3	The PANDA Experiment	17
3.1	FAIR	17
3.2	High Energy Storage Ring (HESR)	20
3.3	The PANDA Physics program	21
3.3.1	Hadron Spectroscopy	22
3.3.2	Nucleon Structure	25
3.3.3	Hadrons in Matter & Hypernuclei	25
3.4	The PANDA Detector	26
3.4.1	Target	27
3.4.2	Magnets	28
3.4.3	Tracking Systems	29
3.4.4	Particle Identification	37
3.4.5	Electromagnetic Calorimeters	42
3.4.6	Luminosity Detector	44
3.4.7	Data Acquisition	45
3.5	Software	46
3.5.1	Data Generation	47
3.5.2	Reconstruction of Charged Particles	49
3.5.3	Event Selection & Reconstruction	51
4	Tracking	53
4.1	Detector Response	53
4.2	Track Finding: An Overview	55
4.2.1	Local vs. Global Tracking	55
4.2.2	Primary vs. Secondary Tracking	56

4.2.3	Online vs. Offline Tracking	56
4.2.4	Track Quality	57
4.3	Existing Track Finders in PANDA	59
4.3.1	Ideal Track Finder	59
4.3.2	Standard Track Finder	60
4.3.3	Cellular Automaton	60
4.4	Hough Track Finder	61
4.4.1	Hough transformation	61
4.4.2	Preselection	69
4.4.3	Merging	70
4.4.4	Results	73
4.5	Speed Optimization of the Hough Track Finder with GPUs	79
4.5.1	General Information About GPUs	79
4.5.2	Hough track finder on a GPU	81
4.6	Apollonius Triplet Track Finder	85
4.6.1	Triplet Finding	85
4.6.2	Track Selection	89
4.6.3	Results	89
5	Investigation of $\bar{p}p \rightarrow \Xi(1820)^-\Xi^+$	97
5.1	Simulated Data	98
5.2	Overview of the Analysis Procedure	100
5.3	Final State Particles	102
5.4	Λ Reconstruction	107
5.5	Ξ Reconstruction	113
5.6	Full Event Reconstruction	117
5.7	Rate Estimate	120
6	Conclusions and Outlook	121
6.1	Tracking Algorithms	121
6.1.1	Hough Track Finder	122
6.1.2	Online capability on GPU	122
6.1.3	Apollonius Triplet Track Finder	123
6.1.4	Combination of Primary and Secondary Track Finders	123
6.2	Application to the reaction $\bar{p}p \rightarrow \Xi^-(1820)\Xi^+$	124
6.3	Remarks & Outlook	125
	Bibliography	127
A	The Problem of Apollonius	137
B	Additional Figures for the Application to $\bar{p}p \rightarrow \Xi(1820)^-\Xi^+$	139
B.1	Final state Particles	139
B.1.1	Proton	140
B.1.2	Kaon	143
B.1.3	Antiproton	146
B.1.4	π^+	149

B.1.5 $\pi^+(\Xi^+)$	152
B.2 Λ Reconstruction	155
B.3 $\bar{\Lambda}$ Reconstruction	158
B.4 $\Xi(1820)^-$ Reconstruction	163
B.5 Ξ^+ Reconstruction	165
B.6 Full Event Reconstruction	168
List of Figures	173
List of Tables	179

Introduction

1

The question of what holds the world together at its core has occupied mankind for thousands of years. The discovery of radioactivity was the beginning of a new era to investigate the basic building blocks of matter systematically. A main discovery was made by Rutherford in the early 20th century. He found out that the atom consists of an atomic nucleus, which contains almost the entire mass and is orbited by light electrons. The first indication that the atomic nucleus must have a substructure arose with the discovery of the neutron. This was the beginning of nuclear physics as it is known today. With the continuous development of new particle accelerators, more and more new particles were discovered in the 1960's. To bring structure to the zoo of new particles Murray Gell-Mann found a way to sort the particles by their quantum numbers into the so-called eightfold way. This laid the basis of today's understanding of matter. Today we know that the structure of the eightfold way can be explained by the inner quark structure of these particles.

Today's understanding of particle physics is described in the [Standard Model of Particle Physics \(SM\)](#). It consists of six quarks and six leptons with the associated antiparticles, which represent the basic building blocks of matter. Additionally, the [SM](#) contains three of the four fundamental interactions, which are the electromagnetic force, the weak force and the strong force. The [SM](#) has been tested over the last 60 years with large accelerator facilities and constantly increasing energies. Although a large part of the predictions of the [SM](#) could be validated with high accuracy, there are still some open questions that have not been sufficiently investigated. Some of these open questions are found in the research field of the strong interaction. For high energies, the strong interaction is described by [Quantum Chromodynamics \(QCD\)](#). However, in the low energy region [QCD](#) can no longer be solved by using perturbation theory. Here, other theoretical models are needed to describe the binding and interaction of hadrons. Of particular interest is the spectroscopy of baryons containing at least one strange quark. These baryons are called hyperons. Existing approaches to describe the low energy region (e.g. lattice QCD) have not yet been able to fully describe the observed excitations and interactions. Excited states are predicted that are not seen in the experimental data and excited states are observed that are not predicted in the theoretical models. To gain a deeper understanding of the binding and interaction mechanisms in the low energy regime, new theoretical models must be found that are able to correctly predict the experimental observations. In addition, good data quality is the basis for the validation of theoretical models. However,

for hyperons containing two or even three strange quarks, the data quality is poor. Already for the lightest double-strange hyperon, the Ξ , the data is mainly based on bubble chamber experiments. The study of these heavy hyperons is challenging, since they often decay into neutral Λ particles with long lifetimes. As a consequence, the final state particles of the heavy hyperons often have a displaced secondary vertex with a distance of a few centimeters from the [Interaction Point \(IP\)](#).

The future [PANDA](#) experiment located at the [Facility of Antiproton and Ion Research \(FAIR\)](#) in Darmstadt is built to investigate the low-energy region of the strong force. The [PANDA](#) experiment is currently under construction and will collide an antiproton beam onto a fixed proton target. It will use beam beam momenta up to 15 GeV/c, corresponding to a center-of-mass energy of 5.5 GeV. By investigating the antiproton-proton reaction, the [PANDA](#) experiment is able to produce hyperon-antihyperon pairs, e.g. $p\bar{p} \rightarrow \Xi^+\Xi^-$, without further recoil particles, and thus achieve significantly higher resolutions for the reactions of interest. In [PANDA](#), a raw data stream of about 120 GB/s is expected. Therefore, the data stream must be reduced before the events are stored. Unlike many previous experiments, [PANDA](#) will use a software trigger that performs a pre-analysis to store only events of physical interest. The basis for any physical analysis is to combine the individual detector hits into particle tracks. The field of track finding, however, is the most computationally intensive task of the analysis. For online trackers, it is therefore essential to be able to process the continuously produced data at high speed. In contrast, speed is of secondary importance for offline trackers. Here, high quality of the reconstructed tracks is required.

In this work, two different tracking algorithms are developed. The first one is a primary track finder based on Hough transformations that finds particle tracks coming from the [IP](#). The algorithm is in a first step optimized as an offline tracker. In a second step, it is investigated to what extent the algorithm can be used as an online tracker. For this purpose, a parallelization on [Graphics Processing Units \(GPUs\)](#) is developed. Additionally, it is important for [PANDA](#) to have a tracking algorithm that is able to deal with tracks not coming from the [IP](#), since hyperons often produce final state particles with a displaced secondary vertex. Currently no secondary track finder in [PANDA](#) exists. Therefore, the third part of this thesis addresses the development of a track finder that can find tracks with a displaced secondary vertex. Finally, the combination of primary and secondary track finders is investigated and applied to a typical hyperon reaction. Here, the reaction $\bar{p}p \rightarrow \Xi^+\Xi^-(1820)$ is analyzed with the different realistic track finders.

The thesis is structured as follows:

Chapter 2 gives an overview of the physics basis for the current research in hyperon spectroscopy relevant for this thesis.

Chapter 3 describes the accelerator, as well as the experiment itself. First, a rough overview of [FAIR](#) is given. Then the accelerator complex is described. As a last part, the chapter describes the research focus of [PANDA](#) as well as the individual subdetectors.

Chapter 4 is introduced with an overview about tracking algorithms. The Hough transformation and the working principle of the primary track finder is described. After discussing the results obtained with the algorithm, the next subchapter deals with [GPU](#) programming. Here first general information about [GPUs](#) is given and then different implementations of the

Hough Track Finder on GPU and the corresponding results are presented. As the last part of this chapter the procedure of the secondary track finder and the achieved efficiencies are shown.

Chapter 5 deals with the application of the different tracking algorithms to the reaction $\bar{p}p \rightarrow \Xi^+\Xi^- (1820)$. A comparison of the achievable efficiencies with the different algorithms is described. The chapter also serves to provide a realistic picture of achievable reconstruction efficiencies.

Chapter 6 summarizes the results of the work described in chapters 4 and 5 and provides an outlook.

This chapter summarizes the background knowledge of particle and hadron physics that is important for the work presented in this thesis. First, the chapter reviews the [Standard Model of Particle Physics](#), discussing the elementary particles and forces. Then, a brief overview of the history of hadron physics and its basic principles is given. Finally, an overview of the current research in the field of hadron physics and hyperon spectroscopy as well as the decay channel reconstructed in this thesis are presented.

2.1 The Standard Model of Particle Physics

The Standard Model of Particle Physics is the generally accepted description of three of the four fundamental forces, which are the electromagnetic, the weak and the strong force. It contains all known elementary particles and the exchange bosons of the three fundamental forces and categorizes these particles according to their quantum numbers. An overview of the particles and their categorizations is shown in Fig. 2.1.

2.1.1 Elementary Particles

First the elementary particles are divided into fermions and bosons. Fermions have half-integer spin and are the building blocks of all visible matter in the universe, while bosons have integer spin and are the exchange particles of the fundamental forces.

Fermions

Fermions can be further categorized into quarks and leptons. Leptons only interact via the electromagnetic and weak forces. In contrast, quarks carry a so-called color charge, enabling them to also interact via the strong force. All fermions can be grouped into doublets with increasing mass. The electromagnetic charge difference between both particles of a doublet is $1e$. Combining the corresponding doublets of quarks and leptons results in three generations of matter. The stable matter is formed by particles from the first generation. For each matter particle an antiparticle exists, which has the same mass, lifetime and spin, but differs only in the sign of the charge.

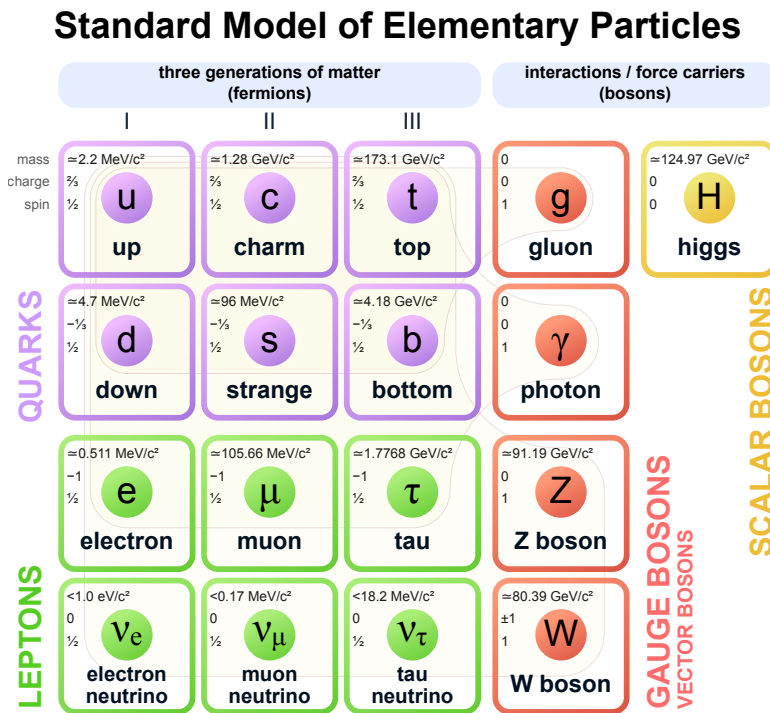


Figure 2.1: The Standard Model of Particle Physics [1].

Bosons

The fermions interact by exchange particles. These particles are called bosons and are also visualized in Fig. 2.1. They are the exchange particles of the three forces covered in this theory. The photon γ is the exchange particle of the electromagnetic force, the W^\pm and the Z^0 bosons are the exchange particles of the weak force and the eight gluons g are the exchange particles of the strong force. In contrast to photons and gluons, which are massless, the exchange bosons of the weak interaction have a high mass of $m_{W^\pm} = 80.4 \text{ GeV}/c^2$ and $m_{Z^0} = 91.2 \text{ GeV}/c^2$. In the standard model this mass is explained by the Higgs mechanism. The corresponding Higgs boson was predicted in 1964 and experimentally proven in 2012 [2]. In 2013 Peter Higgs and François Englert were awarded the Nobel Prize for the theoretical discovery of the Higgs mechanism [3].

2.1.2 The Fundamental Forces

In the following the three fundamental forces described by the standard model are introduced. These are the electromagnetic, the weak and the strong force.

Electromagnetic Force

The electromagnetic force was discovered in the 18th century when Charles Augustin de Coulomb investigated the forces of electric charges. The unification of electrical and magnetic forces was then introduced by James Clerk Maxwell in 1864 [4]. For the extension of the

theory to [Quantum Electrodynamics \(QED\)](#) Richard P. Feynman, Sin-Itiro Tomonaga and Julian Schwinger received the Nobel Prize in 1965 [5]. Here, the photon is described as an exchange particle of the electromagnetic force. The gauge invariant Lagrangian density of QED, shown in equation 2.3, describes the dynamics of a fermion in an electromagnetic field, where the fermion is described by the Dirac-spinor ψ . The Lagrangian density consists of three parts. The first part leads to the Dirac equation with the Dirac matrices γ^μ using the Euler-Lagrange-equations and describes the kinematics of the non-interacting fermion. The second part is introduced to enforce an invariance under local U(1)-gauge theory. This means that the Dirac equation must also be satisfied for a spinor with an additional phase:

$$\psi(x) \rightarrow \psi'(x) = e^{iq\alpha(x)}\psi(x) \quad (2.1)$$

This is only fulfilled if an additional gauge field A_μ is introduced, which transforms under local gauge transformation as:

$$A_\mu \rightarrow A'_\mu(x) = A_\mu(x) - \partial_\mu \alpha(x) \quad (2.2)$$

A_μ can be identified as the photon field with the coupling constant q corresponding to the electric charge. Thus, this part describes the fermion-photon-interaction. The invariance under local gauge transformation additionally leads to the fact that the photon must be massless since a mass term of the photon ($A_\mu m_\gamma^2 A^\mu$) is not invariant under gauge transformation. The last part describes the dynamics of the photon field. Here $F_{\mu\nu}$ is the electromagnetic field tensor: $F_{\mu\nu} = \partial_\mu A_\nu - \partial_\nu A_\mu$. Together with the part of the fermion-photon-interaction, the Euler-Lagrange-equations results in the inhomogeneous Maxwell equations: $\partial_\mu F^{\mu\nu} = j^\nu$, with j^ν the current density. [6]

$$\mathcal{L}_{QED} = \underbrace{\bar{\psi}(i\gamma^\mu \partial_\mu - m)\psi}_{\text{kinematics of non-interacting fermion with mass } m} - \underbrace{q\bar{\psi}\gamma^\mu A_\mu \psi}_{\text{fermion-photon-interaction}} - \underbrace{\frac{1}{4}F_{\mu\nu}F^{\mu\nu}}_{\text{dynamics of photon field } A_\mu} \quad (2.3)$$

Weak Force

The weak interaction has a range of about 10^{-3} fm and has therefore the shortest range of all known fundamental interactions. It affects all fermions and is the only interaction that enables a flavor transition from one particle to another. Here flavor transitions within one generation are more likely. The exact transition probabilities for quarks are summarized in the Cabibbo-Kobayashi-Maskawa (CKM) matrix [7]. Interaction of particles caused by the weak interaction can be divided into three groups: The fully leptonic decays, in which only leptons are involved, the semileptonic decays, in which both leptons and quarks are affected, and the fully hadronic decays, in which only quarks within hadrons are included. The weak interaction is the only interaction for which several fundamental symmetry violations have been found, e.g. parity violation or CP-violation. The most prominent example of the weak interaction is the β -decay. This decay is of special interest because it was the first decay that indicated parity violation of the weak force. For the theoretical background and the establishment of the Lee-Yang theorem Tsung-Dao Lee and Chen Ning Yang were awarded the Nobel Prize in 1957 [8]. In the same year Chien-Shiung Wu provided the experimental confirmation with the famous Wu-experiment, in which she was able to show that the β -decay is an asymmetric decay. As a consequence

she concluded, that the weak force interacts only with left-handed particles and right-handed antiparticles. CP-violation was then discovered in 1964 in decays of the neutral kaon decay (K_0) by observing the decay $K_L^0 \rightarrow \pi^+ \pi^-$, which can only exist if CP is violated. For this discovery, Christenson, Cronin, Fitch and Turlay were awarded the Nobel Prize in 1980 [9].

Today the parity violation of the weak force is described by a $SU(2)_L$ symmetry group, in which left-handed fermions occur in doublets and transitions within a doublet happen via a charged W^\pm boson exchange. Right-handed fermions, however, appear as singlet states and are not affected by the weak force. According to [6] the resulting Lagrangian for the weak interaction is therefore defined as:

$$\mathcal{L}_L = \underbrace{\bar{\psi}_L (i\gamma^\mu \partial_\mu) \psi_L}_{\text{kinematics of the non-interacting fermion}} - \underbrace{g \bar{\psi}_L \gamma^\mu T_a W_a^\mu \psi_L}_{\text{fermion-boson-interaction with the 3 boson fields } W_a^\mu} - \underbrace{\frac{1}{4} W_{a\mu\nu} W_a^{\mu\nu}}_{\text{dynamics of the boson field and 3-fold and 4-fold self-interactions}}, \quad (2.4)$$

where ψ_L describes the left-handed fermion doublets, γ^μ are the Dirac matrices, g is a coupling constant and $T_a = \frac{\sigma_a}{2}$ depends on the Pauli matrices σ_a . In this theory, three new bosons W_a , with $a = 1, 2, 3$, are predicted and the transition between fermions within a doublet state is described. Additionally, the self-interaction of the W_a bosons is predicted and the observed parity violation is included. A problem of the theory is that in the first part of equation 2.4 no fermion mass appears and also no mass of the bosons can exist due to gauge invariance. This problem is solved by a spontaneous symmetry breaking of the unified electroweak interaction. This unification of the electromagnetic and the weak force is one of the main building blocks of the standard model. In 1979, Sheldon Glashow, Abdus Salam, and Steven Weinberg received the Nobel Prize for this work [10]. For the unification, the symmetry group $SU(2)_L$ is combined with an additional symmetry group $U(1)_Y$ to a $SU(2)_L \times U(1)_Y$ symmetry. Here, the symmetry group $U(1)_Y$ contains an additional boson, commonly denoted as B^μ , and the so-called weak hypercharge Y . The combination of the symmetry groups consists of terms including W_1 and W_2 , which can be identified as the charged bosons of the weak interaction $W^\pm = \frac{1}{\sqrt{2}}(W_1 \mp W_2)$. Moreover, an additional interaction term occurs involving the remaining bosons W_3 and B . Finally, a rotation by the Weinberg angle θ_W leads to the electromagnetic interactions of photons to fermions with the photon field A^μ as well as the weak neutral interaction of the Z^0 boson to fermions:

$$\begin{pmatrix} W_3^\mu \\ B^\mu \end{pmatrix} = \begin{pmatrix} \cos\theta_W & \sin\theta_W \\ -\sin\theta_W & \cos\theta_W \end{pmatrix} \begin{pmatrix} Z^\mu \\ A^\mu \end{pmatrix} \quad (2.5)$$

The masses of the fermions and the W^\pm and Z^0 bosons then arise through spontaneous symmetry breaking, postulating a new scalar field - the Higgs field. Experimental evidence of the Higgs boson was finally obtained in 2012 [2].

Strong Force

The strong interaction holds the particles within a nucleus together. It only interacts between particles with color charge, which are the quarks and gluons¹. Here the concept of "color charge" is inspired by the concept of the electromagnetic charge. In contrast to the electromagnetic

¹Color neutral objects are bound by the nuclear force, which is based on a nuclear potential well model.

charge three different color charges exist (red (r), green (g), blue (b)). The name "color" and the names of the charges (red, green, blue) are inspired by the theory of visible colors, in which combinations of three primary colors are used to generate all possible colors. A free quark has never been observed, instead quarks are always bound in a color-neutral state, which is called a hadron. This phenomenon is called "confinement". Color-neutral bound states can be realized by a charge and an anti-charge ($q\bar{q}$) or three charges (qqq). These different color compositions lead to the difference between mesons ($q\bar{q}$), which have integer spin, and baryons (qqq) with half-integer spin. Hadrons with more than three valence quarks are a central topic of current research and have recently been observed. More details on such multi-quark states are described in section 2.3. One additional important difference to QED is that the exchange particles of the strong force - the gluons (g) - also have a color charge. This enables the interaction of gluons with other gluons. In total eight independent color states g^a exist for the gluons. These color compositions are a combination of a color and an anticolor and are determined as:

$$g^a = (r \quad b \quad g) \lambda^a \begin{pmatrix} \bar{r} \\ \bar{b} \\ \bar{g} \end{pmatrix} \quad (2.6)$$

Here λ^a are the eight Gell-Mann matrices. The Gell-Mann matrices describe the generators of the symmetry group SU(3) and span a Lie-algebra. They were named after Murray Gell-Mann, who was awarded the Nobel Prize of physics in 1969 "for his contributions and discoveries concerning the classification of elementary particles and their interactions" [11]. In total, the gluon color states are shown in equation 2.7.

$$\begin{aligned} g_1 &= \frac{1}{\sqrt{2}}(r\bar{b} + b\bar{r}) & g_2 &= \frac{1}{\sqrt{2}}(r\bar{b} - b\bar{r}) & g_3 &= \frac{1}{\sqrt{2}}(r\bar{r} - b\bar{b}) \\ g_4 &= \frac{1}{\sqrt{2}}(r\bar{g} + g\bar{r}) & g_5 &= \frac{1}{\sqrt{2}}(r\bar{g} - g\bar{r}) & g_6 &= \frac{1}{\sqrt{2}}(b\bar{g} - g\bar{b}) \\ g_7 &= \frac{1}{\sqrt{2}}(b\bar{g} + g\bar{b}) & g_8 &= \frac{1}{\sqrt{6}}(r\bar{r} + b\bar{b} - 2g\bar{g}) \end{aligned} \quad (2.7)$$

The theoretical formulation of the strong force is the **Quantum Chromodynamics (QCD)**, which is a non-abelian gauge theory of symmetry group SU(3) and is inspired by the lagrangian formulation of the QED in equation 2.3. The QCD Lagrangian density is shown in eq. 2.8 [12].

$$\mathcal{L}_{QCD} = \underbrace{\bar{\psi}(i\gamma^\mu \partial_\mu - m)\psi}_{\text{kinematics of a non-interacting quark with mass } m} - \underbrace{g\bar{\psi}\gamma^\mu T_a A_\mu^a \psi}_{\text{quark-gluon interactions}} - \underbrace{\frac{1}{4}G_{\mu\nu}^a G_a^{\mu\nu}}_{\text{gluon field propagation and gluonic self interactions}} \quad (2.8)$$

Here the first part of equation 2.8 leads to the Dirac equation and describes the kinematics of a non-interacting quark with mass m , where ψ describes the quark field and γ^μ are the Dirac matrices. The second part describes interactions between quarks and gluons. Here g is the quark-gluon coupling constant, A_μ^a represents the eight gluon fields and $T_a = \frac{\lambda_a}{2}$ is connected to the eight Gell-Mann matrices, which are equivalent to the eight gluon color compositions. The last part shows an important difference between QED and QCD. Similar to QED here $G_{\mu\nu}^a$ is the gluon field strength tensor, which is defined as:

$$G_{\mu\nu}^a = \partial_\mu A_\nu^a - \partial_\nu A_\mu^a + gf^{abc}A_\mu^b A_\nu^c, \quad (2.9)$$

with f^{abc} the structure constants of SU(3). In contrast to QED, not only the field propagation is included but also the gluonic self-interactions that enable the existence for glueballs. These are bound states of only gluons. Candidates of glueballs have been published. For instance, in 2021 the TOTEM collaboration at LHC and the DØ-collaboration at Fermilab published strong evidence of a glueball with an odd number of gluons [13].

Confinement & Asymptotic Freedom

The self-interaction of gluons is considered to be the cause of the absence of single quark states. The reason for the so-called "confinement" is an object of current research. The common explanation is that when two quarks are separated, a gluon flux-tube arises between these quarks [14]. The further the quarks are separated, the stronger the gluon flux-tube becomes until the energy is sufficient to form a quark-antiquark pair, which then results in two new hadrons.

This phenomenon is also visible in the coupling constant of the strong force ($\alpha_s = \frac{g^2}{4\pi}$ where g is the constant used in equation 2.8), which is not a constant but depends on the momentum transfer. This behavior is often called a "running coupling constant". The basic proportionality of the strong coupling constant is shown in equation 2.10. Here α_s depends on μ_R , which is a renormalization scale factor close to the momentum transfer Q , and a constant Λ [15]:

$$\alpha_s(\mu_R^2) \propto \frac{1}{\ln\left(\frac{\mu_R^2}{\Lambda^2}\right)} \quad (2.10)$$

In contrast to the QED coupling constant, the QCD coupling constant increases for lower momentum transfers, which correspond to larger distances of quarks. For higher energies the coupling constant decreases, which leads to the so-called asymptotic freedom of quarks. This discovery was made by David J. Gross, H. David Politzer and Frank Wilczek who were awarded the Nobel Prize in 2004 [16]. Asymptotic freedom describes how quarks have a semi-free state at small distances.

Measurements and theoretical calculations from QCD perturbation theory for the strong coupling constant are shown in Fig. 2.2 [15]. Here α_s is evaluated at a momentum transfer around the mass of the Z^0 boson. For this momentum transfer the world average is $\alpha_s(M_Z^2) = 0.1179 \pm 0.0009$.

At large energies, α_s can be determined by using perturbation theory. Here the assumption is valid that the changes in α_s are small and can therefore be determined by adding small correction terms to the mathematical model. However, for lower energies, where $\mu_s \approx \Lambda$, this assumption is no longer valid. Therefore, Λ describes the scale at which the quarks in the hadron can no longer be assumed to be quasi-free, and therefore perturbative QCD calculations are not valid anymore. This scale is often referred to as Λ_{QCD} [15][17]. Therefore, in the low energy regime ($O(1\text{GeV})$) other theoretical approaches must be developed, which is an object of current research. The two most prominent approaches are Lattice QCD (LQCD) [18][19] and chiral perturbation theory [20]. In LQCD the gauge theory of the 4-dimensional euclidean space-time is discretized as a lattice, with the quark fields represented as sites of the lattice and the gauge fields represented as the links between the sites. In this way, it is possible to solve the non-linear low-energy QCD regions by numerical simulations [21]. Chiral perturbation theory uses the confinement of quarks to hadrons at low energies. Therefore, in

chiral perturbation theory, the degrees of freedom are not quarks and gluons but hadrons. This allows to define an effective field theory that is then solvable. Both theories have been tested during the last decades and are well established. Nevertheless, both theories have limitations. LQCD e.g. is computationally intensive, chiral perturbation theory is limited to the assumptions to simplify the Lagrangian. Therefore, the low energy QCD remains a topic of high interest both experimentally and theoretically.

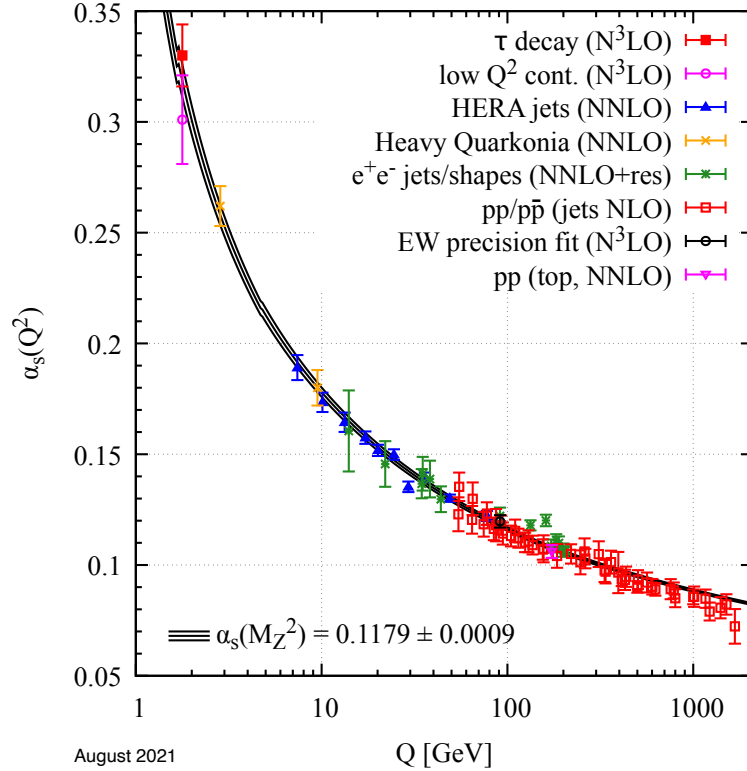


Figure 2.2: Measurements of the strong coupling constant α_s as a function of the energy scale Q . The degree of QCD perturbation theory is indicated in brackets (NLO: next-to-leading order, NNLO: next-to-next-to-leading order, NNLO+res.: NNLO matched to a resummed calculation, N^3 LO: next-to-NNLO). Picture from [15].

2.2 Hadron Physics

In the early days of particle physics, the constituents of hadrons - the quarks - were not yet known. At that time it was believed that the particle spectrum was complete with protons, neutrons, electrons and some cosmic ray particles such as pions. With the discovery of the neutron the quantum number isospin was introduced to describe the proton and the neutron as an isospin doublet with similar properties [22]. However, in 1947 Rochester and Butler [23] discovered a particle whose lifetime was significantly longer than that of other known resonance states of the particles known at that time. This was one of the first indications that the model known until then was not complete. Due to its long lifetime, the particle was assigned another quantum number - the strangeness. With the development of more powerful particle

accelerators, a large number of new particles were found in the 1960s. To bring structure into the particle zoo, the physicists of that time arranged the found hadrons according to their quantum numbers. In 1961, Murray Gell-Mann developed the so-called eightfold way [24]. Here, the particles are sorted according to their strangeness and their isospin. The eightfold way is considered to be an important step toward today's understanding of quarks and the standard model of particle physics. The classification of the eightfold way is shown in Fig. 2.3 and 2.4 for the three lightest quarks u, d, s. Fig. 2.3a and 2.3b show the classification of the mesons with spin 0 and spin 1. The mesons are classified by the 3rd component of the isospin on the x-axis and the strangeness on the y-axis. The same representation can be used for baryons, where all baryons with spin 1/2 are grouped into an octet (Fig. 2.4a) and all baryons with spin 3/2 in a decuplet (Fig. 2.4b).

Today it is known that this representation is a result of the quark composition of the hadrons. The underlying theory is based on group theory. Here the quarks are described as a fundamental representation of the symmetry group SU(3). Therefore a quark-antiquark pair can be described as a tensor product $\mathbf{3} \otimes \bar{\mathbf{3}}$, where $\mathbf{3}$ stands for the three lightest quarks u, d, s and $\bar{\mathbf{3}}$ for their anti-quarks [25]. Following the corresponding theory of Lie-algebra the $\mathbf{3} \otimes \bar{\mathbf{3}}$ representation decays into two irreducible representations $\mathbf{8} \oplus \mathbf{1}$, which is an octet and a singlet for mesons ($\mathbf{3} \otimes \bar{\mathbf{3}} = \mathbf{8} \oplus \mathbf{1}$). For baryons an octet and a decuplet is the result ($\mathbf{3} \otimes \mathbf{3} \otimes \mathbf{3} = \mathbf{10} \oplus \mathbf{8} \oplus \mathbf{8} \oplus \mathbf{1}$) [26]. Here it is possible to show that some of the states are forbidden due to the fact that the total wave function has to be antisymmetric. The wave function $|\Psi\rangle$ is composed of four parts: space, spin, flavor and color, as shown in eq. 2.11.

$$|\Psi\rangle = |\Psi_{space}\rangle \otimes |\Phi_{spin}\rangle \otimes |\chi_{flavor}\rangle \otimes |\xi_{color}\rangle \quad (2.11)$$

Here the spatial wave function is symmetric and the color wave function is antisymmetric. Therefore the combination of spin and flavor has to be symmetric. For baryons therefore only one octet and the decuplet in Fig. 2.4a and 2.4b survive.

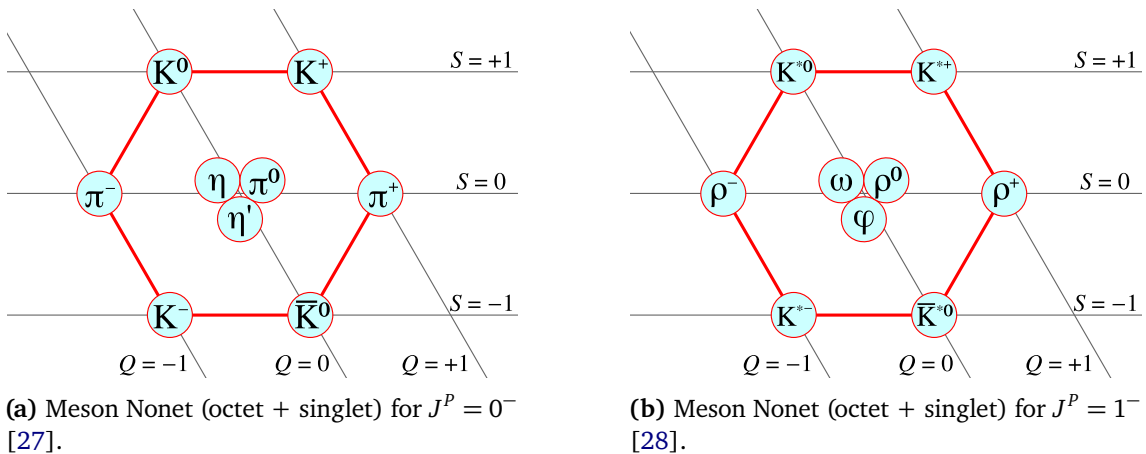


Figure 2.3: Eightfold way for the mesonic states of the three lightest quarks.

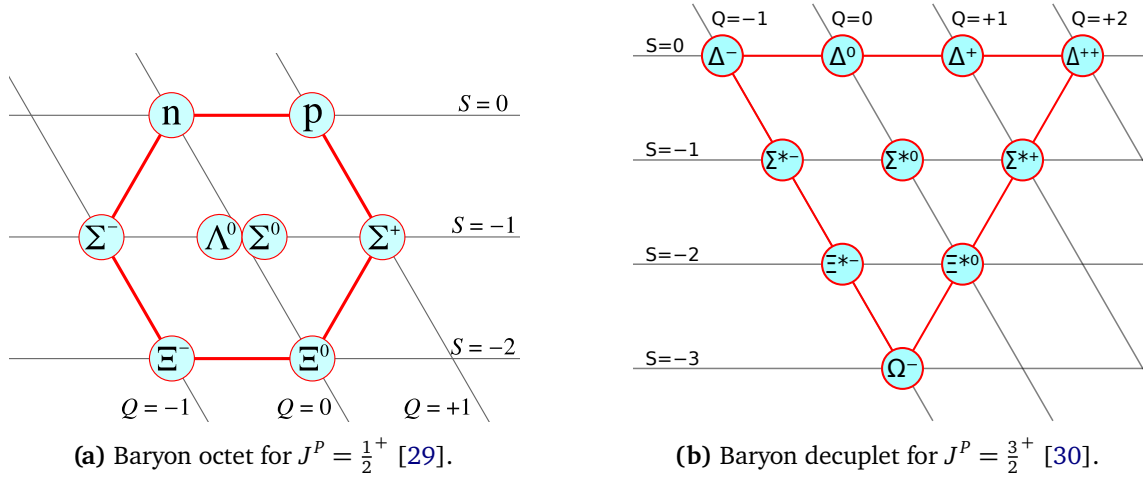


Figure 2.4: Eightfold way for the baryonic states of the three lightest quarks.

2.3 State of the Art in Hyperon Spectroscopy

The strong force is well understood for high energies and short distances, but for lower energies, where perturbative QCD cannot be applied many open questions exist. Here no consistent theoretical description exists. There are different theoretical approaches in low-energy QCD, like Lattice QCD, chiral perturbation theory or non-relativistic potential models. But the agreement of the different models with each other and with the experimentally observed phenomena is surprisingly poor [31]. In the low-energy regime, therefore, theoretical models exist, that describe different production cross-sections, like a one-gluon exchange or a Goldstone-boson exchange, where e.g. a pion act as exchange particle. An example of resonant states for the four bosons Λ with quark content (uds), Σ (dds), Ξ (dss), and Ω (sss) for two different theoretical models is shown in Fig. 2.5. Here the experimentally observed resonances are shown in green, where the uncertainty ranges are visualized in light green. A theoretical model with an one-gluon-exchange is compared to a model with a Goldstone-boson-exchange. The two models are shown as red lines. The one-gluon-exchange model is shown on the left side and the Goldstone-boson-exchange is shown on the right for each resonant state [32]. In the example, it is visible that the models don't predict the same resonances and that the predicted resonances are not in agreement with the experimental data. There are measured resonances that are not predicted by the models and both models predict resonances, which have not been observed. This phenomenon is called the problem of "missing resonances". One reason for predicted but unobserved resonances could be that the accuracy of the experiments is not sufficient. Therefore new detectors are being built in experimental hadron physics to generate precise measurements. Comparison of hadron spectroscopy with theoretical models provides insight into the dynamics of quarks and gluons, and in this way, non-perturbative QCD can be tested.

Non-strange baryons consisting of only the lightest quarks (Δ and N) have already been measured with high statistics. In contrast, the data quality for heavier baryons consisting of at least one strange quark - so-called hyperons - is low or even missing. The PANDA experiment will study heavy baryons like hyperons.

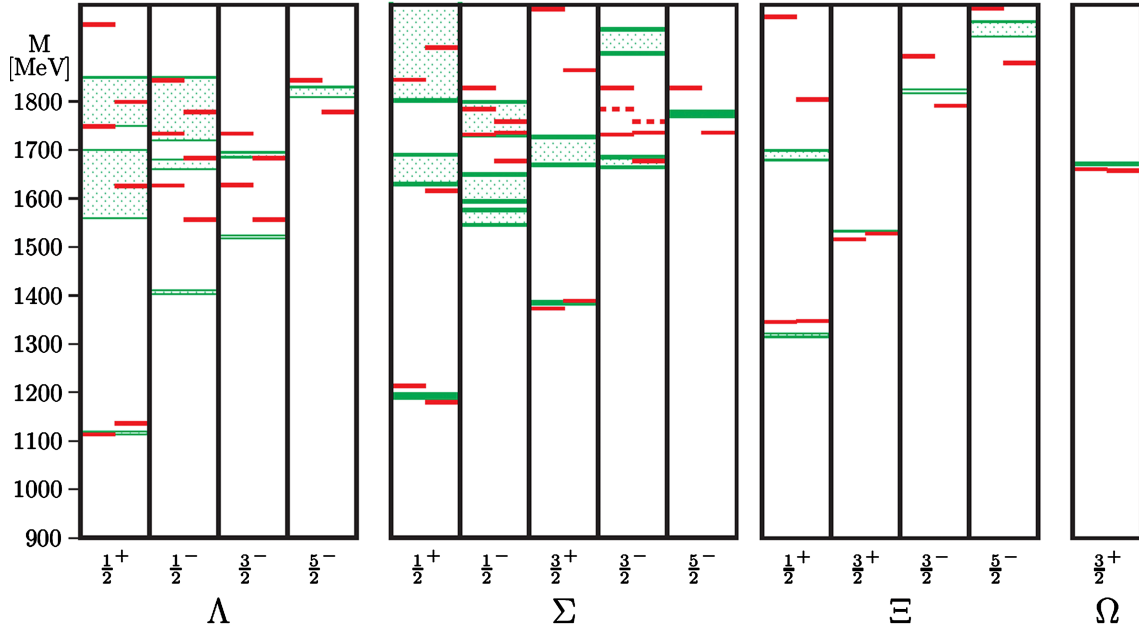


Figure 2.5: Resonances for the lowest levels of Λ , Σ , Ξ and Ω . The experimental measurements with their uncertainties are shown as green areas. The red lines indicate the predictions of an one-gluon-exchange model (left) and a Goldstone-boson-exchange model (right) [32].

Since this thesis later focuses on a Ξ resonance, this baryon will be discussed in more detail. The Ξ is the lightest double strange hyperon. It decays via the weak interaction, in which the strange quarks decay into lighter particles by producing a Λ particle with a branching ratio of $(99.887 \pm 0.035)\%$ for $\Xi^- \rightarrow \Lambda \pi^-$ [33]. The full reaction chain that is used by PANDA to investigate the Ξ decay is shown in Fig. 2.6. Since both Ξ and Λ have lifetimes of about 10^{-10} s, corresponding to a decay length of $O(cm)$, each Ξ has a distinctive decay pattern with two clearly distinguishable vertices, earning them the name "cascade baryon". For the $\Xi^-(1820)$ resonance analyzed in this thesis the overall existence ranges from very likely to certain. Also the predominant decay $\Xi^-(1820) \rightarrow \Lambda K^-$ has a certain to likely evidence. However, the Particle Data Group (PDG) explicitly mentions, that "the branching fractions are very poorly determined" [33] and higher statistics is necessary. In Tab. 2.1 the measurement status of the Ξ resonances is shown. Here it is visible that only the two lightest Ξ states have sufficient statistics. For all other resonances, the existence requires further confirmation. Some resonances have only been measured in bubble chamber experiments more than 35 years ago with low statistics [33]. Here the evidence of existence is only fair or poor. For most Ξ resonances the data quality is insufficient to provide information about the quantum numbers. Therefore better statistics is needed.

Furthermore, the theoretical models also predict more complex structures, as Murray Gell-Mann has already proposed in 1964 [34]. Since 2003 [35], almost 40 years after their prediction, many experiments have found evidence for such exotic structures, like tetraquarks ($q\bar{q}q\bar{q}$) or pentaquarks ($q\bar{q}qqq$). For example, in 2022 the BESIII Collaboration found an isoscalar state with exotic quantum numbers of $J^{PC} = 1^{-+}$ in the J/Ψ decay. The resonance has a mass of $(1855 \pm 9) \text{ MeV}/c^2$ and was named $\eta_1(1855)$ [36]. The particle is of particular interest

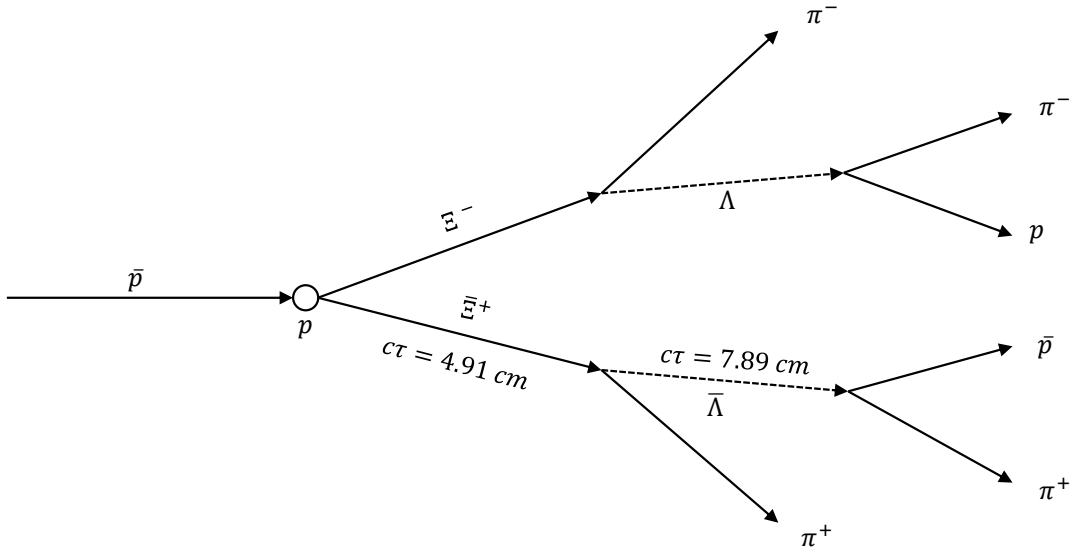


Figure 2.6: Full reaction chain $p\bar{p} \rightarrow \Xi^- \Xi^+$ studied in this thesis. Ξ emits a pion to produce a Λ . The Λ further decays into proton and pion, which results in four clearly distinguishable decay vertices.

Table 2.1: Ξ resonances taken from [33]. Only the two lightest resonances have sufficient statistics. The resonance analyzed in this thesis ($\Xi^-(1820)$) has a very likely to certain evidence, but further statistics are needed to determine the branching fractions.

Particle	J^P	Overall status	Status as seen in –				
			$\Xi\pi$	ΛK	ΣK	$\Xi(1530)\pi$	Other channels
$\Xi(1318)$	1/2+	****					Decays weakly
$\Xi(1530)$	3/2+	****	****				
$\Xi(1620)$		*	*				
$\Xi(1690)$		***		***	**		
$\Xi(1820)$	3/2-	***	**	***	**	**	
$\Xi(1950)$		***	**	**		*	
$\Xi(2030)$		***		**	***		
$\Xi(2120)$		*		*			
$\Xi(2250)$		**					3-body decays
$\Xi(2370)$		**					3-body decays
$\Xi(2500)$		*		*			3-body decays

**** Existence is certain, and properties are at least fairly well explored.
 *** Existence ranges from very likely to certain, but further confirmation is desirable and/or quantum numbers, branching fractions, etc. are not well determined.
 ** Evidence of existence is only fair.
 * Evidence of existence is poor.

because of its exotic quantum numbers. Therefore, there are interpretations for the particle to be a tetraquark [37]. Another example is the double-charmed tetraquark with a mass of $3875 \text{ MeV}/c^2$ found in 2021 by the LHCb collaboration [38]. Other charmonium-like states were also observed by BESIII and Belle in 2013 and 2003, respectively [39][40][35]. LHCb found resonances of the $J/\Psi p$ channel at masses of $(4312.0 \pm 0.7) \text{ MeV}/c^2$, $(4380 \pm 8 \pm 29) \text{ MeV}/c^2$ and $(4449.8 \pm 1.7 \pm 2.5) \text{ MeV}/c^2$ in 2015 and 2019, consistent with pentaquark states [41] [42]. Even heavier exotic states have also been observed such as the bottomium resonances in $\Upsilon(5S)$ decays at masses of $(10,607.2 \pm 2.0) \text{ MeV}/c^2$ and $(10,652.2 \pm 1.5) \text{ MeV}/c^2$ found by the Belle collaboration in 2011 [43]. Further investigation of these exotic states will provide insight to their nature and a better understanding of the binding mechanisms of quarks and gluons.

The PANDA Experiment

3

This chapter describes the [antiProton ANnihilations at DArmstadt \(PANDA\)](#) experiment and the accelerator facility FAIR. First off the accelerator facility with its four main experimental pillars is introduced, followed by an overview of the HESR storage ring. After that the [PANDA](#) experiment and its physics program is discussed. At the end of the chapter the software used to perform realistic simulations for the [PANDA](#) detector is presented.

3.1 FAIR

The [Facility of Antiproton and Ion Research \(FAIR\)](#) is a particle accelerator facility currently under construction. It is located at the [GSI Helmholtz Centre for Heavy Ion Research \(GSI\)](#) in Darmstadt. [FAIR](#) is designed to explore the structure of matter and act as "the Universe in the Laboratory" [44]. Antiprotons and ions will be accelerated to explore fundamental questions of physics. The field of research at [FAIR](#) ranges from nuclear, hadron and particle physics to plasma physics and applications in material science and biomedicine. The research is divided into four scientific pillars, which are embodied by the four experiments [APPA](#), [CBM](#), [NUSTAR](#) and [PANDA](#). The locations of the different experiments and subsystems of [FAIR](#) can be found in [Fig. 3.1](#) and will be introduced in the following.

Currently existing systems are shown in blue in [Fig. 3.1](#). All systems that are planned for the facility are shown in red. The core accelerator of [FAIR](#) is the new SIS100 ring accelerator. With a circumference of 1100 m it will be five times larger than the currently existing accelerators, UNILAC and SIS18, at [GSI](#). These (UNILAC and SIS18) will serve as the injector for SIS100. The [UNIversal Linear ACcelerator \(UNILAC\)](#) is a linear accelerator with a distance of 120 m. It provides three different ion sources for charged ions, from protons to uranium, and accelerates the ions to energies between 3.4 MeV/u and 13.6 MeV/u. The ring accelerator SIS18 is the first ring accelerator at [FAIR](#) and has a circumference of 216 m. The name SIS18 results from the rigidity of the accelerator, which has a maximum rigidity of 18 Tm. It accelerates protons to energies up to 4.5 GeV, which corresponds to 98 % speed of light [45].

In a next step, the SIS100 synchrotron will accelerate the ions up to a velocity over 99 % speed of light. It will be able to accelerate all species of ions from protons to uranium U^{92+} . For protons the SIS100 can reach a maximum energy of 29 GeV with $2.5 \cdot 10^{13}$ protons/cycle [46][47]. From here, the accelerated ions can either be used directly for the experiments such as CBM or NUSTAR's Super-FRS or pass through further storage rings to create beams of so-called

secondary particles. One of these storage rings, the high energy storage ring HESR, is the storage ring where PANDA will be located.

High Energy Storage Ring (HESR) is a storage ring designed for antiprotons. The production of antiprotons at HESR consist of the following steps. First, a proton beam pulse is created with a frequency of 2.7 Hz. The first accelerator, the p-Linac (see Fig. 3.1), accelerates the protons to an energy of 70 MeV. The proton bunches are then injected into the SIS18 pre-accelerator, where they reach an energy of up to 4 GeV. From here four proton bunches are injected into the SIS100. Here the bunches are merged into one single bunch with about $2.5 \cdot 10^{13}$ protons. The SIS100 furthermore compresses and accelerates the bunch to a bunch length of 50 ns with an energy of 28.8 GeV [49]. Antiprotons are created by colliding the high energy proton beam on a nuclear target. The target must fulfill various requirements. To achieve a high antiproton production rate a high density is needed. On the other hand a high density also results in a high temperature increase during the collision. To avoid melting processes of the target but also gain the highest possible production rate an optimum material and target length must be chosen. In HESR this is accomplished by an 11 cm long copper or nickel target rod with a diameter of 3 mm. The production rate is 10^{-5} antiprotons per primary proton. Antiprotons with energies of about 3 GeV and within a cone of 80 mrad are collected by a magnetic horn and separated from all other particles [50]. In the Collector Ring CR (Fig. 3.1) the momentum spread of the antiprotons is then reduced to $\frac{\delta p}{p} \approx \pm 0.1\%$ by stochastic cooling [51]. The proton beam is then injected into the HESR, where it is further accelerated or decelerated to the needed energy of the experiment. The overall antiproton production rate of HESR is then $2 \cdot 10^7 \bar{p}/s$. Further information about HESR is presented in section 3.2.

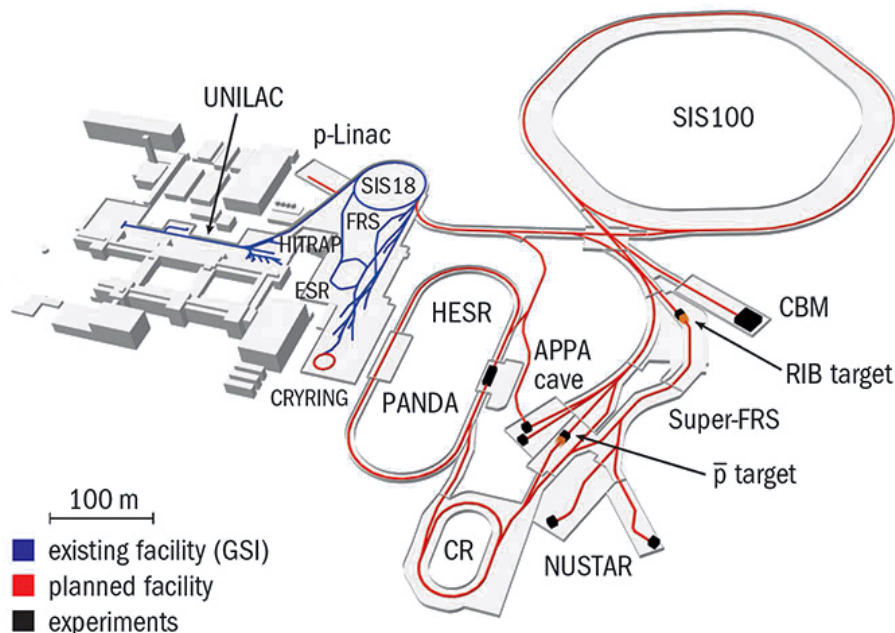


Figure 3.1: The Facility of Antiproton and Ion Research in Darmstadt (FAIR). The currently existing subsystems are shown in blue, all planned accelerators, storage rings and experiments are visible in red. Picture from [48].

APPA: Atomic, Plasma Physics and Applications

Atomic, Plasma Physics and Applications (APPA) is an association of several experiments dealing with mainly non-nuclear physics research topics. These include atom and plasma physics as well as biophysical and material science applications [52] [53]. The various experiments are distributed throughout the total FAIR facility due to their different energy requirements. Both the low-energy pre-accelerator UNILAC with energies of about 10 MeV/u and SIS18, which provides energies of 80-1000 MeV/u, are used. In addition, FAIR's cryring (see Fig. 3.1) is used for APPA to decelerate the ions and thus achieve high charge densities for material and nano science. With the main accelerator SIS100, energies of 0.1-10 GeV/u are achieved. The experiments belonging to APPA are: BIOMAT, SPARC, FLAIR and HED@FAIR. **BIOMAT** is a collaboration combining biology and material science that investigates the influence of radiation on biological targets. On the one hand, this serves the research in cancer and radiotherapy. On the other hand, measures for radiation protection are investigated, which are of particular interest in space radiation research of NASA [54]. The research field of **SPARC** is atom physics with stable and radioactive isotopes. **FLAIR** investigates the low energy regions of antimatter and therefore provides additional storage rings to slow down the beam up to 300 keV [55]. The additional storage rings are the magnetic Low Energy Storage Ring (LSR) and the electrostatic Ultra-low Energy Storage Ring (USR). **HED@FAIR** studies the behavior of different materials in heavy ion beams. The main focus is related to the properties of phase diagrams.

CBM: Compressed Baryonic Matter

The aim of the **Compressed Baryonic Matter (CBM)** Collaboration is to study baryonic matter at high densities to gain a deeper understanding of astrophysical objects like neutron stars or supernova explosions [56]. A fundamental question CBM wants to answer is at which densities do nucleons dissolve into their constituents. With this the phase transitions of baryonic matter will be studied. Extremely high reaction rates are needed for this research. These are achieved by the SIS100 accelerator, which is capable of e.g. Au+Au collisions with a frequency of up to 10 MHz. From SIS100 the ions are directly used by the CBM experiment (see Fig. 3.1).

NUSTAR: Nuclear Structure, Astrophysics and Reactions

The **Nuclear Structure, Astrophysics and Reactions (NUSTAR)** collaboration will study nuclear structure and astrophysics [57]. The core element of the collaboration is NUSTAR's **superconducting fragment separator (Super-FRS)**, which is presented in Fig. 3.2. It can separate exotic nuclei in-flight up to relativistic energies and is therefore able to separate nuclei with very short lifetimes.

PANDA: antiProton ANihilation at DArmstadt

PANDA will study the structure and dynamics of hadrons. The field of research for PANDA thus include hadron spectroscopy, exotic states and the weak and strong force. For this purpose, antiprotons are accelerated and collide with a proton or nuclear target. The antiprotons are collected in the High Energy Storage Ring (HESR), that provides beam momenta of 1.5 - 15 GeV/c. The experiment and its physics program is discussed in more detail below in chapters 3.3 and 3.4. Further information about HESR is in chapter 3.2.

3.2 High Energy Storage Ring (HESR)

HESR (Fig. 3.2) is the storage ring where **PANDA** is located. It has the shape of a race track and a circumference of 575 m. The two straight sections of **HESR** have a length of 132 m each. A maximum beam rigidity of 50 Tm is provided by 48 dipole magnets on the semicircular sides. **HESR** delivers an antiproton beam momentum of 1.5-15 GeV/c with a maximum luminosity of $2 \cdot 10^{32} s^{-1} cm^{-2}$. It has two systems to enable phase space cooling of the beam: the electron cooling system and the stochastic cooling system. The **PANDA** experiment and the stochastic pick up are located on one of the two straight sides of **HESR**, on the other side the electron cooling system and the kicker are located. Besides **PANDA**, **HESR** hosts two further experiments: **SPARC**, which is part of **APPA** [53] and **KOALA** [58], which is part of the **PANDA** collaboration and measures elastic $\bar{p}p$ cross sections, which is *e.g.* needed for a more precise luminosity determination in **PANDA**. In the following the different operation modes of **HESR** are introduced. After that the cooling systems and their components are explained.

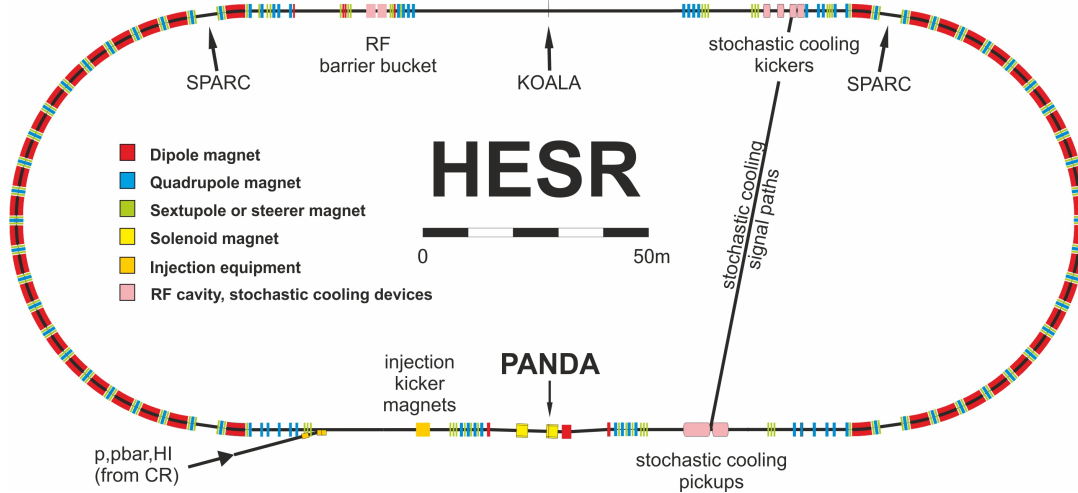


Figure 3.2: The High Energy Storage Ring **HESR**. Picture taken from [59].

Operation Modes

HESR is designed to operate in two different modes [60]: the high resolution mode and the high luminosity mode. In the modularized start version **HESR** will operate with a momentum resolution of $\frac{\Delta p}{p} < 4 \cdot 10^{-5}$ and a luminosity of $2 \cdot 10^{31} s^{-1} cm^{-2}$. The high luminosity mode will be reached as soon as the collector ring CR is extended by the Recuperated Experimental Storage Ring RESR, which can accumulate the cooled antiprotons. **HESR** will then be able to reach a luminosity of $2 \cdot 10^{32} s^{-1} cm^{-2}$, with a momentum resolution of $\frac{\Delta p}{p} = 10^{-4}$.

Stochastic Cooling

Stochastic cooling is a method to reduce the momentum width of the particle bunch in the storage ring. It requires a so-called pick-up sensor, which measures the deviation of individual beam particles from the desired beam momentum. The signal of the pick-up is then send to the kicker. This component is placed on the opposite side of the storage ring. By an electromagnetic

field the kicker corrects the momentum of individual particles with a large deviation from the desired beam momentum. This means that stochastic cooling is most powerful to quickly correct particles that are far off the desired momentum, but has little corrective force near the desired velocity. Further information about stochastic cooling at [HESR](#) can be found in [61].

Electron Cooling

In contrast to stochastic cooling, the electron cooling is not very effective for particles that are far off the desired value. However it is much more effective for particles close to the desired velocity. Thus, the electron cooling is used to further improve the stochastically cooled beam. For electron cooling an electron beam is created with the same average velocity as the beam to be cooled [62]. Both beams are superimposed and the ion beam interacts with the electron beam, exchanging momentum until a thermodynamic equilibrium is reached. This equilibrium is reached when the particles have the same average velocity and velocity dispersion, which reduces the momentum spread of the original ion beam. At the end of the overlap region, the electron beam is decoupled from the ion beam.

3.3 The PANDA Physics program

The [PANDA](#) experiment is one of the four scientific pillars of [FAIR](#) and focuses on physics questions related to [QCD](#). Hadron structure, binding mechanisms of quarks in the nucleus, and exotic particle structures are the main focus of the [PANDA](#) collaboration. The experiment is located at [HESR](#) and operates in a momentum range of 1.5 GeV/c to 15 GeV/c, corresponding to center-of-mass energies up to $\sqrt{s} = 5.5$ GeV. The research topics accessible with this energy are shown in Fig. 3.3. Here the accessible mass range is indicated by the blue dashed lines. This energy range corresponds to the range of non-perturbative [QCD](#) and allows the production of heavy hadrons containing strange and charm quarks.

In [PANDA](#) antiprotons collide with a fixed proton target. This antiproton-proton reaction offers advantages compared to other experiments, in which e.g. e^+e^- collide. In e^+e^- colliders, states having the same quantum number as the photon ($J^{PC} = 1^{--}$) are strongly favored. States with other quantum numbers can only be produced in systems with recoiling particles, so-called production processes, or in higher order production processes. A non-pre-determined part of the initial momentum and energy is carried by the additional recoiling particles. The state of interest has to be reconstructed from the resulting decay products. Since the resolution of the decay products and in particular of the recoil particles depends on the mass resolution of the detector, the precision of the measurement is limited to the resolution of the detector. In contrast, $\bar{p}p$ -annihilation allows direct access to states of all quantum number states accessible to a fermion-antifermion pair. The annihilation of quarks and antiquarks leads to a gluon-rich environment, in which states of all quantum numbers can directly be produced. In contrast, annihilation events, in which the initial system forms exactly one intermediate particle is called formation. Formation processes can achieve a higher mass resolution than the measurement of a production process, because here the resolution of the measurement is only affected by the energy spread of the beam and not by the momentum resolution of the detector, since there are no other recoil particles. The line shape is then determined by a method called a resonance energy scan. Here the same state is measured at different beam momenta. In this way it is possible to separate the resonance distribution from the beam resolution.

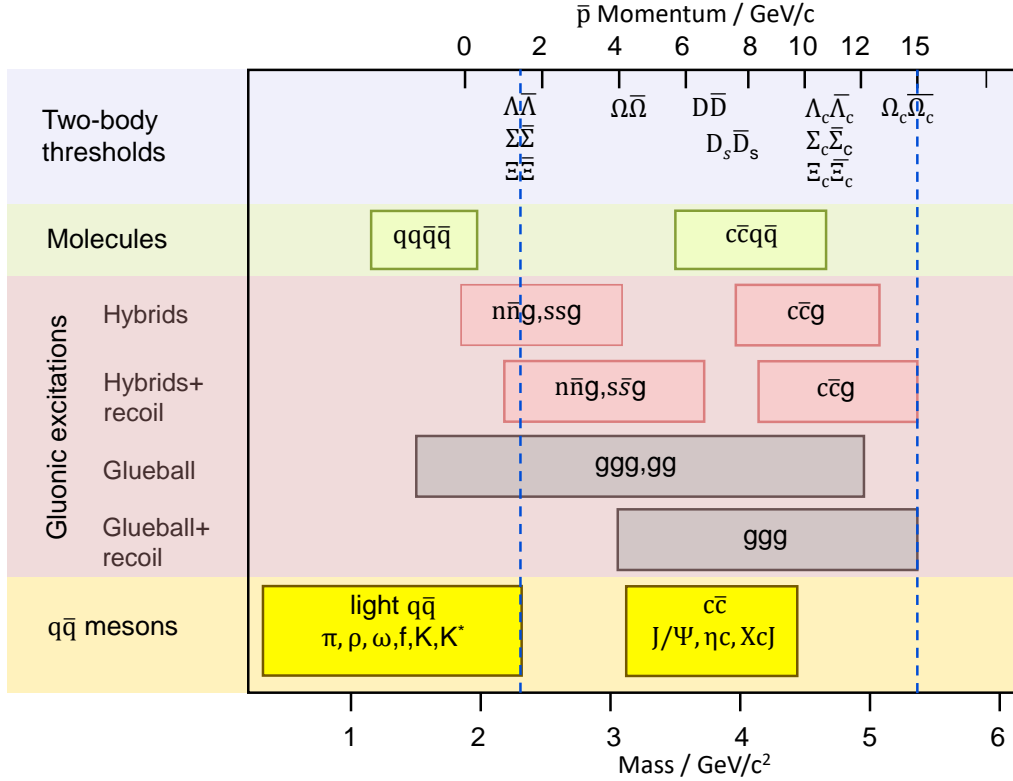


Figure 3.3: The research topics accessible with **PANDA**. The center-of-mass energy range is indicated with the dashed lines. This image has been taken from [31].

In the following, the main research topics of **PANDA** are introduced. This information about **PANDA**'s physics program are taken from [31] and [63].

3.3.1 Hadron Spectroscopy

Hadron spectroscopy is a key topic for **PANDA**'s research efforts, providing fundamental insight into the non-perturbative **QCD** region and the interactions of the hadrons constituents. Within hadron spectroscopy, the research topics are further divided into three subgroups. These are spectroscopy of hadrons with charm constituents, such as charmonium, hyperon spectroscopy, which are baryons including at least one strange quark, and the search for exotic hadrons.

Charmonium

In **PANDA**, charmonium ($c\bar{c}$) is of particular interest since it allows investigations in the field of non-perturbative and non-relativistic **QCD**. The potential describing the interactions inside the charmonium can be described by a Coulomb-like potential with an additional linear part describing the confinement. In the theoretical formulation, there are several approaches to describe the interactions. Here, non-relativistic potential models or effective field theories like **LQCD** are of particular interest. So far, charmonium has been measured mainly in e^+e^- -experiments. These measurements have a fundamental limitation because the charmonium creation is favored for quantum numbers of $J^{PC} = 1^{--}$. Other quantum numbers are only

accessible in higher order processes or in combination with recoil particles, which reduces the resolution of the measurements, as described above. *PANDA* will enable the study of charmonium states of all possible quantum numbers. Due to the $\bar{p}p$ -reaction, where each constituent annihilates with its anti-quark partner, the charmonium system is directly accessible for all quantum numbers available for a bound quark-antiquark system. Proton-antiproton annihilation provides a high mass resolution, which is not limited by the detector but only by the beam momentum spread. In Fig. 3.4 the charmonium spectrum is shown. Eight states below the $\bar{D}D$ -threshold of 3.73 GeV are visible. For these eight states, the theoretical description is in good agreement with experimental data. Above the $\bar{D}D$ -threshold many predicted excitations are still not observed and states are observed which are not predicted.

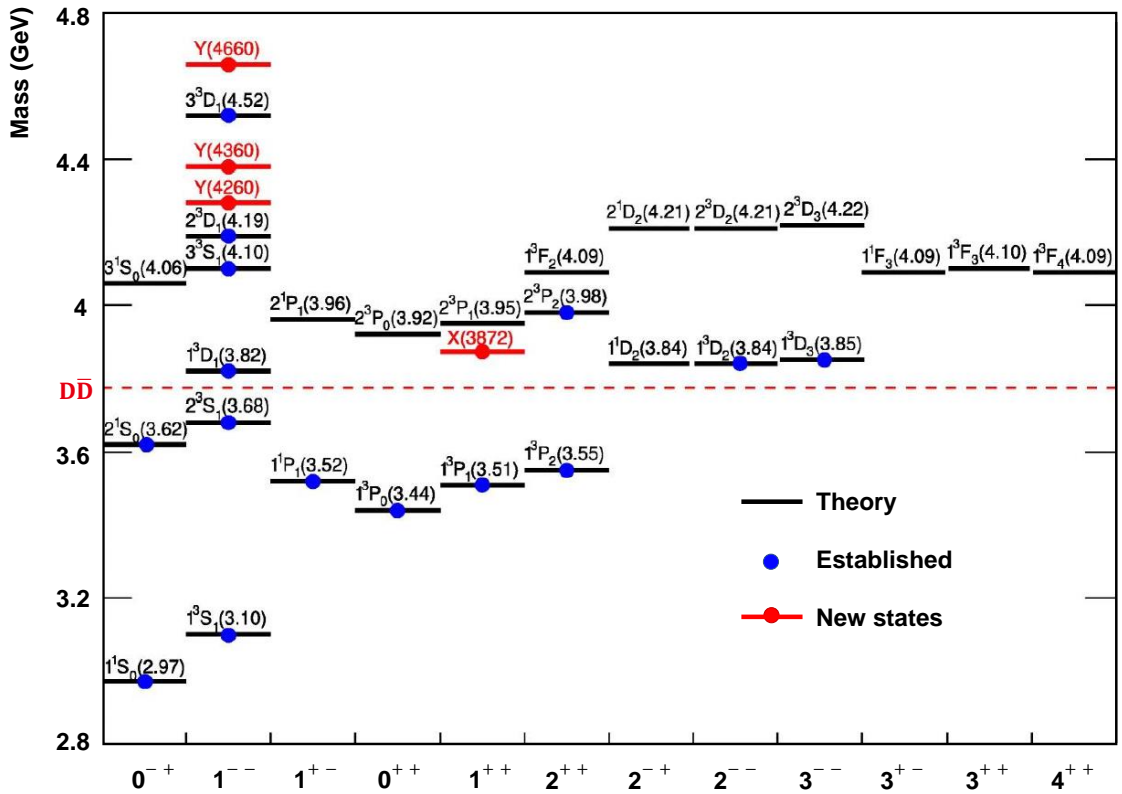


Figure 3.4: A comparison of theoretically determined charmonium excitations and measured data. The red dashed line indicates the $\bar{D}D$ -threshold. The measured resonances are in good agreement with theoretical predictions only for the states below this threshold. Picture taken from [64].

In 2003, the Belle Collaboration observed the first state ($X(3872)$) above the $\bar{D}D$ -threshold that does not fit to the classical charmonium spectrum [35]. Although the mass of the state is in the charmonium region, the measured quantum numbers do not fit to a predicted state. The spin-parity quantum number is measured to be $J^{PC} = 1^{++}$. The only state in the charmonium spectrum with $J^{PC} = 1^{++}$ is expected to have a larger mass of 3.96 GeV/ c^2 . Furthermore, it was observed that there exist decay channels with decay rates about an order of magnitude larger than the decay rates of other charmonium states [64]. Subsequently, various ideas arose to explain the quantum numbers and high decay rates. Today, the most likely explanation is that the particle may be a bound state of four quarks, which was the first indication of a tetraquark.

Furthermore, in recent years many observations above the threshold have been made. These states were initially referred to as the X, Y, Z states. One of the most prominent observations is the charged state $Z_c(3900)$ [39][40], which is in the charmonium energy region, but carries electric charge. Therefore, it cannot be a pure charmonium state consisting of $c\bar{c}$ but must contain additional quarks that provide the electric charge, such as an $u\bar{d}$ combination. Consequently, the observation of the $Z_c(3900)$ state is a strong indication for the existence of tetraquarks, which opens a wide field of research in the non-perturbative QCD regions for PANDA.

In addition, PANDA promises to make outstanding discoveries in the open-charm field. Open-charm systems are systems with non-vanishing charm quantum number and are interesting because they enable the study of a heavy quasi-static color constituent - the charm - and its light counterpart. Here a deeper understanding of chiral symmetry breaking can be expected.

Hyperons

The second subgroup of interest are hadrons containing one or more strange quarks. These particles are called hyperons. In particular for multi-strange hyperons, the existing data is similarly scarce as for charm-containing particles. Also here the agreement between theoretical predictions and experimental data shows inconsistencies. The absence of resonances predicted by theoretical models is called the problem of "missing resonances". Different explanations have been developed by theorists based on the binding mechanism of quarks in the hadron. One possible explanation is a quark-diquark structure, which reduces the number of possible resonances. PANDA will provide high statistics data in the energy region of interest. As a $\bar{p}p$ -system it can directly produce hyperon-antihyperon pairs and therefore no additional final state particles will appear in PANDA. Compared to other $\bar{p}p$ -colliders, such as Fermilab, HESR will provide a higher luminosity and better momentum resolution. Therefore, good statistics of events with low background and a high sensitivity is expected. This will give insight into the hyperon production mechanism, for which various models exist, like a quark-gluon exchange or a meson exchange. In particular, for the multi-strange hyperons Ξ and Ω the resonances are only observed with poor evidence. The particle data group specifically notes "nothing of significance on Ξ resonances has been added since the 1988 edition" [33]. For the Ω baryon the data is even poorer. PANDA is designed to operate in the optimal energy range for hyperon production. Hyperon spectroscopy and partial wave analysis will deliver high precision measurements of properties like mass, spin and parity of the poorly known resonance states.

Exotic states

Another topic of great interest is the search for exotic states, like glueballs, hybrids and multiquarks. Glueballs are bound states that only need gluons as valence particles to describe the quantum numbers. The study of glueballs represents a core element in understanding long-distance QCD. Evidence for glueballs has already been seen in experiments at the Low Energy Antiproton Ring (LEAR). Here the Obelix collaboration found a candidate for a pseudoscalar glueball [65]. LQCD calculations, however, predict the glueball at higher masses. The combination of gluonic excitation states and hadrons is called hybrids. Here exotic quantum numbers can be obtained because the gluon quantum numbers are added to the hadron quantum numbers to produce a state with overall quantum numbers that can not be reached with a fermion-antifermion pair. Therefore, these states are well distinguishable from ordinary hadron states, where these quantum numbers are forbidden. Multiquarks are hadrons consisting of

more than three valence quarks. Different hadron combinations are possible like tetra- or pentaquarks. Evidence for such exotic states has already been found in different experiments, as mentioned in chapter 2.3.

3.3.2 Nucleon Structure

The main goal at **PANDA** is to investigate **QCD** in the non-perturbative region. At the same time, the experimental setup also allows studies in the transition region between perturbative and non-perturbative **QCD**. One topic of **PANDA**'s physics proposal in this region will be to study hard exclusive processes in form of Compton Scattering processes, like deeply virtual Compton scattering or wide angle Compton scattering. Here the processes can be divided into a part calculated by perturbative **QCD** and a part described by **Generalized Parton Distribution Functions (GPDs)**. Various approaches for **GPDs** exist, like generalized distribution amplitudes (GDAs) or transition distribution amplitudes (TDAs). The aim is to get a better understanding of possible theories describing the transition region between perturbative and non-perturbative **QCD** and to what extent **GPDs** are applicable to such processes.

Another topic in the field of nucleon structure studies is the determination of electromagnetic form factors. The electromagnetic charge distribution in a hadron is described by electromagnetic form factors, composed of an electric (G_E) and a magnetic form factor (G_M). The Form factors can be extracted by scattering processes of charged leptons and hadrons and depend on the momentum transfer squared q^2 . For a negative momentum transfer ($q^2 < 0$) the process is denoted as space-like and can be observed in scattering processes such as $e^- + p \rightarrow e^- + p$. In the case of an annihilation process like $\bar{p}p \rightarrow e^+e^-$ the momentum transfer is positive ($q^2 > 0$) and therefore denoted as time-like. Several experiments have determined the time-like region of the electromagnetic form factor under the assumption that $G_E = G_M$. Only two experiments - LEAR [66] and BABAR [67][68] - had sufficient statistics to determine G_E and G_M independently. Their accuracy of the ratio $R = G_E/G_M$ is in the order of 50%. With **PANDA**, data in the accuracy region of a few percent are expected [69].

In addition, **PANDA** will also be able to access the region below $(2M_p)^2$, where M_p is the mass of the proton. This region is accessible by studying reactions of the form $\bar{p}p \rightarrow l^+l^-\pi^0$. As the electromagnetic form factors are complex in the time-like region, they have a phase, that can only be measured with a polarized beam or target. Nevertheless, studying reactions in this region can validate theoretical models describing the cross section of processes like $\bar{p}p \rightarrow e^+e^-\pi^0$ [63].

3.3.3 Hadrons in Matter & Hypernuclei

A further field of research in **PANDA** is the behavior of hadrons in matter. To get a deeper understanding of how hadrons react in nuclear matter and how their properties change in comparison to the vacuum, hadrons are modified in the nucleus. An interesting aspect is the change of the hadron mass inside the nuclear medium due to the partial restoration of chiral symmetry.

Of special interest are hypernuclei, which are nuclei in which a neutron or proton is replaced by a hyperon. This adds an additional quantum number, the strangeness, to the nucleus, which leads to the fact that the hyperon is not restricted to the Pauli principle. Therefore they serve as a hadronic many-body system. Studying hypernuclei therefore gives insight into the nuclear

structure and the interaction between hyperons. As an example comparing a nucleus with a hypernucleus gives insight into the nuclear spin-orbit force [63]. Furthermore the hyperon properties in the bound state can be measured and compared to the vacuum properties of the hyperon. Here decay properties, hyperon spectra and wave functions are the properties of interest. In **PANDA**, Λ or double- Λ bound states are directly accessible and may lead to a better understanding of exotic matter.

3.4 The PANDA Detector

As a fixed-target experiment, **PANDA** is divided into a barrel part surrounding the **Interaction Point (IP)** and a forward part to detect the forward boosted tracks. The overall structure of the **PANDA** detector is shown in Fig. 3.5. The barrel part is called the target spectrometer and has a diameter of about 5 m and a length of about 4 m. It covers nearly the full solid angle of 4π . The target spectrometer is further divided into the barrel part covering polar angles greater than 22° and an endcap for angles greater than 5° in vertical and 10° in horizontal directions. The forward part of **PANDA** (forward spectrometer) extends the detector to its full length of 13 m and covers the forward going tracks below the acceptance limit of the target spectrometer. To enable momentum measurement and particle identification **PANDA** has two magnets. The magnet in the target spectrometer is a 2 T superconducting solenoid magnet, and a large-aperture 2 Tm dipole magnet is used in the forward region. Furthermore, the **PANDA** detector can be divided into subgroups of different detectors, which are explained in more detail in the following sections. First, the target system and the magnets are introduced. Then the four different tracking detectors and the particle identification systems are explained. Finally, the calorimeters and the luminosity detector are presented.

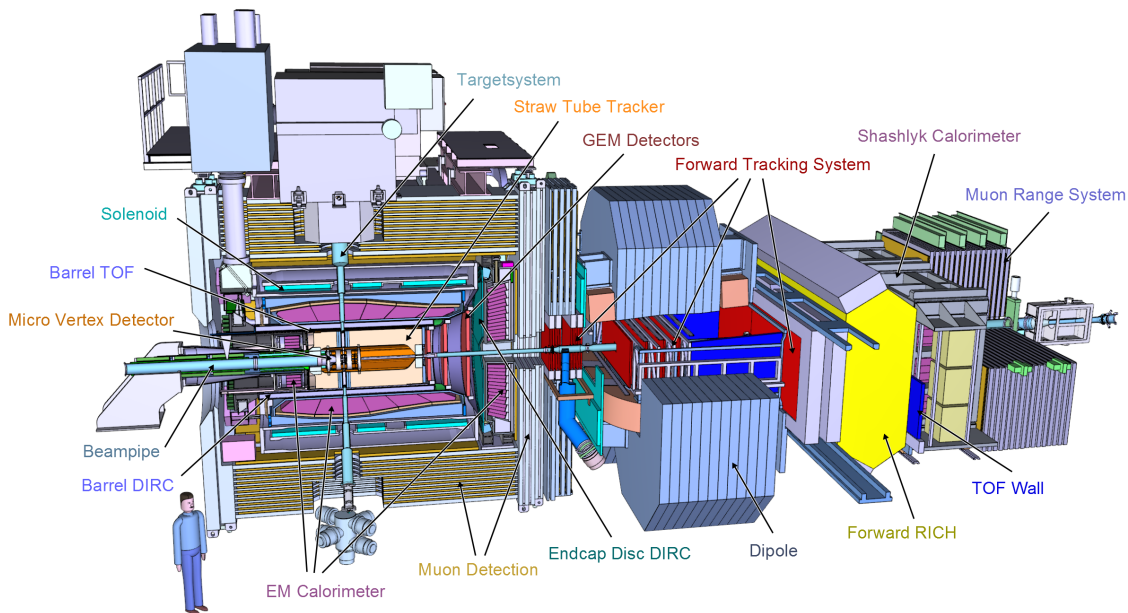


Figure 3.5: Schematic overview of the **PANDA** detector with labeled subdetectors. Picture from [70].

3.4.1 Target

PANDA's target system will inject target nuclei in transverse direction to the beam pipe. To enable a clean and well-defined **IP**, different requirements have to be fulfilled. For most applications a pure proton source is required, which can be accomplished by a hydrogen target. For other applications a nuclear target such as deuterium or heavier targets like ${}^4\text{He}$, N_2 , Ne, Ar, Xe or Kr can be used. For all target materials high purity is necessary since any contamination would cause a physics background that makes event reconstruction more difficult. Furthermore, a clean vacuum must be given to avoid antiproton losses in the beam pipe or an undefined vertex in the interaction region. To achieve the high luminosity of $2 \cdot 10^{32} \text{cm}^{-2} \text{s}^{-1}$ a target areal density of $\rho_{\text{target,max}} = 4.5 \cdot 10^{15} \text{atoms/cm}^2$ is required, assuming **HESR**'s antiproton production rate of $2 \cdot 10^7 \bar{p}/\text{s}$ and a beam revolution frequency of 443 kHz. The target areal density must not be too high (below $10^{16} \text{nucleons/cm}^2$) to minimize beam heating effects and, in addition, a thin target is required to avoid multiscattering. The requirements can be fulfilled in two ways: either by a cluster jet target or a pellet target. Both possibilities are explained below [31][71].

Cluster-Jet Target

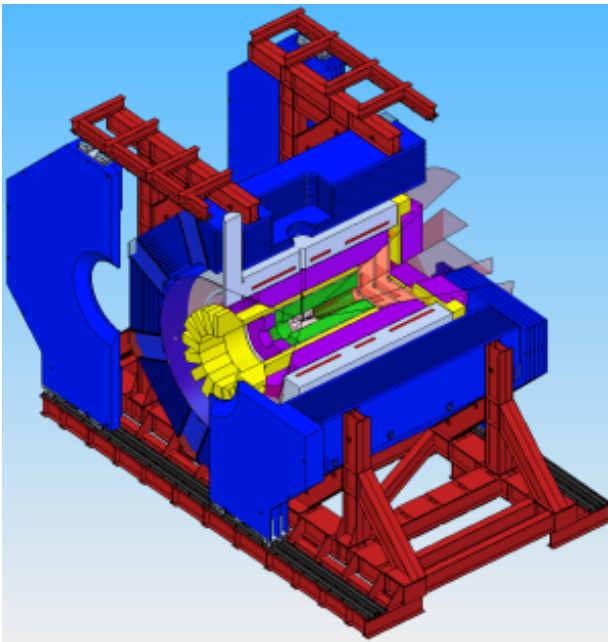
A cluster-jet target is created by injecting pre-cooled hydrogen gas through a Laval-type nozzle into the vacuum. As the gas passes through the nozzle, it cools further by adiabatic cooling, forming a supersonic beam. This causes the hydrogen to condense and form so-called clusters. These clusters consist of about 10^3 to 10^6 hydrogen molecules. The size of the clusters depends strongly on the temperature, density and the shape of the nozzle. The spread transversal to the beam direction is about 2-3 mm and longitudinally about 15 mm. The average separation distance between the clusters is less than $10 \mu\text{m}$. A cluster-jet target can reach areal densities of up to $2 \cdot 10^{15} \text{atoms/cm}^2$ [72], which meets the requirements of **PANDA** for a very thin, homogeneous target with sufficiently high density.

Pellet Target

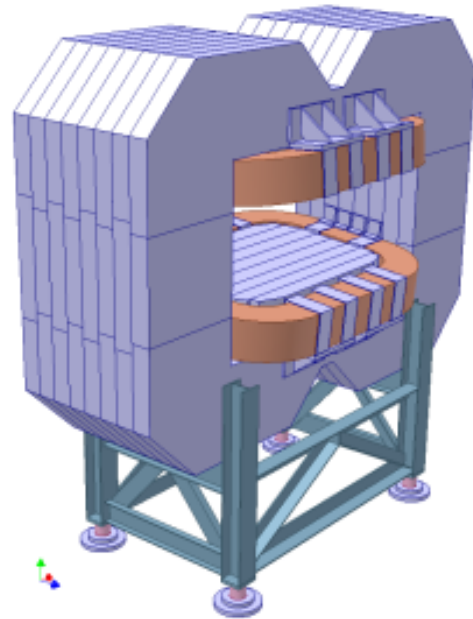
The pellet target is the second possibility to fulfill **PANDA**'s requirements. Here a cryogenic fluid is injected through a nozzle into a gas of the same element as the fluid, that is close to its triple-point. As the fluid passes through the nozzle, the nozzle gets stimulated by a piezoelement, which divides the continuous stream of fluid into droplets, also called pellets. The pellets then enter a vacuum injection capillary. Here the fluid further cools down, which leads to a stream of frozen pellets entering the vacuum of the beam pipe. The individual pellets have a diameter of about $20 \mu\text{m}$, and the stream of pellets has a transverse size of less than 3 mm. The average vertical distance between the pellets is about 2-20 mm. The pellet target system has two main advantages compared to the cluster-jet target. First, the pellets can reach higher average areal densities than the cluster-jet. Densities of up to $5 \cdot 10^{15} \text{atoms/cm}^2$ can be reached for the pellet target, in contrast to $2 \cdot 10^{15} \text{atoms/cm}^2$ for the cluster jet target [73]. The second advantage is that it is possible to measure the exact position of the pellet by an optical device and therefore have additional information of the position of the **IP** on an event-by-event basis [74].

3.4.2 Magnets

In order to determine the rigidity (momentum divided by charge) and the sign of the charge, the deflection of the particle in a magnetic field must be measured. The **PANDA** experiment has two magnets, one in the target spectrometer and one in the forward spectrometer. In the target spectrometer a 2 T solenoid magnet causes a bending of the charged particle's trajectories. The magnet in the forward spectrometer is a large aperture dipole magnet. Both magnets are shown in Fig. 3.6 and are introduced in the following. Further information can be found in the technical design report for the magnets [75].



(a) The solenoid magnet in blue with further construction elements. The magnet has a total length of about 4 m and a free inner diameter of 1.9 m.



(b) The dipole magnet for the forward spectrometer has a length of about 1.5 m and a width of 3.9 m and a height of 5.3 m.

Figure 3.6: The magnets of the **PANDA** detector [75].

Solenoid Magnet

The main requirements of the solenoid magnet in the target spectrometer is to deliver a magnetic field with up to 2 T that has a high homogeneity over the tracking detectors of the barrel part of **PANDA**. This is fulfilled by using a superconducting solenoid magnet with a free inner diameter of 1.9 m and a length of nearly 2.5 m downstream of the **IP** and 1.5 m in upstream direction. Here, the target spectrometer must be movable transverse to the beam direction by 10 m within one week for installation and maintenance reasons. The homogeneity of the provided magnetic field integral must not vary by more than 2%. This is important to achieve sufficient momentum precision when measuring the helix that a charged particle follows in the solenoid field. Neglecting deflection effects like energy loss or multi-scattering the helix can be divided into a linear part in the z -direction and a circle in the x - y -plane. Here the circle radius R is directly proportional to the transverse momentum p_T of the particle. The corresponding

formula can be derived from the equality of the Lorentz force F_L and the centripetal force F_c :

$$\begin{aligned}
 |\vec{F}_L| &= qvB, & |\vec{F}_c| &= \frac{mv^2}{R} \\
 |F_L| &= |F_c| \\
 \Leftrightarrow qvB &= \frac{vp}{R} \\
 \Leftrightarrow R &= \frac{p}{qB}
 \end{aligned} \tag{3.1}$$

with q , v , m and p the particle's charge, velocity, mass and momentum and B the magnetic field. For a particle velocity in the relativistic region the relativistic momentum $p = \gamma m_0 v$ with $\gamma = 1/\sqrt{1 - (v/c)^2}$ must be used. Transforming the units to GeV and assuming a unit charge leads to the following useful relation between the circle radius and transverse momentum:

$$R[m] = \frac{p_T[GeV/c]}{0.3 \cdot B[T]} \tag{3.2}$$

Dipole Magnet

In the forward spectrometer tracks are detected if they have a polar angle relative to the beam direction of less than $\pm 5^\circ$ in vertical and below $\pm 10^\circ$ in horizontal direction. Here a large aperture resistive dipole magnet is used with a field integral of 2 T·m. The dipole magnet enables a momentum reconstruction accuracy of $\Delta p/p < 1\%$ and will be part of the accelerator lattice of **HESR**. The magnetic field in forward direction will be decoupled from the solenoid field by five layers of 6 cm thick iron.

Compensating Magnets

Due to the high magnetic fields and the magnetic length of the solenoid and the dipole magnet, an affection of the antiproton beam by **PANDA**'s magnets is expected. To ensure that the antiproton beam does not diverge and is not deflected, additional solenoid and dipole magnets are needed to compensate the divergence and deflection of the antiproton beam. These additional magnets are a compensating solenoid and a so-called chicane consisting of two dipole magnets. It is essential to match the magnetic fields of the chicane and the compensating solenoid with the spectrometer magnets. Detailed information about the spectrometer magnets and the compensation magnets can be found in the technical design report of the magnets [75].

3.4.3 Tracking Systems

PANDA provides four different tracking systems, where three tracking detectors are located in the target spectrometer and the last one in the forward spectrometer. In the following section all tracking detectors are described.

3.4.3.1 Micro Vertex Detector

The **Micro Vertex Detector (MVD)**, shown in Fig. 3.7, is the innermost tracking detector in the target spectrometer. Its main goal is the precise measurement of the impact parameter of a

track close to the interaction point. Here, the D meson decay is of particular interest. D mesons have a displaced vertex of a few hundreds micrometer. Therefore, the aim of the high spatial resolution of the **MVD** is to better distinguish daughter particles originating from the displaced vertex of the D meson from the background.

The **MVD** is a semiconductor detector consisting of silicon pixels and silicon strips. In total the detector will consist of about 10.3 million pixels and 200,000 strip readout channels to enable the high spatial resolution of the detector [76]. As a semiconductor detector, its working principle is based on the generation of electron-hole pairs by ionization. Ionization occurs when a charged particle passes through the silicon. An electric field then causes the electrons to move which leads to an electric current. The measurement of this current provides information on whether a pixel or strip has been hit. From this information and the precise knowledge of the position of the individual pixel or strip, 3D position information can be reconstructed with a precision depending on the granularity of the detector pixels and strips and the charge resolution. In addition, information about the energy loss of the particle is given due to the amplitude of the measured charge. Thus, the **MVD** is able to generate information about the momentum and the particle type. In order to cover nearly the full solid angle, the **MVD** consists of a barrel part and a forward end cap. In the barrel part the silicon sensors are arranged in four layers with an inner radius of 25 mm and an outer radius of 135 mm. In the innermost region, the hit density is particularly high and therefore a high granularity is required here. For a high-precision measurement in this region, the layers 1 and 2 consist of silicon hybrid pixels (shown in red in Fig. 3.7). Each pixel-module consists of a 116×110 cell matrix, with each cell having a side length of $100 \mu\text{m}$, so that the **MVD** provides a spatial resolution on the order of several tens of μm , *i.e.* in the x-direction of $\sigma_x = 6.9 \mu\text{m}$ [76]. The two outer layers (3 and 4 shown in green) in the barrel part are double-sided silicon strip layers. Different shapes and dimensions are foreseen to minimize the material budget and thus minimize multiple scattering in the silicon layers. As an example, the three different geometries for the strip part are shown in Fig. 3.8. The largest sensor has 512×896 strips on an active area of $58.3 \times 33.3 \text{ mm}^2$. Here a spatial resolution in the x-direction of $\sigma_x = 12.4 \mu\text{m}$ can be achieved [76].

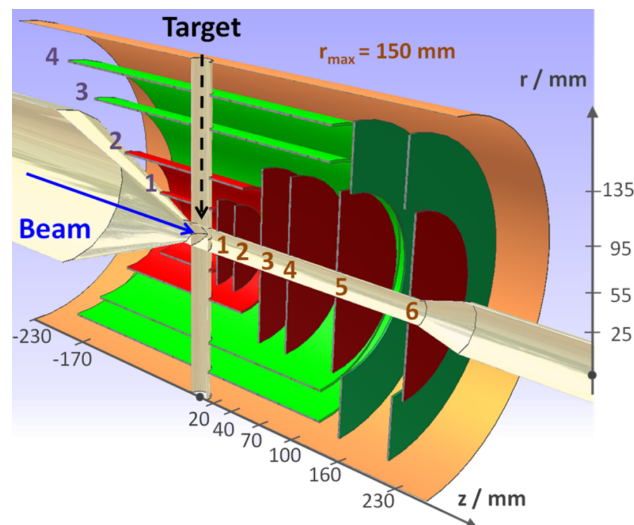


Figure 3.7: Conceptual sketch of the Micro Vertex Detecor (**MVD**) consisting of four layers of silicon sensors in the barrel part and six sensor discs in the endcap [76].

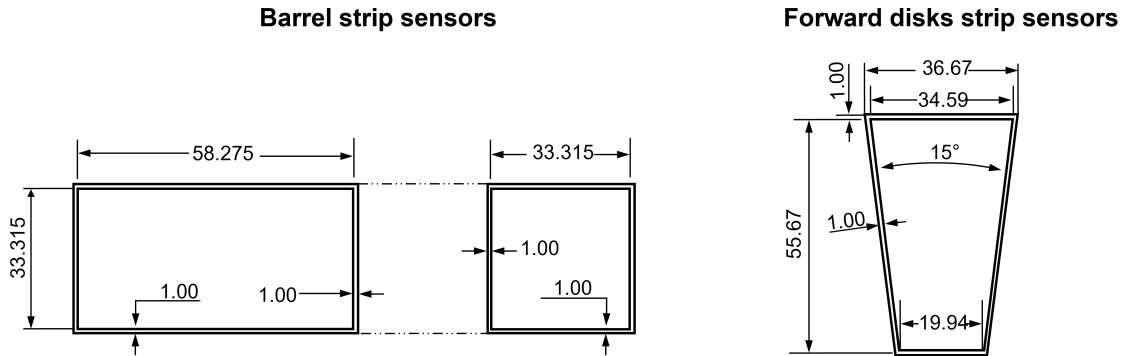


Figure 3.8: Geometry of the different silicon sensors installed in the **MVD**. On the left and in the middle a silicon strip sensor of the barrel part is shown and on the right a trapezoidal strip sensor for the end cap is visualized. All distances are in units of mm. Picture based on [76] and [77].

In total, the **MVD** covers polar angles from 3° to 150° , with the barrel part covering 40° to 150° and the angles 3° to 40° are covered by the forward endcap. The endcap consist of six disks arranged perpendicular to the beam axis. The first four disks consist of pixel sensors (shown in red), the last two disks are a combination of pixels and strips (shown in red and green). The outer strip sensors have a trapezoidal shape. The positioning of the different silicon sensors is shown in Fig. 3.9. Here, the pixel sensors are visualized in green, the strip sensors are indicated in gray and the trapezoidal sensors of the end cap in yellow.

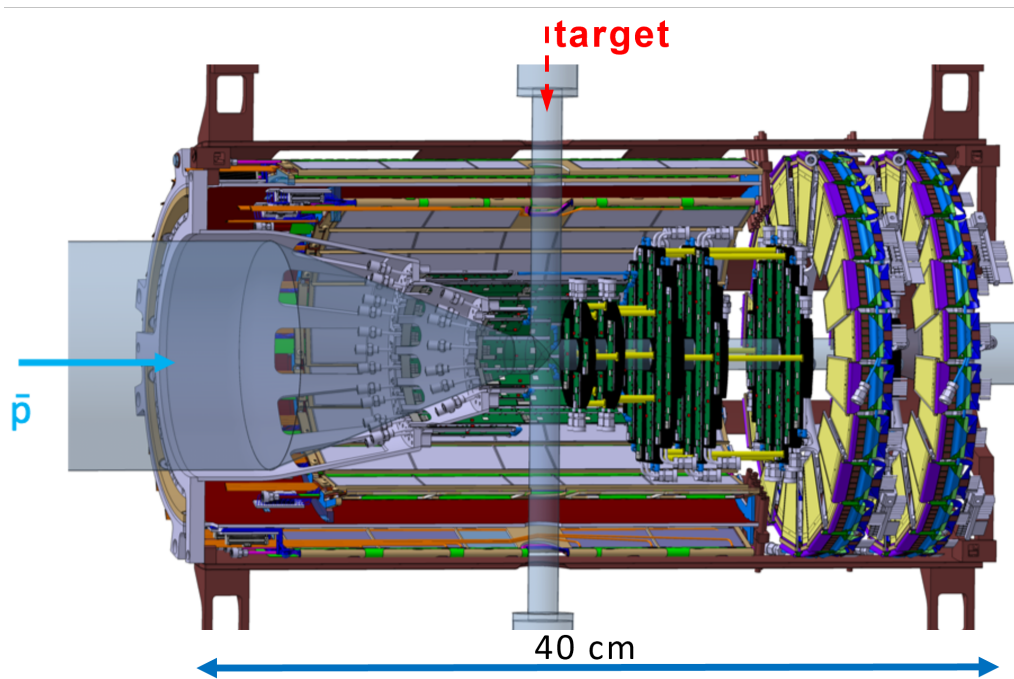


Figure 3.9: A detailed view of the **MVD** showing the location of the different silicon sensors [78]. The pixel sensors are shown in green, in gray the strip sensors for the barrel part are illustrated and in yellow the trapezoidal sensors for the end cap discs are shown.

The **MVD** has to cope with **PANDA**'s high event rate of 2×10^7 events/s. Therefore, a fast and flexible readout electronics is necessary providing a time resolution of less than 10 ns. The time resolution is important for the event separation. Here, **HESR** operates in time intervals of $2 \mu\text{s}$, so-called bursts, with $1.6 \mu\text{s}$ of beam on target, followed by a 400 ns gap without beam. Within one burst 3–4 events are expected. The overlapping events make it difficult to determine the start time for each event. However, the start of an event is an important parameter for other detectors like the **Straw Tube Tracker (STT)** (see sec. 3.4.3.2). With the high time resolution, the **MVD** is able to separate events within a burst and thus determine the start time of an event. In addition, the material must be able to withstand the time-integrated event rate and therefore needs to have a high radiation hardness of $5 \times 10^{14} \text{ n}_{\text{eq}}/\text{cm}^2$ [79]. A detailed overview of the **MVD** can be found in the technical design report [76].

3.4.3.2 Straw Tube Tracker

The **Straw Tube Tracker (STT)**, shown in Fig. 3.10, comprises the largest volume for track finding in the target spectrometer and is therefore **PANDA**'s main tracking detector in the barrel part. It consists of 4224 gas filled drift tubes densely packed around the beam axis. The **MVD** is surrounded by the **STT**, which is located at a radial distance from 15 cm to 41.8 cm with a length along the beam pipe of 140 cm and covers a polar angle of 10° to 140° . The drift chamber based detector structure of the **STT** has beneficial properties like a small radiation length of 1.2% for a particle traversing all 26 layers of the **STT** radially or a high radiation hardness in terms of aging effects. The straws are organized in a hexagonal shape with 18 layers of tubes parallel to the beam axis and 8 layers slightly rotated by $\pm 3^\circ$.

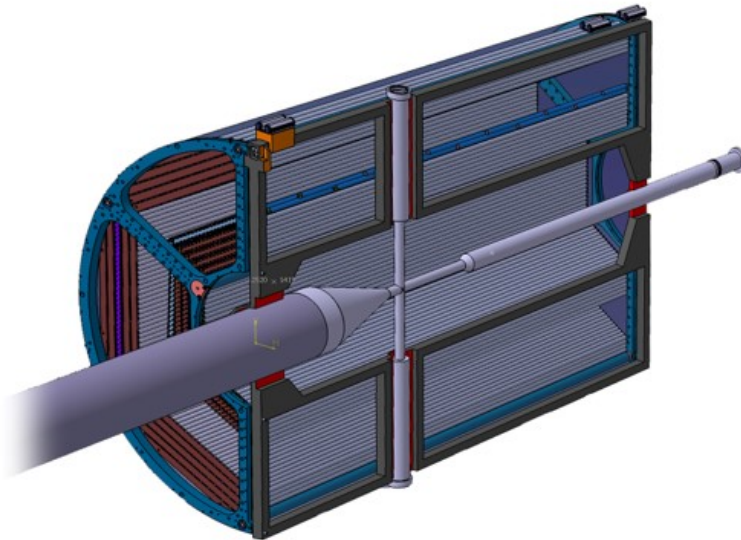
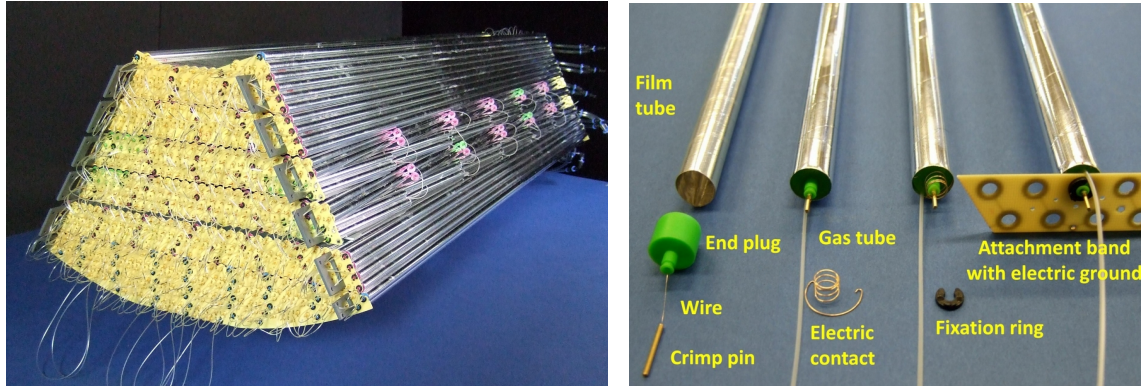


Figure 3.10: Half-section view of the basic structure of the Straw Tube Tracker. In the middle the beam pipe is shown. The **STT** surrounds the beam pipe with a radial distance ranges from 15 cm to 41.8 cm and an active length of 140 cm. Image taken from [80].



(a) One of the six segments of the STT is shown. The axial tubes in the inner and outer region are visible as well as the eight skewed layers in between. Credit: Peter Wintz (IKP, FZ Jülich) [81].

(b) Single Straw Tubes with electric contacts for the anode wire and the cathode wall. Picture taken from [82].

Figure 3.11: Pictures of the STT construction.

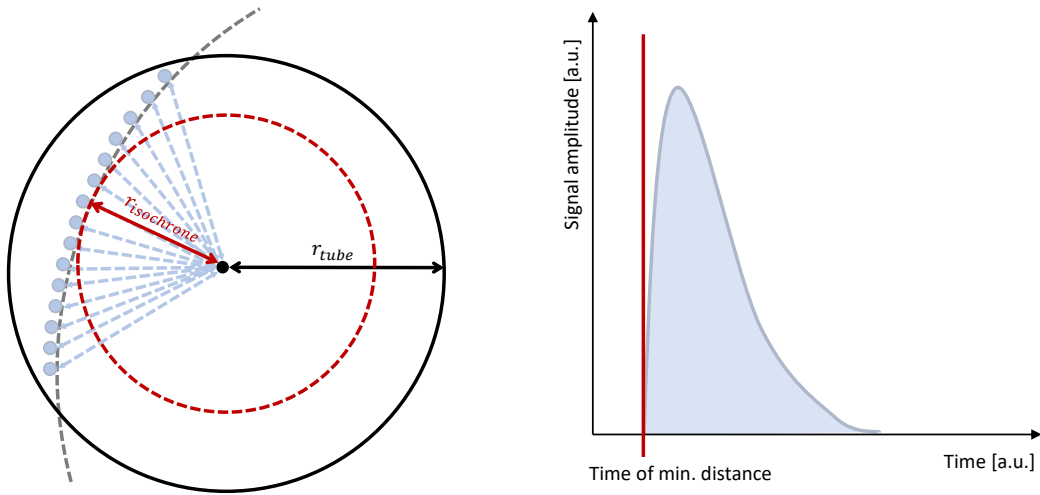
In Fig. 3.11a one sector of the six hexagonal subelements is shown. Here it is visible that the STT consist of an inner and outer part of axial tubes and a range of skewed layers in between. In Fig. 3.11b the components of the individual straw tubes are shown. Each straw tube has an inner diameter of 1 cm and is filled with a gas mixture consisting of 90 % argon and 10 % carbon dioxide as a quenching gas. The gold-plated tungsten/rhenium wire in the middle of the tube acts as anode and has a thickness of 20 μm . The cathode is represented by the wall of the tube and is made of double-layered, aluminized polyester foil (Mylar foil) of 27 μm thickness. To keep the straw tubes in shape and to ensure a constant tension of the anode wire, the tubes are operated with 1 bar overpressure.

The working principle of a single straw tube is shown in Fig. 3.12. When a charged particle travels through the drift tube, it ionizes the gas in the tube (Fig. 3.12a). The electrons resulting from the ionization move to the anode wire due to the electric field between the anode and cathode. The applied voltage in the kV range is sufficient to produce an avalanche, with a signal amplification of the electrons of $10^4 - 10^5$. The detector response is then an electric signal pulse induced on the wire by the electrons in the avalanche. The signal pulse is shown in Fig. 3.12b. The start time of the pulse corresponds to the arrival time of the first electron, *i.e.* the electron with the shortest distance to the anode. This drift time encodes a radius, thus defining a circle. This circle is called the isochrone circle because it corresponds to all the points of closest approach with the same drift time. Determining the drift time of the electron closest to the anode is a challenging process, as described in [83]. Basically, the measured time signal of the straw tube consists of several components, as given in equation 3.3.

$$t_{\text{STTSignal}} = t_{\text{DriftTime}} + t_0 + t_{\text{ToF}} + t_{\text{Offset}} \quad (3.3)$$

Here, t_0 describes the start time of the event measured by *e.g.* the Time-of-Flight detector. The time of flight t_{ToF} describes the time taken by the particle to travel from the IP to the straw tube. The last component t_{Offset} is the time delay of the signal caused by the electronics. Considering all these components, it is possible to measure the drift time spectrum for each straw tube, as shown in Fig. 3.13a. Assuming a uniformly illuminated straw tube, the drift time spectrum can

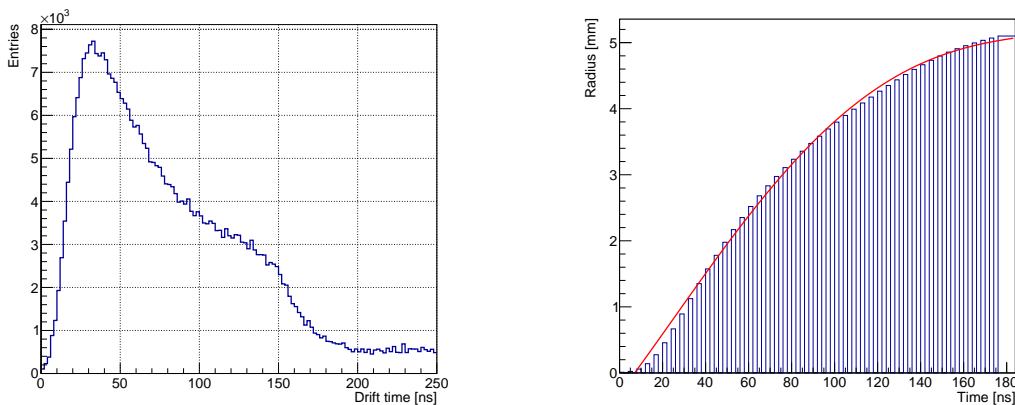
be used to determine the radial distance as a function of drift time. Here, the maximum time of the spectrum corresponds to the radius of the straw tube, *i.e.* 5 mm. Finally, the integrated drift time spectrum (shown in Fig. 3.13b) is inverted to produce a calibration curve that maps the drift time of an electron to the corresponding distance in the drift tube, which is the isochrone radius of the hit. Considering the isochrone information and the calibration, the STT has a spatial hit resolution in the x-y-plane of about $150\ \mu\text{m}$. Thus, the isochrone information significantly improves the spatial resolution of the detector. Without isochrone information a resolution of $1/\sqrt{12}\ \text{cm}$ must be assumed.



(a) A charged particle ionizes the gas in the tube and the electrons drift to the anode wire. All the points of closest approach of the track to the anode wire define the isochrone circle.

(b) The earliest arrival time of the drift electrons is a measure of the minimum radial distance of the track to the wire.

Figure 3.12: Working principle of a single straw tube.



(a) Drift time spectrum of a single straw tube.

(b) Calibration curve of a single straw tube to determine the isochrone radius from the drift time.

Figure 3.13: Drift time spectrum and calibration curve of a straw tube [84].

Additionally, it is important to note that the axial tubes of the **STT** do not provide any information about the z-component of the hits. This is the reason why **PANDA** included the skewed layers. The eight skewed layers provide z-information with a spatial resolution of about 3 mm by being rotated by an angle of $\pm 3^\circ$ relative to the beam axis. Further details of the **STT** can be found in [82] and [83]. The parameters and dimensions mentioned in this paragraph are updated values from the technical design report, taken from private communication with the developers of the **STT** [85].

3.4.3.3 Gas Electron Multiplier

The **Gas Electron Multiplier (GEM)** detector is the last tracking detector in the target spectrometer. It is located close to the forward endcap and therefore represents the connection between the barrel part of **PANDA** and the forward tracking system. It covers polar angles between 3° to 20° and consists of three double planes at distances of 117 cm, 153 cm and 189 cm downstream from the **IP** and diameters of 90 cm, 112 cm and 148 cm. In Fig. 3.14 the three **GEM** planes are shown.

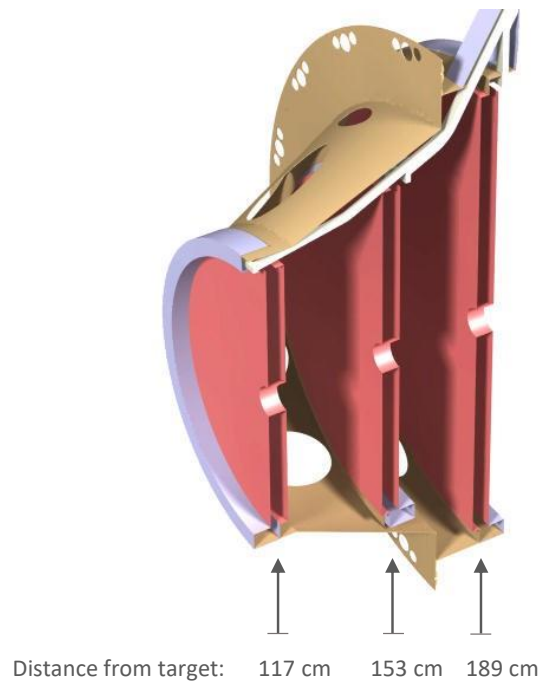
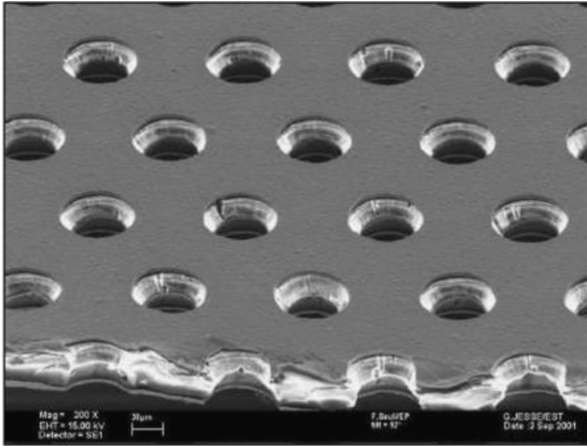


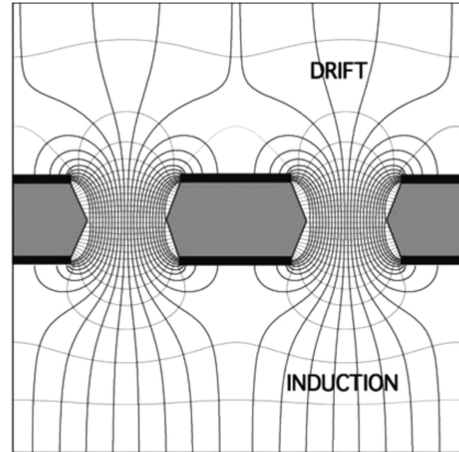
Figure 3.14: Structure of the **GEM** detector. The three double planes of the **GEM** detector are located downstream from the target.

It is designed as gaseous micropattern detector with **GEM** foils as amplification. The gaseous micropattern detectors provide a homogeneous electric field and include a Ne/CO_2 gas mixture. The **GEM** foils are composed of $50\ \mu\text{m}$ thick kapton foils with a $2\text{-}5\ \mu\text{m}$ thick copper coating. The foil is perforated with tiny holes of a diameter of about $70\ \mu\text{m}$ and a hole density of $10^4\ \text{holes}/\text{cm}^2$ as shown in Fig. 3.15a [86][87]. If a charged particle ionizes the gas, the electrons will be guided by the electric field to the **GEM** foils. In the tiny holes of the **GEM** foil the electric field lines are focused and causes an electron multiplication (Fig. 3.15b). The total amplification

rate after the three GEM foils is expected to be a factor of 10^4 . The readout pads are electrodes with a size of about 1.5 mm arranged in a hexagonal pattern. The entire read-out plane of the GEM detector will have about 80,000 electrodes to measure the position of the incoming electrons. The final GEM hit creation is then performed by a clustering algorithm that combines the signals from adjacent pads originating from one hit into a cluster. The hit position is then reconstructed by a weighted mean of all pads within a cluster. With this method, a 3D position resolution of about $100\ \mu\text{m}$ can be achieved.



(a) Perforated GEM foil with high hole density [88].

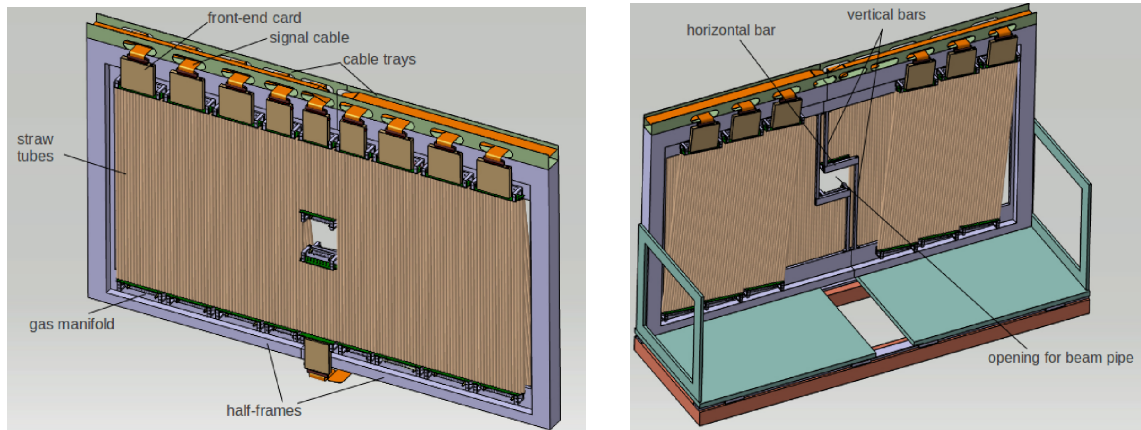


(b) Working principle of the GEM foil [88].

Figure 3.15: Picture of a GEM foil with high hole density on the left and principle of a GEM foil on the right.

3.4.3.4 Forward Tracker

The **Forward Tracking System (FTS)** is the tracking detector that detects forward boosted tracks in a polar angle region below 10° in the horizontal plane and below 5° in the vertical plane [89]. The tracking system is based on the same straw tubes used for the **STT**. Here the straw tubes are arranged in planes perpendicular to the beam pipe. In total there are three pairs of tracking stations in the forward direction. The first pair is located directly after the target spectrometer and before the dipole magnet at distances in the z -direction of 2.954 m and 3.274 m. They consist of 1024 straw tubes each. The second pair is located inside the dipole magnet at distances of 3.945 m and 4.385 m and consist of 1536 tubes each. The last pair is located behind the dipole magnet at distances of 6.075 m and 7.475 m. Here 3200 and 4736 straws are installed. Each tracking station consists of four double-layers of straw tubes. The first and the last double layer contain vertical tubes with 0° , the two double layers in the middle contain skewed tubes rotated by $+5^\circ$ and -5° , as shown in Fig. 3.16. Using parallel and skewed tubes, the FTS is able to provide 3D position information with a resolution of about $100\ \mu\text{m}$ perpendicular to the straw axis, similar to the **STT**. Due to the magnetic field of the dipole magnet charged particles will be deflected. In combination with the low material budget of $0.3\% X_0$ per tracking station this enables a momentum reconstruction with a resolution of 1%. For the FTS a track multiplicity of about one track per event is expected.



(a) A double layer of the FTS with vertical straw tubes.

(b) A double layer of the FTS with straw tubes rotated by 5° .

Figure 3.16: Schematic illustration of a double layer of the FTS. Pictures taken from [90].

3.4.4 Particle Identification

The next essential step is the **Particle Identification (PID)**. For this purpose, **PANDA** has several different detector systems. Basically, the subdetectors for **PID** can be divided into detectors specialized for low momentum tracks below $1 \text{ GeV}/c$ and tracks above $1 \text{ GeV}/c$. For low momentum tracks, **PANDA** provides Time-of-Flight detectors, for tracks above $1 \text{ GeV}/c$ Cherenkov detectors are used. An additional detector system is specialized for muon detection. These dedicated detectors for **PID** are presented in the following subsections.

3.4.4.1 Time of Flight Detectors

PANDA has two **Time-of-Flight (ToF)** detectors, one in the barrel part [91][92] and one in the forward part [93]. The detector consist of scintillating material. When a charged particle travels through the detector, the material will be excited and releases the energy in form of visible light. The light is then directed to a photocathode, which converts the light signal into an electric signal that is amplified by a photomultiplier. This signal enables the measurement of a reference time at which the charged particle hit the **ToF** detector and a position information because the detector system is highly granular. Since **PANDA** has no detector providing a start time of the event, both **ToF** detectors are relative Time-of-Flight counters. This means that the particle identification with the **ToF** detector in **PANDA** is based on an iterative algorithm where a hypothesis for the species of each measured particle is evaluated based on the measured times, assuming the same start time of the event for each particle.

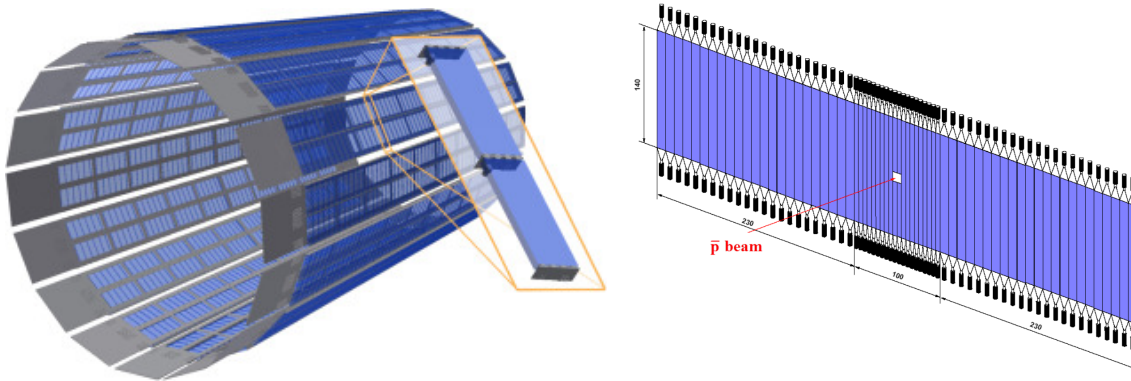
Barrel ToF

In the target spectrometer, the barrel-**ToF** detector surrounds the **STT** with a radius of 50 cm and covers a polar angle of 22.5° to 140° . The acceptance in the z -direction ranges from -50 cm to 150 cm relative to the **IP**. The detector has to fulfill several requirements. In order to minimize the disturbances in subsequent detector parts like the electromagnetic calorimeter the radiation length must not exceed a few percent. In addition, the Barrel **ToF** will be placed inside the

solenoid magnet. This means it must consist of a non-magnetic material and the space limitations and event rate have to be considered. To fulfill these requirements the detector is made of 1920 scintillator tiles, each 20 mm thick with a surface area of $87 \times 29.4 \text{ mm}^2$. The scintillator tiles are arranged in a 2×60 matrix array, which is called a supermodule. In total, the detector consist of 16 fully independent supermodules. The structure of the Barrel ToF detector is shown in Fig. 3.17a. The material of the plastic scintillators is optimized for fast response and good time resolution with the best time resolution of about $\sigma_t \sim 55 \text{ ps}$. With this time resolution, the detector exceeds the original design goal of 100 ps.

Forward ToF

In the forward spectrometer a flat ToF wall is foreseen to detect and perform particle identification on hadrons with a momentum below 4 GeV/c. The wall will be placed at 7.5 m downstream of the IP and consist of 66 scintillator plates. In the central part 20 plates with a width of 5 cm are attached, in the outer region 23 scintillators with 10 cm are placed on each side (see Fig. 3.17b). In total a width of 5.6 m is covered. One scintillator plate has a height of 140 cm and a thickness of 2.5 cm. As material the plastic scintillator BC-408 is used which has good timing parameters. For the forward ToF the same time resolution of 100 ps as for the Barrel ToF is specified. In prototype experiments time resolutions of 70 ps could be reached [93].



(a) Structure of the Barrel ToF detector consisting of 1920 scintillators tiles [92].

(b) Design of the Forward ToF as a flat wall. The precision of the inner region is twice as high as the outer region because scintillators with 5 cm width are used instead of 10 cm [93].

Figure 3.17: Design of the Time-of-Flight (ToF) detectors. On the left the Barrel ToF is shown, on the right the Forward ToF.

3.4.4.2 Cherenkov Detectors

For particle identification of particles with momentum above 1 GeV/c *PANDA* has different Cherenkov detectors in the barrel and the forward part. Cherenkov detectors are based on detecting Cherenkov light. This is light emitted when a particle traverses a dielectric medium with a speed higher than the speed of light in that medium. The Cherenkov effect is thus the optical counterpart of the sonic boom. The angle of the emitted light cone (θ_C) depends on the

velocity v of the particle and the refractive index n of the medium:

$$\cos(\theta_c) = \frac{1}{n\beta}, \quad (3.4)$$

with $\beta = \frac{v}{c}$ and c the speed of light. The information about the emission angle and the measured momentum of the particle by the tracking detectors yields information about the particle's mass. PANDA has two different types of Cherenkov detectors: The **Detection of Internal Cherenkov Light (DIRC)** detector is located in the target spectrometer and the **Ring Imaging Cherenkov (RICH)** detector detects particles in the forward spectrometer.

DIRC

The **DIRC** detector, described in detail in the technical design report [94], is divided into a barrel part and a disc system. The barrel part is located between the **STT** and the electromagnetic calorimeter. It shares the construction with the Barrel ToF detector, where the Barrel ToF has a slightly larger radius, as shown in Fig. 3.18 This compact construction system in the target spectrometer is advantageous because all detector systems must be housed inside the solenoid magnet and therefore have very strict space limitations. The disc system is located in the endcap after the **GEM** detector.

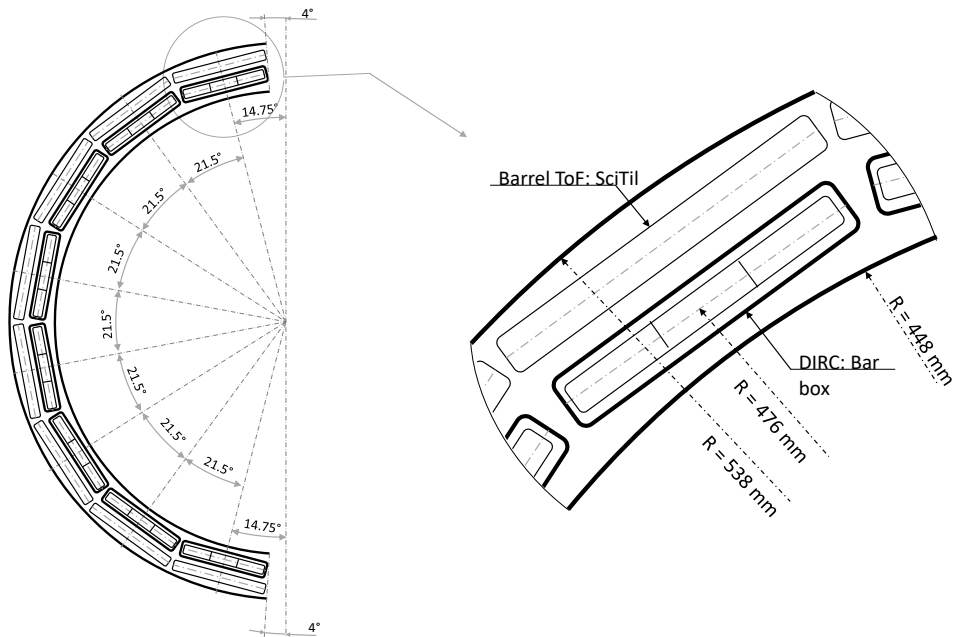
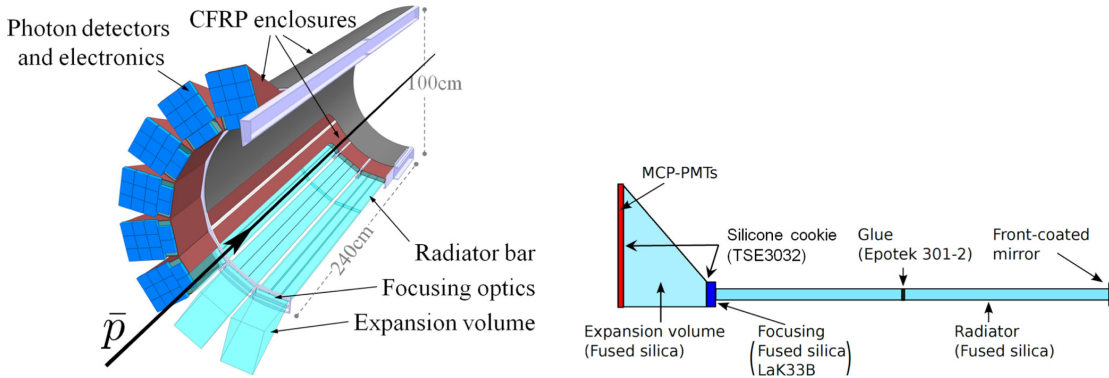


Figure 3.18: Schematic illustration of the mechanical structure holding both the Barrel DIRC detector and the scintillator tiles of the Barrel ToF detector [94].



(a) The 16-sided polygonal cylinder of the Barrel DIRC with radiator bars, focusing optics and expansion volume [94].

(b) Schematic side view of one sector of the Barrel DIRC with radiator bar, focusing optics and expansion volume [94].

Figure 3.19: Design of the Barrel DIRC detector.

The Barrel DIRC has a radial distance of 47.6 cm and a length of 2.4 m. It covers polar angles of 22° to 140° and is able to cleanly separate pions from kaons for momenta from 0.5 GeV/c to 3.5 GeV/c with a precision of at least three standard deviations. The detector uses internally reflected Cherenkov light and consists of 16 independent sectors arranged side-by-side to form a 16-sided polygonal cylinder as shown in Fig. 3.19a. Each sector consists of a so-called bar box and a quartz prism forming the expansion volume (see Fig. 3.19b). The bar box is made of three radiator bars made of fused silica with a refractive index of $n = 1.473$ to produce the Cherenkov light. The material is chosen because of its properties like radiation hardness, light transmission and dispersion. Each bar is 17 mm thick, 2400 mm long and 53 mm wide. The light is reflected via total reflection in the direction of the photon detectors. For a maximum light yield, each bar has a mirror at the forward end that additionally reflects light, which would otherwise have left the prism at the forward end. The light is reflected to the focusing lens system and the expansion volume with the photon detectors. The expansion volume is also made of fused silica. It has a length of 30 cm and an opening angle of 33° . At the end of the expansion volume an array of 11 lifetime-enhanced Microchannel Plate Photomultiplier Tubes (MCP-PMT) each with 8×8 pixels of $6.5 \text{ mm} \times 6.5 \text{ mm}$ size is attached. The MCP-PMTs are located outside the region of possible particle tracks. This method has the advantage that the Cherenkov detector can be built to be much more compact than conventional Cherenkov detectors. The MCP-PMTs enable the measurement of the location and the arrival time of the photons with resolutions of 2 mm and 100 ps, respectively.

A second DIRC detector in disc geometry is mounted on the endcap [95]. It has a maximum radial size of 150 cm and is divided in four optically separated quadrants forming a dodecagon to cover polar angles of 5° to 22° (Fig. 3.20). The endcap disk is also made of fused silica and has a thickness of 2 cm. The particle creates Cherenkov radiation in the radiator which is then transmitted via total reflection towards the Readout Modules (ROM), as shown in Fig. 3.20b. Each outward-facing side of the radiator contains eight ROM units, where each ROM unit houses three readout units. The readout units are made of a quartz bar and a Focussing Element (FEL). The mirror is attached at the outer side of the FEL, which focuses the photons onto the MCP-PMT. To further reduce dispersion effects, an optical filter is placed in front of the

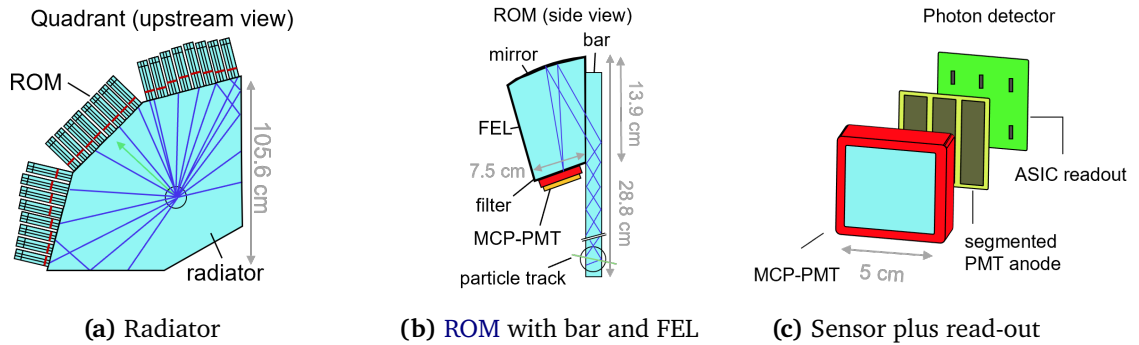


Figure 3.20: Design of a quadrant of the disc DIRC. Images taken from [96].

MCP-PMT, which enables a precision of a few mrad. Overall, a resolution of about 2 mrad can be achieved.

RICH

A aerogel-based Ring Imaging Cherenkov Counter (RICH) is used in the forward spectrometer. It covers polar angles smaller than 10° in the x-direction and smaller than 5° in the y-direction to separate pions and kaons in a broad momentum range of 2 GeV/c to 10 GeV/c. The detector is designed as a double layer radiator with different refracting indices of aerogel and gas. The aerogel layer is limited to a thickness of about 4 cm. The overall dimensions of the detector are $3 \text{ m} \times 1 \text{ m} \times 0.8 \text{ m}$. Particles traversing the radiator layers produce Cherenkov light, which is then focused by a mirror to an array of photomultipliers outside the active volume. The basic design of the RICH detector is shown in Fig. 3.21. Recent tests showed a separation accuracy of pions and kaons of at least three standard deviations across the momentum range of 2 GeV/c to 10 GeV/c. A separation of muons and pions can also be achieved with an accuracy of three standard deviations for momenta of 0.5 GeV/c to 2 GeV/c. Further information about the RICH detector can be found in [97].

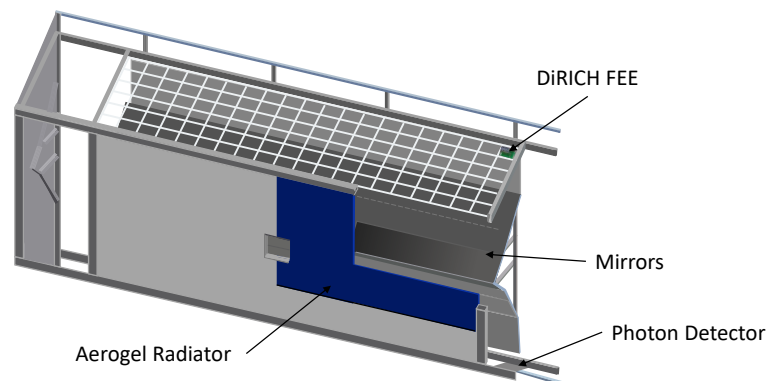


Figure 3.21: Schematic Illustration of the Forward RICH detector. Image is based on [97].

3.4.4.3 Muon Detector

For muon identification, **PANDA** provides a muon detector based on the range system technique located outside the magnets. This technique consist of alternating layers of iron absorbers and **Mini Drift Tube (MDT)** detectors. The **MDTs** are made of aluminum drift tubes with an anode wire in the center of the tube. They are operated either as drift tubes or in a proportional mode and therefore provide 2D position and timing information.

The aim of the muon system is to distinguish primary muons from background originating from low momentum pions or secondary muons. The range system offers the possibility to roughly determine the energy of the muons stopped by the iron absorber as well as the minimum energy of the muons not stopped by the iron absorber, since iron has a stopping power of about 1.5 GeV per meter for relativistic muons with $dE/dx \approx 2 \text{ MeV}\cdot\text{cm}^2/\text{g}$. Pattern recognition, matching the tracks found with the **MDT** layers with the tracks found with the tracking detectors inside the magnet, enables the identification of primary muons which are relevant for the decay channels of interest. The muon system is able to identify muons with momenta up to 10 GeV/c. In the target spectrometer three muon systems are installed. The first one is the barrel muon system surrounding the solenoid magnet. The second and third systems are the endcap muon system and the muon filter after the endcap. A forward range system is placed in the forward spectrometer.

The barrel part consist of 13 sensitive layers alternating with iron absorber layers. All layers have a thickness of 3 cm except for the first and last iron absorber which have a thickness of 6 cm. In total the barrel part consist of 2133 **MDTs**.

For the endcap and the muon filter 6 cm thick iron absorbers are used for a better detection of muons with higher energies. Six sensitive layers with a total of 618 **MDTs** and five iron absorbers are installed in the endcap. The muon filter after the endcap in the gap between the solenoid and the dipole magnet consist of five sensitive layers with 424 **MDTs** and four iron absorbers. The purposes of the muon filter are to increase the absorber depth and to serve as a magnetic shield between the solenoid magnet and the dipole magnet.

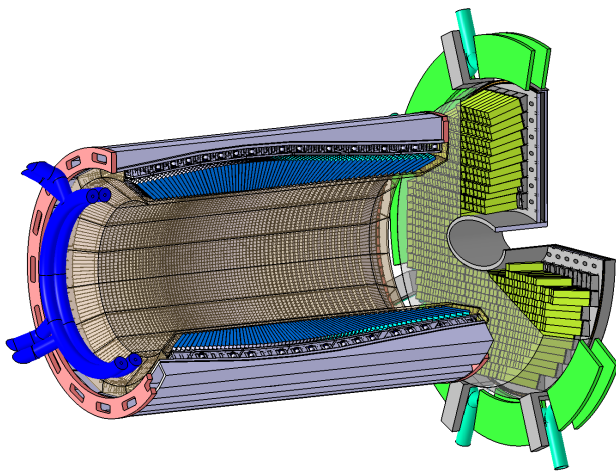
In the forward spectrometer the **Forward Range System (FRS)** is installed at a distance of about 9 m from the target. It detects high momentum muons at low angles. The **FRS** consists of four modules, each consisting of four iron layers and four detector layers. A total of 16 iron plates, each 6 cm thick, and 576 **MDTs** are installed in the forward spectrometer. Further information about the muon detector is presented in [98].

3.4.5 Electromagnetic Calorimeters

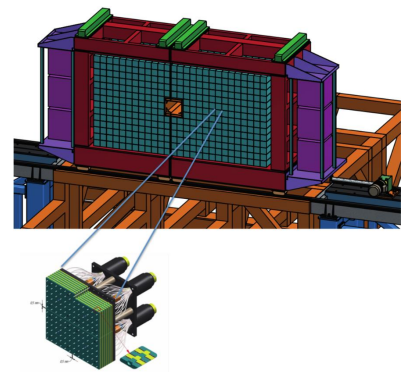
To determine the energy of the particles and thus improve the identification and resolution, **PANDA** is equipped with several **Electromagnetic Calorimeters (EMCs)**. These calorimeters stop electromagnetically interacting particles, such as electrons, positrons or photons, by an absorber material. The absorber induces an electromagnetic shower in which electrons emit bremsstrahlung photons, which in turn each form an electron-positron-pair. This proceeds until the electron energy falls below the so-called critical energy E_c . Below E_c the electrons primarily lose energy by ionizing the surround material. The absorber consists of a scintillator material, that converts the energy of the electron into optical wavelength photons that can be measured by a photomultiplier. The calorimeters in **PANDA** are divided into calorimeters in the target spectrometer [99] and a calorimeter in the forward spectrometer [100].

3.4.5.1 Target Spectrometer Calorimeter

The target spectrometer calorimeter is located inside the solenoid magnet and shown in Fig. 3.22a. Covering almost the entire solid angle it consists of a barrel part with a length of 2.5 m and includes two endcaps. It is designed as a homogeneous lead tungstate ($PbWO_4$) calorimeter comparable to the one used in the CMS experiment at CERN. Lead tungstate is an inorganic scintillator, and the version used by PANDA has been optimized for a high light yield with a factor of two higher than the one used by the CMS experiment. The light yield can be further improved by a factor of four by operating the detector at temperatures of -25°C instead of 25°C . Furthermore lead tungstate has a good radiation hardness, that can withstand the expected radiation dose of 125 Gy per year at full luminosity. The calorimeter consists in total of 15,744 $PbWO_4$ crystals, each with a front size of $2.1 \times 2.1 \text{ cm}^2$ and an average mass per crystal of about 0.98 kg. The crystals are wrapped in a highly reflective foil and stabilized by light-weight carbon fiber alveoles. In the barrel part 11,360 crystals are arranged at a radial distance of 57 cm around the target. The forward and backward endcap are constructed with 3856 and 524 crystals, respectively. The crystals have a length of 20 cm corresponding to a radiation length of $22X_0$ and are able to cover energies between 10 MeV and 15 GeV. Here the covered energy range depends on which part of the calorimeter is considered. The barrel part is able to cover polar angles of 22° to 140° , where an energy range of 10 MeV to 7.3 GeV is expected. The forward endcap covers small polar angles of 5° to 23.6° . Here high energies between 10 MeV to 14.6 GeV are expected. In the backward region the endcap covers polar angles of 151.4° to 169.7° with energies between 10 MeV and 0.7 GeV. The lead tungstate crystals provide an energy resolution of 3% at 1 GeV and a good time resolution of 1 ns at energy deposits of 100 MeV. This time resolution enables a good discrimination between events at PANDA's high event rate of 10 million events per second. In addition, the EMC provides a spatial information with a resolution of 1.1 mm at 10 GeV.



(a) CAD drawing of the Electromagnetic Calorimeter in the target spectrometer [99].



(b) Illustration of the Forward Spectrometer Calorimeter [100].

Figure 3.22: Schematic images of the Electromagnetic Calorimeters.

3.4.5.2 Forward Spectrometer Calorimeter

In the forward spectrometer a shashlyk-type calorimeter will be installed (see Fig. 3.22b). It is located behind the dipole magnet between the forward ToF and the forward muon detector at 7 m distance from the target. The planar design of the calorimeter covers an angular range of $\pm 5^\circ$ in the vertical and $\pm 10^\circ$ in the horizontal direction. It consists of alternating layers of lead sheets and polystyrene plastic scintillator tiles. A total of 380 layers, each 1.5 mm thick, are arranged behind each other, achieving a radiation length of $19.6X_0$. In addition, the scintillator plates are wrapped in reflector sheets made of 0.15 mm to 0.2 mm thick Tyvek paper. The active area of the calorimeter is formed by cells with a size of $55 \times 55 \text{ mm}^2$. In total 54×28 cells are installed, which results in an active area of $1540 \times 2970 \text{ mm}^2$. To further improve the light output, the side surfaces are coated with white reflector paint. The forward spectrometer calorimeter covers an energy region from 10-20 MeV to 15 GeV [100] and an energy resolution of $\sigma_E/E = 1\% \oplus ((2-3)\%/\sqrt{E/\text{GeV}})$ is required, where \oplus indicates the quadratic sum. The electronics as well as the photomultiplier are placed separated from the scintillator and lead plate arrangement behind a 30 mm thick aluminium-alloy plate.

3.4.6 Luminosity Detector

To maximize the physics output of PANDA the absolute time-integrated luminosity is needed in order to determine the absolute cross section of specific decay channels. This is of particular importance when performing resonance scans. To determine the integrated luminosity two different approaches exist. The first is an approach independent of PANDA, which is measured by HESR. Here, the time integrated luminosity is directly accessible as the product of the target thickness n_T and the beam current n_B : $L = n_B \cdot n_T$. However, the large drawback of this method is the measurement of the target thickness, which is determined by an analysis of how the target affects the beam properties. This means, for this measurement it is required to turn off the beam cooling system, which makes a concurrent measurement of the luminosity during the PANDA operation impossible. As a consequence, PANDA developed a Luminosity Detector (LMD) capable of measuring the relative luminosity during operation and extracting the total time-integrated luminosity. For this purpose, PANDA measures elastically forward scattered antiprotons at low four-momentum transfer, where the Coulomb and the strong interaction interfere, and back propagates the tracks to the IP. The backpropagated track distribution $N(\theta_{rec})$ depends on the scattering angle θ_{rec} . In this energy region the Coulomb amplitude can be used to get an absolute measure of the luminosity. The luminosity can then be calculated using equation 3.5.

$$N(\theta_{rec}) = L \cdot \int \sigma(\theta_{MC}) \cdot \epsilon(\theta_{MC}) \cdot R(\theta_{rec}, \theta_{MC}) d\theta_{MC}, \quad (3.5)$$

where $\sigma(\theta_{MC})$ is the probability of an antiproton to be scattered into an infinitesimal angle $d\theta_{MC}$ and $\epsilon(\theta_{MC})$ is the detection probability at this angle. The parameter $R(\theta_{rec}, \theta_{MC})$ includes the reconstruction precision of the LMD. With this method, an accuracy of the total time-integrated luminosity of 5% and a precision of the relative time-integrated luminosity of 1% is expected [101]. To achieve this precision goal, track reconstruction and back propagation must be as good as possible. For this purpose, four detector planes will be placed at a distance of 10.5 m downstream from the target. The planes have a radius of 15 cm and are equipped with a total

of 400 thin silicon pixel sensors with integrated front-end electronics, so called HV-MAPS (High Voltage Monolithic Active Pixel Sensors). Each sensor has an area of $2 \times 2 \text{ cm}^2$ and a spatial resolution of $\Delta x = 23 \mu\text{m}$. To reduce track distortion, the detector planes are enclosed in a vacuum box. The **LMD** will measure the polar angular region of 3 to 9 mrad. To achieve the desired absolute accuracy of the luminosity determination, additional data in the range of very low four-momentum transfers below $0.1 (\text{GeV}/c)^2$ are needed. Therefore, an additional experiment located at **HESR**, the **KOALA** experiment [58], will provide the necessary input parameters for the **PANDA** experiment. **KOALA** is located on the opposite side of **HESR** with respect to **PANDA**. It will be operated in parallel to **PANDA** and will measure the differential cross section of the elastic antiproton-proton scattering [102].

3.4.7 Data Acquisition

For the **PANDA** detector, a raw data stream of about 120 GB/s is expected for the low luminosity phase. Before storage on a hard disk drive, this amount of data must be reduced by a factor of 100. Unlike many other experiments, **PANDA** does not use a classical hardware trigger to reduce the data, but performs an online analysis to filter out events with no relevant physical content. This software trigger must operate at high speed and with limited resources. Therefore, an effective **Data Acquisition (DAQ)** is the key element for an efficiently working software trigger. In the following, the steps of **DAQ** are summarized and visualized in Fig. 3.23. The information is taken from the technical design report of the **DAQ** [103].

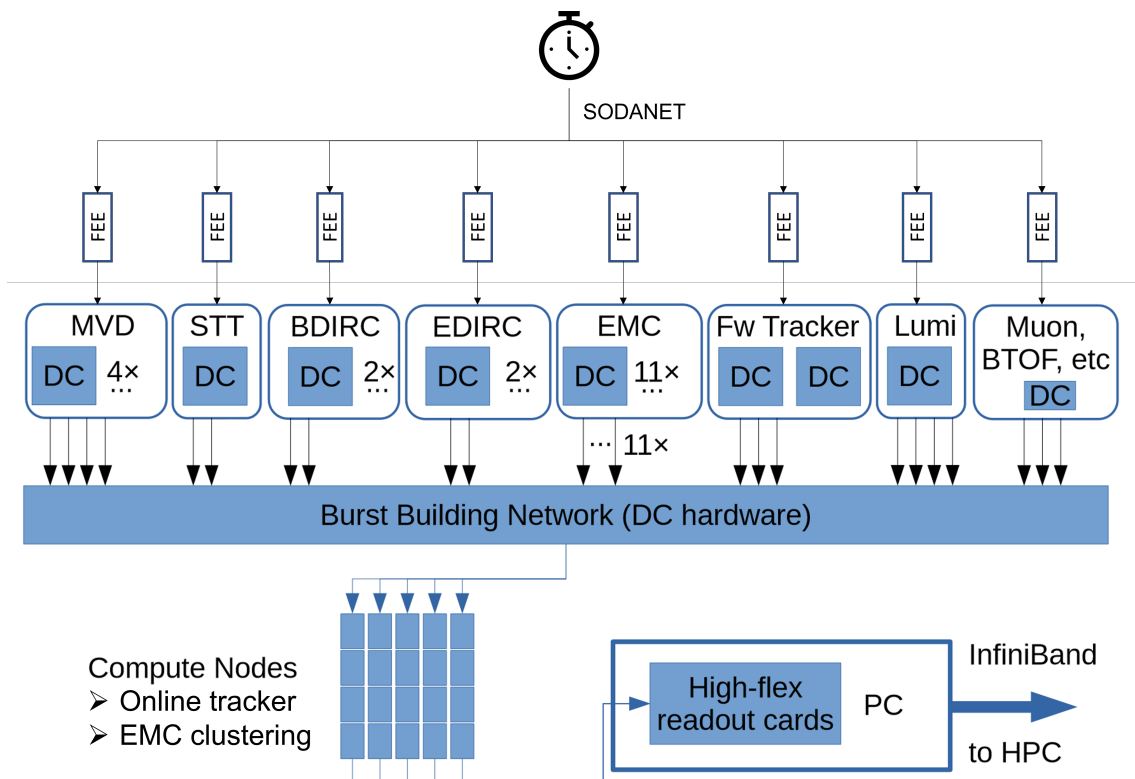


Figure 3.23: The data acquisition chain of PANDA. Picture is based on [103].

In **PANDA**, each subdetector works completely independently with a self-triggered **Front-End-Electronics (FEE)** read-out. Since the read-out speed is different for each detector part, synchronization with a global clock is required to combine hits from different subdetectors. Each **FEE** communicates with the global clock via the SODANET-system. SODA (Synchronization Of Data Acquisition) [104] is a synchronization tool based on signal transmission via optical-fiber connections with a time resolution of about 20 ps. For synchronization, the raw data is buffered in so-called **Data Concentrators (DCs)** and ordered according to their time-stamps. In a next step, the data is collected into so-called bursts by a **Burst-Building Network (BBN)**. A burst is a time period predefined by the HESR operation. HESR has a specific operation pattern with a total duration of $2\ \mu\text{s}$. During $1.6\ \mu\text{s}$ it delivers a continuous antiproton beam followed by a 400 ns gap. This $2\ \mu\text{s}$ pattern is called a burst and typically includes 3 – 4 $\bar{p}p$ collisions. From the **BBN** the data are streamed to the **Compute Nodes (CNs)**. On the **CNs**, the actual online processing of the data is performed. Here, the online algorithms such as an online track finder and fitter as well as a clustering algorithm for the **EMC** are implemented. At this stage of the **DAQ**, a data reduction by a factor of 10 is expected. To ensure the required speed for online computation, the **CNs** are based on FPGAs. For the final event building, the data is then processed by a high-performance computing cluster consisting of GPUs. Here, the final software trigger will reduce the amount of data by another factor of 10.

3.5 Software

The following section presents the software used to simulate realistic performance of the **PANDA** detector. The software is based on **ROOT**, a data analysis framework developed by CERN and used by various physics collaborations [105]. **ROOT** is an object orientated program mainly written in C++. Based on **ROOT**, **FAIR** has developed a simulation, reconstruction, and data analysis tool, that provides the basic methods for all experiments located at **FAIR**. This tool is called **FairRoot** and allows each **FAIR** internal experiment to implement its detector within a common framework [106]. The **PANDA** collaboration extends **FairRoot** by implementing its own software package, **PandaRoot**, that describes in detail the structure and subdetectors of **PANDA** and is therefore able to produce realistic simulations of the detector performance [107]. **PandaRoot** is used for several applications. First, detector performance can be optimized and different subdetector designs can be tested. This allows the detector to be tested in a virtual environment without the need to build detection concepts in reality, that may not be used in the final detector design. As a second point, particle behavior in the detector can be analyzed for an optimal track and event reconstruction. It is possible to get an impression of the weaknesses of the detector that remain after the detector design optimization, and solutions can be developed before data taking. Additionally, software can be implemented and optimized that is needed for the data taking, *e.g.* online track finding algorithms. For the physics analysis, feasibility studies can be performed and expectations for future results can be created. For this purpose, software can be implemented prior to data acquisition.

In the following the different steps from simulation and digitization to reconstruction and analysis are presented. These steps are shown in Fig. 3.24. The first step is the creation of data. As long as no data is taken with **PANDA**, realistic data must be simulated. For this purpose, first an event is generated and the resulting particles are propagated through the detector. In the propagation step the particles interact with the detector materials and produce ideal hits. These

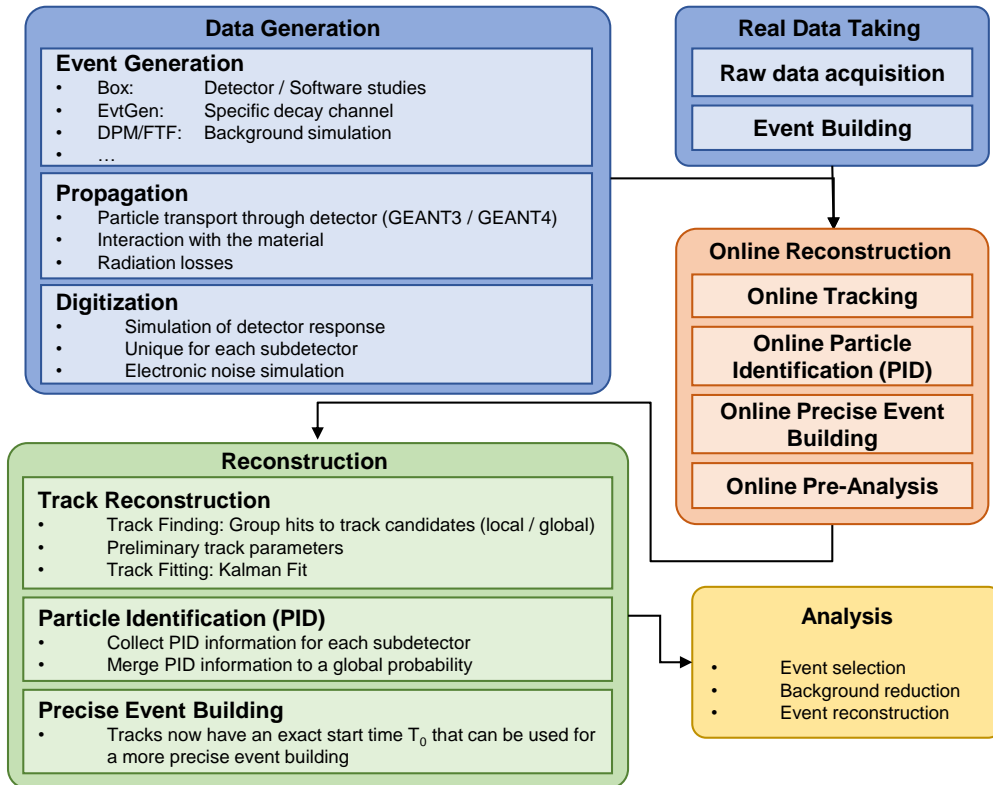


Figure 3.24: Simulation and analysis chain in PandaRoot.

ideal hits must be converted into realistic data points, which is performed in the digitization step. After that, the simulated data are as close as possible to the real data. However, unlike real data, simulation has the advantage that the data can already be stored event wise. In the simulation, it is also possible to mimic the original not-eventwise stored data as the so-called time-based data. In the real data taking case, the assignment of individual hits to a specific event is an additional non-trivial step, which is called event building. Here, the data have to be reconstructed based on information like timestamp and position, and assigned to a specific event. However, it must be noted that multiple events can overlap. After the event building, the software trigger performs an online pre-analysis, to decide if an event is of physical interest and must be stored or can be discarded. Once the data have been created, assigned to its events and passed the software trigger, the tracks must be reconstructed and a particle species identified. In a last step the events can be used for further analysis. Here, usually the event reconstruction is the first step. The individual steps are described in detail in the following sections.

3.5.1 Data Generation

Simulated data are required for any analysis of the performance of PANDA and must be as realistic as possible. Therefore, the data generation is divided into event generation, propagation and digitization. In the event generation, the simulated reaction and the corresponding particles are created. The interaction of these particles with the detector material and further resulting decays are included in the propagation, where the particles are propagated through the detector. For

the simulation of realistic data the digitization is important, where the ideal hits are converted into the expected detector response.

3.5.1.1 Event Generation

For event generation `PandaRoot` provides several generators for different purposes. The most important ones are described below:

- **Box Generator:** The simplest event generator is the box generator. Here, predefined particles are created without physical constraints. No conservation laws or production mechanisms need to be considered. The box generator is usually used for detector or software studies, since all parameters of the created particle, such as momentum, angle or position, can be specified.
- **EvtGen:** For an event generation with physical meaning, where conservation laws are satisfied and branching ratios are considered, EvtGen is used [108]. EvtGen requires an input file with the corresponding decay channel. The decay is written in a simplified form as shown below:

```

1 Decay pbarpSystem
2 1.0 Xi(1820)- anti-Xi+ PHSP;
3 Enddecay
4
5 Decay Xi(1820)-
6 1.0 Lambda0 K- PHSP;
7 Enddecay
8
9 Decay Lambda0
10 Enddecay
11
12 End

```

In the example a $\bar{p}p$ -system is allowed to decay. The second line specifies the daughter particles and their branching ratio. Here the $\bar{p}p$ -system will decay with 100 % into $\Xi^-(1820)\bar{\Xi}$ distributed according to an N-body phase space (PHSP). The lines below indicate the branching ratios of the daughter particles. All physical aspects of the decay, such as angular correlations between daughter particles or probability and spin density matrices, are calculated within EvtGen. However, EvtGen is not able to take the interaction with the detector into account. Therefore, the propagation of the particles and the subsequent decays are managed by GEANT4.

- **DPM:** For a general high-energy particle collision between hadrons or nuclei the Dual Parton Model (DPM) generator is used [109]. The DPM describes soft and semi-soft particle processes without large momentum transfers, that can be calculated via non-perturbative QCD. It is based on the parton structure of hadrons and scattering processes calculated via the Regge theory. Hadrons are collided by exchanging color via colored

fragments. It incorporates elastic scattering and production processes. Usually the DPM generator is used for background studies.

- **FTF:** An alternative to the DPM generator is the Fritiof (FTF) generator for background simulations of hadron or nucleus collisions [110]. The FTF generator simulates high energy collisions as the DPM generator, but uses a different theoretical description. In contrast to the DPM model the FTF generator simulates an interaction without color exchange, but with momentum exchange. At these energies this generally produces two excited states that decay independently [111].

3.5.1.2 Propagation

After event generation, the created particles are propagated through the detector. Here, the interaction with detector material and resulting scattering and decay processes are simulated. This requires a detailed implementation of the detector. Both the active detection material and the passive material used for construction, shielding and magnetic reasons are included. For the propagation the software tools GEANT3 [112] or GEANT4 [113] are used. These take into account electromagnetic and hadronic processes, as well as bending forces in a magnetic field and energy losses due to radiation as particles pass through the material. Both software tools have a common interface that simplifies the handling of the different GEANT versions. This interface is called Virtual Monte Carlo (VMC) [114] and was developed by the ALICE Collaboration. In the propagation Monte Carlo (MC) points and MC tracks are produced. These points contain position and momentum information as well as the energy deposited in the detector and a time information. The MC points do not account for resolution effects and are recorded with perfect precision.

3.5.1.3 Digitization

In the digitization the MC points are converted into realistic detector response signals, which are called digis. The aim of the digitization is to create the most realistic data possible. Therefore, the digitization for each of PANDA's subdetectors varies and mirrors the data generation for each detector as it will be produced in the real detector. Thus, information that cannot be measured by the real subdetector is also not included in the digis. The resolution of the subdetectors is taken into account as well as electronic noise or signal thresholds.

The connection to the MC data is stored in so-called FairLinks. The FairLinks do not contain physical information, but instead the position in the data file and the connection between hits and MC points. This connection is important for later analysis tools to calculate efficiencies or accuracies.

3.5.2 Reconstruction of Charged Particles

After the data generation and digitization the data are reconstructed. The aim is to perform all following steps without MC information. The MC information is only used to calculate efficiencies. For the reconstruction of the data, first the hit points must be reconstructed to particle tracks and then a particle species (e.g. e^\pm , π^\pm , K^\pm , p , \bar{p} , ...) has to be assigned to these tracks.

3.5.2.1 Track Reconstruction

In the track reconstruction phase, detector hits are grouped into track candidates using track finding algorithms. These track candidates are a set of digitized hits and are stored in the data class *PndTrackCand*. In addition, a first estimate of the track parameters can be calculated in this step. After that the corresponding particle track is determined in a track fitting procedure by using the software package GenFit [115]. GenFit is a fitting tool developed by the PANDA collaboration, that basically consists of a Kalman Filter as its core element. The Kalman filter creates a PndTrack object containing the hits of the track as a PndTrackCand and the start and end parameters of the particle track which are the first and last hit with position, momentum and charge information.

Different algorithms exist for track finding, which are further divided into track finding in the target and in the forward spectrometer. It is possible to perform an ideal track finding using the MC data to group into a track candidate all hits that originated from the same MC track. In addition, realistic track finding algorithms have been developed, which are discussed in detail in section 4.3.

A Kalman filter, which is a commonly used tool in track reconstruction, is used for a precise track parameter determination [115]. It has a recursive structure where it starts with an estimate and compares the estimate to the observation, in this case the hit points of the detector. The difference between the estimate and observation leads to a correction of the track model. This correction is then further used to determine the improved track parameters. The Kalman filter takes into account the detector materials and geometry, as well as the magnetic field and energy losses due to radiation. Scattering processes are also considered, as well as the uncertainty of each detector hit. The Kalman filter uses a covariance matrix to calculate the variance of the particle track and provides therefore the final errors of the track parameters as the square root of the diagonal elements of the covariance matrix.

3.5.2.2 Particle Identification

After the track is reconstructed, a particle hypothesis must be assigned to each track. First of all, neutral particles are separated from charged particles. This is done by matching the EMC entries with the charged tracks found by the tracking detectors. After that, the charged particles are further analyzed. In PandaRoot, five particle hypotheses for the charged particles are distinguished: e , π , μ , K , p . In order to identify the type of the particle, the information from all subdetectors must be combined, because each subdetector is specialized in distinguishing specific particle species in different momentum regions. Therefore, particle identification is divided into a local identification, where the information from each subdetector is extracted, and a global identification, where the information of all subdetectors is merged. For the local identification, the following information is used:

- The specific energy loss dE/dx is measured by the MVD and STT. For particle identification the Bethe-Bloch-equation is used. It determines the energy loss as a function of the velocity of the particle. Since the momentum is measured by the curvature of the particle, the velocity leads to the mass of the particle.
- Particles below 1 GeV/c are identified with the Time-of-Flight detectors. Combining the Time-of-Flight information with the path length determined by the tracking detectors

enables the velocity to be determined. Then the mass is calculated with the equation $p = \gamma\beta m$, which is reformulated to $m^2 = p^2 \cdot (1/\beta^2 - 1)$.

- Particles above 1 GeV/c are identified with Cherenkov detectors. The Cherenkov angle $\Theta_c = \arccos(1/(n\beta))$ depends on the velocity of the particle in a dielectric medium with index of refraction n . Since the momentum is given by the tracking detectors, the Cherenkov angle leads to the mass of the particle.
- Muons are identified with the muon detector. The principle is that all particles except muons and neutrinos are absorbed by the inner detector and magnet materials. The muons can then easily be detected behind the shielding.

Each subdetector calculates the probability for a track to be each of the five charged particle hypotheses based on its measurements. In the global particle identification, the information from the subsystems is combined to produce a total probability for the particle to be any one of the five possible particle types. A likelihood scheme is used for this global identification. The likelihood function can then be used to determine the global probabilities using Bayes' Theorem [116].

3.5.3 Event Selection & Reconstruction

At the stage of the event selection and reconstruction all information about the particles (*e.g.* species, momentum, energy, time, position) is given and can be used to combine particles and reconstruct mother particles. For this purpose, `PandaRoot` provides the `Rho` package [117], which contains methods for combining of particles, performing selections and applying fits. Some of the selections and fits are a mass selection, a vertex fit and a 4C-Fit. The mass selection combines reconstructed particles within a certain mass range around the expected mass for further analysis. The vertex fit reconstructs the decay vertex of two daughter particles and forces these particles to originate from a common vertex. Therefore, the vertex fit modifies the track parameters of the particles to satisfy this condition. The quality is represented by a χ^2 distribution and the corresponding probability. These parameters can then be further used for constraints to reduce background and improve the analysis. The 4C-Fit is an energy and momentum constraint fit, in which the four-momentum of the final state particle(s) must match the four momentum of the initially simulated data sample (*e.g.* the $\bar{p}p$ -system). The four-momenta of the daughter particles are corrected to match the initial four-momentum, which again results in a χ^2 distribution and a probability. The selections and fits chosen in this work are described in chapter 5.

Tracking 4

Tracking is an essential element of nearly all physics analyses using data from [PANDA](#) and furthermore, it is the most computationally expensive part. Already during the data acquisition, track finding is an indispensable tool. With an average event rate in phase one of two million events per second, a data stream of 120 GB/s is expected for [PANDA](#). This data stream is then processed by a software trigger that decides whether to save or discard an event. The software trigger contains an online track finder, which must thus be able to process the high data streams at a rate compatible with the production rate of the data. After data acquisition, further tracking algorithms are required. These have a different focus than the online track finder. Here, the focus is less on the speed of the track finder and more on the efficiency and background suppression.

This chapter covers the topics relevant for this thesis regarding track finding, as well as the tracking algorithms developed during this thesis. First, the characteristics of the tracking detectors and their hits are described. This is followed by a discussion of the various areas of track finding and a summary of important terms and definitions. The following chapters deal with different tracking algorithms developed for [PANDA](#). First, existing algorithms and their advantages and disadvantages are discussed. Finally, the procedure and results of the algorithms developed in this work is described.

4.1 Detector Response

For the development of a tracking algorithm, knowledge about the detector geometry and the hit information provided by the different subdetectors is essential. Therefore, an overview of the data response relevant for tracking algorithms is given in this section. Since this work focuses on the development of tracking algorithms in the target spectrometer, only the [MVD](#), [STT](#) and [GEM](#) detector is discussed here.

An example of the detector hits of a particle track passing the [MVD](#) (blue crosses), the [STT](#) (pink squares and circles indicating the isochrones) and the [GEM](#) detector (red crosses) in the x-y-projection, as well as the structure of [PANDA](#)'s target spectrometer is shown in Fig. 4.1. The axial [STT](#) tubes are visualized in grey and the skewed layers in light grey. The [MVD](#) and [GEM](#) structure is not shown for reasons of clarity. For a first approximation of the track parameters in the track finding step, the 3D track reconstruction is divided into a 2D reconstruction in the

x-y-plane and a separate reconstruction of the z-component. In the x-y projection, a circle is approximated for the particle track caused by the solenoid field in the target spectrometer. The characteristics of the various detector hits in these three subdetectors are summarized below.

MVD

The **MVD** provides high-resolution hit points for each **MVD** layer with a resolution in the order of several tens of μm . However, the detector consists of only four layers in the barrel part and six discs in the end cap to minimize energy loss, multiple scattering and photon conversion of the tracks due to interactions with the detector material. Consequently, the number of hits provided by the **MVD** is limited. For tracks at polar angles between 40° and 150° , the **MVD** provides a maximum of four hits located at radii of about $r = 2.5$ cm, 5.0 cm, 9.5 cm and 13.5 cm. For polar angles between 5° and 40° , the maximum number of hits is six, which corresponds to the number of discs in the end cap. These are located at distances of $z = 2$ cm, 4 cm, 7 cm, 10 cm, 16 cm and 23 cm from the **IP**.

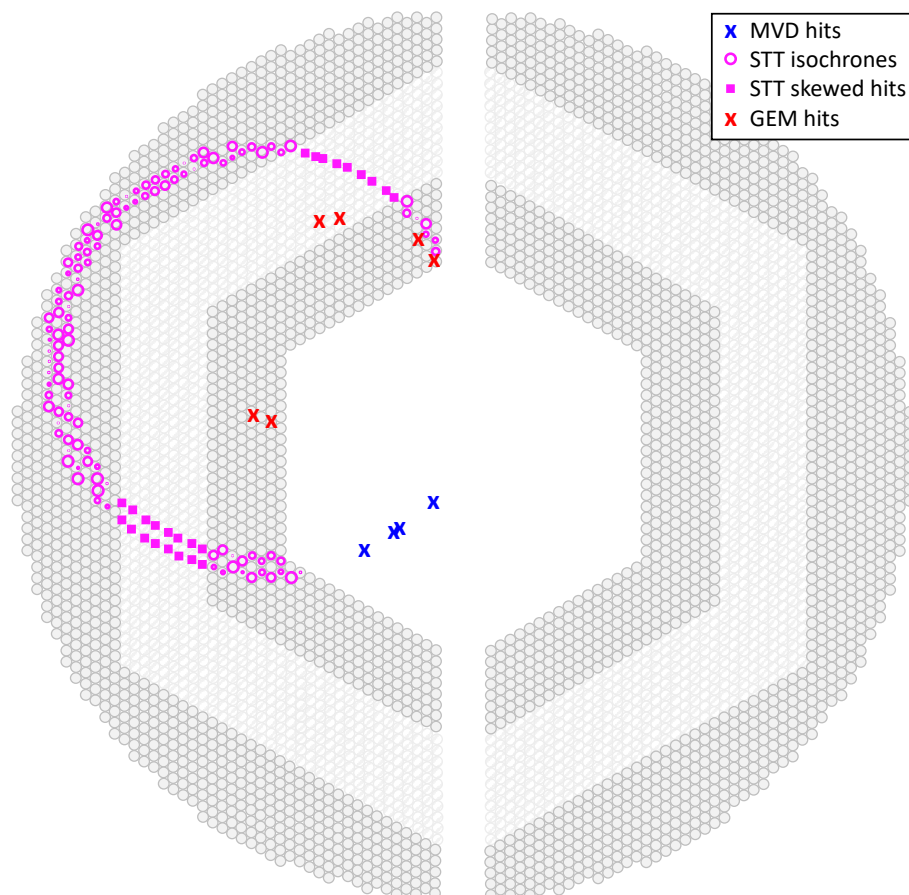


Figure 4.1: A particle track passing the **MVD** (blue crosses), the **STT** (purple isochrones for axial tubes and purple boxes for skewed layers) and the **GEM** detector (red crosses).

STT

The **STT** is **PANDA**'s main tracking detector in the barrel part. It is a drift chamber based tracking detector consisting of straw tubes arranged in a dense packing. In the current design, eight layers of axial tubes are aligned in the inner part of the **STT**, after that eight skewed layers are placed and in the outer part five to ten axial tube layers are attached. In Fig. 4.1 it is visible that the **STT** provides most of the hits (visualized in purple) usable for a track finding algorithm in the target spectrometer. The axial straw tubes provide the position of the center of the tube and an isochrone radius resulting in a spatial resolution in the x-y-projection of about $150\ \mu\text{m}$. In the figure the isochrones are shown by the purple circles. The particle track must be tangent to the isochrones produced by the axial tubes. However, the axial tube layers give no information about the z-component of the hits. The z-component is provided by the eight skewed layers with a spatial resolution of 3 mm in the z-direction. The hits of the skewed layer are indicated as purple squares.

GEM

The **GEM** detector is a tracking system developed for the forward boosted tracks in the target spectrometer and covers polar angles between 3° and 20° . It produces 3D-hit information with a spatial resolution of about $100\ \mu\text{m}$. However, the detector is constructed as three double planes in the forward direction, which means that the number of hits is limited to a maximum of six hits for particle tracks passing all **GEM** planes. The planes are placed at 117 cm, 153 cm and 189 cm downstream of the target. Furthermore, for track reconstruction, it is important to know that the outer **GEM** planes do not experience the full 2 T magnetic field of the solenoid. Consequently, the particles are less strongly curved in this region and a deviation from the circle approximation in the x-y-projection is expected.

4.2 Track Finding: An Overview

Track finding is a broad field, in which many different types of algorithms exist with different purposes and requirements. The algorithms can be divided into larger categories summarizing classes of similar goals or approaches. In this chapter, a rough overview of these categorizations is given as well as basic terminologies in the field of track finding.

4.2.1 Local vs. Global Tracking

The first subcategory is the difference between local and global track finding. Here, local track finding is performed with a subset of the data, e.g. from only one subdetector, whereas global track finding uses all available information from all subdetectors. In local track finding, first the tracks for each subdetector are determined. Then, either the tracks from several local tracking algorithms are combined or hits from other subdetectors are added to the tracks found with a local tracking algorithm. An advantage of local track finding is that the algorithms can be more specialized to a specific subdetector and therefore can use information only valid for this particular detector. Furthermore, it is not necessary to wait until the data of other subdetectors are available. A disadvantage is that the algorithm is limited to the hits from one detector, which

means that information from other detectors is either missing and the algorithm has to work with a smaller number of hits or the information of other local algorithms for other subdetectors must be added. In this case it is again necessary to wait for these other local algorithms. In contrast, global track finding uses all available information from all subdetectors. This means that no merging procedure has to be performed afterwards that merges subtracks from different local algorithms and all information can directly be used.

In [PANDA](#), a pure global tracking algorithm is not easily possible, thus tracking is always divided into track finding for the target spectrometer and track finding for the forward spectrometer. The reason for this is that both parts have a different track topology, since the target spectrometer uses a solenoid magnet and the forward spectrometer deflects the particles with a dipole magnet. Consequently, a global tracker for the target spectrometer in [PANDA](#) describes an algorithm that uses the hits from [MVD](#), [STT](#) and [GEM](#), whereas a local algorithm in the target spectrometer uses *e.g.* only hits from the [STT](#).

4.2.2 Primary vs. Secondary Tracking

One of the main research topics of [PANDA](#) is hyperon spectroscopy. Multistrange hyperons, such as Ξ or Ω , usually decay into neutral Λ particles. The Λ baryon has a lifetime of 2.6×10^{-10} s and a mean decay length of about 8 cm in the detector before it further decays into the final state particles (see sec. 2.3). The result is a high number of tracks that do not originate from the [IP](#) but instead originate from a displaced vertex. These tracks are called secondary tracks. Since primary tracks originate from the [IP](#), track finding can be simplified by using information of the [IP](#). This strongly reduces the number of hit combinations used for track finding and also simplifies the determination of the track parameters. For secondary track finding this assumption is not valid, thus the number of combinations strongly increases and the track parameterization becomes more complex. Consequently, the calculations of the tracking algorithms also become more complicated, which in general leads to an increase in runtime.

4.2.3 Online vs. Offline Tracking

A further subdivision describes the difference between online and offline track finding. Both subgroups have different requirements, as they are used in different stages of the data processing chain. Online tracking is part of the software trigger and is performed during the operation of the detector. Since the amount of produced data must be reduced before storage, a pre-analysis must be performed to decide whether a recorded event is potentially of physical interest and must be stored for later analysis or if the event can be discarded. Since the aim is to record as many events of physical interest as possible and at the same time limit the amount of stored data, the online track finder must have a high track finding efficiency, since events that are discarded by the trigger cannot be recovered later. The main constraints for an online tracker are the average speed of the algorithm and its finding efficiency. It must be able to process the continuous data stream produced by the detector. To enable fast runtimes in online processing, GPUs and FPGAs are used rather than CPUs. These types of computing devices contain hundreds of computing cores, to which the calculations can be distributed. Therefore, the online tracker must be parallelizable in order to fully utilize the available computing cores and to overcome the latency due to data transfer. In addition, the algorithm must consist of calculations with low memory requirements, since GPUs and FPGAs do not provide a large memory for calculations

and any memory access will cause the algorithm to slow down. At this stage of data processing, the precision of the online reconstruction (*e.g.* momentum resolution) is less important, because this type of analysis is performed after data taking in the offline tracking phase.

Offline tracking is performed after data acquisition. Therefore, the speed of the algorithm is less important here. The aim of offline tracking algorithms is to reconstruct the particle tracks as well as possible. This means that high tracking efficiency and good momentum resolution are important here. Furthermore, for offline tracking the number of falsely reconstructed tracks must be reduced, because these tracks lead to a wrong physical analysis. Usually, these tracks appear as background in the analysis.

4.2.4 Track Quality

This section presents the parameters that are used to describe the quality of a track. Parameters exist that describe the quality of a tracking algorithm, and parameters exist that describe the quality of the found tracks. The main parameters to describe the quality of a tracking algorithm is the efficiency and the momentum resolution of the tracks. The efficiency is the main parameter for the track finding part, whereas the momentum resolution is mainly influenced by the track fitting, which is performed by a Kalman filter. Since in this thesis track finding algorithms are developed, the focus here is on the efficiency. It describes the probability for a track to be found. For the efficiency it is important to note that not all simulated tracks are reconstructible by a tracking algorithm. For example, if only two hits of a track are given it is mathematically impossible to uniquely reconstruct the 3D helix. This is described by defining a so called "fiducial volume", where the detector is sensitive enough to find enough hits to fully describe a particle track. The efficiency of a tracking algorithm strongly depends on the definition of the fiducial volume, which is thus defined here.

In [PANDA](#), different definitions exist depending on the subdetectors used. The definitions of the fiducial volume are called selectors in [PANDA](#). Below the selectors used in this thesis are shown:

- **Standard Track Selector:** $N_{\text{Hits}} > 3 \text{ MVD}$ or $N_{\text{Hits}} > 5 \text{ MVD} + \text{STT} + \text{GEM}$
For tracking algorithms using all target spectrometer detectors ([MVD](#), [STT](#), [GEM](#)). It defines a track to be within the fiducial volume if it has either more than 3 hits in the [MVD](#) or more than 5 hits in all target spectrometer detectors together.
- **Only STT Selector:** $N_{\text{Hits}} > 5 \text{ STT}$
For local algorithms, that use the [STT](#). It defines a track to be within the fiducial volume if it has more than 5 hits in the [STT](#).
- **FTS Track Selector:** $N_{\text{Hits}} > 5 \text{ FTS}$
For tracking algorithms in the forward spectrometer. It defines a track to be within the fiducial volume if it has more than 5 hits in the [FTS](#).

The efficiency of a tracking algorithm is then defined as the ratio of the number of found tracks to the number of tracks within the fiducial volume. This efficiency can be further divided into an efficiency for primary tracks and secondary tracks.

$$\epsilon = \frac{N_{\text{found}}}{N_{\text{fiducial}}} \quad \epsilon_{\text{prim}} = \frac{N_{\text{found prim}}}{N_{\text{fiducial prim}}} \quad \epsilon_{\text{sec}} = \frac{N_{\text{found sec}}}{N_{\text{fiducial sec}}} \quad (4.1)$$

Dividing the efficiency into these categories makes an optimization of the algorithms more accurate and improves their specialization. In this way, it is possible to achieve a better total efficiency by combining track finders with different specializations, *e.g.* primary and secondary track finders.

The quality of the found track is then described by the *Completeness* and the *Purity*. The *Completeness* describes the number of correctly found hits in a track compared to the number of simulated hits per track. It is therefore a quantity that describes whether only a small fraction of the track was found or the complete track. The *Purity* on the other hand describes the number of correctly found hits compared to all found hits of a track. Here it does not matter if the track was found completely or not, but it describes how many wrong hits are in a track.

$$\text{Completeness} = \frac{N_{\text{correctly found}}}{N_{\text{MC hits}}} \quad \text{Purity} = \frac{N_{\text{correctly found}}}{N_{\text{all hits}}} \quad (4.2)$$

Based on these definitions, the tracks are categorized into four subgroups: fully pure, fully impure, partially pure, and partially impure. If a track contains only hits from one MC track, it is a pure track. If all MC hits are found, it is a fully pure track. If not all MC hits are found, it is a partially pure track. A track is fully or partially impure if it contains hits from more than one MC track. In this case it is not clear to which MC track it belongs. Therefore, the most likely MC track is determined as the MC track with the most hits in the track. Based on this, the track is defined as partially impure if more than 70 % of the hits in the track originate from this MC track (*Purity* > 70 %). If the *Purity* of the track is lower than 70 % (*Purity* ≤ 70 %) the track is no longer defined as a found track, but as ghost track. A summary of the definitions is shown below:

- **Fully pure:** $N_{\text{MC tracks}} == 1$ & *Completeness* == 1
- **Fully impure:** $N_{\text{MC tracks}} > 1$ & *Completeness* == 1
- **Partially pure:** $N_{\text{MC tracks}} == 1$ & *Completeness* < 1
- **Partially impure:** $N_{\text{MC tracks}} > 1$ & *Purity* > 70%
- **Ghosts:** $N_{\text{MC tracks}} > 1$ & *Purity* ≤ 70%

The ghost ratio is then defined as fraction of all ghost tracks to the number of tracks in the fiducial volume.

$$\epsilon_{ghost} = \frac{N_{ghost}}{N_{fiducial}} \quad (4.3)$$

For a tracking algorithm, the ghost ratio is one of the main quality quantities, along with efficiency. It must be kept low, because too many wrong tracks make an analysis more difficult. If a MC track is found multiple times, these tracks are counted as clones. Here, the number of tracks that found one MC track reduced by one describes the number of clones for this specific MC track.

For online and offline tracking, these parameters have different weights. For offline tracking a good efficiency as well as a high *Completeness* and *Purity* are important. For online tracking,

however, efficiency and speed are more important than *Purity*.

Another important parameter to describe the quality of a track is the momentum resolution. Both the total momentum resolution and the relative momentum resolution are considered:

$$\Delta p = p_{reco} - p_{MC} \qquad \Delta p_{rel} = \frac{p_{reco} - p_{MC}}{p_{MC}} \qquad (4.4)$$

Here, the momentum can be divided into total momentum p , transverse momentum p_T , and longitudinal momentum p_L . Especially in offline tracking, it is important to reconstruct the momentum of the track as well as possible because a good momentum resolution is essential for a high-quality analysis to be performed. As for the quality parameters also the momentum resolution is mainly important for offline tracking algorithms. For online trackers, more emphasis is placed on the speed and efficiency of the algorithm.

4.3 Existing Track Finders in PANDA

Several track finding algorithms exist in PandaRoot. The purpose of developing and studying different types of tracking algorithms is, on the one hand, to cover different areas of track finding (e.g. online and offline tracking) and to optimize the algorithms for a specific application (e.g. primary and secondary tracking). Combining tracking algorithms optimized for different applications leads to an overall optimization in all areas of track finding as the relative strengths of each algorithm can be used. On the other hand, by developing multiple algorithms with the same purpose, the best algorithm for subsequent online or offline tracking can be selected. The algorithms developed in PANDA range from standard methods based on the computation of combinatorics or seed combinations [118] and space transformations [119] to novel algorithms based on machine learning [120].

However, in this chapter, only the existing algorithms that are relevant for this thesis are described. First, the Ideal Track Finder is introduced, which was not developed as a realistic track finder, but uses MC information to reconstruct particle tracks and thus represents the best case for track finding. The Ideal Track Finder is currently used for physics analyses in order to not falsify the results by choosing a track finder that has not yet been optimized. Furthermore, the Ideal Track Finder is used to determine efficiencies and other quality parameters for realistic track finders.

For the realistic track finders this chapter focuses on algorithms designed for PANDA's target spectrometer. The currently used Standard track finder and its working principle is introduced. Additionally, a local algorithm based on a Cellular Automaton (CA) is presented. This algorithm serves as a preselection for the algorithms developed in this thesis, but is also the basis for an alternative barrel tracker, whose development focuses on time-based data [121].

4.3.1 Ideal Track Finder

The Ideal Track Finder uses MC information while reconstructing the tracks. Therefore, the tracker is not a realistic tracking algorithm, but the ideal case. The algorithm collects all hits created by the MC track in a so-called *PndTrackCand*. Since MC data are used, the tracker has by design a *Completeness* and *Purity* of 100%. After that the algorithm applies the predefined selector (see chapter 4.2.4). This means that only tracks that are within the defined fiducial volume are used for the final track creation. The MC data are again used to determine the track

parameters. At this stage of the algorithm, it is possible to include a user defined smearing. In this case, the track parameters are convoluted with a Gaussian distribution of a user-defined width. In a final step, it is possible to apply an efficiency factor to the algorithm. Tracks are randomly discarded depending on the defined efficiency. In this thesis the Ideal Track Finder without smearing and an efficiency of 100 % is used to calculate the quality parameters for the realistic track finders.

4.3.2 Standard Track Finder

Currently, the most commonly used realistic track finder in *PANDA* is the so-called *BarrelTrackFinder* [118], which will be referred to as the Standard tracker in the following. Since the algorithms developed in this thesis will be compared to the Standard tracker, a rough overview of the working principle is given. The Standard track finder is a global primary track finder. It does not prefer any sub-detector in the barrel part of *PANDA*. Randomly one hit after another is selected, independent from the detector type (MVD, STT or GEM). For each hit, the algorithm tries to add it to an existing track. This is done through various conditions on the distance of the hit in both the transverse and the $r\varphi - z$ -planes to the existing tracks. In case of a match the track parameters are recalculated to get more precise track parameters. Otherwise the hit is added to the pool of unmatched hits. If two hits in this pool fulfill certain conditions, *e.g.* are closer than a maximum distance from each other, these hits are used to calculate new tracks by calculating circles from two hits and the IP. This condition (two hits + IP) limits the algorithm to primary tracks. In a final step, a cleanup procedure is implemented to remove short tracks and tracks that were found several times. The Standard tracker is a fast algorithm implemented sequentially on CPU. It achieves an acceptable efficiency for primary tracks, but has poor performance for secondary tracks. The algorithm includes the isochrone information of the STT and is able to reconstruct not only the xy -parameters of the tracks but also the z -component. More detailed analyses of the efficiency can be found in chapter 4.4.4.

4.3.3 Cellular Automaton

The Cellular Automaton (CA) is a local algorithm working exclusively with the STT data, since it uses the neighborhood information of the STT. It is a clustering algorithm that connects all neighboring hits. If hits are unambiguously connected, *i.e.* they have one or two neighbors, they must originate from the same particle track and therefore are filled into the same tracklet. This is visualized in Fig. 4.2. Here two particle tracks cross in the STT. The CA detects the unambiguously connected hits and divides the two crossing tracks into four smaller tracklets. The algorithm is independent of the IP and thus works for primary tracks as well as for secondary tracks. The CA is implemented as a fast online tracker in parallel on GPUs, but can also be used on CPUs. The algorithm itself only connects hits that unambiguously belong together and collects these tracklets in *PndTrackCands*. Therefore, no track parameters are determined and also no ambiguities are resolved, making it a basis for other algorithms but not a complete track finder. The CA is mainly used as a basis for the so-called *CellTrackFinder*, which is currently under development for time-based data. How the *CellTrackFinder* resolves ambiguities and includes other sub-detector hits to form a particle track is found in [121].

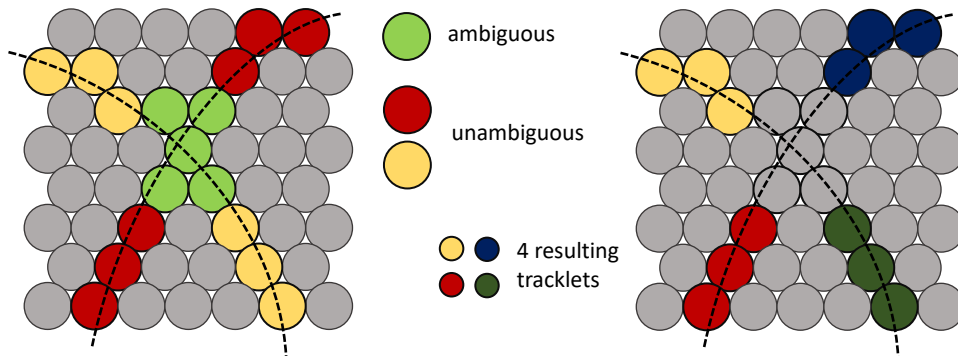


Figure 4.2: Working principle of the [Cellular Automaton \(CA\)](#). Unambiguously connected hits are combined to form tracklets. The two crossing particle tracks in the [STT](#) result in four tracklets. Picture taken from [122] based on [123].

In this work only the tracklet generation of the [CA](#) is used for the preselection. Further steps, such as merging the tracklets and determining the track parameters, are then included in the algorithms developed in this thesis and are discussed in the following sections.

4.4 Hough Track Finder

The algorithms developed in this work are track finders focusing on the target spectrometer. Here, a solenoidal field forces the charged particle tracks to follow a helical trajectory. In track finding, a common method is to divide the three dimensions of the helix into a circle approximation in the x - y -plane and a line in the $r\varphi - z$ -plane, where $r\varphi$ is the distance along the track in the x - y -plane. The algorithms introduced here focus on the reconstruction of the x - y -component of the tracks. The z -component is added at a later stage.

The first algorithm developed in this work is a global primary track finder based on a classical track finding method, namely the Hough transformation. In order to improve the performance of the algorithm, it consists of a preselection, where the hits are divided into subsets of hits that might belong together. After that, the actual Hough transformation is applied to each subset of hits and a track for each subset is determined. In a next step, tracks that were separated by the preselection are merged into one track. In the following the different steps are introduced, starting with the Hough transformation, since it is the core element of the algorithm.

4.4.1 Hough transformation

The Hough transformation is a commonly used pattern recognition tool developed by Paul V. C. Hough in 1962 [124]. The idea is to find a parameter space that projects each measured point into a set of possible solutions, which are then filled into a so-called Hough-space. Maxima in the Hough space can then be identified as true solutions to the pattern recognition problem. For a better understanding, the simplest form of the Hough transformation for two points of a line is shown in Fig. 4.3. For each point of the line all possible solutions are computed. In

Fig. 4.3 this is shown for the two points p_1 and p_2 . The possible solutions are shown as dashed lines, with the solutions for point p_1 shaded in red and the solutions for point p_2 shaded in blue. The parameters of the solutions are then entered into a parameter space, called the Hough space, shown on the right side of Fig. 4.3. For the case of a linear Hough transformation, it is sufficient if the Hough space is two-dimensional, since a straight line is uniquely described by two orthogonal parameters. In the Hough space the possible solutions for each point are indicated as a line. The dashed red line M_1 illustrates the line formed by the solutions of p_1 and the blue dashed line M_2 describes the line for all possible solutions of point p_2 . The intersection of the two lines in the Hough space (q_{12}) then describes the parameters of the line connecting the two points p_1 and p_2 .

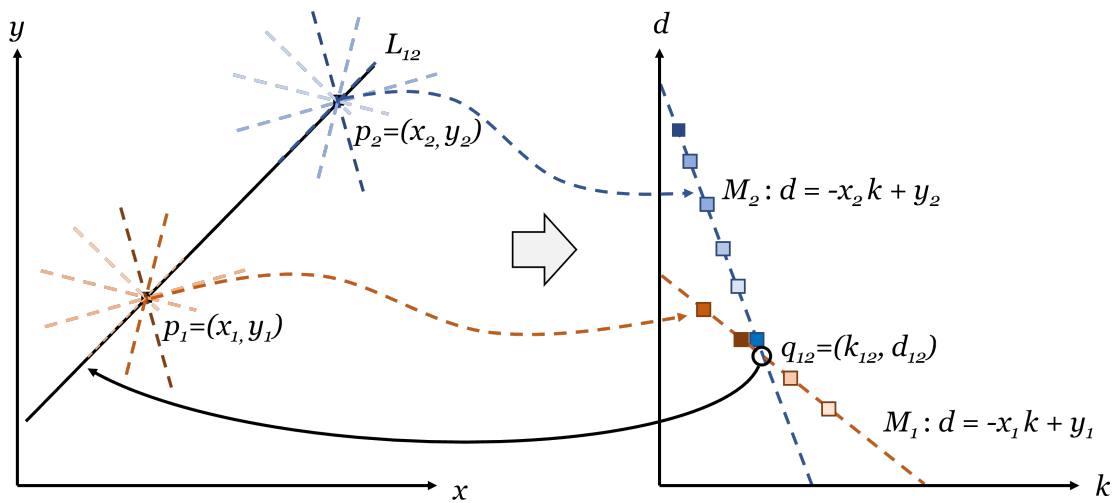


Figure 4.3: Working principle of a linear Hough transformation for two points (p_1 and p_2) of a line. For each point all possible solutions are calculated and filled into the parameter space (Hough space). The solutions of one point describe a line in the Hough space. The intersection point of the corresponding lines in the Hough space describe the actual line parameters. Picture based on [125].

If multiple lines in an image are to be found, the Hough transformation is able to transform the image in a parameter space, where all lines are described as maxima in the parameter space. This is shown in Fig. 4.4. Here the image contains four lines on a noisy background. Transforming this image into the parameter space shows that all lines are now visible as maxima in the parameter space. The Hough transformation is thus robust against noise and is able to find all lines, while only using one transformation.

In particle and hadron physics the Hough transformation is used for track finding because of its global and robust working principle. Here, all hits - independent of the subdetector - can be transformed into the Hough space, where then all tracks of the events are visible as maxima. Moreover, the Hough transformation is not only robust against noise but also against detector inefficiencies such as missing hits. The Hough transformation is a computationally intensive tracking method since for each hit all possible track solutions must be calculated. However, an advantage is that the calculation of the possible solutions is independent from each other and therefore can be parallelized very efficiently.

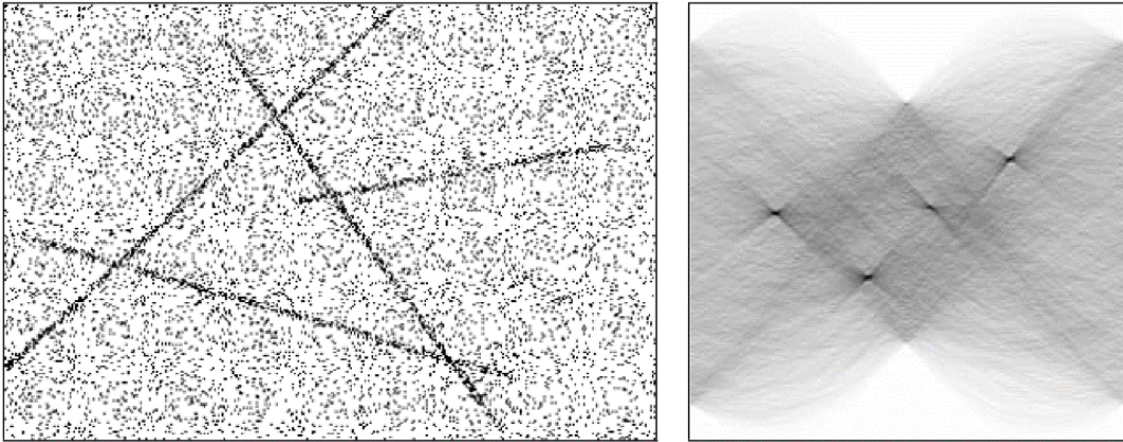
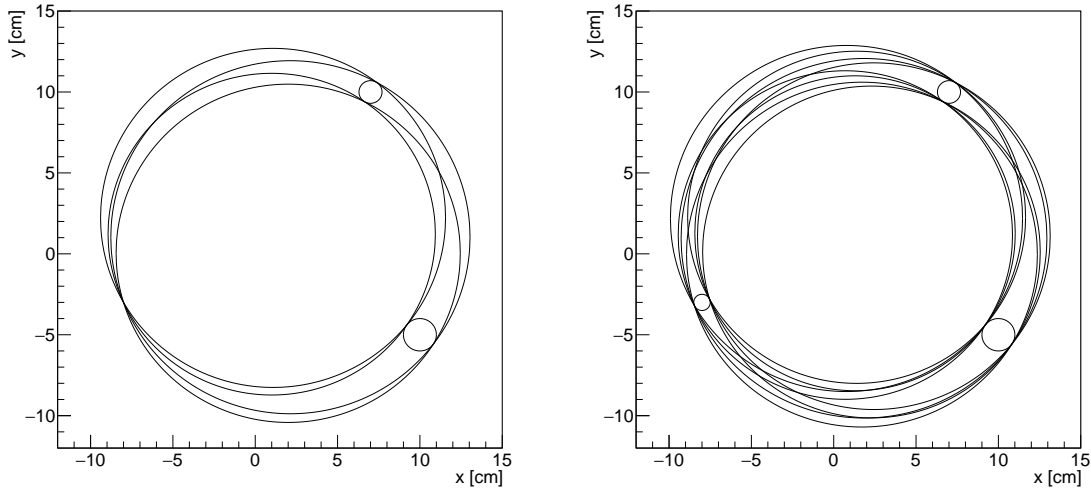


Figure 4.4: Linear Hough transformation to find four lines in an image with noisy background. The lines are visualized on the left. The Hough space with the four maxima is shown on the right. Picture taken from [125].

In the target spectrometer, the particle tracks describe a circle in the x - y -projection. Therefore, instead of a linear Hough transform a circular transformation is needed. Moreover, in **PANDA** not only hit points are given, but - in the case of the **STT** - isochrones, to which the track must be tangent. The implementation and analysis of a Circle Hough transformation including the isochrones for **PANDA**'s target spectrometer was part of an earlier work [119]. However, that work was limited to only find primary particles and focused for the runtime analysis of the algorithm only on the calculation of the possible solutions and not on the entire Hough transformation. Since the results in [119] are promising, the algorithm presented here includes knowledge gained in that work.

The main focus of this thesis is on the extension to find secondary particles to improve the reconstruction rate of events including hyperons. With this extension, the computational effort for the Hough transformation increases dramatically, since now three free parameters (circle center (x,y) + radius) instead of two (φ + radius) are given. Therefore, in addition to an optimization of the efficiency, an improvement of the runtime of the algorithm was investigated by reducing the number of possible solutions that are filled into the Hough space. In the case of primary track finding it was shown in [119] that the centers of all possible circles that are tangent to an isochrone and go through the **IP** lie on two hyperbolas. For two isochrones the intersection points of the corresponding hyperbolas describe then the parameters of the circles that is tangent to both isochrones. This idea leads to a reduction of the number of entries in the Hough space. Adding only the intersection points of the hyperbolas to the Hough space strongly reduces the background in the Hough space, which simplifies the maximum finding in the Hough space. This idea led to the development of the first algorithm implemented and analyzed in this thesis. This algorithm does not use all possible circles but instead only those circles that are also tangent to a second hit. This is calculated by the so-called Problem of Apollonius, which is the mathematical solution for the problem of connecting three circles with a fourth circle that is tangent to the other three circles. The Apollonius problem is visualized in Fig. 4.5. By design, the Problem of Apollonius includes the isochrone information of the **STT** and enables secondary track finding, because neither the Hough transform nor the circle



(a) Four solutions exist for the case of two circles and a point. This case is used for primary track finding.

(b) The general Apollonius Problem. Eight solutions exist for the case of three circles. This case is used for secondary track finding.

Figure 4.5: The Problem of Apollonius for two circles and a point (CCP) on the left, and three circles (CCC) on the right.

calculation uses the IP as a fixed point. The Problem of Apollonius was first solved geometrically by Apollonius of Perga in the ancient geometry about 200 BC. The analytical solutions used today were developed in the late 18th to 19th century and basically use the three circle equations of the given circles to determine the three free parameters describing the Apollonius circles. In Fig. 4.5 the Apollonius Problem is shown for two different cases. The first case (Fig. 4.5a) connects two circles and one point (CCP) and the second case (Fig. 4.5b) connects three circles (CCC). The second case is the classical Apollonius Problem, where the circles k_i with $i = 1, 2, 3$ are connected with the eight possible Apollonius circles. Each circle k_i with center (x_i, y_i) and radius r_i fulfills the circle equation:

$$k_1 : (x - x_1)^2 + (y - y_1)^2 - (r \pm r_1)^2 = 0 \quad (4.5)$$

$$k_2 : (x - x_2)^2 + (y - y_2)^2 - (r \pm r_2)^2 = 0 \quad (4.6)$$

$$k_3 : (x - x_3)^2 + (y - y_3)^2 - (r \pm r_3)^2 = 0 \quad (4.7)$$

The Apollonius circles can then be calculated by inserting the three equations into each other and solving for the parameters x , y and r . The analytical solutions for the Apollonius circles are:

$$x = \frac{A_x + B_x \cdot r_k}{N} \quad y = \frac{C_y + D_y \cdot r_k}{N} \quad r = \frac{-B + \sqrt{D}}{2 \cdot A} \quad (4.8)$$

with

$$\begin{aligned} A_x &= b'd - bd' & B_x &= bc' - b'c & C_y &= ad' - a'd \\ D_y &= a'c - ac' & N &= ab' - a'b \end{aligned} \quad (4.9)$$

$$\begin{aligned}
A &= \frac{B_x^2}{N^2} + \frac{D_y^2}{N^2} - 1 \\
B &= \frac{2 \cdot B_x}{N} \cdot \left(\frac{A_x}{N} - x_1 \right) + \frac{2 \cdot D_y}{N} \cdot \left(\frac{C_y}{N} - y_1 \right) - 2 \cdot s \cdot r_1 \\
C &= \left(\frac{A_x}{N} - x_1 \right)^2 + \left(\frac{C_y}{N} - y_1 \right)^2 - (s \cdot r_1)^2 \\
D &= B^2 - 4 \cdot A \cdot C
\end{aligned} \tag{4.10}$$

$$\begin{aligned}
a &= 2(x_1 - x_2) & a' &= 2(x_1 - x_3) \\
b &= 2(y_1 - y_2) & b' &= 2(y_1 - y_3) \\
c &= 2(\pm r_1 \pm r_2) & c' &= 2(\pm r_1 \pm r_3) \\
d &= (x_1^2 + y_1^2 - r_1^2) - (x_2^2 + y_2^2 - r_2^2) & d' &= (x_1^2 + y_1^2 - r_1^2) - (x_3^2 + y_3^2 - r_3^2)
\end{aligned} \tag{4.11}$$

The complete derivation can be found in appendix A. The result is eight possible solutions for Apollonius circles that are tangent to the three circles k_1 , k_2 and k_3 . For each circle a solution exists that is tangent to the inner side of the circle and a second solution is tangent to the outer side of the circle.

A first step in this work is the analysis of the reduced Hough transformation for primary tracks using the Apollonius problem. Since the track finder will first search for primary tracks, the case of two circles and a point is used for the Apollonius calculation, and equation 4.8 is simplified by setting $r_3 = 0$ for the point. Here the circles represent the **STT** hits of the track and the point is always the **IP** to simplify the calculation. In the Hough transformation all combinations of two hits and the **IP** are determined. For each combination the resulting Apollonius circles are calculated and filled into a two dimensional Hough space as shown in Fig. 4.6. In [119] it was shown, that the shape of the entries in the Hough space in x-y-coordinates has a nearly linear structure. The reason for this is that all Apollonius circles have the **IP** in common. Assuming a hit point and the **IP**, the centers of all possible circles going through these two points lay on the perpendicular bisector between the two points. This means that the Apollonius circles for these two points also are on the perpendicular bisector. In case of an isochrone instead of a hit point the centers of the circles are on two hyperbolas on each side of the perpendicular bisector with a large opening angle as shown in [119] and visualized in Fig. 4.7. These perpendicular bisectors and hyperbolas result in the broad linear structure of the Hough space in the x-y-plane as shown in Fig. 4.6 for a single particle track.

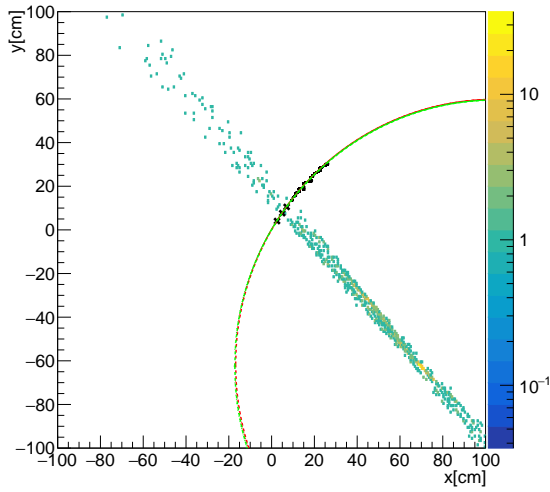


Figure 4.6: The Hough space for a particle track in the x - y -plane. The black circles and crosses describe the hits of the track, the red circle shows the found particle track and the entries of the Hough space are shown in the color scheme from blue to yellow.

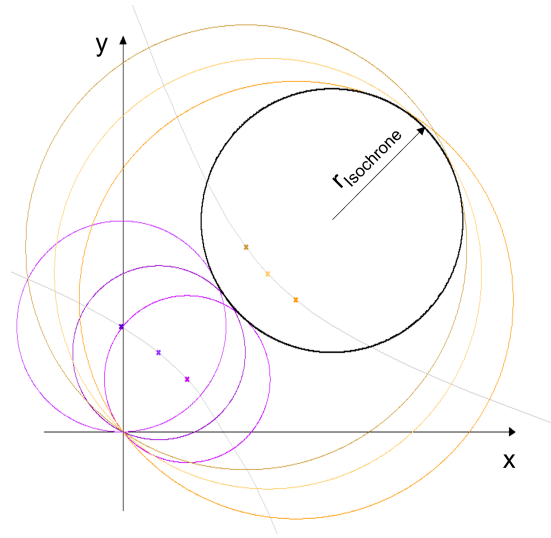
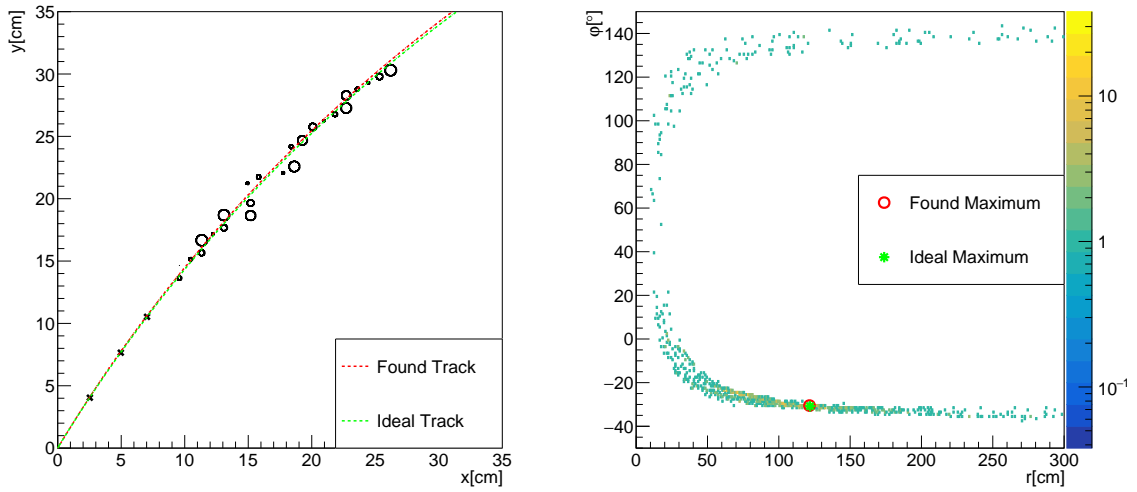


Figure 4.7: The centers of the Apollonius circles (orange and violette) of an isochrone and the IP are on two hyperbolas (gray) at each side of the perpendicular bisector between the IP and the center of the isochrone. Picture is based on [119].

In this work the parameters of the Hough space are defined as the radius of the Apollonius circle and the angle φ to the center of the circle. An example for one track in an event and the resulting Hough space can be found in Fig. 4.8. Here the MVD hits are indicated as black hit points and the STT hits as black circles representing the isochrones. The red fit describes the found track parameters and the green dashed line is the ideal particle track from the MC simulation. The corresponding Hough space is shown on the right. Here a hyperbolic shape of the entries in the Hough space is visible resulting from the transformation of the linear structure in the x - y -plane explained above to the r - φ -coordinates. The lower branch of the hyperbola is more densely populated than the upper one. The upper, less dense hyperbola results from Apollonius circles with the opposite curvature than the particle track. The lower dense branch of the hyperbola contains the maximum of the Hough space indicated as a filled red circle. In this work, the track parameters are then determined by first finding the maximum bin and then computing the average of all entries in that bin. With this method, it is possible to further improve the precision of the Hough transformation and to be more independent from the chosen binning of the Hough space. The MC track parameters are shown as a green cross in Fig. 4.8b and have nearly the same position as the found maximum, which shows that the Hough transformation based on the Apollonius problem works for a single track in an event. An analysis with more statistics for a simulated data sample of 10,000 events of one pion per event originating from the IP with momenta from 0 GeV/c to 1 GeV/c showed that the efficiency based on the tracks within the fiducial volume (eq. 4.1) is 94.6% when using the Standard Track Selector to define the fiducial volume. The efficiency as a function of the transverse momentum is shown in Fig. 4.9. Here it is visible that the finding rate increases for higher momenta. The reason for the decrease at low momenta is that these tracks often do not reach the STT but decay beforehand and the track finder only can find the daughter particle.



(a) The hits of the particle track. MVD hits are shown as black crosses, STT hits as black circles indicating the isochrone. The track found with the Hough transformation is shown in red, the MC track is shown in green. (b) The Hough space for the particle track. The found maximum is shown as the red circle, the MC parameters are shown as the green star. Both parameters are nearly identical.

Figure 4.8: Hough transformation based on the Apollonius problem for one primary particle track in an event.

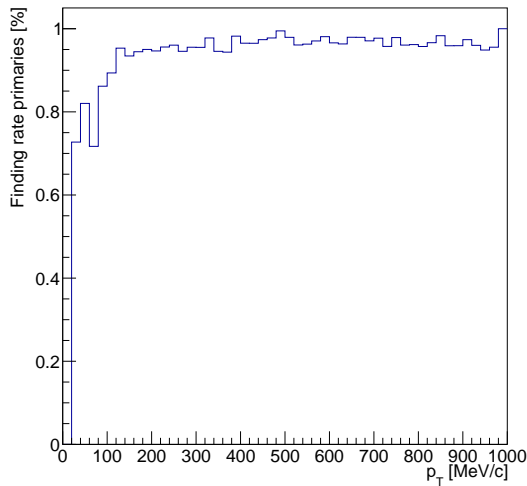


Figure 4.9: Efficiency as a function of the transverse momentum p_T for one track per event. The decrease for low momentum results from primary tracks that decay before they reach the STT, and thus are defined as not found.

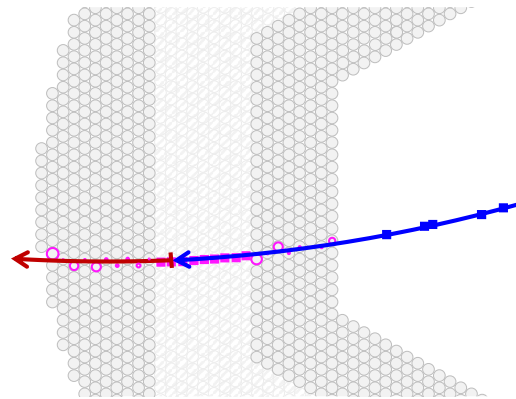
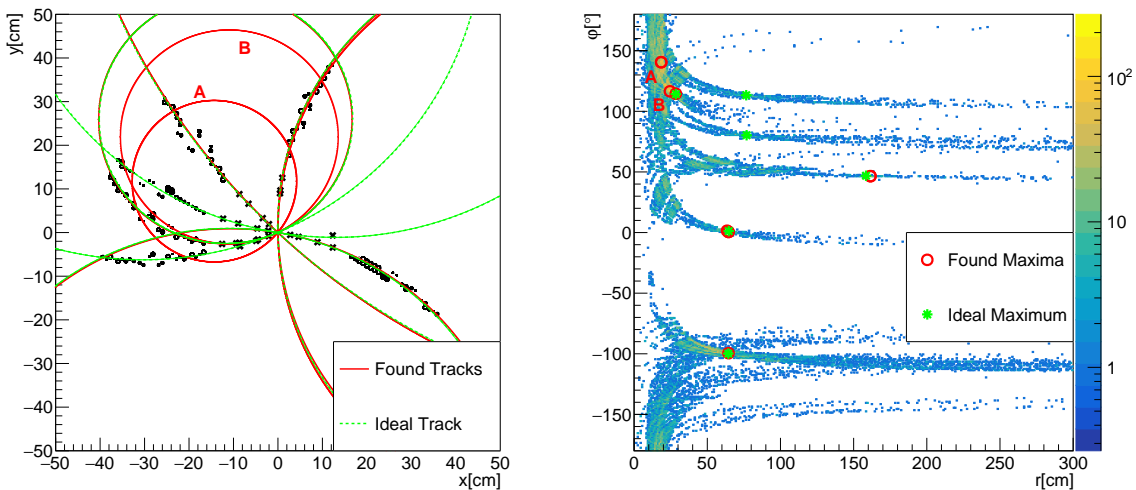


Figure 4.10: An example event of a primary track visualized in blue that was not found. The reason is, that the primary track decays into a secondary track shown in red with about the same momentum. Therefore the primary is defined as a ghost because too many hits of the daughter particle are included.

Therefore, the missing events mostly are not found due to a definition problem of a track to be found. Here a track is found if it has a *Purity* of at least 70 %. However, if a pion decays into a muon and a neutrino, with the muon taking nearly all of the momentum of the pion, the two particle tracks are not distinguishable for this tracking algorithm. Nevertheless, these tracks are defined as ghosts and therefore not found, because a hit fraction larger than 30 % belongs to the muon track. An example for such an event is shown in Fig. 4.10. Here a primary pion, visualized as blue line, decays into a muon, shown as red line, with nearly the same momentum as the pion. The track finder creates a particle track with the correct momentum but hits from both the pion and the muon. Therefore, the track is defined as a ghost and not found.

In *PANDA* the average track multiplicity in the target spectrometer is about six tracks per event at a beam momentum of 15 GeV/c. The Hough transformation using the Apollonius problem is based on calculating all possible combinations of hits in an event. Applying the algorithm to an event with multiple tracks therefore leads to many false hit combinations and a dramatic increase in computing time. These false combinations produce a large background in the Hough space. An example of an event with six tracks and the corresponding Hough space is shown in Fig. 4.11. In Fig. 4.11a the hits are shown in black, the red circles indicate the found tracks and the green dashed lines are the MC simulated tracks. In Fig. 4.11b the entries of the Hough space are shown in the color scheme on the right, the red circles represent the found maxima and the green crosses indicate the parameters of the MC tracks. A recursive method is used to find the maxima. First, the track for the maximum in the Hough space is created. A new Hough transformation is applied to all remaining hits not belonging to that track. Four of the six tracks in the event were found and two ghost tracks have been created. The ghost tracks are shown as red circles (A and B) in Fig. 4.11a without a corresponding MC track (green).



(a) An event with six tracks. The hits are shown in black, the MC created tracks in green and the tracks found with the Hough transformation are shown in red.

(b) The Hough space for the event with six tracks. The large combinatorial background makes it difficult and slow to find the correct track parameters.

Figure 4.11: Hough transformation for an event with six tracks.

In the Hough space the maxima corresponding to the ghost tracks are shown as red circles with the track name A and B. It is visible that the maxima of the ghosts are located in a dense region of the Hough space from false combinations, where the background in the Hough space is even larger than the signal. To reduce the combinatorics and thus make the algorithm faster, a preselection is performed. The Hough transformation is then applied to the preselected data.

4.4.2 Preselection

The aim of the preselection is to quickly find groups of hits, which might belong to the same track. In an ideal case one group would contain all hits of one track and only of one track. In reality the group usually contains hits belonging to two or more tracks or contains a subset of a track. Two different methods with different advantages and disadvantages were investigated for the preselection.

The first one is an existing algorithm in PandaRoot based on the CA [121] [123]. It connects all hits that unambiguously belong together to smaller tracklets. The algorithm was already introduced in chapter 4.3.3. The advantage is that the CA creates mostly pure tracklets, *i.e.* with little to no contamination. The disadvantage is that crossing tracks are always separated since the hits in a crossing region are ambiguous. Furthermore, the CA can only use hits from the STT. Therefore, tracks containing no or only one STT hit cannot be found with the CA. The result of the track finder are therefore relatively pure but small tracklets containing only a fraction of the hits of a track. This makes the Hough transformation fast, but also leads to the problem that the Hough space is only sparsely filled. A sparsely filled Hough space results in the maximum not being clearly defined, but several maxima with the same number of entries in the histogram can occur. As a consequence, a method is needed to decide which maximum best describes the track. In this work, the minimum distance in the x-y-plane from the hits to the circle is used to decide which maximum to select. Another disadvantage is that each track is divided into two tracklets on average. Therefore, a merging procedure is needed afterwards to combine tracklets originating from the same particle to a single track candidate.

The second preselection algorithm is based on the assumption that tracks coming from the IP and have a high transverse momentum are continuously and can therefore be divided by histogramming the φ coordinate of the hits. Regions with hits and regions without hits must be visible in the histogram, as shown in Fig. 4.12 [122]. Here on the left a sketch of the detector with different tracks going in different directions is visible. On the right the φ histogram is shown. The hits of each track are close in φ and can be separated from the hits of another track by the gaps in between. Only the STT hits are used for the histogram, because the STT provides a continuous track structure due to the dense packing. Therefore, the gaps are easily visible here. The MVD and the GEM are designed in a layered structure. Therefore, no continuous hit pattern is expected for a track due to the distance between the layers. For the creation of the subsets all hits within a φ range between two gaps are added. So here also the MVD and GEM hits with a φ value within this range are added to the subset. Since the algorithm divides the detector hits into different segments, the algorithm is called the Segmentation Preselection in the following. In contrast to the CA, the Segmentation Preselection creates subtracks with more hits but which are less pure. This has the advantage that it is more likely that a single track is not divided into multiple tracklets. On the other hand, this means that *e.g.* in case of crossing tracks several tracks cannot be distinguished and are combined into one subset. Consequently,

it is not sufficient to perform one Hough transformation for one tracklet but a recursive method must be used to find all tracklets belonging to one track.

In this work, a combination of both preselection methods is used. First the **CA** is performed and for all remaining hits the Segmentation preselection is applied. This procedure has the advantage, that most of the tracklets are pure tracks calculated with the **CA** and large subsets containing many crossing tracks, which would slow down the algorithm due to many false combinations, are avoided. The subsequent application of the Segmentation preselection allows tracks to be found that have a large overlap with other tracks or which have too few **STT** hits. Since the **CA** divides tracks into several tracklets, the method used here also necessitates an additional merging procedure after the Hough transform in order to combine all tracks belonging to the same particle track.

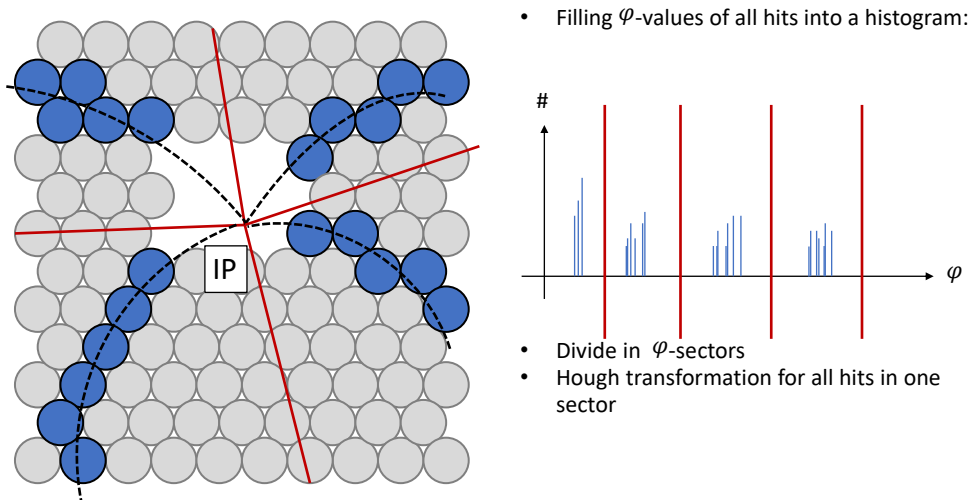
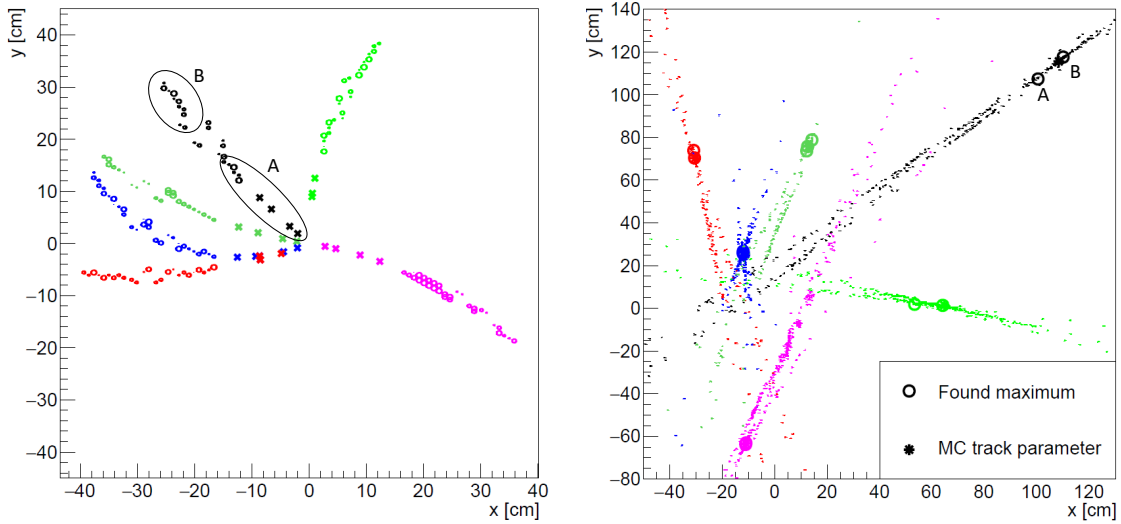


Figure 4.12: Preselection method by dividing the x-y projection of the detector hits into segments based on a φ histogram. Picture based on [122].

4.4.3 Merging

The merging of tracklets belonging to one particle track is done directly after the Hough transformation and before the actual *PndTrack* is created. The merging is based on the hypothesis that tracklets of a particle track have similar track parameters. Considering the Hough Space, the conclusion arises that the maxima of these tracklets must be grouped together and that the distance to each other must be smaller than the distance to maxima from other **MC** tracks. In Fig. 4.13 this is shown for an event with six tracks. Here, the six **MC** tracks are shown in different colors. Each **MC** track consists of several preselected tracklets. The tracklets belonging to one **MC** track have the same color as the **MC** track. For one **MC** track (the black one) the different tracklets are indicated by ellipses. These mark all hits belonging to a tracklet and are labelled with A and B. On the right side, the Hough space for all tracklets is shown. The entries in the Hough space belonging to one **MC** track have the corresponding color. Each tracklet has one maximum in the Hough space, which is added as a circle in the respective color. Consequently,

the black **MC** track, consisting of two tracklets, must have two maxima in the Hough space, which are also labelled as A and B. It can be seen that the distance between maxima belonging to the same **MC** track is smaller than the distance between maxima belonging to different **MC** tracks. For reference, the true parameters of the **MC** tracks are added as stars. It is also visible, that the corresponding maxima are grouped around the true **MC** parameters.



(a) An event with six **MC** simulated tracks. The hits of the tracks are visualized in different colors for each **MC** track. The tracks are further divided into 13 preselected tracklets, of which two are labeled A and B.

(b) The Hough space for all tracklets, where the entries have the same color as the corresponding **MC** track. The small circles indicate the found maxima for each tracklet and the color again indicates the corresponding **MC** track. The stars depict the **MC** parameters.

Figure 4.13: Example event for the merging procedure. The maxima of tracklets originating from the same **MC** track are closer to each other than the maxima of tracklets not belonging together. The maxima are visualized as small circles on the right picture. The colors indicate the corresponding **MC** track.

A distance cut in the Hough space is defined that decides whether two tracklets belong to the same **MC** track and must be merged. For this purpose, the distance between the maxima in the Hough space is determined. For the merging procedure a cut must be chosen where a high efficiency is still achieved but the number of clones is strongly reduced. The cut value is chosen by maximizing the difference between the efficiency and the clone ratio. Since reaching a high efficiency for primary tracks is more important than removing clones, the efficiency is scaled with a higher weight. Here, as an assumption a weight of a factor of two is chosen. The optimization function ($2 \cdot \epsilon_{prim} - \text{clone ratio}$) depending on the distance cut in the Hough space is shown in Fig. 4.14. The maximum is reached at a distance cut of 7 cm as indicated by a blue circle in Fig. 4.14. Here, an efficiency for primary tracks of 81.1 % and a clone rate of 10.7 % is achieved. Tracklets with maxima closer than the threshold of 7 cm are merged into a single track. If two tracklets are merged the hits of the tracklets are added and a mean value is calculated for the maximum.

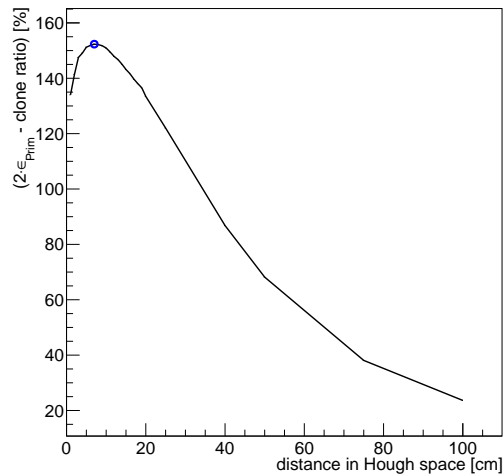
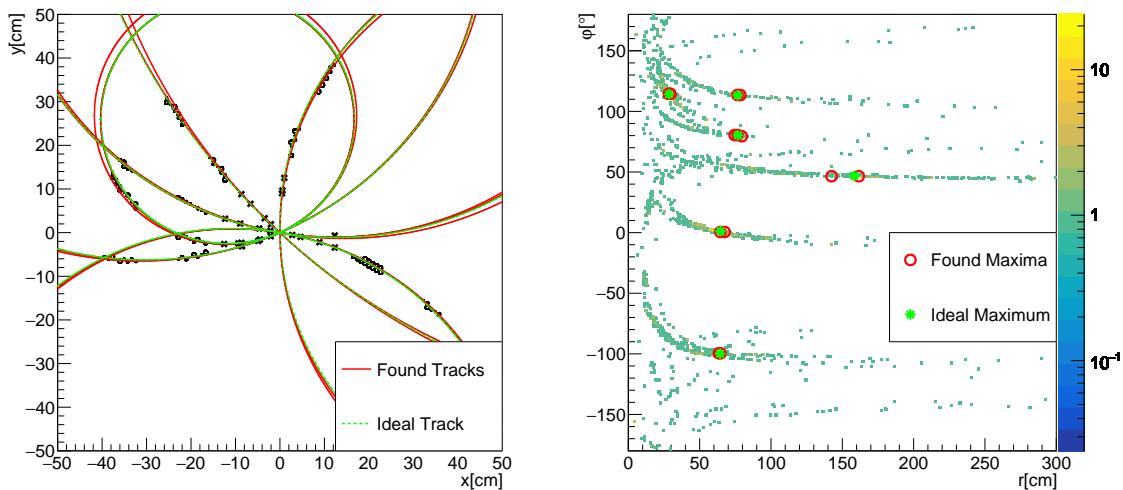


Figure 4.14: Optimization function for the merging procedure. The difference between efficiency for primary tracks and the clone rate is optimized. Here, the efficiency is weighted with a factor two. The maximum is indicated by the blue circle.

Fig. 4.15a shows an example of the same event as in Fig. 4.11 for comparison. Again, the red circles indicate the found tracks and the green circles describe the ideal track parameters. With the preselection and the merging the algorithm is now able to find all tracks in the event. On the right in Fig. 4.15b the corresponding Hough space is shown with the found maxima for the preselected tracks in red and the ideal track parameters in green. In comparison to the case without preselection and merging, the Hough space now has fewer entries because wrong combinations of hits not belonging to the same particle track could be suppressed.



(a) Example event as comparison to Fig. 4.11 with preselection and merging. **(b)** Corresponding Hough space for preselected tracks with the maxima for each preselected track in red and the ideal parameters in green.

Figure 4.15: Tracks and Hough space for an example event as in Fig. 4.11. With preselection and merging the algorithm correctly finds all tracks.

4.4.4 Results

The evaluation of the quality parameters strongly depends on the definition of a track being within the fiducial volume, as already mentioned in section 4.2.4. To get a better understanding of the functional dependence of the quality parameters, efficiency for primary tracks and secondary tracks and ghost and clone ratio, Fig. 4.16 shows these quality parameters as a function of the number of hits in a track required for it to be considered within the fiducial volume. An increase in efficiency for primary and secondary tracks is shown for a stricter definition of the fiducial volume. For primary particles the finding rate increases from about 70 % to 90 % for a higher number of required hits per track. Also observable is that the ghost and clone ratio increases. Here the ghost ratio increases from 8 % to 15 %.

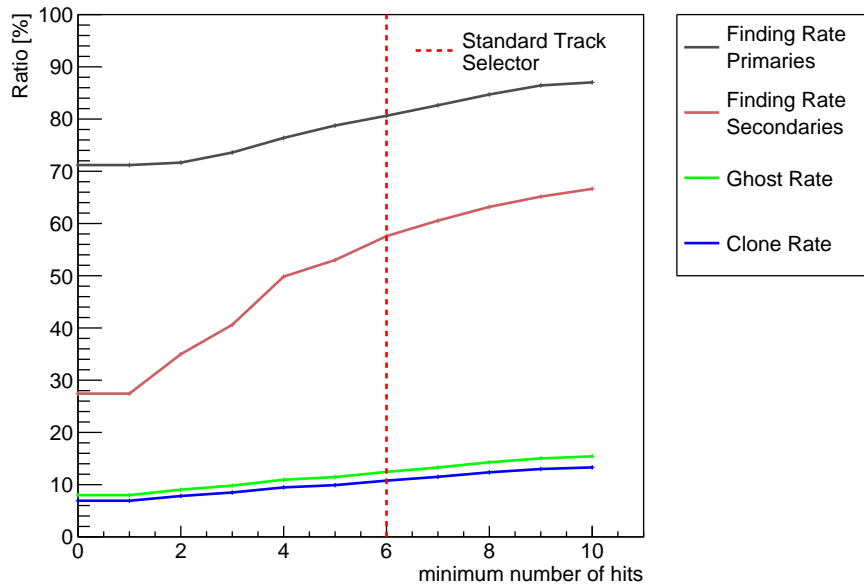


Figure 4.16: Quality parameters versus the minimum number of hits required for a track to be considered within the fiducial volume. These results were determined for a simulated data sample of background events generated with the FTF generator at a beam momentum of 7 GeV/c.

The red dashed line indicates the definition of the Standard Track Selector. The Standard Track Selector was used for the analysis of the Hough track finder, which means that tracks are defined to be within the fiducial volume if they consist of more than three *MVD* hits or more than five hits in all tracking detectors (*MVD* + *STT* + *GEM*).

A simulated data sample with 20,000 events is used. Background events are generated with the FTF generator at a beam momentum of 7 GeV/c. The data sample consist of 97,234 primary MC tracks and 97,245 secondary MC tracks. Based on the Standard Track Selector, 60.2 % of all primary MC tracks and 37.5 % of all secondary MC tracks are within the fiducial volume. On average, each event has five to six tracks within the fiducial volume. Here, about 62 % of the tracks are pions, 18 % electrons and positrons and 16 % protons and antiprotons. Kaons and muons only account for a few percent. A summary of the generated particle distribution can be found in Tab. 4.1.

Table 4.1: Summary of the distribution of generated particles in the data sample. The particles are the MC simulated particles that are within the fiducial volume defined by the Standard Track Selector.

	P	K	π	μ	e
particle	11.6 %	1.2 %	30.9 %	1.4 %	10.7 %
antiparticle	4.8 %	1.2 %	31.3 %	1.5 %	7.2 %

The momentum distributions of the tracks are shown in Fig. 4.17 and 4.18. In Fig. 4.17 the distributions are divided into primary particles in black and secondary particles in blue. On the left the transverse momentum and on the right the longitudinal momentum is shown. For transverse and longitudinal momentum it is observable that the distributions for primary tracks peak at about $0.2 \text{ GeV}/c^1$, whereas the distributions for secondary tracks increase to lower momenta. In Fig. 4.18 the momentum distributions are divided into the different particle species. Here it is again visible that the pions dominate the distribution. The large increases to low momenta for secondary particles is caused mainly by electrons originating from subsequent muon decays or from pair-production.

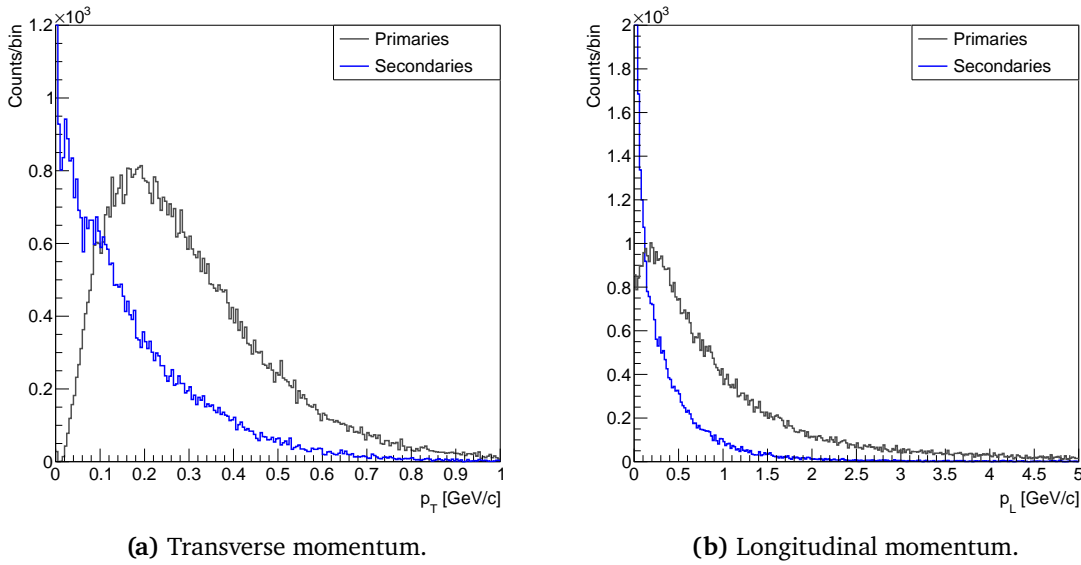


Figure 4.17: Momentum distributions for the simulated data. Only tracks within the fiducial volume are taken into account. Primary particles are shown in black and secondary particles in blue.

A summary for the results of the Hough track finder consisting of a preselection, the Hough transformation for the preselected tracks and a merging procedure can be found in Fig. 4.19. Here, the tracking quality is compared to the quality parameters achievable with the currently used realistic track finder in PANDA, which was introduced in chapter 4.3.2. Fig. 4.19 shows the efficiencies for primary and secondary tracks, the ghost and clone ratio and the speed of the algorithm. On average the efficiency for primary tracks is 81.1 % for the Hough track finder

¹Primary particles with low transverse momentum ($p_T < 0.05 \text{ GeV}/c$) do not reach the STT. However, they are usually strongly forward boosted and therefore produce hits in the MVD and GEM detector, which is the reason that they are still within the fiducial volume.

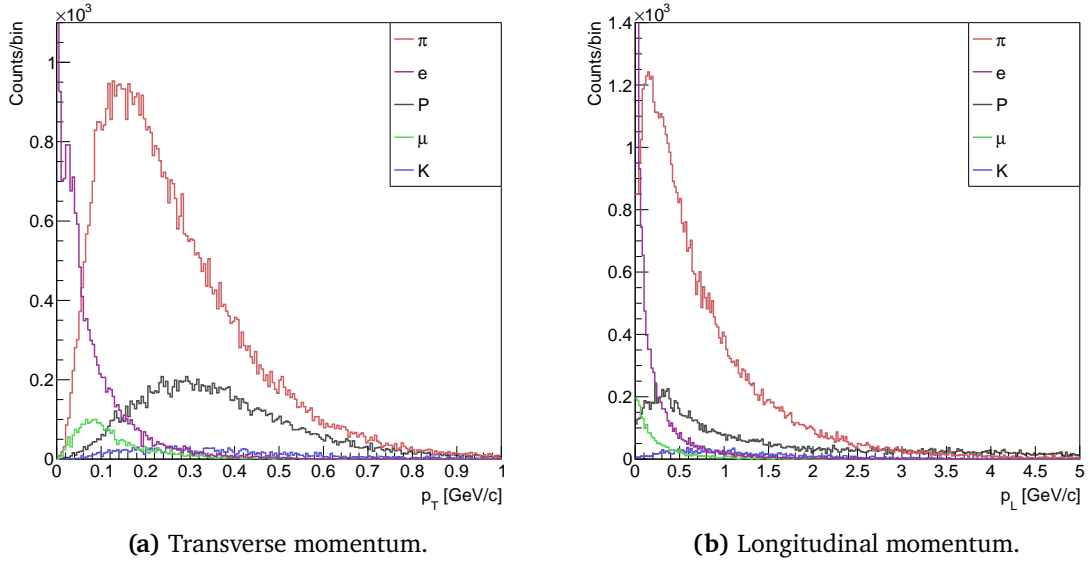


Figure 4.18: Momentum distributions for the simulated data. Only tracks within the fiducial volume are taken into account. The distributions for the different particle species are shown.

as well as for the Standard tracker. An acceptable ratio of ghosts and clones can be achieved of 11.1 % and 10.6 %, respectively. In comparison to the Standard tracker the ghost ratio is 3.4 % points lower, the clone ratio is in a similar region with a difference of 1.1 % points. The Hough track finder reaches a speed of 13.6 ms/event, which is much slower than the Standard tracker, which takes only 2.2 ms/event. Nevertheless, the speed of the Hough track finder is still acceptable for offline tracking. For online tracking, however, other methods must be investigated, which is introduced in the next chapter. Strikingly in Fig. 4.19 is the high efficiency of the Hough track finder to find secondary particles, which is 51.6 %, nearly twice as large as the 27.2 % of the Standard tracker.

The transverse momentum distributions are shown in Fig. 4.20. In red the ideal momentum distributions created with the Ideal Track Finder are shown for primary (left) and secondary (right) particles. This distribution therefore represents the momentum distribution of all tracks within the fiducial volume. In blue and black the MC momenta of the tracks found by the Standard and the Hough tracker are shown. Secondary particles have fewer entries observed by the Standard tracker. For higher p_T secondary tracks the number of found particles vanishes.

The ratio of each distribution to the corresponding ideal distribution results in the finding rate as a function of the transverse momentum, as shown in Fig. 4.21. For primary tracks, the efficiency for both track finders are similar. For higher momenta, the efficiency increases to about 90 % for both track finders. For very low momenta under 100-200 MeV/c the efficiency decreases dramatically. Since the momentum is directly proportional to the radius of the circles, as shown in equation 3.2, $p_T = 200$ MeV/c corresponds to a circle radius of 33 cm. Thus, these low momentum tracks are tracks that are strongly curved or even curl up inside the detector, which makes the track finding difficult for both track finders.

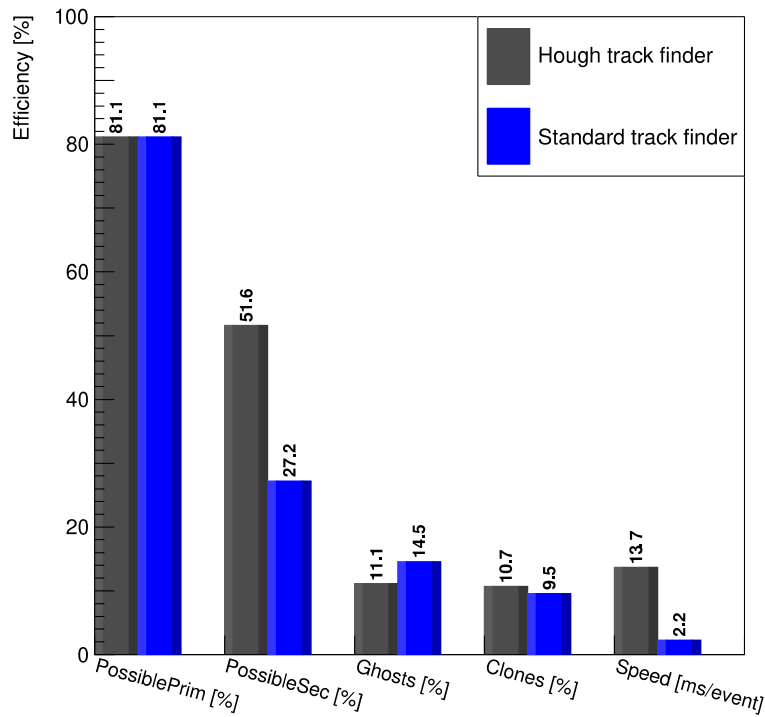
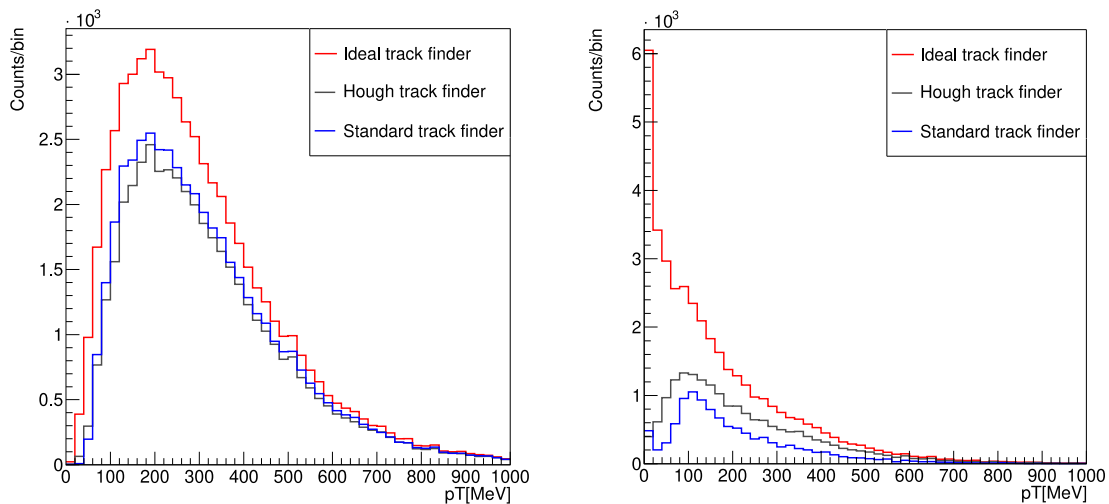


Figure 4.19: Quality parameters for a simulated data sample of background events generated with the FTF generator at a beam momentum of 7 GeV/c.



(a) Transverse momentum distributions for primary tracks.

(b) Transverse momentum distributions for secondary tracks.

Figure 4.20: Transverse momentum distributions for the Standard tracker in blue, the Hough track finder in black and the ideal distribution in red.

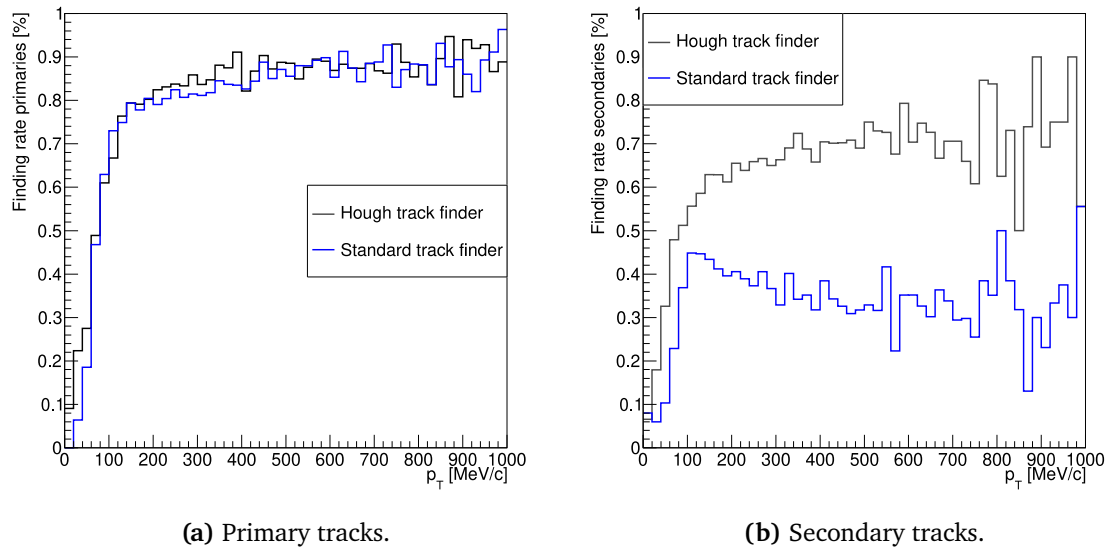
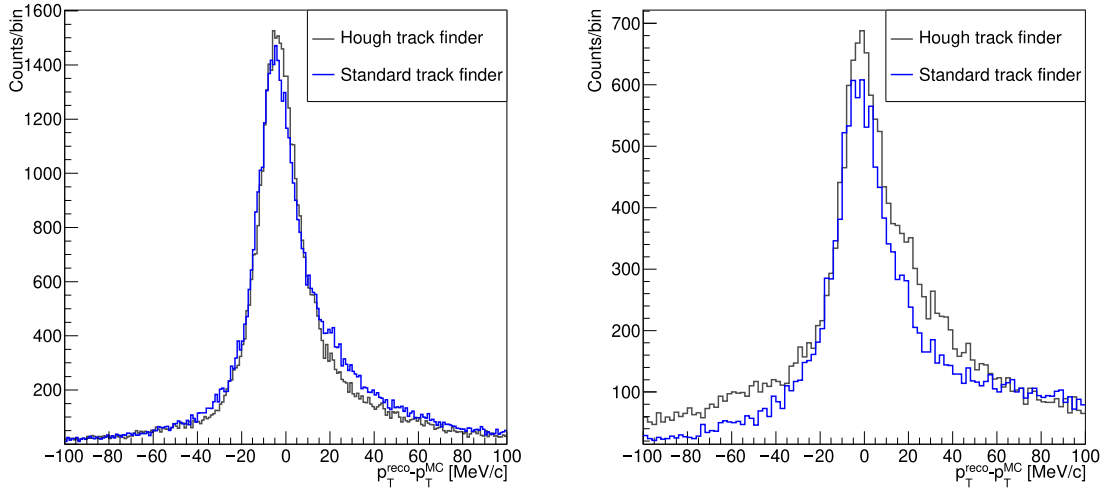


Figure 4.21: Finding rate as a function of transverse momentum for primary and secondary tracks.

For secondary tracks, the finding efficiency of the Standard track finder is much lower. For the Hough track finder the distribution is similar to the distribution for primary tracks with a strong decrease for very low momenta and an increase in efficiency for higher momenta. The efficiency of the Standard tracker also shows the decrease for very low momenta. However, for higher momenta neither an increase nor a constant behavior is visible, as shown in Fig. 4.21b.

The transverse momentum resolution for primary and secondary particles is shown in Fig. 4.22. The momentum resolution for primary particles is very similar for the Hough track finder and the Standard track finder with a **Full Width Half Maximum (FWHM)** of 19 MeV/c and 20 MeV/c and a **Root Mean Square (RMS)** of 27.4 MeV/c and 29 MeV/c, respectively. Here, it is also visible, that both algorithms have the same efficiency for primary tracks. It is striking that the distributions are not symmetric but the track finders tend to determine too large transverse momenta. For the Hough track finder only a slight deviation from a symmetric distribution is observed. The relative momentum resolution, shown in Fig. 4.23a, shows this deviation at a relative momentum resolution of about 10% to 20%. The deviation mainly originates from strongly forward boosted tracks, consisting of mainly **GEM** hits. Since the outermost layer of the **GEM** detector leave the homogeneous 2 T magnetic field, the particle tracks are less strongly curved in this region, which explains why tracks consisting mainly of **GEM** hits are shifted to higher momenta. For the Standard tracker the deviation is even stronger and ranges from about 5% to 25%. A reason for this could be that the Hough track finder mainly focuses on the **STT** as it does not reconstruct the z-information. However, the Standard tracker puts more emphasis on hits with z-information like the **MVD** and the **GEM**. For secondary particles the Hough track finder has a **FWHM** of 32 MeV/c and the Standard tracker of 26 MeV/c and a **RMS** of 16% in both cases. For the relative momentum resolution in Fig. 4.23 the difference is better visible in the **RMS**, where the Hough track finder has an **RMS** of 35.4% and the Standard tracker of 28.0%. The reason for the difference here is the difference in finding efficiency of the Hough track finder and the Standard track finder. In the relative momentum resolution, it can be seen

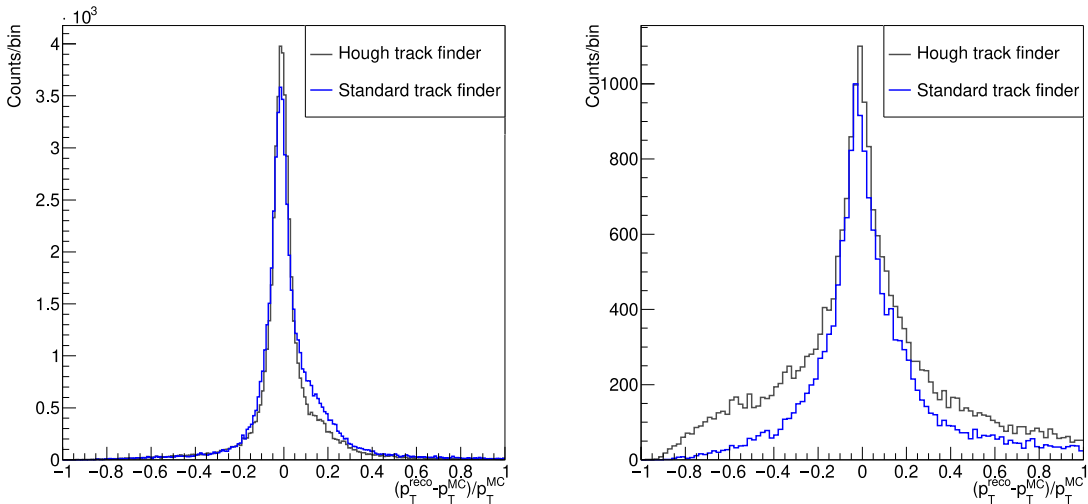
that the Standard tracker has a worse finding rate, but the resolution is better. The Hough track finder finds more tracks, but with a larger deviation from the MC data. These poorly reconstructed tracks lead therefore to a broad distribution producing a background distribution for larger relative momentum deviations. Therefore, a dedicated secondary track finder is still needed. The results for the momentum resolutions are summarized in Tab. 4.2.



(a) A comparison of the transverse momentum resolution for primary tracks for Standard vs. Hough tracker.

(b) A comparison of the transverse momentum resolution for secondary tracks for Standard vs. Hough tracker.

Figure 4.22: Transverse momentum resolution for primary (left) and secondary (right) particles.



(a) A comparison of the relative transverse momentum resolution for primary tracks for Standard vs. Hough tracker.

(b) A comparison of the relative transverse momentum resolution for secondary tracks for Standard vs. Hough tracker.

Figure 4.23: Relative transverse momentum resolution for primary (left) and secondary (right) particles.

Table 4.2: Summary of the **FWHM** and the **RMS** for the transverse momentum resolutions.

		Hough track finder		Standard track finder	
		absolute	relative	absolute	relative
		[MeV/c]	[%]	[MeV/c]	[%]
FWHM	primary tracks	19	7	20	8
	secondary tracks	32	16	26	16
RMS	primary tracks	27.4	16.1	29.0	17.5
	secondary tracks	39.9	35.4	38.3	28.0

4.5 Speed Optimization of the Hough Track Finder with GPUs

The initial idea to develop the Hough track finder was to use it as a fast online tracker that is able to find primary and secondary particles. The reason for this assumption was that the Hough transformation can be extended to find secondary tracks, and on the other hand the Apollonius calculations can easily be parallelized. Since the secondary extension will strongly increase the computing effort, first the speed of the algorithm must be improved in a way, that the increase in computing effort due to the secondary extension will not have a large influence. Basically, this means that the algorithm must be implemented in a parallel way, where the computations can be spread over many computing cores. To improve the computation and speed of an algorithm it can be beneficial to understand how the algorithm is processed on the machine. For this purpose, this chapter first compares the design of a **Central Processing Unit (CPU)** and a **GPU**. This knowledge is essential to understand the differences between a **CPU** and a **GPU**, which has a much larger potential to speed up parallel algorithms. After that, the performance of the Hough track finder is evaluated on a **GPU**.

4.5.1 General Information About GPUs

In Fig. 4.24 the basic structure of a **CPU** on the left and of a **GPU** on the right is shown. The **CPU** is designed for sequential computations of complex calculations. For this purpose, it consists of the so-called von Neumann architecture, consisting of four main components:

- **Control:** Controls all calculations
- **ALU:** Performs the calculations
- **Cache:** A small but very fast buffer memory
- **RAM:** A nonpermanent memory

The main part of the **CPU** is the *Control* unit, which coordinates the operations and data movements. The *ALU* (arithmetic logic unit) is an execution unit, that performs the operations and calculations of the program. It calculates all arithmetic (addition (ADD)) and logical (negation (NOT), conjunction (and-connection, AND)) calculations. The *Cache* (L1-, L2-, L3-Cache) is a small data memory for fast data retrieval. The *RAM* (random-access memory) is the next level of data storage. It is not a permanent memory, but loses its information after rebooting the computer.

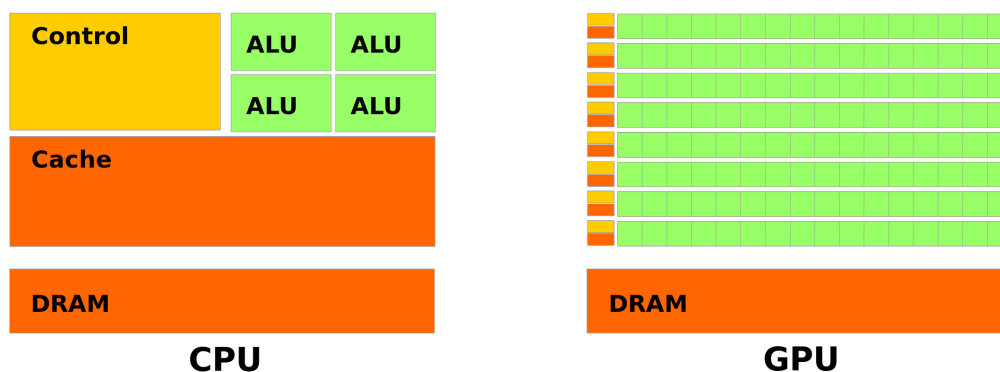


Figure 4.24: Architecture of a CPU (left) and a GPU (right). The GPU has many more computing entities but less control and memory. Picture taken from [126].

Most of the common CPUs have two, four or eight cores, where each core consist of a *Control*, *ALUs* and the *Cache*. The *RAM* is shared by all cores. In sequential single-core programming, only one of the cores is used. Therefore, the total computing power of a CPU is not fully utilized. If a program divides several processes across all cores, this is called *multiprocessing*. In this case, every process is completely independent of the other processes and it is not possible that the process can switch to another core or receive information about calculations performed in parallel on other cores. The difference between CPUs and GPUs is that they are designed for different purposes. A CPU is designed for complex calculations and handling of a large amount of data. Therefore, the *Control* and the *Cache* memory are large. In contrast, a GPU is designed for many small calculations in parallel, where the single *Control* and *Cache* units are small. Therefore, a GPU is not designed for complex calculations with large data accesses and many different tasks. However, the advantage is the number of cores, which perform the same calculation hundreds or thousand of times in parallel. The GPU has many more *ALUs* than the CPU to deal with a large number of small and simple calculations. A GPU is divided into so-called *Streaming Multiprocessors (SMs)*, which pass the calculations to the cores of the GPU. In this work, the medium class GPU NVIDIA GeForce RTX 2060 was used. The GPU has 1920 Cores distributed over 30 *SMs* each with 64 cores. It has a global memory of 6 GB and a maximum clock rate of 1.20 GHz. The bandwidth of the device ranges from 12.7 GB/s for copying data from Host to Device and 13.0 GB/s for copying data from Device to Host to a maximum internal bandwidth (Device to Device) of 228.6 GB/s. A summary of the parameters of the GPU used can be found in Tab. 4.3.

In this work, the software tool CUDA [127] was used for GPU programming. It is a commonly used software developed by NVIDIA and is a low-level programming language, that allows the user to explicitly access the different cores, threads and memories in a GPU. CUDA is based on implementing CUDA *Kernels*. These *Kernels* can then be distributed across a specific number of blocks and threads, where a block is a collection of multiple threads. The *Kernel* is thus computed independently on each thread.

Table 4.3: Properties of the GPU NVIDIA GeForce RTX 2060, as determined by the CUDA *deviceQuery* and *bandwidthTest* of the CUDA samples [128]. Further information can be found on [129].

NVIDIA GeForce RTX 2060		
Streaming Multiprocessors		30
Cores		1920
Global GPU Memory		6 GB
GPU Max Clock Rate		1.20 GHz
Band width	Host to Device	12.7 GB/s
	Device to Host	13.0 GB/s
	Device to Device	228.6 GB/s

4.5.2 Hough track finder on a GPU

The Apollonius calculation of the Hough track finder consists of many independent and simple calculations and promises to be efficiently parallelizable and thus well suited for a GPU application. Therefore, only the Apollonius calculation was tested on a GPU in this thesis. For testing, a simulated data sample with 20,000 background events generated with the FTF generator at a beam momentum of 7 GeV/c is used. Since the advantage of the GPU is its computing power for many parallel calculations, it is beneficial to parallelize the algorithm not only for a single track, but calculate many events in parallel on the GPU. For this purpose, a data buffer is implemented that collects a predefined number of events and sends this event collection to the GPU. On the GPU all events are then calculated in parallel and copied back to the CPU. In a post-processing step, the results must then be divided into the different events. Consequently, the runtime of the entire algorithm consist of three parts: the actual calculation on the GPU, which is called the Kernel, the data copy processes from CPU to GPU and vice versa, and the pre- and post-processing to collect data in a data buffer and split the result back into the corresponding events. Since the pre- and post processing strongly depends on the data acquisition and the way the data are stored on disc, this part is omitted for the runtime comparison presented below. Therefore, the compared runtimes only consist of the actual track finding algorithm and the data copy between CPU and GPU.

In GPU programming, it is a common issue to keep the amount of copied data low, since copying data between the CPU and GPU usually has a lower bandwidth than the data access on the GPU. For the GPU used in this work, the bandwidth for copying data within the GPU is about 20 times faster than for the data transfer between CPU and GPU (12.7 GB/s for CPU to GPU and 13.0 GB/s for GPU to CPU vs. 228.6 GB/s on GPU). On the CPU the Hough track finder first calculates all possible hit combinations and then computes all possible Apollonius circles for each hit combination. Due to the copying speed, it is not beneficial to first calculate all combinations and then copy these combinations to the GPU. Instead, only the hits are copied and the combinatorics is also determined on the GPU. For comparison, the Apollonius calculation is performed on the CPU and the runtime is compared to the Apollonius calculation on the GPU. An acceleration value is determined as the ratio of the CPU runtime to the GPU runtime. The dependence of the acceleration factor on the number of buffered events computed in parallel is shown in Fig. 4.25. The red line indicates the acceleration factor of the GPU Kernel, the blue line shows the more realistic case with data copy from host to device and copying the results back from GPU to CPU. A Kernel runtime of 24.1 μ s per event was achieved when calculating

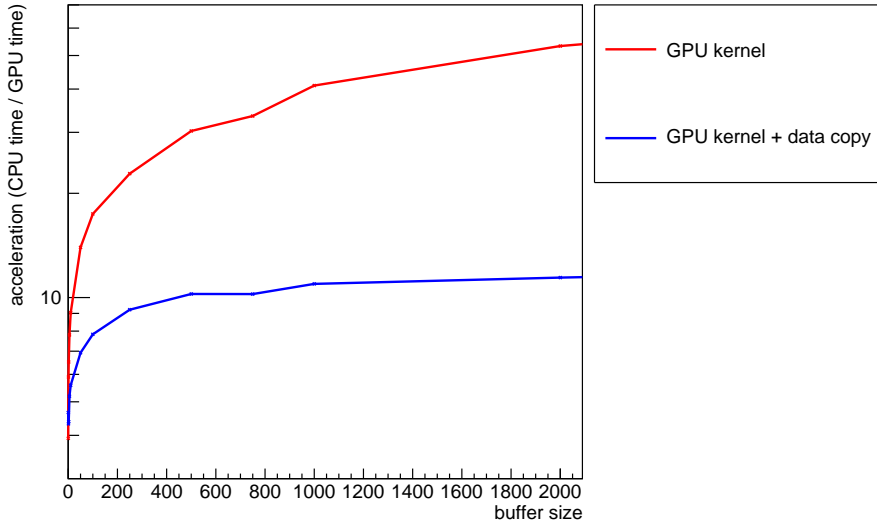


Figure 4.25: Comparison of the acceleration factor between GPU calculation of the Apollonius circle (red) and the additional data copy to GPU and copying the results back to CPU (blue).

10,000 events in parallel with an offset for data copying of about $200 \mu\text{s}$ per event. Thus, the data copy has almost 10 times more impact on the runtime of the algorithm than the computing time itself, which means that the Apollonius calculation can be efficiently parallelized on the GPU. The data copy offset mainly originates from copying the result array back to the CPU, where the result array contains an integer number for each calculated circle. This corresponds to an array of a size calculated by equation 4.12, where all calculated circles are determined as a sum over all tracklets. For each tracklet, the number of possible combinations are calculated and for each combination four possible Apollonius circles exist. Here, still the case of primary tracks is assumed, where two hits and the IP are used to calculate four possible Apollonius circles.

$$N_{\text{All Circles}} = \sum_{i=0}^{N_{\text{Tracklets}}} \binom{N_{\text{Hits of Tracklet } i}}{2} \cdot 4 \quad (4.12)$$

Two possibilities exist to complete the Apollonius calculation with the remaining parts of the Hough track finder. The first one is to calculate only the Apollonius calculation on the GPU and the Hough transformation and merging on the CPU. The second option is to implement the entire algorithm with Hough transformation and merging on the GPU. The Hough transformation and the merging are not as efficiently parallelizable as the Apollonius calculation. Therefore, here the parallelization must result from performing the tracking for each tracklet in one thread of the GPU and implementing the merging for each event on one thread. Both possibilities were investigated in this work and are presented in the following.

Performing only the Apollonius calculation on the GPU and the Hough transformation and merging on the CPU results in an additional runtime offset. In Fig. 4.26 the comparison is shown between the acceleration factor of the Apollonius calculation and the entire algorithm, where

the Hough transformation and the merging is performed on the CPU. In the two blue shades, the Apollonius calculation on the GPU is visible and in red, the combination of Apollonius calculation on the GPU and Hough transformation and merging on the CPU. The two shades for the blue and the red case indicate the offset due to copying data from the CPU to the GPU and back. In comparison to the runtime offset due to the CPU calculation the data copy is negligible. Therefore the distributions of the two red shades are nearly identical. The runtime for the Hough transformation and the merging takes on average the same amount of time as the Apollonius calculation, which means that the total runtime of the algorithm can be improved by a factor of about two from 13 ms/event to 7 ms/event. This factor is a constant offset that cannot be improved by a more powerful GPU. Consequently, the speed up is a large improvement for offline tracking, but it is not sufficient for online tracking. Therefore, for online tracking it is not beneficial to combine the Apollonius calculation on the GPU and the Hough transformation and merging on the CPU.

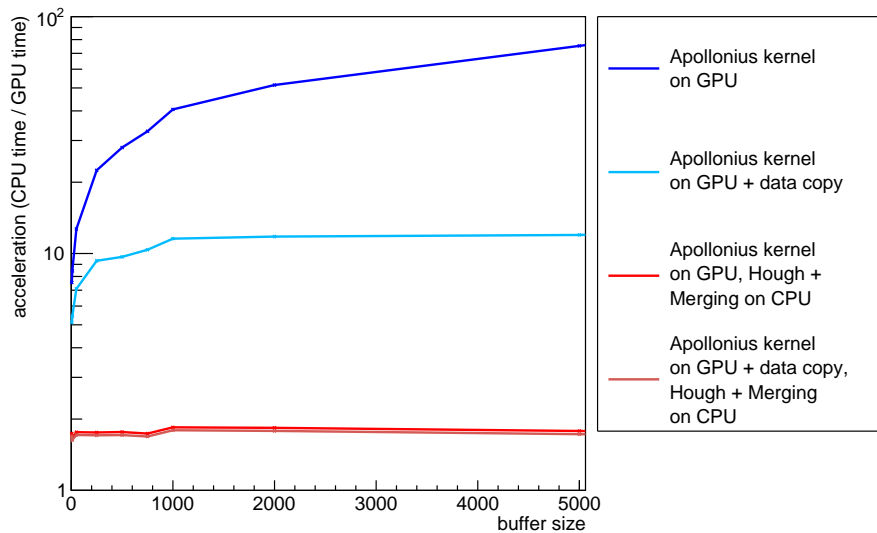


Figure 4.26: Acceleration factor of the total Hough track finder and the Apollonius calculation. The Apollonius calculation is shown in blue, the Hough track finder where only the Apollonius calculation is performed on the GPU and Hough transformation and merging is performed in CPU is shown in red.

The second option is to implement the entire Hough track finder on the GPU. Since the Hough transformation and the merging can not be as effectively parallelized, the Hough transformation has to be parallelized on a per tracklet basis and the merging done event-wise. Therefore, a significantly higher number of events must be calculated in parallel to benefit from the GPU. Fig. 4.27 shows a comparison between the acceleration factors of the full Hough track finder. In magenta, the combination of the Apollonius calculation on the GPU and Hough transformation and merging on the CPU is shown. In red and blue the speed for the entire algorithm on the GPU is shown. Here, red indicates the pure Kernel acceleration and blue depicts the acceleration with data copy. The reason why the data copy is not only a constant offset as in the Apollonius calculation is that the algorithm is implemented with multiple Kernels to improve the occupancy of the GPU. Thus, the Apollonius calculation itself is a Kernel, where each circle is calculated

in parallel, whereas the Hough space is implemented as another **Kernel** that calculates the Hough space per tracklet in parallel. The **Kernel** with the lowest **GPU** occupancy is the merging, because here each event is computed in parallel. The usage of the different **Kernels** and the data handling between the **Kernels** results in a non-constant data handling offset.

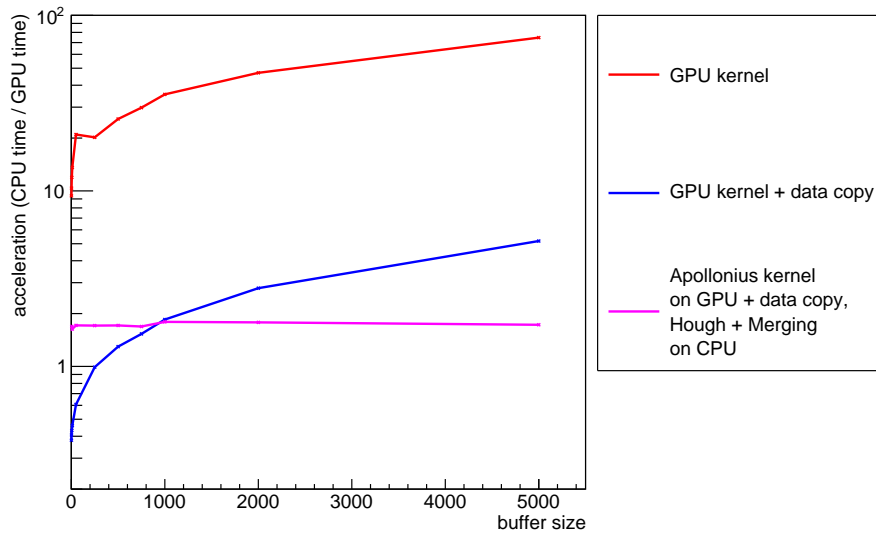


Figure 4.27: Comparison of the acceleration factor of the total Hough track finder. The Apollonius circles calculated on the **GPU** and Hough transformation and merging performed on the **CPU** is shown in magenta. Calculating the entire algorithm on the **GPU** is shown in red and blue, where the **GPU** Kernel is indicated in red and the Kernel plus data copy is visualized in blue.

The **Kernels** without data copying reach a speed of $176.1 \mu\text{s}/\text{event}$, corresponding to an acceleration factor of about 75 compared to the **CPU** runtime. However, this does not include the data handling between the different **Kernels**. When calculating 5000 events in parallel, the algorithm reaches a speed of $2.5 \text{ ms}/\text{event}$ with data copy and handling between the **Kernels**, which is a factor of five faster than the **CPU** case. As already mentioned, calculating the entire algorithm on the **GPU** requires a much higher number of events calculated in parallel to benefit from the **GPU**. Therefore, in Fig. 4.27 it can be observed that the **GPU** version of the Hough track finder takes even more time than the **CPU** version when calculating less than 500 events in parallel, corresponding to an acceleration factor below one. The data copy from the **CPU** to the **GPU** and back takes more time than computing the algorithm on the **CPU**.

Furthermore, it should be mentioned that the speed of the algorithm on the **GPU** is limited by the amount of memory. The medium size **GPU** used in this work has a global memory of 6 GB, which limited the number of events calculated in parallel to about 5000 events. As Fig. 4.27 shows, an asymptotic increase of the acceleration factor with increasing number of events calculated in parallel is observable. However, the memory consumption increases linearly with the number of events. In the current implementation, the algorithm requires about 1 MB per event on the **GPU**. The impact of a larger **GPU** with more global memory would only slightly improve the speed of the algorithm, since the acceleration factor in Fig. 4.27 is already in the region of low increase. Consequently, a better data handling and **GPU** occupancy is necessary to further improve the speed of the Hough track finder.

The results of the GPU calculation indicate that it is not beneficial to extend the Hough track finder to secondary tracks. This would be possible by exchanging the IP with a third hit. On the one hand, this would increase the combinatorics, which can be handled well by the GPU. On the other hand, however, a three-dimensional Hough space would be needed to describe a circle without the knowledge of the IP. The Hough space currently has the main impact on the required memory. Already in the primary finding case, the memory consumption of the Hough space limits the speed up of the algorithm to a factor of five. In case of a three-dimensional Hough space this memory consumption would be even larger. Thus, the required memory for the Hough space is the main obstacle for an efficient GPU usage. Before the Hough track finder can be extended to secondary tracks, a way must be found to significantly reduce the required memory. In this work, it was decided to develop a different, less computing intensive algorithms for finding secondary particles instead.

4.6 Apollonius Triplet Track Finder

The Apollonius Triplet track finder is the second algorithm developed in this thesis. The algorithm is developed as a fast secondary track finder with low memory consumption. In the track finding, first the primary tracks in an event are found with a primary track finder and afterwards the remaining hits are used for secondary tracking with the Apollonius Triplet track finder. To further reduce the number of hits a preselection of the hits is performed with the segmentation preselection (see section 4.4.2). The Apollonius Triplet track finder identifies a set of three STT hits, calculates the corresponding eight Apollonius circles and finally decides for one of them to be the particle track. Similar to the Hough track finder, a combination of three hits is used for the Apollonius calculation. Thus the runtime of the algorithm strongly correlates with the number of investigated triplets. Therefore, an essential step of the algorithm is the triplet finding. Here, it is important that not too many triplets are tested for runtime reasons, but still enough are tested to achieve a high tracking efficiency. After the triplet finding, the Apollonius circles are calculated, which was discussed in chapter 4.4.1. Finally, the track selection is important to keep the efficiency high but also reduce the number of ghosts and clones. In this chapter, first the triplet finding is explained. After that, the track selection is presented. As the last part of the chapter, the results of the algorithm as a stand-alone algorithm and in combination with the Standard tracker and the newly developed Hough track finder are shown.

4.6.1 Triplet Finding

Only STT hits are used for triplet finding. Therefore, the Apollonius Triplet track finder is a local algorithm, where a solution for one subdetector - the STT - is determined and the hits of the other subdetectors are added afterwards. The aim of the triplet finding is to find a combination of three hits that belong to the same particle track. These three hits should be as far apart as possible to minimize the uncertainties in the radius of the Apollonius circle [130] and thus the found particle track. Additionally, the algorithm must be able to determine the number of tracks per event. The basic idea of the triplet finding is to define a set of inner, mid and outer STT hits and combine these sets with each other. The reason why the STT is chosen as the starting detector is that the straws are arranged in a dense packing. On the one hand, this means that it is possible to define specific layers of the STT. These are the rows in the radial direction. Then,

the sets of inner, mid and outer hits can be defined as specific layers, from which the hits for a triplet are taken. On the other hand, it is possible to count the number of hit straws within one layer. This leads to an estimate for the number of tracks per event.

The procedure of the algorithm is explained based on Fig. 4.28. Here an event from a background simulation (FTF) with 7 GeV/c beam momentum is shown. First of all, the hits of the event are preselected with the Segmentation algorithm, which divides the hits of this event into four subsets. These are the upper right π^- , the right proton-antiproton pair, the lower proton and one large subset containing all hits in the upper left region ($p, \pi^-, 2 \times \pi^+$). Assuming slightly curved tracks, each particle track produces one or at most two hits per STT layer, such as the upper right π^- in Fig. 4.28. For curved tracks, it can happen that one particle track produces more than one hit per layer, as the proton in subset four. Nevertheless, these hits must be directly adjacent to each other. This means that the layer structure of the STT contains

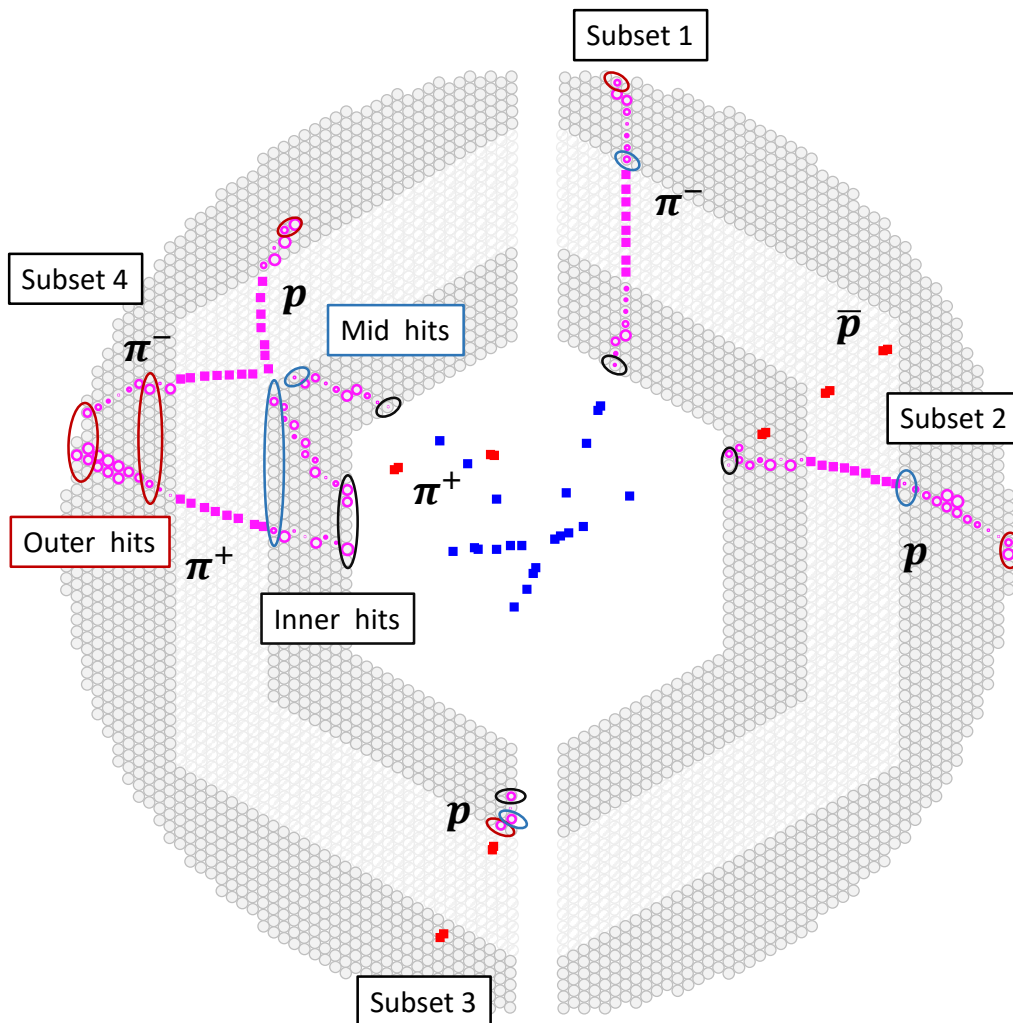


Figure 4.28: Illustration of the working principle of the Apollonius Triplet track finder for a background event (FTF) with 7 GeV/c beam momentum.

information about the number of tracks per event and the trajectory of the particles. Thus, it is assumed that the maximum number of disconnected hits per layer represents the number of tracks in an event. For a better understanding, the layer structure of the fourth subset is shown in Fig. 4.29. Here, the number in brackets represent the tube ID. Directly adjacent tubes are contained in a bracket, which is in the following called a hit cluster. One layer can consist of several hit clusters, which are represented as several brackets in a layer. The maximum number hit clusters per layer is assumed to be the number of tracks. In Fig. 4.29, the number of hit clusters per layer is shown in the column on the right. The assumed number of tracks in subset four is three tracks.

For the triplet construction, the layer with the lowest number that has the maximum number of hit clusters is used as the inner set of hits (here layer 0, in Fig. 4.28 shown in black). The layer with the highest number that contains the maximum number of hit clusters is used as the outer set of hits (here layer 18, in Fig. 4.28 shown in red). This procedure has the advantage that tracks can be found that either decay within the *STT* or leave the *STT* in the forward direction and therefore do not have hits in all layers of the *STT*. In this example, the proton in subset four is such a vanishing track. A disadvantage is that the distance between the inner and outer layer is always limited to the distance of the shortest track. This can lead to poorer momentum resolution. Therefore, to improve the momentum resolution of tracks going through the entire

				Number of hit clusters	
Layer 0:	(13),	(22/23),	(27)	3	← Inner hits
Layer 1:	(118),	(127),	(132)	3	
Layer 2:	(229),	(238),	(243)	3	
Layer 3:	(346/347),	(354/355),	(361)	3	
Layer 4:	(470),	(476/477),	(484)	3	
Layer 5:	(599),	(604/605),	(613)	3	
Layer 6:	(734/735),	(738/739),	(749)	3	
Layer 7:	(876),	(878/879),	(890)	3	
Layer 8:	(1017),	(1019),	(1042)	3	
Layer 9:	(1214),	(1220),	(1238)	3	
Layer 10:	(1414),	(1434),		2	
Layer 11:	(1620),	(1641),		2	
Layer 12:	(1836),	(1861),		2	
Layer 13:	(2059),	(2086),	(2109)	3	
Layer 14:	(2285/2286),	(2306),	(2312)	3	
Layer 15:	(2521/2522),	(2544),	(2549)	3	
Layer 16:	(2768/2769),	(2784),	(2793)	3	
Layer 17:	(2979/2980),	(2998),	(3006)	3	
Layer 18:	(3196/3197),	(3217),	(3225)	3	← Outer hits
Layer 19:	(3443),	(3450),		2	
Layer 20:	(3672),	(3678/3679),		2	
Layer 21:	(3890),	(3895/3896),		2	
Layer 22:	(4084),	(4088/4089),		2	
Layer 23:	(4257),	(4260/4261),		2	
Layer 24:	(4400),			1	

Figure 4.29: Layer structure used for the Apollonius Triplet track finder for the 4th subset in Fig. 4.28.

STT the last layer of the **STT** with a hit is always added to the set of outer hits.

Finally, the set of mid hits is defined as the layer in the middle between the inner and the outer layer. The set of mid hits can have a lower number of hit clusters than the maximum number. The Apollonius Triplet track finder only uses layers with axial tubes for triplet creation. Therefore, if a skewed layer is in the center between inner and outer layer the next axial layer to the outside is used.

The procedure works well for slightly curved tracks. However, strongly curved tracks can lead to a major runtime increase due to higher combinatorics. An example event is shown in Fig. 4.30. On the left a low momentum track, μ^+ originating from π^+ , is visible reaching only the first few layers of the **STT**. The outer layer is in this example defined as layer seven, since here the maximum number three hit clusters occur. Due to the low transverse momentum, the track is not able to leave the **STT** and produces nine hits in its outer layer. Consequently, the number of combinations drastically increases, since all combinations for each hit in the outer layer must be calculated. To reduce the runtime for these cases, a method is implemented to reduce the number of combinations. For this purpose, the **CA** introduced in chapter 4.3.3 is used. The **CA** connects all hits that unambiguously belong together. This can be used to reduce the number of hits in a set of the inner, mid or outer hits, by checking if hits belong to the same **CA** tracklet. If this is the case, only one of the hits is used. Additionally, this information can be used to reduce the number of combinations by checking whether hits of the inner and the mid set or the mid and the outer set belong to one **CA** tracklet. If a match is found, the other combinations are not calculated. A last method to reduce the number of combinations is to check if a triplet was already found in a previously found track. Here, only tracks are used which already went through different tests to check if the track is a reasonable track. These tests are presented in the next chapter.

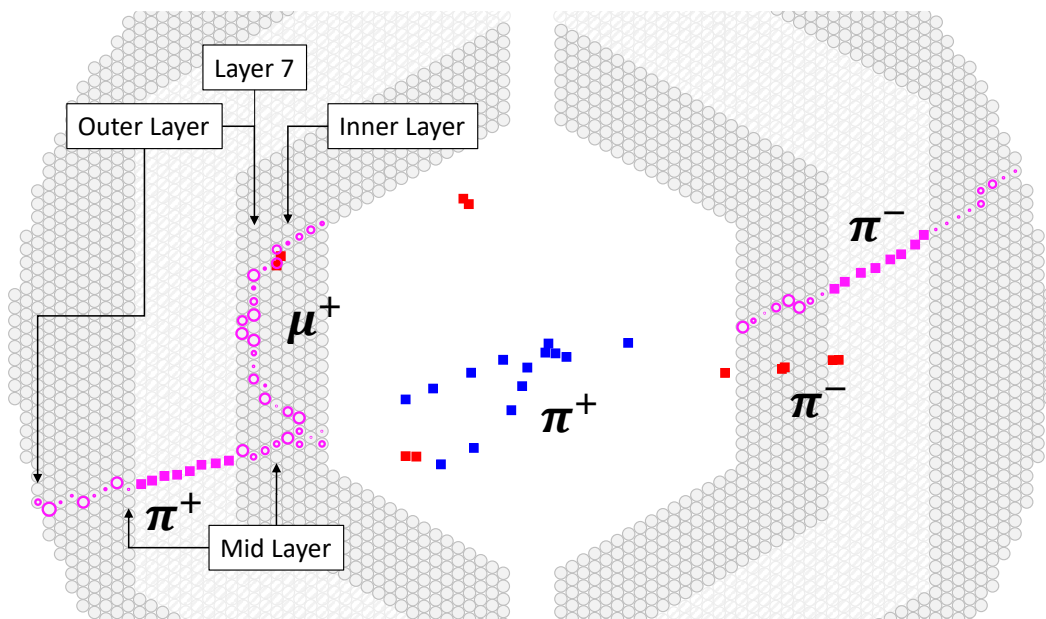


Figure 4.30: Example of a background event with a strongly curved, low momentum muon track reaching only the first few **STT** layers. The muon is a daughter particle of the π^+ .

4.6.2 Track Selection

After the triplets are created, eight Apollonius circles are calculated for each triplet. For the correct triplet combination, only one of the eight Apollonius circles describes the track parameters. Furthermore, some wrong combinations remain, although many wrong combinations were already removed during the triplet finding. In the track selection step, the final particle track assumptions are created. Here, the remaining wrong combinations must be removed as well as the best of the eight possible Apollonius circles must be found. First, **STT** hits that are close to the Apollonius circles are added to the track. Here, a maximum distance of 0.5 cm is used. The distance is calculated as the distance from the isochrone to the circle. After that, a so-called continuity check is performed. It is assumed that a particle track must be continuous in the **STT**. Since the **STT** is designed in a dense packing, it is possible to check if two hit tubes neighbor each other. If there are gaps within the found solution, it is not a correct solution and can be discarded. In the current implementation, the skewed layers are not included. This means, that the continuity check only inspects if the first layer before and after the skewed layers contains a hit.

For the remaining continuous tracks, the other detector hits are now added. For the **MVD** hits, a minimum distance of 1 cm is required. This value is larger than for the **STT** because of the larger radiation length of the **MVD**. Therefore, the circle assumption is not correct anymore. The closer the **MVD** hit is to the **STT**, the smaller the deviation from the circle assumption. The use of a dynamic distance selection depending on the **MVD** layer was tested. The dynamic distance however resulted in both more correctly included but also more wrongly added **MVD** hits closer to the **IP** since the **MVD** hit density is higher closer to the **IP**. Therefore, the dynamic distance selection was discarded. For the **GEM** detector a maximum distance of 1 cm was used for the same reasons as for the **MVD**. Also for the **GEM** detector, the circle assumption of the particle is not correct, since the outermost **GEM** plates do not experience the full 2 T magnetic field of the solenoid magnet. However, a dynamic distance cut depending on the position of the corresponding **GEM** plate has not yet been tested.

Based on the number of hits per track and the mean square distance of the hits to the Apollonius circle, one Apollonius track is selected. First, the Apollonius circles per triplet are sorted based on the number of hits. If multiple Apollonius circles with the maximum number of hits exist, the one with the lowest mean square distance is chosen. In a last step, the number of remaining tracks is further reduced to the assumed number of tracks in the event (see chapter 4.6.1). To reduce the number of tracks, combinations of tracks are determined. When combining two tracks, the hits of both tracks are merged without double counting. The best combination of hits is then determined as the combination with the highest number of found hits.

4.6.3 Results

The Apollonius Triplet track finder is a local algorithm starting with the **STT** hits and adding the other detector hits afterwards. Therefore, applying the same definition for tracks to be within the fiducial volume to the results of the Apollonius Triplet track finder as used before in Fig. 4.19 is an inappropriate comparison. Both the Standard tracker and the Hough track finder are global algorithms, which means they are also capable to find tracks with no or very few **STT** hits. The Apollonius Triplet track finder, however, is not able to find such tracks, since it always requires at least three **STT** hits. Consequently, a different definition of a track to be within the fiducial volume is used for comparison. Here, the Standard Track Selector is not used,

but instead the Only *STT* Selector (see chapter 4.2.4), which defines a track to be within the fiducial volume if it has at least six *STT* hits. Due to the change in the definition of the fiducial volume, higher efficiencies are now expected for all track finders, as already shown in Fig. 4.16. For the analysis and comparison of the Apollonius Triplet track finder with the Hough and Standard tracker 20,000 simulated events of the reaction $\Xi^-(1820)\bar{\Xi} \rightarrow K^- p \pi^- \pi^+ \bar{p} \pi^+$ were used. This reaction produces many secondary tracks with displaced vertices due to the long lifetimes of the Ξ^+ and the Λ . Furthermore, the $\Xi^-(1820)$ hyperon is the resonance studied in chapter 5 and is of particular interest for the *PANDA* experiment, see chapter 3.3.1. In Fig. 4.31 a comparison of the presented tracking algorithms is shown. Here, the Standard track finder in *PANDA* is shown in grey, the Hough track finder, for finding primary tracks, is shown in blue and the Apollonius Triplet track finder is shown in green. It is visible that the Apollonius Triplet track finder has a lower efficiency for primary tracks than the other two track finders. Since the algorithm is planned as an extension for a primary track finder, the efficiency for primary tracks is less crucial here. More interesting is the efficiency to find secondary tracks. Here, an efficiency of 65.2 % is achieved, which is similar to the Hough track finder.

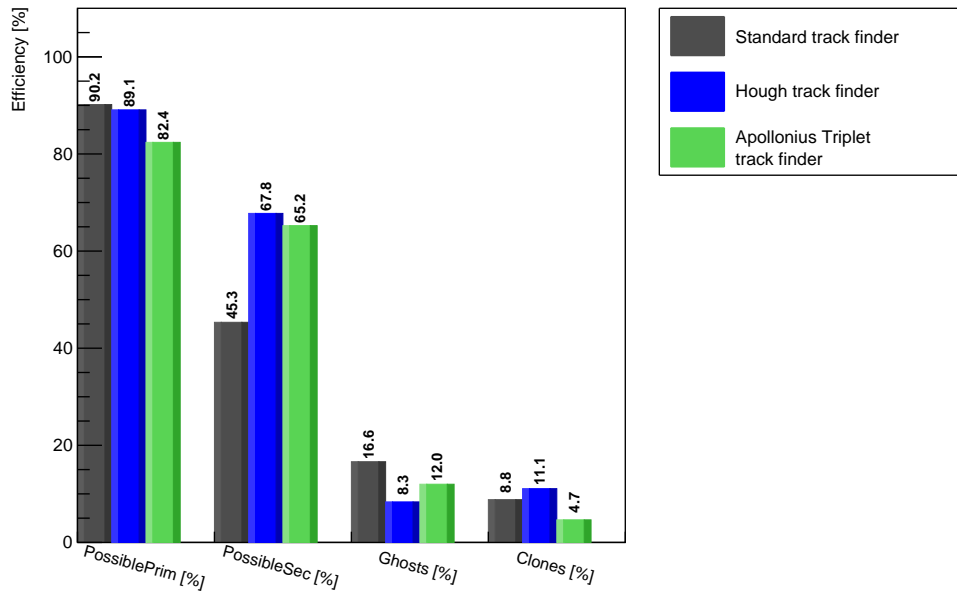


Figure 4.31: A comparison of the quality parameters of the Standard tracker, the Hough track finder and the Apollonius Triplet track finder for 20,000 events of the decay $\bar{p} p \rightarrow \Xi^-(1820)\bar{\Xi} \rightarrow K^- p \pi^- \pi^+ \bar{p} \pi^+$.

To understand the high efficiency of the Hough track finder for secondary tracks, an example of secondary tracks with a displaced vertex and the results found with the Hough track finder as well as the Apollonius Triplet track finder are shown in Fig. 4.32. Here, the solution of the Hough track finder is shown in blue and the solution of the ApolloniusTriplet track finder is shown in green. It is visible that the Hough track finder splits the secondary tracks into several subtracks and connects these tracks to the *IP*. The ApolloniusTriplet track finder, on the other hand, is able to find the complete particle track with a much better momentum resolution. To further investigate the secondary tracks, the [distance of Point of Closest Approach \(dPCA\)](#)

is introduced, which is the shortest distance between the circle describing the particle track to the IP. The quantity is visualized in Fig. 4.33. Based on the observation in Fig. 4.32, the *Completeness* of the found secondary tracks is investigated as a function of the *dPCA*. Here, in Fig. 4.34a, a clear difference between the three algorithms is recognizable. The Standard track finder has not only the worst finding rate for secondary tracks but also the worst *Completeness* of the found tracks. The Hough track finder is also unable to reconstruct the secondary tracks in an acceptable way, producing tracks with less than 50 % *Completeness*, which is another indication that the Hough track finder splits the secondary tracks into subtracks and connects these subtracks to the IP, as shown in Fig. 4.32.

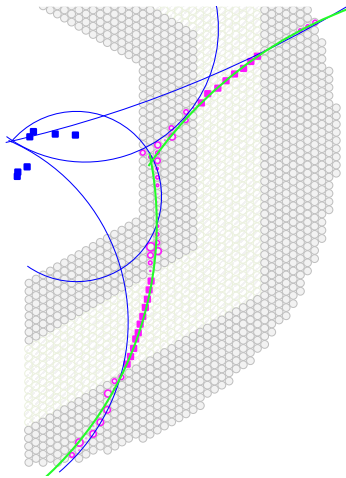


Figure 4.32: Example event of secondary tracks with solutions found by the Hough track finder (blue) and solutions found by the Apollonius Triplet track finder (green).

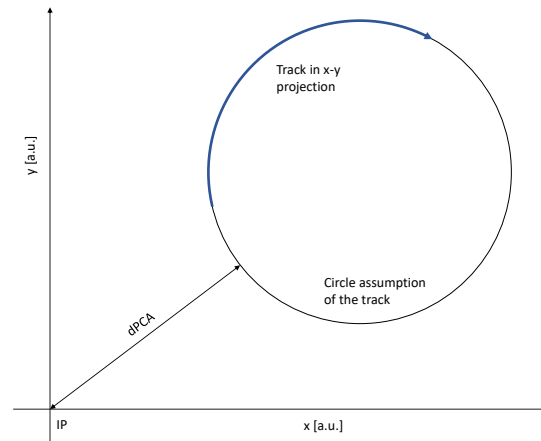
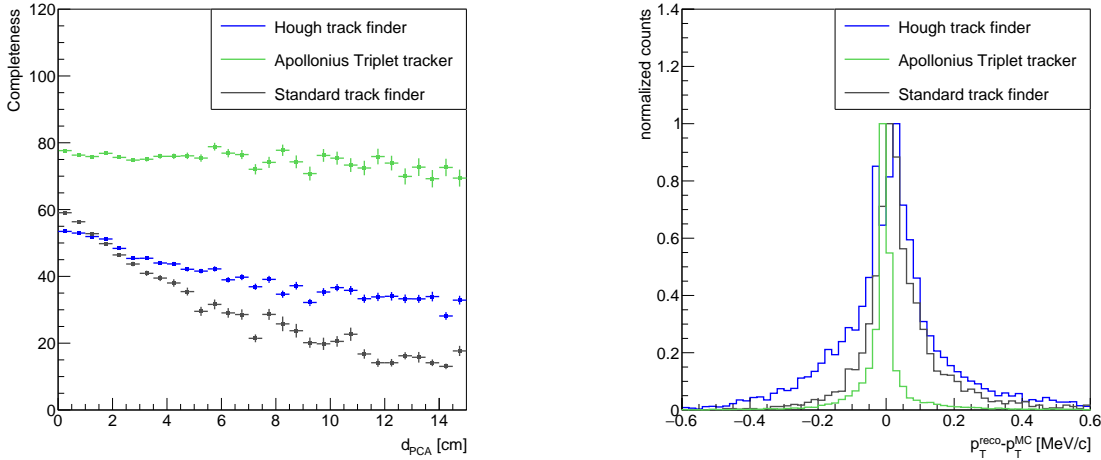


Figure 4.33: Illustration of the distance of Point of Closest Approach (*dPCA*).

For larger *dPCA*, the *Completeness* of the primary track finders drops drastically far below 50 %. However, the Apollonius Triplet track finder is able to find the secondary tracks. Here, a constant behaviour in the *Completeness* is shown. Thus, on average, the Apollonius Triplet track finder is able to find the secondary tracks with a *Completeness* of 80 %. The missing 20 % are on the one hand a consequence of the averaging in Fig. 4.34a. So here, also tracks are taken into account that are poorly found with a *Completeness* of less than 50 %. On the other hand, the algorithm focuses mainly on the *STT* hits. Therefore, the inner *MVD* hits may not be found due to the larger radiation length of the *MVD*, and the outer *GEM* hits are also often not found, since the outermost layers of the *GEM* detector do not experience the full 2 T magnetic field strength. Additionally to the *Completeness*, the difference between the number of MC generated hits and the number of found hits per track is plotted against the number of MC generated hits per track. These plots are shown in Fig. 4.35a and 4.35b for all secondary tracks found by the Hough track finder and by the Apollonius Triplet track finder, respectively. It is visible that the Apollonius Triplet track finder has a clear maximum for fully found tracks. For the Hough track finder no clear maximum is visible, which reflects the observations already seen in Fig. 4.34a that the Hough track finder is only able to find parts of the tracks. Additionally, an interesting behavior is shown for the Hough track finder where an increase in entries can be observed for tracks with about six missing hits. The reasons for the six missing hits are manifold. One reason is that the



(a) Completeness of the secondary tracks found with the different tracking algorithms.

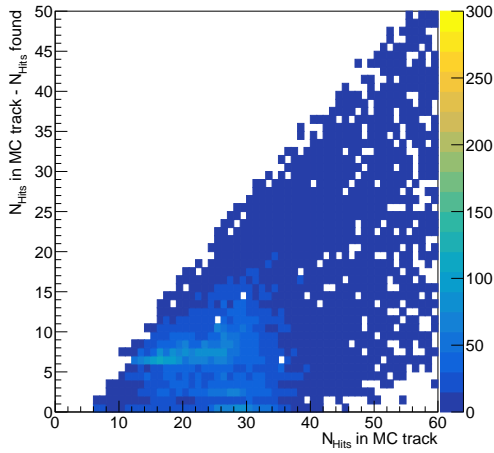
(b) Momentum resolution for secondary tracks with a $d_{PCA} > 3$ cm.

Figure 4.34: Comparison of three track finding algorithm of the *Completeness* of all secondary tracks (a) and the momentum resolution for all secondary tracks with a $d_{PCA} > 3$ cm (b).

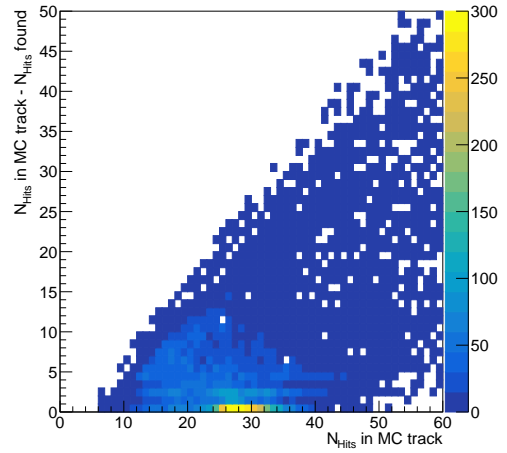
six GEM hits are missing for some tracks. However, also tracks are included, where only parts of the STT hits are found.

The superiority of the ApolloniusTriplet track finder for secondary tracks can also be seen in Fig. 4.34b. Here, the momentum resolution for secondary tracks with d_{PCA} greater than 3 cm is shown. For these tracks, both the Hough track finder and the Standard track finder have a broad distribution of tracks that do not fit well to the correct particle momentum. However, the Apollonius Triplet track finder has a sharp peak where the reconstructed transverse momentum equals the MC generated transverse momentum. In Fig. 4.36a and 4.36b the relative reconstructed transverse momentum (p_T^{RECO}/p_T^{MC}) is plotted against the MC generated transverse momentum for the Hough and the Apollonius Triplet track finder for all secondary particles. For the Hough track finder a smaller peak at the correct momenta can be seen mainly originating from secondary tracks with a d_{PCA} smaller than 3 cm. For the Apollonius Triplet track finder more tracks can be found with a correctly reconstructed transverse momentum and therefore the peak is clearer.

Finally, to optimize the overall finding efficiency for primary and secondary tracks, the primary track finders are combined with the secondary track finder. This means that first a primary track finder is applied to the data sample. After that, the ApolloniusTriplet track finder uses the remaining hits of the event to find the secondary tracks. In Fig. 4.37 the quality parameters for each tracking algorithm and for the combination of primary and secondary track finders are shown. Here, first the Standard tracker is combined with the Apollonius Triplet track finder (red), and in comparison the Hough track finder is combined with the Apollonius Triplet track finder (magenta). The finding rate for the primary track is nearly identical for both combinations with 93.1 % and 93.2 %. The Hough track finder combined with the Apollonius Triplet track finder has the best finding efficiency for secondary tracks with 79.1 %. Striking is the high ghost rate of the Standard tracker combined with the Apollonius Triplet track finder

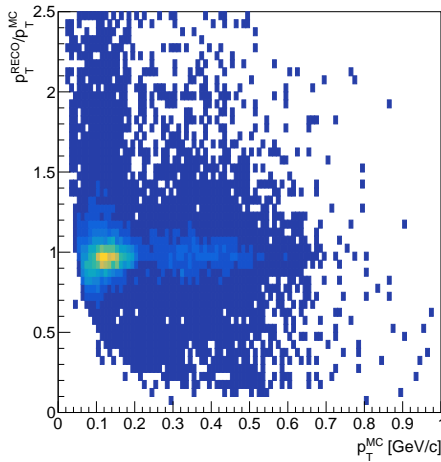


(a) Hough track finder.

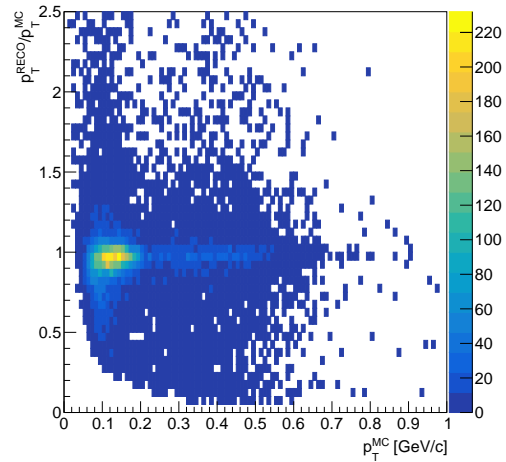


(b) Apollonius Triplet track finder.

Figure 4.35: Difference between number of MC generated hits minus the number of found hits vs. the MC generated number of hits in a secondary track. On the left the Hough track finder and on the right the Apollonius Triplet track finder is shown.



(a) Hough track finder.



(b) Apollonius Triplet track finder.

Figure 4.36: The relative reconstructed transverse momentum is plotted against the generated transverse momentum for all found secondary particles. On the left the Hough track finder and on the right the Apollonius Triplet track finder is shown.

and the high clone rate for both combinations. The ghost rate is more problematic than the clone rate, because ghosts can lead to a wrong physics analysis with a large background. For the combination of Hough and Apollonius Triplet track finder, the ghost rate of 15.6% is still just within an acceptable range², considering that the Standard tracker alone has a comparable ghost rate. However, the ghost rate of the Standard plus Apollonius Triplet track finder is high,

²Acceptable is here equal to or better than the Standard tracker.

so methods must be developed to reduce the number of ghosts. This can either be implemented directly for the Standard tracker but also after combining both algorithms. In the second case, the combination of Hough and Apollonius Triplet track finder could also benefit from such a ghost reduction procedure. In case of the clone ratio, the Hough track finder combined with the Apollonius Triplet track finder performs worse with 19.2% clones compared to the 15.7% clones of the combination of Standard and Apollonius Triplet track finder. The high number of clones is a consequence of the primary track finders finding parts of the secondary tracks and connecting these parts to the IP, as seen in Fig. 4.32. Afterwards, the Apollonius triplet track finder uses the remaining hits of the secondary tracks to find them a second time. Thus, these secondary tracks are double counted, where it can be assumed the solution found with the Apollonius Triplet track finder has a better momentum resolution. Here, either a merging procedure must finally be performed, merging the small tracklets found with the primary trackers to the more accurate tracks found with the Apollonius Triplet track finder, or a method must be developed to remove these short tracks which are parts of secondary tracks directly in the procedure of the primary track finder. This second option, however, is challenging because also small tracks occur that decay within the STT, which makes it difficult to distinguish these correctly found short tracks from the short tracks which were found as part of a larger secondary track.

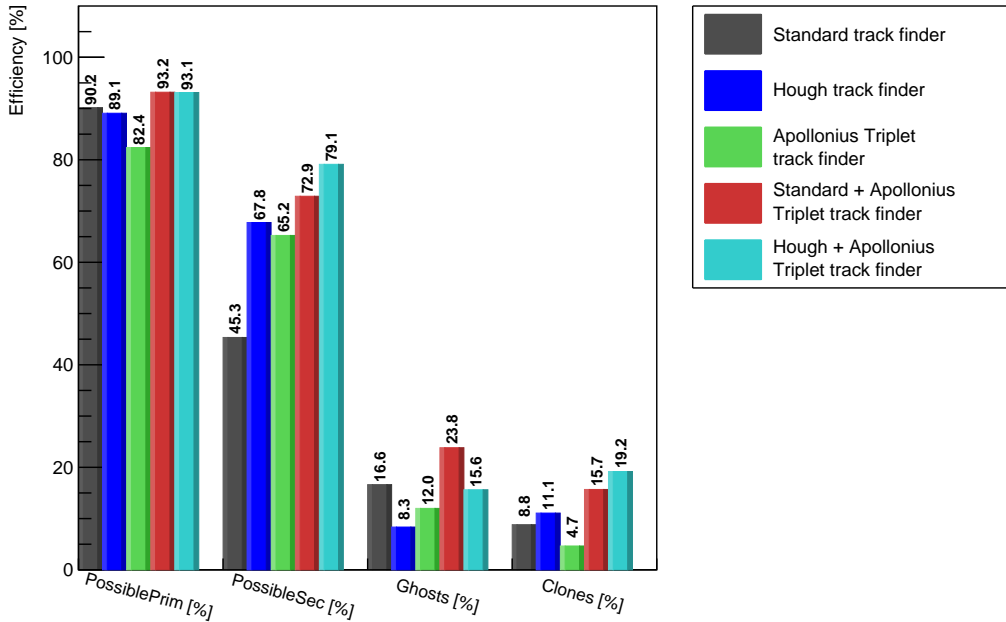
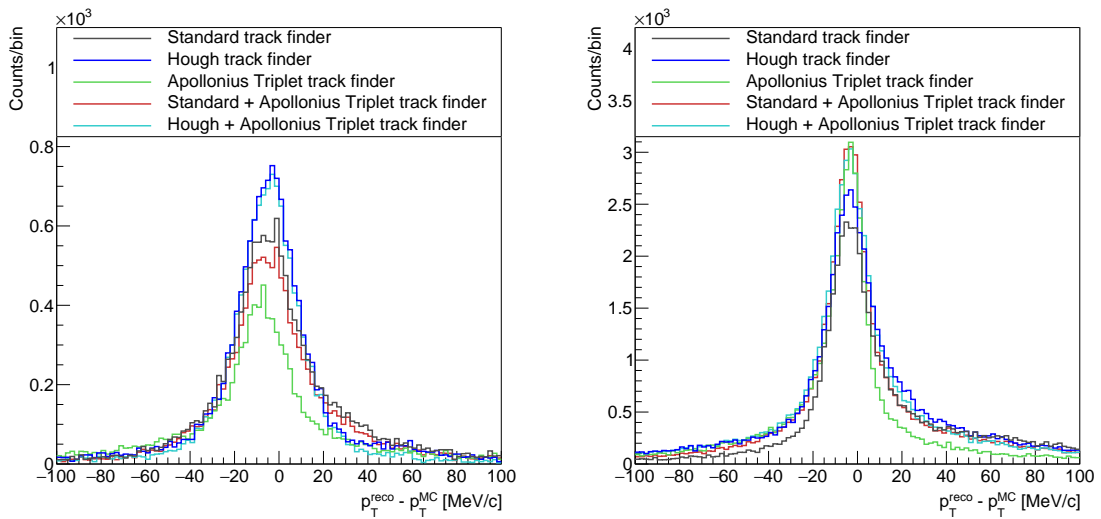


Figure 4.37: Final comparison of the Quality parameters of the three algorithms as stand alone algorithms and the combination of a primary track finder (Standard or Hough) and the Apollonius Triplet track finder for 20,000 events of the decay chain $\bar{p}p \rightarrow \Xi^-(1820)\Xi^+ \rightarrow K^-p\pi^-\pi^+\bar{p}\pi^+$.

In Fig 4.38 and 4.39 the absolute and relative momentum resolutions for all investigated tracking algorithms are shown³. Here, the primary particles are shown on the left and the secondary particles on the right. The corresponding *FWHM* and *RMS* can be found in Tab. 4.4 and 4.5. For the Apollonius Triplet track finder, shown in green, a shift in the absolute and relative momentum resolution to lower momenta is visible. This shift is a consequence of the energy loss of the particles within the *MVD*. Since the Apollonius Triplet track finder is a local algorithm focusing on the *STT*, this shift to lower momenta is expected. The shift of the Standard tracker, shown in grey, to higher momenta has already been discussed previously and originates from the *GEM* hits, that do not experience the full 2 T magnetic field. In Tab. 4.4 and 4.5 the *FWHM* and the *RMS* are shown for the primary and the secondary tracks, respectively. Here, no improvement of the momentum resolutions of the combined algorithms can be seen in comparison to the stand alone algorithms. A reason for this is the missing merging procedure, needed to combine multiple found tracks. Therefore, some tracks are included that were poorly found with a low *Completeness* and a large momentum deviation. The improvement due to the combination of primary and secondary tracks is therefore currently only visible in the efficiency.

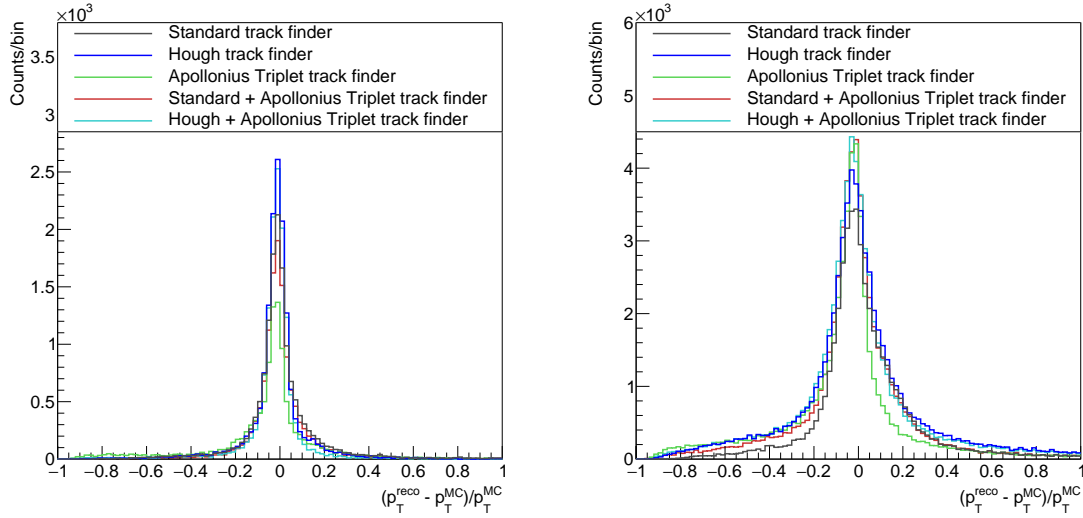


(a) A comparison of the transverse momentum resolution for primary tracks for all investigated track finders.

(b) A comparison of the transverse momentum resolution for secondary tracks for all investigated track finders.

Figure 4.38: Transverse momentum resolution for primary (left) and secondary (right) particles.

³A comparison to the momentum resolution after the Kalman fit is shown in the next chapter.



(a) A comparison of the relative transverse momentum resolution for primary tracks for all investigated track finders.

(b) A comparison of the relative transverse momentum resolution for secondary tracks for all investigated track finders.

Figure 4.39: Relative transverse momentum resolution for primary (left) and secondary (right) particles.

Table 4.4: Summary of the **FWHM** and the **RMS** for the transverse momentum resolution for primary tracks.

	FWHM		RMS	
	absolute [MeV/c]	relative [%]	absolute [MeV/c]	relative [%]
Standard	28	7	29.7	16.9
Hough	28	7	27.3	14.6
Apollonius Triplet	24	6	34.1	24.3
Standard + Apollonius Triplet	16	4	28.5	15.2
Hough + Apollonius Triplet	28	7	22.9	14.1

Table 4.5: Summary of the **FWHM** and the **RMS** for the transverse momentum resolution for secondary tracks.

	FWHM		RMS	
	absolute [MeV/c]	relative [%]	absolute [MeV/c]	relative [%]
Standard	21	16	33.6	22.3
Hough	23	17	34.8	28.6
Apollonius Triplet	15	11	30.6	27.6
Standard + Apollonius Triplet	15	12	32.2	24.6
Hough + Apollonius Triplet	21	15	33.0	28.1

Investigation of $\bar{p}p \rightarrow \Xi(1820)^-\Xi^+$

5

In this chapter, the expected performance for [PANDA](#) to measure the reaction $\bar{p}p \rightarrow \Xi(1820)^-\Xi^+$ is investigated. A previous work [131] investigated this channel using an ideal tracking procedure. However, since the reaction contains mainly secondary particles, no realistic track finder in [PANDA](#) was available at that time to reconstruct the channel satisfactorily. In this work, realistic primary and secondary track finders have been developed, allowing a realistic reconstruction of the reaction for the first time. The aim is to determine the expected performance of [PANDA](#) to measure this reaction. In this work, the Ideal Track Finder is replaced by the combination of realistic primary and secondary track finders developed in this work.

Hyperons are of particular interest for the [PANDA](#) physics program. They are produced in an energy region that describes the transition from non-perturbative to perturbative [QCD](#). [QCD](#) is already well verified in the perturbative regime. However, the non-perturbative [QCD](#) region is not yet fully understood and significant discrepancies between theoretical models and experimentally measured data still exist. One reason for predicted but not observed resonance states could be poor data quality. In particular, for the multistrange hyperons, data with higher statistics are needed to be able to confirm or excluded predicted states experimentally with sufficient accuracy. The existing data are poor even for the lightest multistrange hyperon, the Ξ hyperon. Here, the PDG explicitly mentions that the branching fractions for the resonances are only poorly determined and the data are mostly from bubble chamber experiments [33]. To understand the inner structure and production mechanisms of hyperons, better data quality is indispensable.

The Ξ resonances have a very distinctive decay pattern as they decay into Λ particles. The Λ is neutral and has a long lifetime. Consequently, its mean decay length is about 8 cm. In [PANDA](#), therefore, good tracking algorithms for particles originating from displaced vertices are required. Currently, [PANDA](#) does not have a standard secondary track finder. Therefore, in this chapter, a realistic track finding using the newly developed track finders is investigated for the reconstruction of the full decay chain. First, the currently used standard tracker in [PANDA](#) is compared to the alternatively developed Hough track finder, which is also a primary track finder. Then, the two primary track finders are each extended with the secondary track finder developed in this thesis.

5.1 Simulated Data

In this work 400,000 events of the reaction $\bar{p}p \rightarrow \Xi(1820)^-\Xi^+$ were simulated¹. The decay tree is shown in Fig. 5.1. The $\Xi(1820)^-$ decays effectively instantaneously into ΛK^- , which is the dominant decay mode of the resonance $\Xi(1820)^-$. However, the branching fraction has not yet been measured. The particle data group describes the decay into ΛK^- as the dominant decay with a large branching fraction, which is poorly determined [33]. In the reaction investigated here the K^- is thus the only measurable charged particle emitted directly from the primary vertex. All other final state particles have a displaced vertex with a mean decay length of about 5 cm for the π^+ originating from the Ξ^+ decay and about 7 cm for the Λ decay. The dominant decay of the Ξ^+ is the decay into $\bar{\Lambda}\pi^+$ with a branching fraction of $(99.887 \pm 0.035)\%$ [33]. Λ and $\bar{\Lambda}$ decay predominantly into $p\pi^-$ and $\bar{p}\pi^+$ with a branching fraction of $(63.9 \pm 0.5)\%$ [33]. In this analysis the decay tree shown in Fig. 5.1 is investigated exclusively.

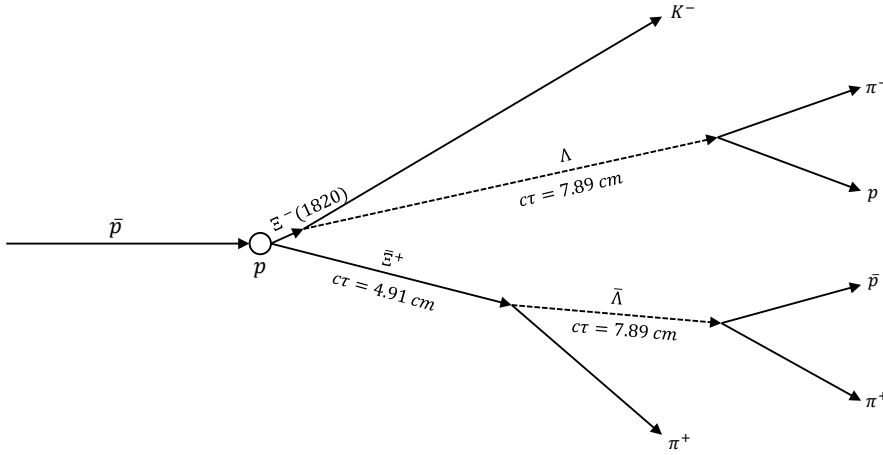


Figure 5.1: Reaction chain of $p\bar{p} \rightarrow \Xi(1820)^-\Xi^+$. The decay daughters of both Ξ include a Λ , which results in four clearly distinguishable vertices and six final state particles.

Therefore, the events were generated with *EvtGen* [108], where both the Ξ and the Λ decay are forced to decay as mentioned above with a branching fraction of 100%. Furthermore, a phase space (PHSP) model is chosen for the decay $\bar{p}p \rightarrow \Xi(1820)^-\Xi^+$ as a simplification due to the absence of experimental data or theoretical predictions. This is plausible since the beam energy corresponds to a small excess energy and the fact that two of the three pairs of valence quarks in the initial state must annihilate. The PHSP model creates an isotropic angular distribution and ensures therefore that the Ξ^+ and $\Xi(1820)^-$ are underlying the same detector acceptance. A beam momentum of $p = 4.6 \text{ GeV}/c$ is chosen, which corresponds to a center-of-mass energy of 3.25 GeV, which is a little bit above the threshold of $m_{\Xi^+} + m_{\Xi(1820)^-} = 3.14 \text{ GeV}$. The center-of-mass-energy leads to a mean Lorentz boost factor of the $\Xi(1820)^-$ of $\gamma = E/m = 1.775$ corresponding to a mean velocity of $v_{\Xi(1820)^-} = 0.83 \cdot c$ in the laboratory reference frame. The Ξ^+ has a lower mass leading to a slightly higher mean Lorentz factor of $\gamma = E/m = 1.811$.

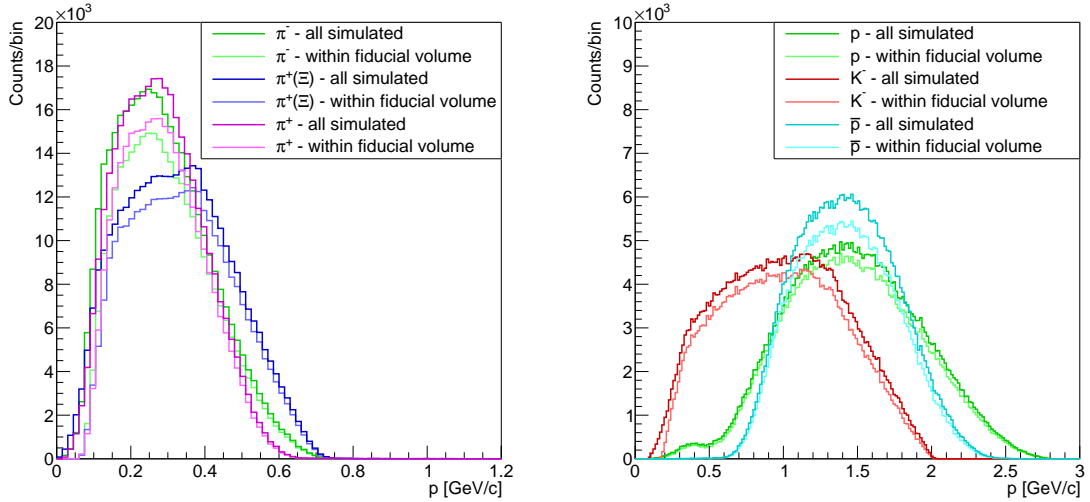
¹PandaRoot version: v.13.0.0

Not all particle tracks are reconstructible in *PANDA*. Thus, the Standard Track Selector is used to define if a track is within the fiducial volume, which means that more than three hits in the *MVD* or more than five hits in total in the *MVD*, *STT* and *GEM* detectors are required. Tab. 5.1 shows the fraction of tracks within the fiducial volume to all simulated tracks for each final state particle.

Table 5.1: Fraction of final state particles within the fiducial volume.

particle	K^-	P	π^-	$\pi^+(\Xi^+)$	\bar{P}	π^+	all final state particles
fraction within fiducial volume	89.1 %	94.5 %	84.4 %	85.3 %	86.7 %	82.5 %	49 %

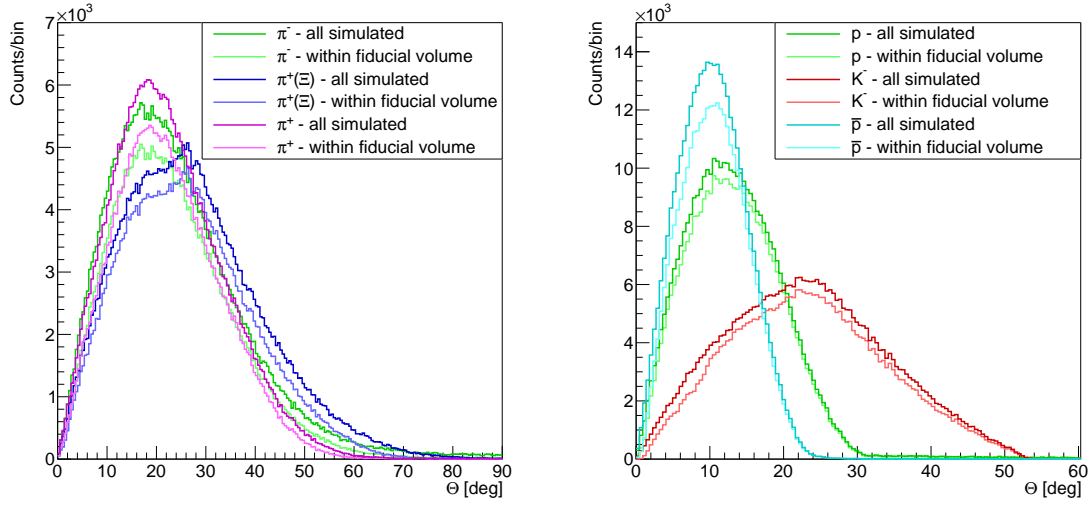
Fig. 5.2 shows the momentum distributions of the six final state particles. The distribution with the darker color for each particle indicates the simulated data, the lighter color depicts the particles within the fiducial volume. The pions (shown in Fig. 5.2a) are expected to have lower momenta with mean values of about 0.3 GeV/c for the pions originating from the Λ decays and 0.35 GeV/c for the π^+ originating from the Ξ^+ . The heavier particles (shown in Fig. 5.2b) have broader momentum distributions, reaching up to 3 GeV/c. Here, mean momenta of 1.0 GeV/c for the kaon, 1.41 GeV/c for the antiproton and 1.46 GeV/c for the proton are observed. Additionally, it can be seen, that the pions (in green and purple in Fig. 5.2a) are less likely to be within the fiducial volume due to their low momenta. Fig. 5.3 shows the angular distribution of the final state particles. Here, the polar angle θ is measured relative to the beam axis. In Fig. 5.3b it is visible that the proton and the antiproton are forward boosted



(a) Momentum distribution of π^- , π^+ , $\pi^+(\Xi^+)$. All simulated particles and those that are within the fiducial volume are shown in different shades of the corresponding color.

(b) Momentum distribution of p , K^- , \bar{p} . All simulated particles and those that are within the fiducial volume are shown in different shades of the corresponding color.

Figure 5.2: Momentum distribution of the six final state particles.



(a) Angular distribution of π^- , π^+ , $\pi^+(\Xi^+)$. All simulated particles and those that are within the fiducial volume are shown in different shades of the corresponding color.

(b) Angular distribution of p , K^- , \bar{p} . All simulated particles and those that are within the fiducial volume are shown in different shades of the corresponding color.

Figure 5.3: Angular distribution of the six final state particles.

with mean polar angles of 13.6° and 10.8° , respectively. Thus, the forward peaked angular distribution of the \bar{p} leads to a larger fraction outside the fiducial volume. The kaon and π^\pm are emitted in a broader range with mean polar angles of 23.7° for the kaon, 26.0° for the π^+ originating from Ξ^+ and about 23.0° for the pions originating from the Λ decay. In total, 49.0% of simulated events have all final state particles within the fiducial volume. A full event reconstruction containing mass window cuts and vertex and kinematic fits as shown in [131] has an efficiency of 14.7% to reconstruct events in which all final state particles are within the fiducial volume.

5.2 Overview of the Analysis Procedure

In the first step the final state particles are selected. These are the particles found by the different tracking algorithms. Only the K^- is a primary particle. The other five final state particles come from a displaced vertex and are therefore classified as secondary tracks.

Four different cases of tracking algorithms are compared.

1. the Standard tracker, which is a pure primary track finder. Therefore, the finding rate for primary tracks is expected to be high. The reconstruction algorithm is, however, not expected to perform well for secondary tracks.
2. the Hough track finder, which is also designed as a pure primary track finder, but has a higher efficiency to find secondary tracks than the Standard tracker.

3. the combination of the Standard tracker and the Apollonius Triplet track finder. Here, first the Standard track is applied to the data sample. The remaining hits are then used by the Apollonius Triplet track finder to find the secondary tracks.
4. the combination of Hough track finder and Apollonius Triplet track finder. Here, the Hough track finder is used as a primary track finder and the secondary tracks are subsequently found by the Apollonius Triplet track finder.

Since both the Apollonius Triplet track finder and the Hough track finder reconstruct only the x-y-component of the track, a reconstruction of the z-information is still missing. In this work, the z-component is calculated by scaling the reconstructed transverse momentum with $\tan(\theta)$:

$$p_z^{reco} = p_T^{reco} \cdot \frac{p_z^{MC}}{p_T^{MC}} = \frac{p_T^{reco}}{\tan(\theta)} \quad (5.1)$$

This procedure leads to a correlation between the transverse and the longitudinal momentum resolution. For a realistic calculation of the z-component a combination of the algorithms with a realistic p_z -finder is still missing.

The investigated tracking algorithms are designed for the target spectrometer. Since a full decay analysis also requires information about tracks that enter the forward spectrometer, an ideal track reconstruction is used for those tracks. Here a finding efficiency of 100 % is assumed with a momentum smearing of 5 % and a vertex smearing of 0.5 mm in each direction. The fraction of the particles reconstructed in the forward spectrometer is shown in Tab. 5.2. Here, the fraction is calculated as the number of tracks found by the ideal forward tracker to the number of tracks within the fiducial volume including barrel and forward part.

Table 5.2: Fraction (in %) of the final state particles found by the ideal forward tracker.

particle	K^-	P	π^-	$\pi^+(\Xi^+)$	\bar{P}	π^+
fraction of tracks found by the ideal forward tracker	5.7	19.5	27.0	18.9	28.0	36.9

After the track finding, a Kalman filter is used to improve the momentum resolution of the found tracks. The Kalman filter is an iterative algorithm and uses the track parameters of the track finding as the start parameters to fit the track to the set of hits found by the track finding algorithms. In this work, the task *PndGFRecoTask* of PandaRoot is used for the Kalman filter. It uses a pion hypothesis to fit the tracks and performs two iteration steps. The algorithm attempts to fit a particle track to all given hits. Consequently, it is sensitive to the order of the hits and to the *Purity* of the track, *i.e.* false hits in the track. Since the track finders developed in this work only reconstruct the x-y-component of the track, hits may be added to the track, that fit in the x-y-projection even though it is clear from the z-projection that the hits do not belong to the track. Since the z-component is not reconstructed by the algorithms developed in this work, it is assumed, that a cleanup procedure, which removes these wrong hits, must be performed after the reconstruction of the z-component. Therefore, in this work, the cleanup procedure is performed based on the MC knowledge. For a completely realistic tracking algorithm this step must be included within or after a realistic p_z -finder.

Furthermore, neither the Standard Track Selector nor the tracking algorithms ensure that the found track contain sufficient hits with z-information. If a track has no hits with z-information, the Kalman filter is not able to fit the track and it is removed from the subsequent analysis.

As the final step of the track reconstruction, particle identification must be performed. For this purpose, an ideal particle identification is used, since only the different track finders are compared here. A realistic particle identification would therefore introduce an additional uncertainty into the comparison, since it is not clear which effects are a consequence of the track finding or the realistic particle identification.

For the event reconstruction, the Rho package is used [117]. The package allows the selection of final state particles according to their particle ID and further constraints such as a mass constraint. After that, the final state particles are combined by adding the 4-momenta. This procedure is done until the final $\bar{p}p$ -system is fully reconstructed.

5.3 Final State Particles

Since the reaction includes six final state particles, in the following only a subset of all the distributions available are shown. The distributions of all remaining particles can be found in appendix B. A Kalman filter is applied after track finding. However, not all found tracks can be fit by the Kalman filter, *i.e.* if a track has too few hits with z-information. In the momentum distribution, these tracks then appear with a relative momentum deviation from the MC simulated track of $(p_T^{RECO} - p_T^{MC})/p_T^{MC} = -1$, as seen in Fig. 5.4. Here, the relative momentum deviation is shown as an example for the track finding using a combination of the Hough and Apollonius Triplet track finders. All tracks are included without distinguishing the different particle types. The relative momentum distributions directly after track finding and

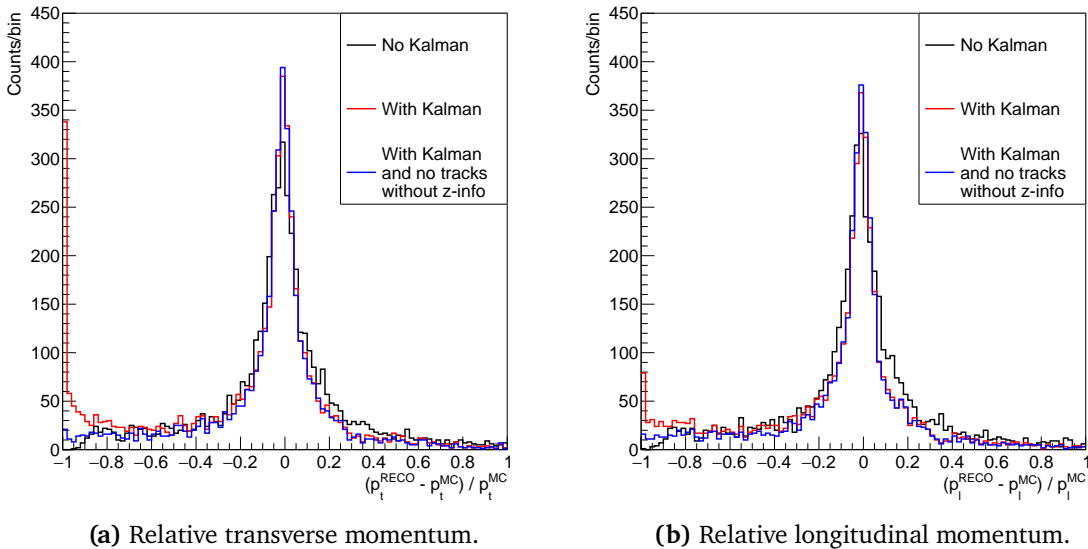


Figure 5.4: Comparison of the relative momentum distributions for tracks with and without applying the Kalman filter, as well as the case where tracks without z-information are excluded. Here, particle tracks created by the combination of Hough and Apollonius Triplet track finder are shown.

before applying the Kalman filter are shown in black. In red and blue the relative momentum distributions after the Kalman fit are shown. Red contains all found tracks and blue excludes tracks without hits containing z-information. In all cases the expected peak around zero is visible. However, in the case of the Kalman filter that still contains tracks without hits with z-information (red) another peak is visible at a relative momentum deviation of -1. These are the tracks that the Kalman filter is not able to fit because the z-information is missing. In the longitudinal momentum the peak at -1 is smaller. The reason for this is that the tracks that cannot be fit are in the underflow of the histogram, since in the longitudinal momentum also negative reconstructed p_z values can occur, which is not possible for the transverse momentum. In the blue distribution, where these tracks, that do not contain z-information, are excluded, the peak at -1 disappears. The FWHM shown in Tab. 5.3 underscores the observations in Fig. 5.4, where it is additionally visible, that the Kalman filter improves the FWHM of all tracks with z-information compared to the raw data without the Kalman filter. A momentum resolution of about 8 % could be achieved.

Table 5.3: Summary of the FWHM for the momentum resolutions with and without the Kalman filter.

	FWHM [%]	
	p_T^{rel}	p_l^{rel}
No Kalman	14	12
With Kalman	8	8
With Kalman + no tracks without z info	8	8

Consequently, those tracks without hits containing z-information are removed. The track reconstruction efficiency after the Kalman filter is therefore reduced compared to the efficiency directly after track finding. In Tab. 5.4 the tracking efficiencies for the different final state particles and the different tracking algorithms before and after the Kalman filter are shown. These are the efficiencies based on the number of tracks within the fiducial volume, which are therefore comparable to the efficiencies shown in the previous chapter. Here the different columns indicate the different track finding cases. In the first column the current Standard track finder is shown. The Standard track finder is a primary track finder. Therefore, the finding efficiencies for the secondary tracks are lower than the finding rate for the K^- , which is the only primary particle in the event. The finding rate for the π^- and the π^+ is lower than 50%. The reason for this is that these particles have a high dPCA, since the Ξ^+ and the $\bar{\Lambda}$ both have long lifetimes. Furthermore, these particles have low momenta, as shown in Fig. 5.2, which makes the track finding even more difficult. Next to the Standard tracker the efficiencies of the Hough track finder are shown. The Hough track finder is also a primary track finder but has a higher efficiency for secondary tracks. This was already shown in chapter 4.4.4, where a poor momentum resolution was associated with these secondary tracks found with the Hough track finder. In Tab. 5.4, this behavior is again visible. Here, a strong decrease in finding efficiency for the secondary tracks (e.g. π^\pm) is observed after applying the Kalman filter to the tracks. This confirms the behavior that these secondary tracks found with the Hough track finder are small parts of the secondary tracks which have been connected to the IP. Consequently, the momentum resolution before the Kalman filter is poor and the Kalman filter is not able to correct these poorly found secondary tracks. In the last two columns in Tab. 5.4 the primary track finders are combined with the Apollonius Triplet track finder to improve the

finding efficiency for secondary tracks. In both cases, an increase in efficiency is observed. The reconstruction efficiencies for both combinations is comparable. The combination of Standard and Apollonius Triplet track finder achieves slightly better results for four of the six final state particles. In particular, the reconstruction efficiency of the π^\pm benefits from the combination with the Apollonius Triplet track finder. The Standard track finder achieves an improvement of 13.6 %-points for the π^+ daughter of the Ξ^+ . Since the Hough track finder is able to find some of the secondary tracks the benefit from the Apollonius Triplet track finder is lower with a maximum increase of 8.9 %-points for the $\pi^+(\bar{\Lambda})$. It is visible that the combination of the Hough track finder with the Apollonius Triplet track finder loses more tracks after the Kalman filter, which is expected, since the poorly found secondary tracks found by the Hough track finder still remain after applying the Apollonius Triplet track finder.

Table 5.4: Reconstruction efficiencies (in %) of the final state particles found by the barrel trackers before and after the Kalman filter is applied.

	Standard		Hough		Standard + Apollonius Triplet		Hough + Apollonius Triplet	
	Before Kalman	After Kalman	Before Kalman	After Kalman	Before Kalman	After Kalman	Before Kalman	After Kalman
K^-	88.2	88.2	82.4	81.2	88.8	88.2	86.5	84.6
P	61.6	61.6	62.3	57.9	71.5	68.3	70.4	64.7
π^-	43.2	43.2	62.8	51.5	65.7	56.8	73.5	60.0
$\pi^+(\Xi^+)$	52.5	52.5	69.2	62.0	73.6	66.1	78.3	69.3
\bar{P}	50.9	50.9	51.9	43.9	56.5	53.9	58.6	49.5
π^+	32.3	32.3	51.6	36.2	56.0	45.2	63.5	45.1

The efficiencies shown in Tab. 5.4 are the efficiencies of the barrel track finders $\epsilon_{\text{Reco}}^{\text{Barrel}}$. Additionally, the ideal forward tracker is used to identify forward boosted tracks. In contrast to the ideal track finding, the realistic track finders also produce clone tracks, which means that tracks can be found several times. In the efficiencies these clone tracks are not double-counted. Consequently, the total efficiency (barrel + forward tracker) is not equal to the sum of each efficiency.

$$\epsilon_{\text{Reco}}^{\text{Barrel}} = \frac{N_{\text{Barrel}}}{N_{\text{fiducial}}} \quad \epsilon_{\text{Reco}}^{\text{Forward}} = \frac{N_{\text{Forward}}}{N_{\text{fiducial}}} \quad \epsilon_{\text{Reco}}^{\text{Total}} \neq \epsilon_{\text{Reco}}^{\text{Barrel}} + \epsilon_{\text{Reco}}^{\text{Forward}} \quad (5.2)$$

Here, the number of tracks considered to be within the fiducial volume N_{fiducial} is defined as the number of tracks that each have a minimum number of hits in either the forward or barrel part. The fraction for the particles found by the ideal forward tracker was already shown in Tab. 5.2. When combining the barrel and forward tracker, forward boosted tracks can be found by the barrel trackers and the forward tracker. Therefore, the number of clones is expected to be larger than the clone rate shown in the previous chapter. The fraction of produced clones is shown in Tab. 5.5.

Table 5.5: Fraction (in %) of clone tracks for all final state particles for the different tracking algorithms combined with the ideal forward tracker. Here the clone rate follows the definition of the efficiency and is calculated as a fraction of the number of tracks within the fiducial volume of the full detector, including barrel and forward part.

	Standard	Hough	Standard + Apollonius	Hough + Apollonius
K^-	13.0	20.3	15.6	20.8
P	17.6	20.9	17.7	22.5
π^-	17.7	16.3	23.3	21.9
$\pi^+(\Xi^+)$	18.1	18.1	16.7	22.4
\bar{P}	17.0	16.4	16.3	17.6
π^+	14.5	16.1	24.2	22.7

In Fig. 5.5 the pull distributions for the transverse and longitudinal momentum for the different track finders are shown for the π^- . The distributions of the other particles can be found in appendix B. The pull distributions describe the ratio of the momentum deviation to the corresponding error $((p_T^{\text{reco}} - p_T^{\text{MC}})/\sigma_{p_T^{\text{reco}}})$. The error is determined by the Kalman filter and is the square root of the diagonal elements of the corresponding covariance matrix [132]. No differences in the distributions are visible for the different track finders. The **FWHM** and the **RMS** for all final state particles and all track finders are shown in Tab. 5.6 and 5.7. The **FWHM** is always below 1.0, whereas the **RMS** is larger with values of about 1.5. The reason for this difference is that the distributions are not Gaussian distributed, but have a narrower peak and wider base, resulting in a smaller **FWHM**. The reason for this is not yet fully understood, but indicates an overestimation of the errors calculated by the Kalman filter.

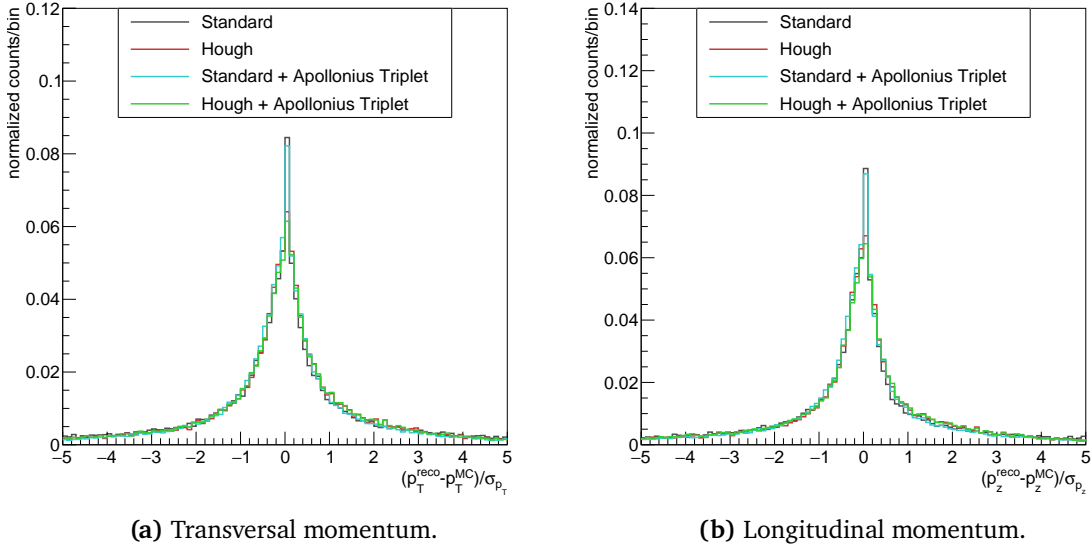


Figure 5.5: Pull distributions for π^- originating from Λ .

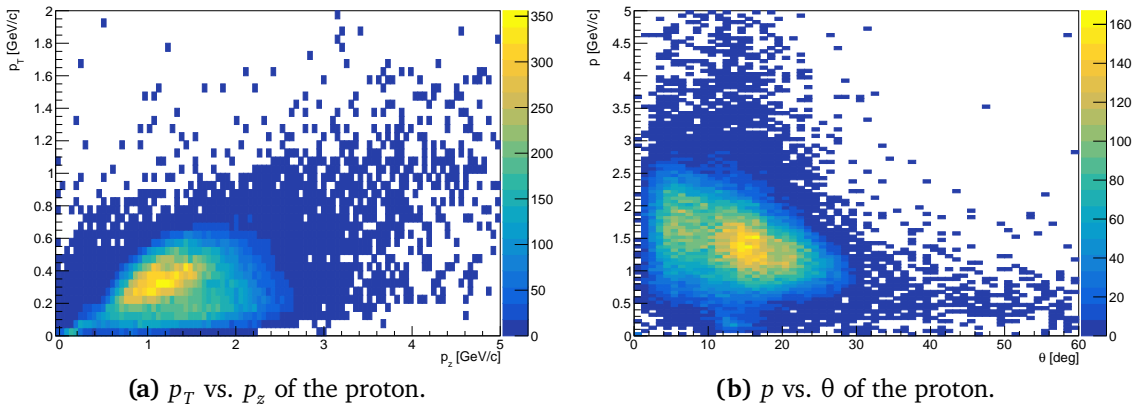
Table 5.6: FWHM and RMS for the pull distribution of the transversal momentum of all final state particles for the different tracking algorithms.

	Standard		Hough		Standard + Apollonius Triplet		Hough + Apollonius Triplet	
	FWHM	RMS	FWHM	RMS	FWHM	RMS	FWHM	RMS
K^-	0.6	1.7	1.2	1.5	1.0	1.2	1.2	1.5
P	0.6	1.6	1.2	1.6	1.2	1.4	1.2	1.6
π^-	0.4	1.7	0.6	1.6	0.8	1.5	0.8	1.6
$\pi^+(\Xi^+)$	0.2	1.7	1.0	1.6	0.8	1.5	1.0	1.6
\bar{P}	0.4	1.6	1.0	1.6	1.0	1.5	1.0	1.6
π^+	0.2	1.7	0.4	1.6	0.6	1.5	0.8	1.6

Table 5.7: FWHM and RMS for the pull distribution of the longitudinal momentum of all final state particles for the different tracking algorithms.

	Standard		Hough		Standard + Apollonius Triplet		Hough + Apollonius Triplet	
	FWHM	RMS	FWHM	RMS	FWHM	RMS	FWHM	RMS
K^-	0.4	1.6	1.0	1.4	0.8	1.1	1.0	1.4
P	0.4	1.4	0.9	1.4	1.0	1.2	1.0	1.4
π^-	0.3	1.7	0.5	1.7	0.6	1.5	0.8	1.7
$\pi^+(\Xi^+)$	0.2	1.7	0.6	1.6	0.6	1.5	1.0	1.6
\bar{P}	0.5	1.4	0.7	1.3	1.0	1.2	1.0	1.3
π^+	0.3	1.7	0.2	1.7	0.7	1.6	0.8	1.7

In Fig. 5.6 and 5.7, the distributions of p_T vs. p_z and p vs. θ are shown for the proton and π^- for the combination of Hough and Apollonius Triplet track finder. The proton typically has a larger total momentum and a lower polar angle. The observations correspond to the expected distributions shown in Fig. 5.2 and Fig. 5.3. The distributions for the other final state particles and the other tracking algorithms can be found in appendix B.

**Figure 5.6:** Distributions of the transverse momentum p_T vs. the longitudinal momentum p_z and total momentum p vs. polar angle θ for the proton for Hough + Apollonius Triplet tracker.

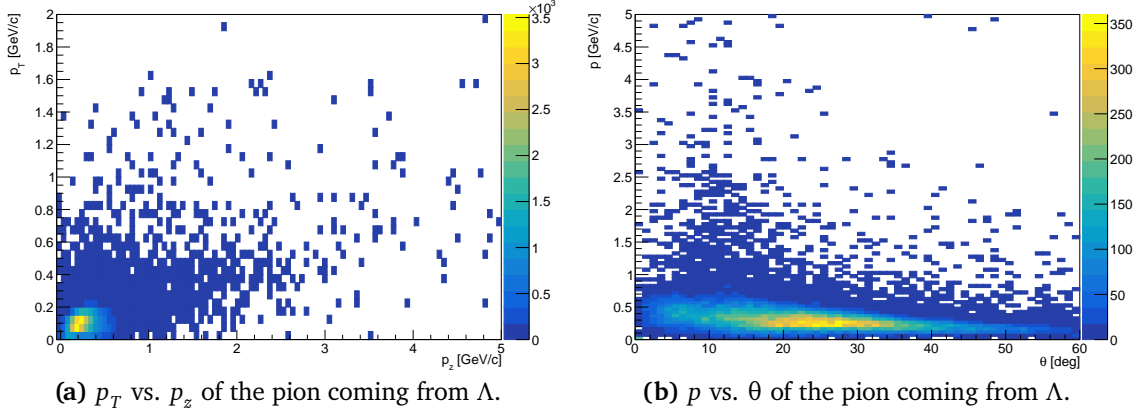


Figure 5.7: Distributions of the transverse momentum p_T vs. the longitudinal momentum p_z and total momentum p vs. polar angle θ for the π^- originating from Λ for Hough + Apollonius Triplet tracker.

5.4 Λ Reconstruction

In a next step, the final state particles are combined to form their mother particles. Only those events are considered, in which all final state particles are found. This condition strongly reduces the number of events. Only about 49.0% of the events have all six particles within the fiducial volume. Since the different track finders have a finding rate of less than 100%, the number of events containing all final state particles is even lower. Tab. 5.8 shows the percentage of the events, in which all final state particles are found. Here MC-truth matching² is included.

Table 5.8: Comparison of the rate to find all final state particles for events in which all final state particles are within the fiducial volume.

	Standard	Hough	Standard + Apollonius Triplet	Hough + Apollonius Triplet
$\epsilon_{\text{reco Events}} [\%]$	16.9	24.6	44.5	38.3

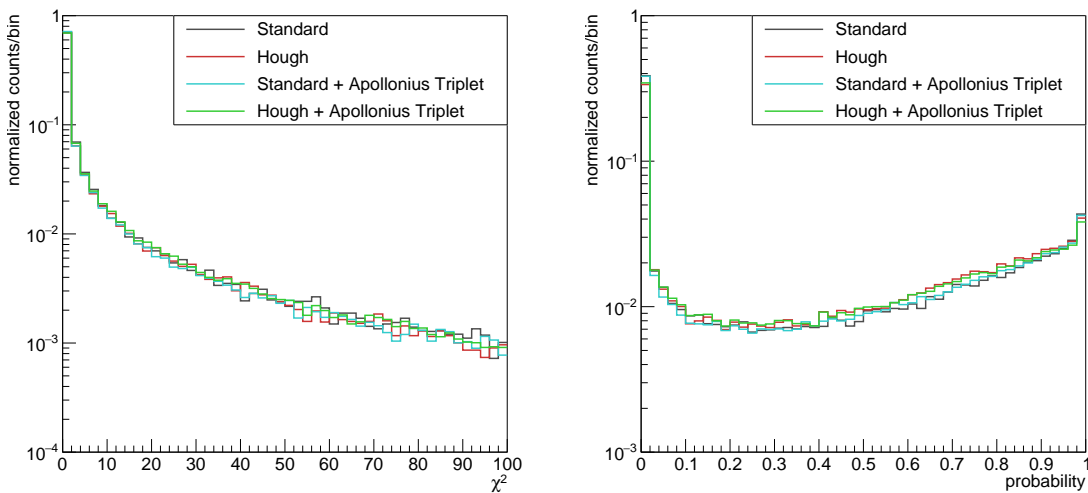
Since this work shows a comparison of different track finding algorithms, the percentage corresponds to the number of events in which all final state particles are found divided by the number of events in which all final state particles are within the fiducial volume:

$$\epsilon_{\text{reco Events}} = \frac{N_{\text{all final state particles are found}}}{N_{\text{all final state particles are within fiducial volume}}} \quad (5.3)$$

As seen in the table, the Hough track finder has a significantly higher efficiency than the Standard tracker. However, the benefit from the combination with the secondary track finder is lower. Nevertheless, a large improvement from just the primary to the combination of primary and secondary track finders is clearly visible. As shown in the previous section, the combination of Standard and Apollonius Triplet tracker leads to the best result with 44.5% of events in which all final state particles were found.

²MC-truth match means that the found track is associated to a specific MC track. Tracks that can not be associated to a MC track are discarded.

The 4-momenta of the proton and the π^- are combined in order to generate a Λ candidate. The $\bar{\Lambda}$ reconstruction is performed analogously, and the corresponding plots can be found in appendix B. In the analysis all particle tracks are used for the reconstruction. This means that also recoil particles or clone tracks are used. Consequently, the finally reconstructed particles can include wrongly reconstructed particles or particles reconstructed multiple times. The aim of the analysis here is to remove as many wrong combinations as possible, while maximizing the number of reconstructed particles. Thus data selections and fits are applied to identify wrong combinations and improve the resolution of the correct combinations. To quantify the quality of the reconstruction a purity specification and a clone rate is given. The purity is defined as the number of MC-truth matched particles divided by all found particles. A mass window of $\pm 0.15 \text{ GeV}/c^2$ placed symmetrically around the Λ mass $m_\Lambda = 1.116 \text{ GeV}/c^2$ reduce the number of wrong particle combinations. After that, a vertex fit is performed for each combination within the mass window. Here, the *PndKinVtxFitter* of the Rho package was used. The vertex fit forces both particles to originate from a common vertex and therefore modifies the track parameters of each particle to fulfill this condition. The quality of the fit is quantified by a χ^2 and equivalently a probability distribution. The shape of the χ^2 distribution depend on the number of degrees of freedom of the fit. Since the vertex fit has one degree of freedom, the χ^2 distribution is expected to have a peak at $\chi^2 = 0$ for a well-fit particle reconstruction. The higher the χ^2 value for a specific event the worse is the fit. For a poor fit the probability is close to zero. For Gaussian distributed errors the probability distribution is expected to be flat, while wrong combinations should aggregate close to zero. In Fig. 5.8 the χ^2 and probability distributions for the different track finders are shown. As expected, the χ^2 distribution has a peak at zero and then decreases. The probability distribution has a sharp peak at zero for very unlikely fits. However, the behavior for higher probabilities increases. This increase originates from the non-Gaussian pull distribution shown in Fig. 5.5 indicating a overestimation of the errors. The distributions are normalized by the total number of entries. Consequently, the

(a) χ^2 distribution for the Λ candidates.(b) Probability distribution for the Λ candidates.**Figure 5.8:** χ^2 and probability distribution for the vertex fit for various realistic track finders.

different efficiencies of the track finders are not visible here, but it is shown that the normalized distributions look similar for all track finders. The probability distribution is used as a selection criterion by requiring a fit probability better than 0.01. In this way, all reconstructed events with very unlikely fit results are removed. For illustration purposes a binning of 0.02 is chosen here for the probability distribution. A finer binning of the probability distribution can be found in appendix B.

After the vertex fit, a kinematic fit with a mass constraint is performed, that forces the 4-momenta of the combined particles to match the invariant Λ mass. The mass-constraint fit is only used as a quality cut, meaning that a cut at probabilities smaller or equal 0.01 is used to further remove unlikely Λ reconstructions. The χ^2 distributions and the probability distributions for all track finders are shown in Fig. 5.9. For the probability distribution a finder binning is shown in appendix B. The mass constraint fit is used to remove wrong particle combinations and improve the purity of the reconstructed Λ . However, for the further analysis, the corrected 4-momenta after the vertex fit (and not after the mass constraint) are used, since using the 4-momenta after the mass constraint fit did not improve the results of the subsequent analysis.

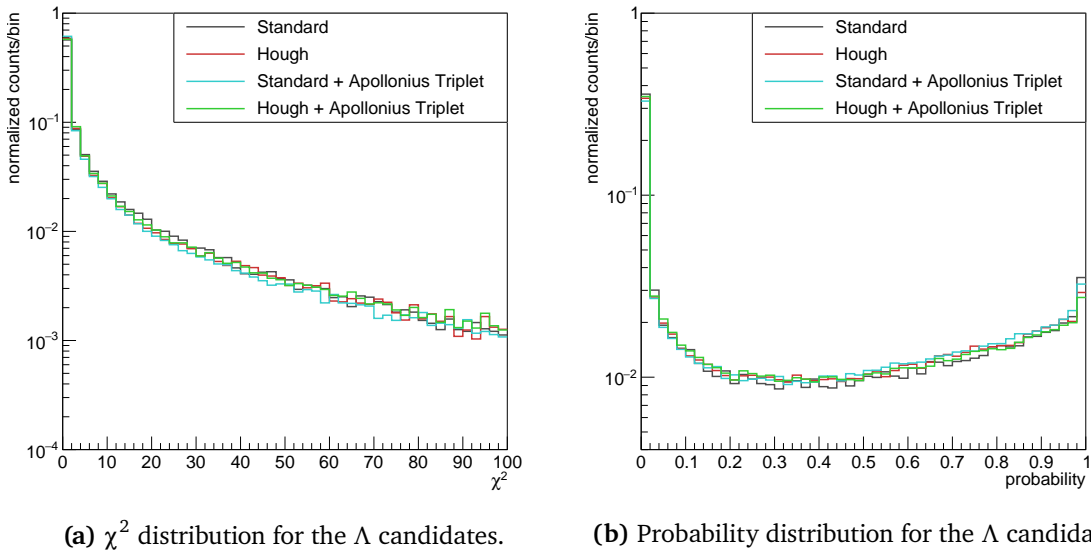
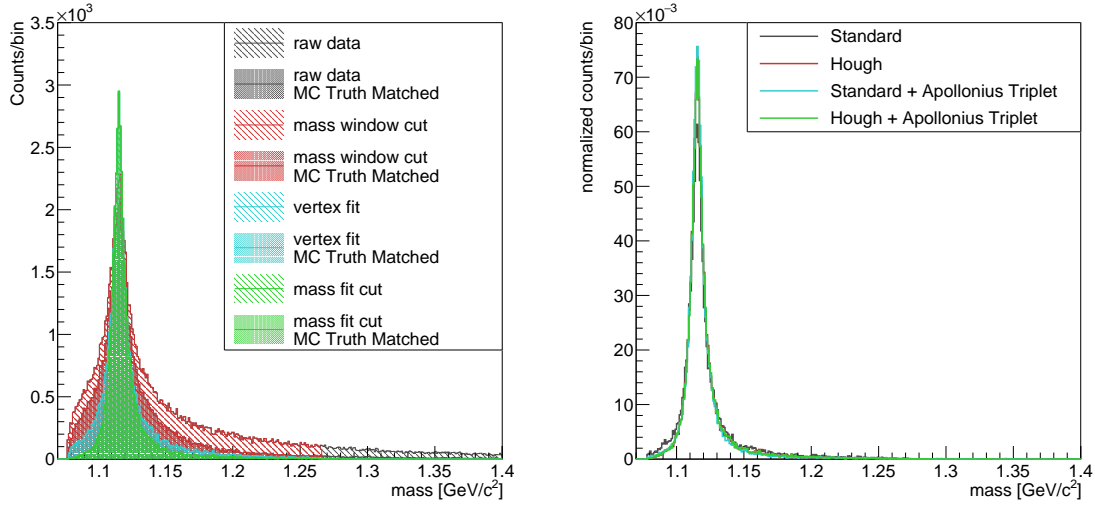


Figure 5.9: χ^2 and probability distribution for the mass constraint fit for all realistic track finders.

Fig. 5.10a shows results for the Λ reconstruction using the combination of Hough and Apollonius Triplet track finder. Fig. 5.10a shows the Λ mass distributions before and after applying the different fits and cuts. The diagonal filled histograms show the distributions without MC-truth match, whereas the vertically filled histograms contain only MC-truth matched particles. The Λ raw data contain 100,688 Λ candidates. 62.1 % of these are MC-truth matched (62,560). The mass window cut removes 15,216 Λ candidates. 80.4 % of the entries removed are not MC-truth matched. The vertex fit further reduces the number of found Λ to 57,197, where 59.6 % of the removed particles are not MC-truth matched. The Λ mass distribution after the vertex fit shown in cyan in Fig. 5.10a has a purity of 83.1 % and 29.7 % clones. To further improve the purity a kinematic fit with mass constraint is applied. Here, only candidates with a fit probability larger than 0.01 survive. In total 28,483 candidates are removed by the mass



(a) Comparison of the invariant mass distribution of Λ -candidates for the different cuts and fits to the combination of Hough and Apollonius Triplet track finder.

(b) Comparison of the normalized invariant mass distribution of Λ -candidates for the different tracking algorithms.

Figure 5.10: Comparison of the mass distribution of Λ -candidates. Left: ideal case after different fits and cuts. Right: realistic tracking cases after all fits and cuts.

constraint fit, which contain 22.9% not MC-truth matched candidates and 50.2% MC-truth matched particles that were found more than once.

In total 28,714 Λ candidates remain after all fits and cuts, with a purity of 91.3%. The clone tracks are removed by taking only the Λ particle with the best χ^2 , which leads to a 100% suppression of clones. Finally, after the MC-truth match 26,216 Λ candidates remain, which are 19.5% of the Λ particles within the fiducial volume. Thus, the reconstruction efficiency of the Λ particle is a combination of the track finding efficiencies of the final state particles ϵ_{reco}^P and $\epsilon_{reco}^{\pi^-}$ and an additional factor caused by the applied fits and cuts.

The efficiencies to reconstruct Λ and $\bar{\Lambda}$ as well as the purity for the different track finders are shown in Tab. 5.9. The efficiency is already MC-truth matched and the clones are removed. Here, ϵ_{reco} stands for the number of reconstructed Λ particles to the number within the fiducial volume. Additionally, the total reconstruction efficiency including the detector acceptance is shown as ϵ_{MC} , which is defined as the number of correctly reconstructed particles divided by the number of simulated particles.

A significant improvement in the efficiency is visible when combining the primary track finders with the Apollonius Triplet track finder. The combination of Standard and Apollonius Triplet track finder shows the largest reconstruction efficiencies with 24.0% and 19.9% of the Λ and $\bar{\Lambda}$ particles, respectively, within the fiducial volume. The high purity of the $\bar{\Lambda}$ is striking. The reason for this is that the decay of Ξ^+ produces two π^+ , one coming from the Ξ^+ and a second from the $\bar{\Lambda}$. Since both π^+ have similar momenta it is difficult to distinguish the pions from each other. Consequently, both combinations ($\bar{p} + \pi^+(\Xi^+)$ and $\bar{p} + \pi^+(\bar{\Lambda})$) appear as possible combinations in the $\bar{\Lambda}$ reconstruction, thereby causing the low purity.

Table 5.9: MC-truth matched reconstruction efficiencies for Λ and $\bar{\Lambda}$ and the purity for the different track finding algorithms. The efficiencies and the purity are given in %.

	ϵ_{reco}		ϵ_{MC}		purity	
	Λ	$\bar{\Lambda}$	Λ	$\bar{\Lambda}$	Λ	$\bar{\Lambda}$
Standard	10.1	8.6	3.6	2.7	84.2	56.4
Hough	13.3	11.3	4.8	3.5	91.5	66.6
Standard + Apollonius Triplet	24.0	19.9	8.6	6.1	90.0	66.5
Hough + Apollonius Triplet	19.5	16.6	7.1	5.2	91.3	66.7

The applied fits and cuts lead to an additional improvement of the width of the mass distribution by a factor of more than two. The **FWHM** of the raw data is $18 \text{ MeV}/c^2$ and after the vertex fit and the mass constraint it improves to $7 \text{ MeV}/c^2$. Furthermore, the mass distributions for the different track finders are shown in Fig. 5.10b. Since the mass distribution does not follow a Gaussian curve, the peak position is taken as the reconstructed Λ and $\bar{\Lambda}$ mass with an uncertainty of the $1 \text{ MeV}/c^2$ bin width. All track finders reconstructed a Λ and $\bar{\Lambda}$ mass of $1.116 \text{ GeV}/c^2$. The **FWHM** and **RMS** are given in Tab. 5.10. It can be seen that the mass distributions of the different track finders are comparable with only small deviations in the width of the distributions. The $\bar{\Lambda}$ has a slightly lower width than the Λ . A possible reason could be that the $\bar{\Lambda}$ is more forward boosted, which means that its daughter particles are found more often by the ideal forward tracker. Since the ideal forward track finder uses **MC** information the momentum resolution is better than that of the realistic barrel trackers. Further research is needed here by replacing the ideal forward tracker with a realistic forward tracker.

Table 5.10: **FWHM** and **RMS** for the Λ and $\bar{\Lambda}$ mass for the different tracking algorithms.

	Λ		$\bar{\Lambda}$	
	FWHM [MeV/c ²]	RMS [MeV/c ²]	FWHM [MeV/c ²]	RMS [MeV/c ²]
Standard	6	24	4	30
Hough	7	19	6	22
Standard + Apollonius Triplet	7	19	6	25
Hough + Apollonius Triplet	7	20	6	22

Fig. 5.11, 5.12, 5.13 and 5.14 show the distributions of p_T vs. p_z and p vs. θ for Λ and $\bar{\Lambda}$ when using the Hough and Apollonius Triplet track finder. Fig. 5.11 and 5.13 show the **MC** generated distributions as a reference. The $\bar{\Lambda}$ is more strongly forward boosted with a mean polar angle of about 10° compared to the Λ originating from the heavier $\Xi(1820)$ resonance with a mean polar angle of about 13° . This corresponds to the slightly lower reconstruction efficiencies of the $\bar{\Lambda}$ for all tracking algorithms, as shown in Tab. 5.9.

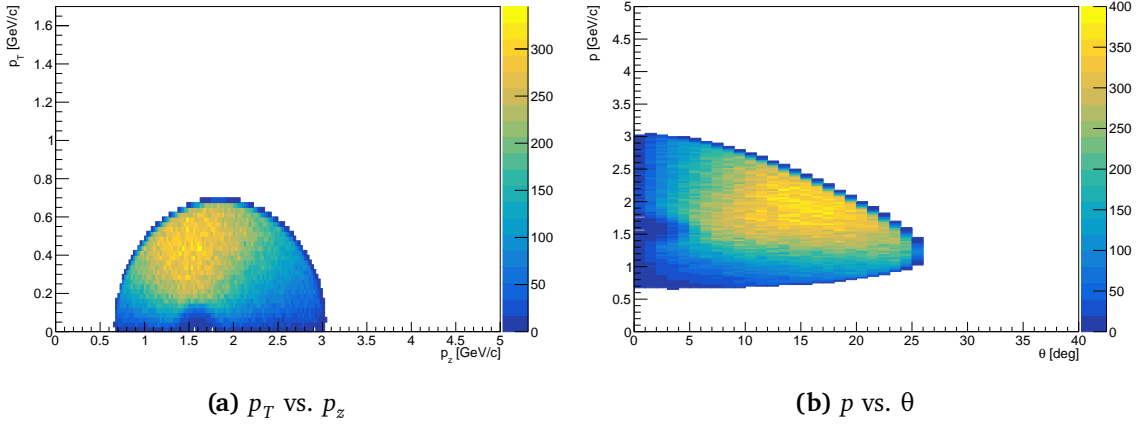


Figure 5.11: MC generated distributions of p_T vs. p_z and p vs. θ for Λ .

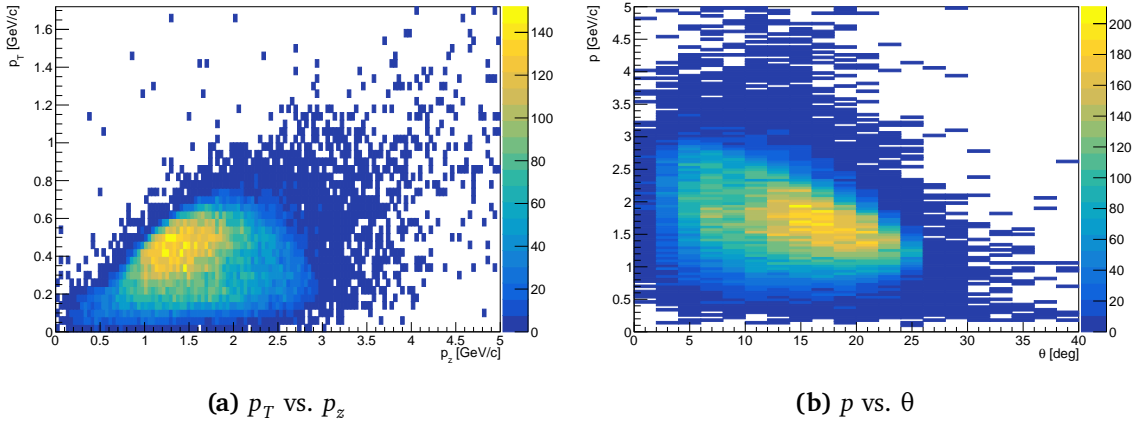


Figure 5.12: Distributions of p_T vs. p_z and p vs. θ for Λ based on the output from the Hough + Apollonius Triplet tracker.

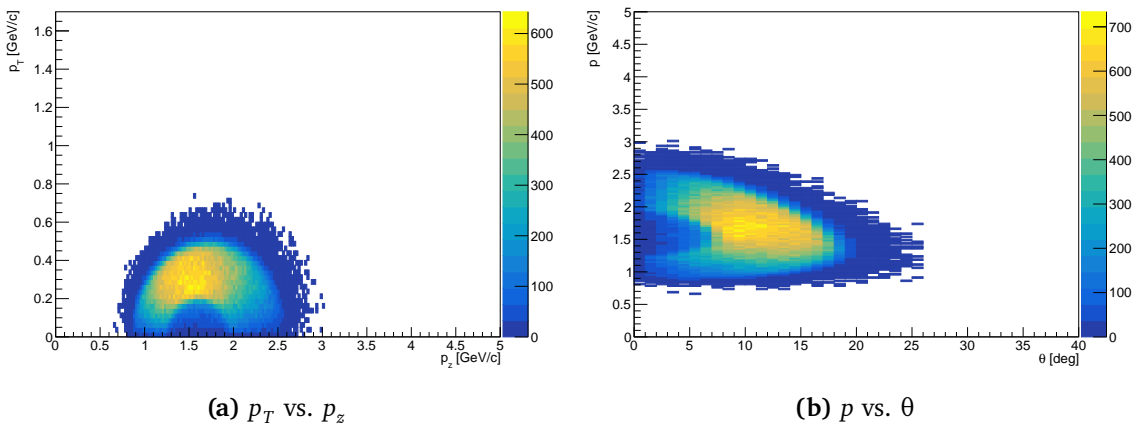


Figure 5.13: MC generated distributions of p_T vs. p_z and p vs. θ for $\bar{\Lambda}$.

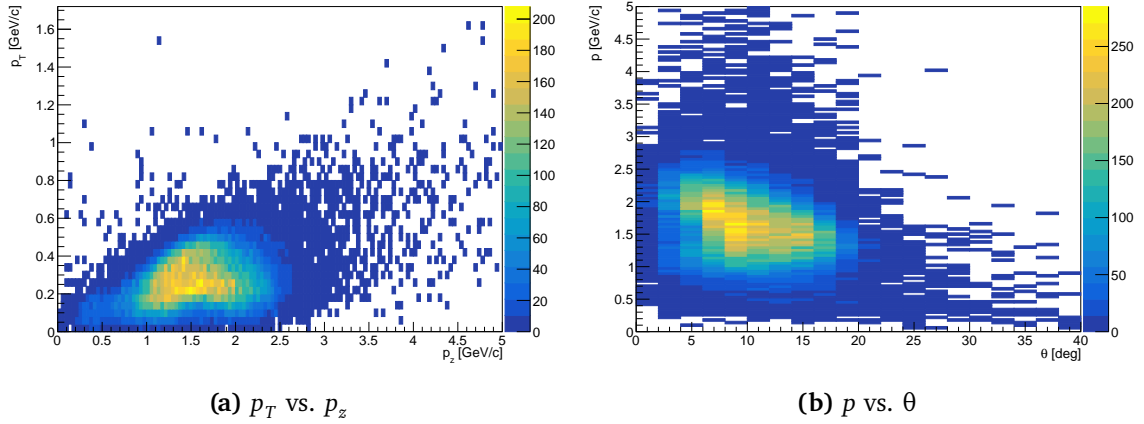


Figure 5.14: Distributions of p_T vs. p_z and p vs. θ for $\bar{\Lambda}$ for the Hough + Apollonius Triplet tracker.

5.5 Ξ Reconstruction

The Ξ reconstruction follows the same steps as the Λ reconstruction. $\Xi(1820)^-$ is reconstructed as a combination of Λ with K^- and wrong combinations are removed by performing a symmetric mass window of $\pm 0.3 \text{ GeV}/c^2$ around $m_{\Xi(1820)^-} = 1.823 \text{ GeV}/c^2$. After combining the Λ and K^- , a vertex fit with the *PndKinVertexFitter* and a mass constraint fit is performed. Again, the χ^2 and probability distributions of the fits are used to select the Ξ candidates with a probability larger than 1%. The distributions of the fit results for the different track finders are shown in Fig. 5.15 and 5.16. A finer binning of the probability distributions can be found in appendix B.

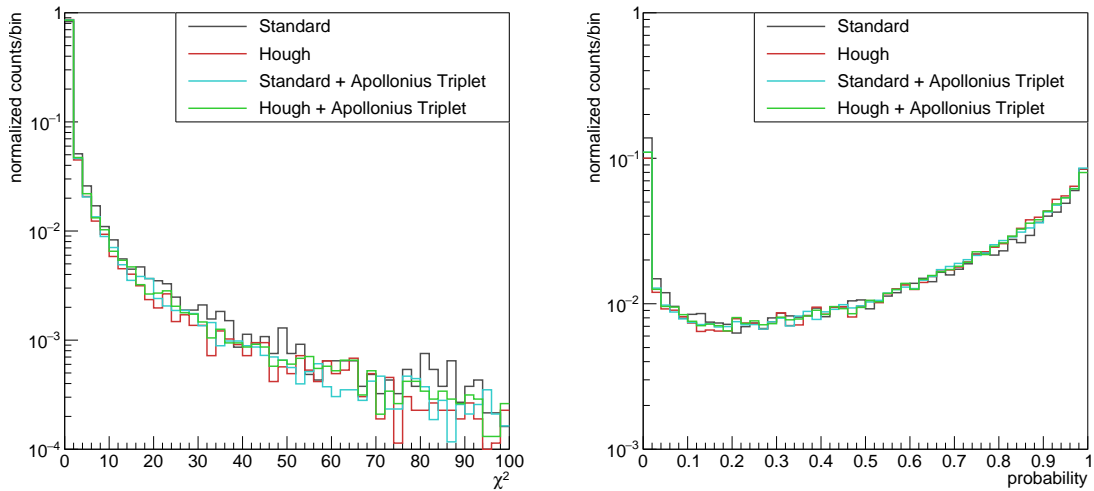
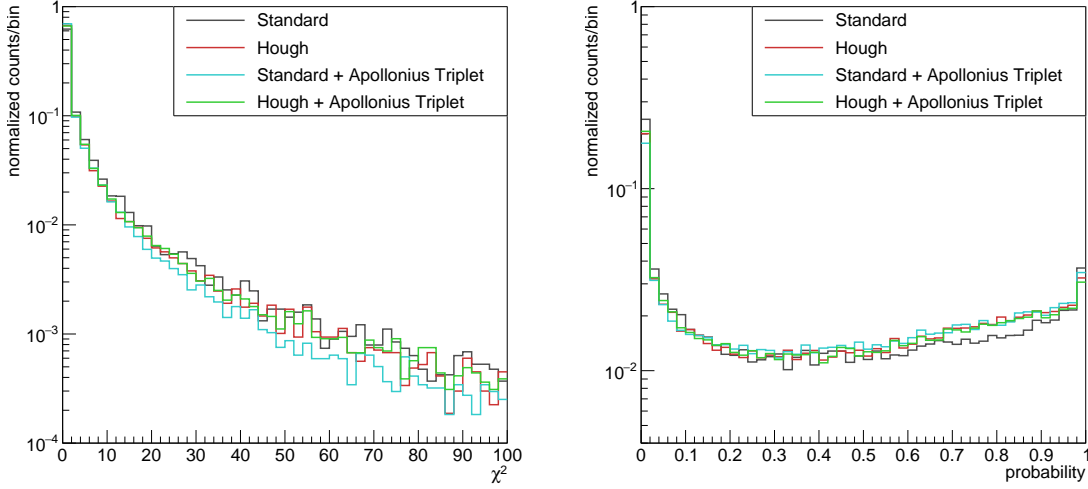


Figure 5.15: χ^2 and probability distribution for the vertex fit for all track finders.



(a) χ^2 distribution of the mass constraint fit for the $\Xi(1820)$ candidates.

(b) Probability distribution of the mass constraint fit for the $\Xi(1820)$ candidates.

Figure 5.16: χ^2 and probability distribution for the mass constraint fit for all track finders.

The fit parameters behave as expected with a decreasing χ^2 distribution toward higher χ^2 and a probability distribution with a sharp peak at zero describing combinations with very unlikely fit parameters. As seen in the Λ reconstruction, an increase in the probability distribution of the vertex fit is observed towards high values of probability, originating from the non-Gaussian pull distributions and the overestimation of the errors. The different overall reconstruction efficiencies of the track finders are not visible here since the distributions are normalized to make them comparable. The χ^2 and probability distributions have similar shapes for all track finders.

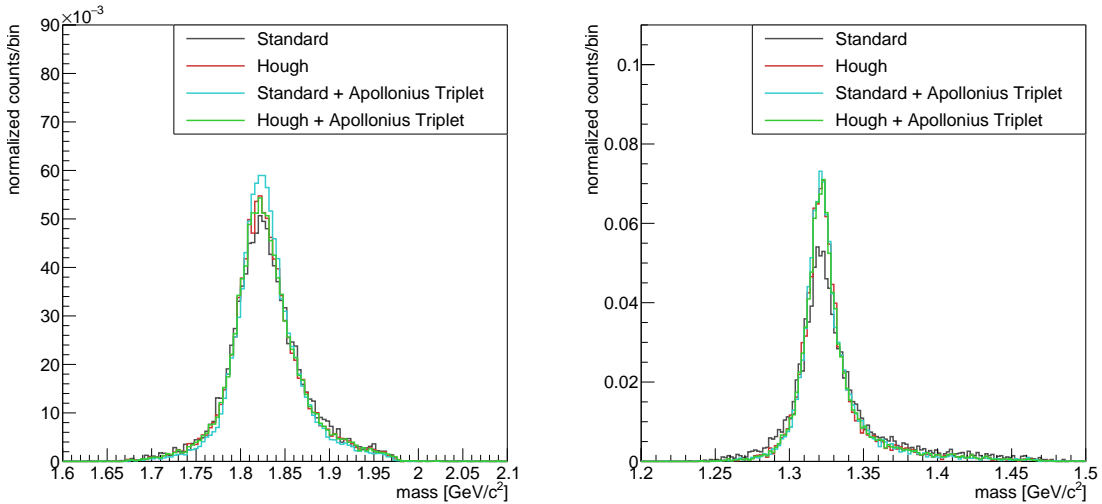
The reconstruction efficiencies and purities achieved after selecting the candidates based on the vertex and the mass constraint fit are shown in Tab. 5.11. As shown before, the reconstruction efficiency of the Hough track finder is significantly larger than the efficiency of the Standard tracker. Both primary track finders benefit from the combination with the Apollonius Triplet track finder as an additional secondary track finder. However, the benefit for the Standard tracker is higher than for the Hough track finder. For the Standard tracker an increase by a factor 2.6 is observed when combining the Standard tracker with the Apollonius Triplet tracker. For the Hough track finder an increase by a factor 1.4 is achieved. The reason for the smaller increase for the Hough track finder is that the Hough Track finder is currently optimized for highest efficiency for primary and secondary tracks. However, in combination with the Apollonius Triplet track finder, an optimization to find primary tracks and ignore secondary tracks leaving these tracks to the Apollonius Triplet track finder is promising. Currently, the best reconstruction efficiency is obtained with the combination of Standard and Apollonius Triplet track finder with an efficiency of 26.1 % for $\Xi(1820)$ and 14.4 % for Ξ^+ . The reconstruction efficiencies are defined as mentioned in the Λ reconstruction. As expected, the efficiency for the Ξ^+ reconstruction is lower than for the $\Xi(1820)$. As a resonance, the $\Xi(1820)$ decays nearly instantaneously into K^- and Λ , resulting in a K^- that originates from the interaction point. The

Ξ^+ , on the other hand, has a long lifetime, which means that both decay particles (π^+ and $\bar{\Lambda}$) originate from a displaced secondary vertex, which makes the reconstruction more challenging. Thus, the lower finding rate of secondary particles results in the lower reconstruction efficiency of the Ξ^+ . The purity behaves as noted previously for the Λ reconstruction. Here a purity of about 90% can be achieved for the $\Xi(1820)^-$ and only about 50 - 60% for the Ξ^+ as a consequence of the two π^+ in the final state.

Table 5.11: MC-truth matched reconstruction efficiency (in %) for the $\Xi(1820)^-$ and Ξ^+ and the purity and clone rate for the different track finding algorithms.

	ϵ_{reco}		ϵ_{MC}		purity	
	$\Xi(1820)^-$	Ξ^+	$\Xi(1820)^-$	Ξ^+	$\Xi(1820)^-$	Ξ^+
Standard	9.9	5.3	2.9	1.3	87.4	43.5
Hough	14.6	8.8	4.2	2.8	93.8	58.1
Standard + Apollonius Triplet	26.1	14.4	7.6	4.5	92.4	54.8
Hough + Apollonius Triplet	20.9	12.7	6.2	3.2	93.7	57.2

Fig. 5.17 shows the mass distributions of the reconstructed Ξ^+ and Ξ^- candidates for the different track finders. Again, the peak position is taken as reconstructed mass with an uncertainty of the $4 \text{ MeV}/c^2$ bin width. A mass of $1.822 \text{ GeV}/c^2$ for the $\Xi(1820)^-$ and $1.322 \text{ GeV}/c^2$ for the Ξ^+ was determined with all track finders. The **FWHM** and the **RMS** are shown in Tab. 5.12. The mass distributions of the Standard track finder are noticeably worse with a larger **FWHM** and **RMS**, which is a consequence of the low finding efficiency of the Standard tracker for secondary tracks.



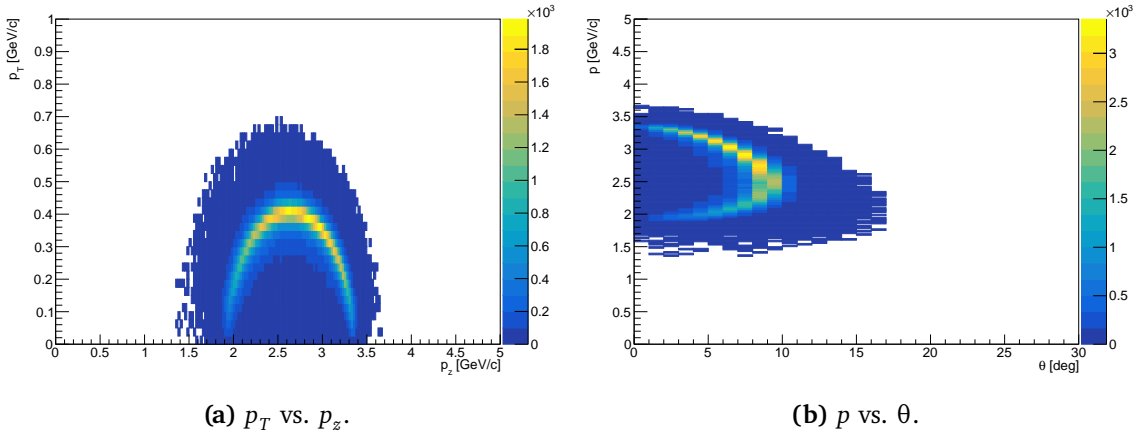
(a) Mass distribution for $\Xi(1820)^-$ for the different track finders. **(b)** Mass distribution for Ξ^+ for the different track finders.

Figure 5.17: Mass distribution for the reconstructed Ξ^+ and Ξ^- for the different track finders.

Table 5.12: FWHM and RMS for the $\Xi(1820)^-$ and Ξ^+ mass for the different tracking algorithms.

	$\Xi(1820)^-$		Ξ^+	
	FWHM [MeV/c ²]	RMS [MeV/c ²]	FWHM [MeV/c ²]	RMS [MeV/c ²]
Standard	67	43	24	33
Hough	55	42	19	26
Standard + Apollonius Triplet	50	38	16	25
Hough + Apollonius Triplet	55	42	18	26

The generated and reconstructed momentum distributions p_T vs. p_z and p vs. θ for $\Xi(1820)$ candidates are shown in Fig. 5.18 and 5.19, respectively. Here, Fig. 5.18 shows the MC generated distributions as reference distributions and Fig. 5.19 shows the reconstructed momentum distributions for the combination of Hough and Apollonius Triplet track finder. The MC-generated distributions show that an elliptic population of the histograms is expected, originating from the two-body decay. The longitudinal momentum ranges from 1.5 GeV/c to 3.5 GeV/c and the transverse momentum up to 0.7 GeV/c with a peak at a transverse momentum of 0.388 GeV/c. For the p vs. θ distribution a similar behavior is expected. Here, the generated data predict a distribution of the polar angle up to 17° and a total momentum in the range from 1.8 GeV/c to 3.7 GeV/c. In the reconstructed case a similar behavior in both cases is observed. However, entries outside the kinematically allowed region are observed due to the finite momentum resolution.

**Figure 5.18:** MC generated distributions of p_T vs. p_z (a) and p vs. θ (b) for $\Xi(1820)^-$.

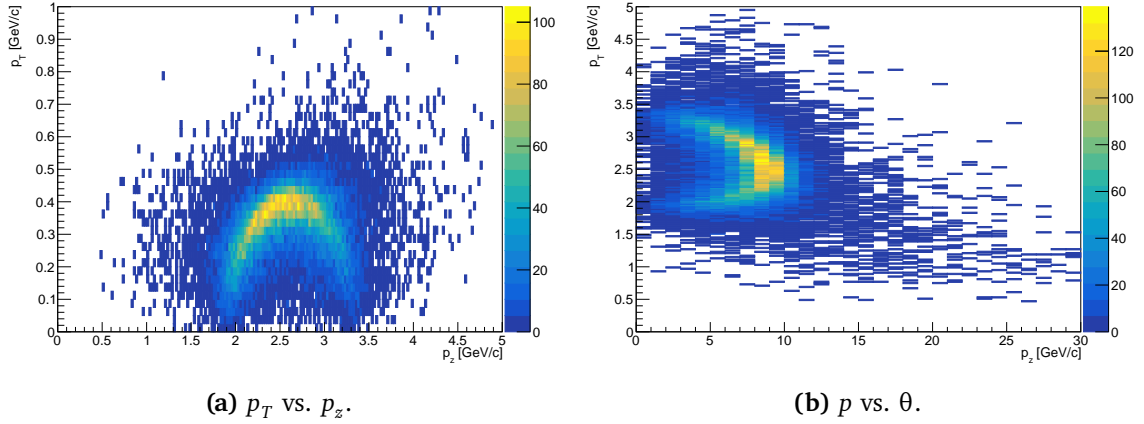


Figure 5.19: Distributions of p_T vs. p_z (a) and p vs. θ (b) for the $\Xi(1820)^-$ for the Hough + Apollonius Triplet tracker.

5.6 Full Event Reconstruction

In the final stage, the full reaction of the $\bar{p}p$ -system decaying into $\Xi^+\Xi(1820)^-$ is reconstructed. Here, the combination of Ξ^+ and $\Xi(1820)^-$ is expected to match the initial 4-momentum $(p_x, p_y, p_z, E) = (0, 0, 4.6, 5.63)$. Consequently, a kinematic fit with a 4-momentum constraint is performed. The corresponding fit results are shown in Fig. 5.20. Again, the probability distribution was used to remove events with unlikely fit results. As before, a minimum probability of 1% was required. The probability distribution with a finer binning is shown in appendix B.

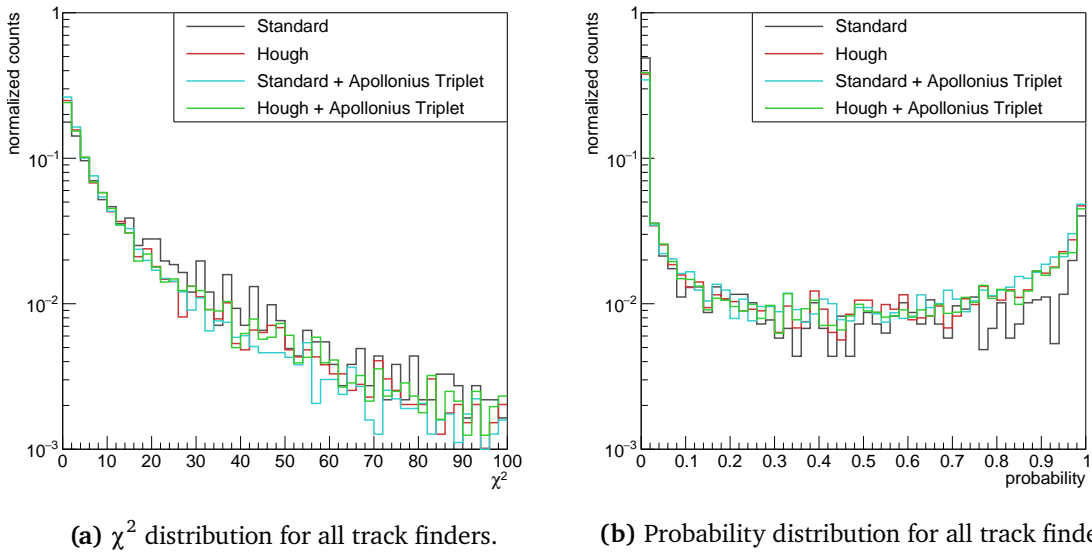


Figure 5.20: Fit results for the kinematic fit with 4-momentum constraint.

The final reconstruction efficiencies for the different track finders are shown in Tab. 5.13. Here, ϵ_{reco} is defined as the number of correctly reconstructed events divided by the number of events in the fiducial volume, ϵ_{MC} includes the detector acceptance and is defined as the number of correctly reconstructed events divided by the number of simulated events. For both efficiencies a MC-truth matching is performed and clones are avoided. Additionally, the purity is given in Tab. 5.13.

Table 5.13: MC-truth matched reconstruction efficiency for the full event reconstruction $\bar{p}p \rightarrow \Xi^+\Xi(1820)^-$ for the different track finding algorithms without clones as well as the purity of the reconstructed events. All values listed are in %.

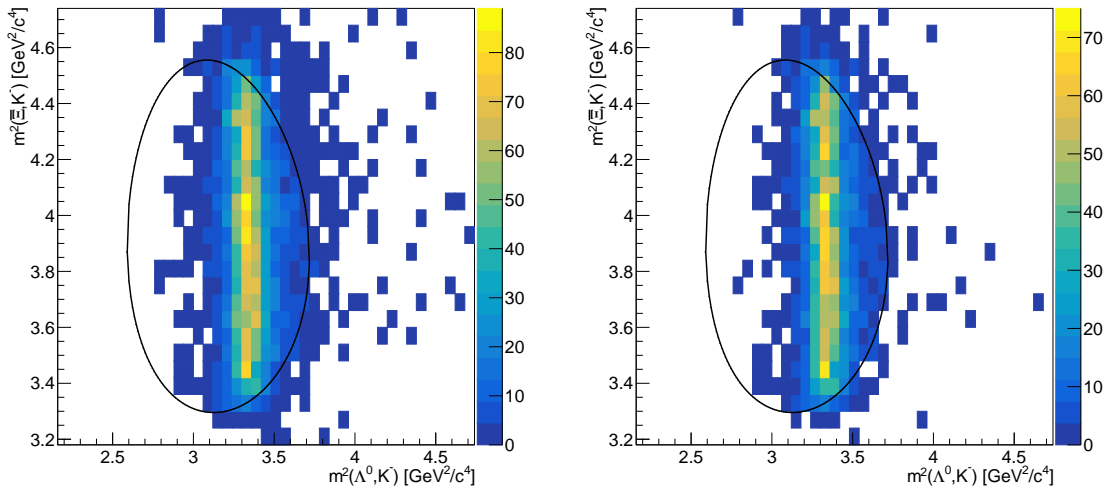
	ϵ_{reco}	ϵ_{MC}	purity
Standard	2.4	0.3	59.2
Hough	5.9	0.7	74.9
Standard + Apollonius Triplet	9.9	1.2	70.1
Hough + Apollonius Triplet	8.2	1.0	74.8

The reconstruction efficiency could be improved by a factor of 2.5 by developing a new primary track finder based on Hough transformations compared to the Standard tracker. Additionally, the reconstruction rate in both cases benefits from adding a newly developed secondary track finder. Here, the efficiency could be improved by a factor of four by combining the Standard tracker with the Apollonius Triplet tracker. Adding the secondary track finder to the newly developed Hough track finder also improves the final reconstruction rate. However, the improvement is less pronounced and does not reach the 9.9% for the combination of Standard and Apollonius Triplet track finder. The reason for the less pronounced improvement is that the Hough Track finder is currently optimized for highest finding rate for both primary and secondary tracks at the same time. Consequently, the Hough track finder is able to find parts of the secondary tracks with a poorly reconstructed track momentum. However, the track momentum often cannot be corrected by the Kalman filter, because hits with z-information are missing in these small parts of the secondary tracks (see Tab. 5.4). Additionally, the Apollonius Triplet track finder is added before the Kalman filter fits the tracks found by the Hough track finder and therefore the parts of the secondary tracks found by the Hough track finder are no longer available for the Apollonius Triplet track finder. A possible improvement for the combination of Hough and Apollonius Triplet track finder is to remove the tracks with no hits containing z-information from the Hough track finder, since these tracks cannot be fit by the Kalman filter. This method would increase the probability for the Apollonius Triplet track finder to find the corresponding tracks.

The purity ranges from 59.2% to 74.9% depending on the track finder. The reason for the relatively low purity is that the Ξ^+ reconstruction has a low purity, since it is difficult to decide which of the π^+ originates from the Ξ^+ and which one from the $\bar{\Lambda}$. Consequently, both possibilities are included in the final reconstruction and lead to the low purity.

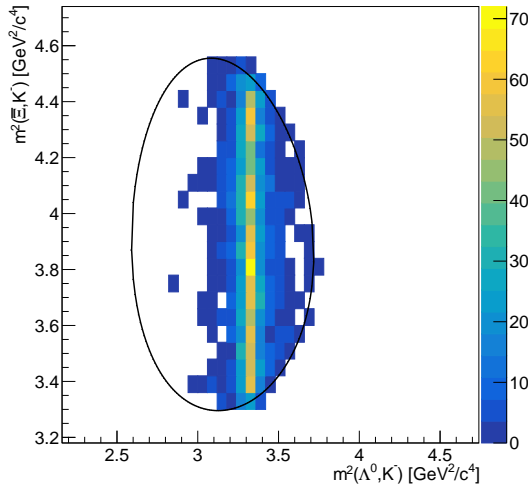
As a last step of the analysis, the Dalitz plot of the investigated reaction is shown in Fig. 5.21. The Dalitz plot is a two dimensional representation of a three body decay, in which the squared invariant mass of two unique pairs of particles is plotted. If the particles are correlated, *i.e.* two of the three particles come from an intermediate particle, the Dalitz plot shows the mass of the intermediate particle as a band in the plot. For the reaction investigated in this thesis, the squared mass of the ΛK^- system is plotted against the squared mass of the $\Xi^+ K^-$ system.

Fig. 5.21a shows the Dalitz plot for the combination of Hough and Apollonius Triplet Track finder without MC-truth matching. In Fig. 5.21b the Dalitz plot with MC-truth matching is shown. The kinematically allowed region is marked by the black curve. As expected, in both cases the Dalitz plot shows a resonance at a squared mass of $m_{\Lambda K^-}^2 = 3.31 \text{ GeV}^2/c^4$ corresponding to the squared mass of the $\Xi(1820)$ resonance. Without MC-truth matching the resonance is clearly visible. However, more entries outside the kinematically allowed region exist. Also the MC Truth matched Dalitz plot shows entries outside the kinematically allowed region. These entries occur due to the finite momentum resolution of the final state particles. This is shown in Fig. 5.21c, where the same reconstructed events are plotted as in Fig. 5.21b but with the MC generated 4-momenta of the particles.



(a) Dalitz plot of the final reaction without MC-truth matching.

(b) Dalitz plot of the final reaction with MC-truth matching.



(c) Dalitz plot of the final reaction with MC-truth matching and the MC 4-momenta of the found particles are used.

Figure 5.21: Dalitz plot for the Hough + Apollonius Triplet tracker. The black curve indicates the kinematically allowed region.

5.7 Rate Estimate

Finally, a rate estimate \dot{N} is determined for the reaction $\bar{p}p \rightarrow \Xi(1820)^-\Xi^+$ and an estimate for the number of days needed to perform a reasonable partial wave analysis of the reaction is shown. The investigation of the reaction will be part of the so-called "phase one" physics program of PANDA [63], where a luminosity of about $\mathcal{L} = 1 \cdot 10^{31} \text{ cm}^{-2}\text{s}^{-1}$ will be achieved. The rate of the reaction can be calculated as shown in eq. 5.4.

$$\dot{N} = \mathcal{L} \cdot \epsilon_{MC} \cdot \sigma(\bar{p}p \rightarrow \Xi(1820)^-\Xi^+) \cdot BR \quad (5.4)$$

The efficiencies ϵ_{MC} including the detector acceptance achieved with the different track finding algorithms are summarized in Tab. 5.13. The cross section of the reaction is currently still unknown. However, a cross section for the reaction $\bar{p}p \rightarrow \Xi^+\Xi^-$ is given in [133] of about $2 \mu\text{b}$ at beam momenta of 3 GeV/c. In this work, a cross section for the reaction $\bar{p}p \rightarrow \Xi(1820)^-\Xi^+$ is assumed to be $1 \mu\text{b}$. In the analysis shown in this work branching fractions of 100 % are assumed. However, for a rate estimate the results must be scaled with the expected branching fractions BR for the Ξ^+ , $\Xi(1820)^-$ and the Λ and $\bar{\Lambda}$ decay. Since the branching fraction of the $\Xi(1820)^-$ decay is unknown, a fraction of 100 % is assumed. The branching fraction of the Ξ^+ is $BR(\Xi^+ \rightarrow \bar{\Lambda}\pi^+) = (99.887 \pm 0.035)\%$ [33]. Λ and $\bar{\Lambda}$ decay into $p\pi^-$ and $\bar{p}\pi^+$ with a branching fraction of $BR(\Lambda \rightarrow p\pi^-) = (63.9 \pm 0.5)\%$ [33]. With these assumptions a rate of about 4200 events per day are expected using the combination of Standard and Apollonius Triplet track finders. The expected rates for all tracking algorithms are summarized in Tab. 5.14. Additionally, the number of days needed to collect 20,000 events is shown. This number is assumed to be the number of events needed for a reasonable partial wave analysis. It is shown, that five days of data taking are needed for 20,000 events.

Table 5.14: Expected number of $\Xi^+\Xi(1820)^-$ events per day of data taking for the different track finding algorithms and the days of data taking needed for a reasonable partial wave analysis.

	\dot{N} [events/day]	days of data taking to collect 20,000 events
Standard	1057	18.9
Hough	2467	8.1
Standard + Apollonius Triplet	4229	4.7
Hough + Apollonius Triplet	3524	5.7

Conclusions and Outlook

6

In this thesis, track finding algorithms for [PANDA](#)'s target spectrometer have been developed and were applied to the reaction: $\bar{p}p \rightarrow \Xi^+\Xi^- (1820)$ in order to evaluate the expected performance of [PANDA](#) to measure this channel. Two main topics have been investigated, which are:

1. primary track finding and a possible online application
2. secondary track finding

6.1 Tracking Algorithms

In [PANDA](#), track finding is divided into online and offline tracking. Online tracking is part of the software trigger and must operate with the same average rate with which the detector produces the tracks (in the order of a million tracks per second). It is more important for the online algorithm to optimize the performance in terms of speed and efficiency than for the momentum resolution. Offline tracking is performed after data taking and puts more emphasis on the precision of the track parameters. Furthermore, track finding algorithms distinguish between primary and secondary tracks. For primary tracks, the known primary [Interaction Point \(IP\)](#) can be used as a fix point on the track, which drastically simplifies the track finding task. In contrast, this information is not available for secondary tracks. This is especially true for *e.g.* hyperons, which have decay vertices that are typically centimeters away from the primary [IP](#). Therefore, secondary tracking is essential for hyperon reconstruction, despite being significantly more computationally intensive.

Currently, different approaches for tracking algorithms exist in [PANDA](#). However, only a primary track finder for offline tracking is currently used as the realistic track finder. For other applications (*e.g.* secondary track finding and online tracking) no default track finder currently exists. In this thesis, an online primary track finder based on Hough transformations was developed and its online capability using [GPUs](#) was tested. The second part of the thesis dealt with the development of a secondary track finder.

The main results achieved for the track finders are summarized in [Tab. 6.1](#). Here, the efficiency is divided into primary and secondary tracks and in addition the ghost and clone rates are shown. These are incorrectly found tracks and tracks found several times, respectively. In track

Table 6.1: Efficiencies for the different track finders investigated in this thesis.

	Standard	Hough	Apollonius Triplet	Standard + Apollonius Triplet	Hough + Apollonius Triplet
ϵ_{Prim} [%]	90	89	82	93	93
ϵ_{Sec} [%]	45	68	65	73	79
Ghosts [%]	17	8	12	24	16
Clones [%]	9	11	5	16	19

finding the ghost rate is more problematic than the clone rate since ghosts can lead to a wrong physics analysis, whereas clones can be merged in a subsequent step.

6.1.1 Hough Track Finder

The first algorithm developed in this thesis is a primary track finder based on Hough transformations, the so-called Hough track finder. In a Hough transformation, all possible track solutions that exist for a single hit or pair of hits are filled into a parameter space (Hough space) and the most frequent entry in the Hough space is used to estimate the actual track parameters. In this work the possible solutions are determined using the solution to the Apollonius Problem, which connects three circles with a fourth circle that is tangent to the other three circles. Consequently, the algorithm determines all combinations of two hits and the **IP** and fills the parameters of the resulting Apollonius circles into the Hough space.

The results in Tab. 6.1 show that the Hough track finder can be used as an alternative primary track finder to the Standard tracker. It achieves a similar efficiency for primary tracks and exceeds the efficiency of the Standard tracker for secondary tracks by more than 50%. Additionally, the number of wrongly found tracks is only half that of the Standard tracker.

Using the Hough Track finder for secondary tracks

The original idea was to extend the Hough Track finder to secondary particles, which is possible by using three hits instead of two hits and the **IP** for the Apollonius calculation. However, the Hough space must also be expanded to three dimensions instead of two. Therefore, the large memory consumption led to the decision not to extend the Hough track finder to secondary tracks, but to develop another secondary track finder called the Apollonius Triplet track finder.

6.1.2 Online capability on GPU

Motivated by the good results of the Hough track finder, the online capability was tested by porting the algorithm to a **GPU**. Here, the Apollonius calculation can be efficiently parallelized. However, to benefit from the **GPU**, the entire algorithm must be ported to the **GPU**, including filling the Hough space and the maximum finding in the Hough Space. Since these parts of the algorithm can not be parallelized very well, the parallelization must be performed on a per-event basis, meaning that the events are computed in parallel.

While calculating 5000 events in parallel, a kernel runtime of 176.1 μs /event was achieved, which corresponds to a speed-up factor of 73.8 compared to the **CPU** runtime of about 13 ms/event. However, copying data from the **CPU** to the **GPU** and back has a ten times larger impact on the

runtime and therefore the runtime with data transfer took about 2.5 ms/event which is already about 20 % of the runtime of the CPU.

The limiting factor was the memory usage on the GPU. The medium size GPU used in this thesis had a GPU memory of 6 GB. For each event a memory of about 1 MB had to be allocated on the GPU, which corresponds to roughly 5000 events. Thus, to further improve the runtime of the algorithm, an improvement in the data management needs to be found to make the algorithm useful for online analysis.

By parallelizing the algorithm on the GPUs, the runtime of the algorithm could be accelerated by a factor of five compared to the CPU. For an even larger improvement, further work is needed. Due to the continuous development of computer hardware, growing GPU capacities promise higher runtime improvements in the future.

6.1.3 Apollonius Triplet Track Finder

The Apollonius Triplet track finder is a secondary track finder based on finding a well-chosen set of three hits to calculate a hypothesis for a particle track. For this purpose, an innermost, mid and outermost layer of the STT is defined. By combining the hits of the three layers, Apollonius circles can be calculated, and hits close to these Apollonius circles are added to the corresponding track candidate. Continuity conditions in the STT and a χ^2 condition are used to determine particle tracks.

The achieved results can be found in Tab. 6.1. Since the efficiency for primary tracks is lower than for the primary track finders, it is recommended to use it in combination with a primary track finder, where first the primary track finders are applied and then the remaining hits are used for the secondary track finder. As expected, the Apollonius Triplet track finder showed a significantly better performance for secondary tracks than the primary track finders. It increases the efficiency for secondary tracks from 45 % for the Standard tracker to 65 % for the Apollonius Triplet track finder. Compared to the Hough track finder the efficiency for secondaries is similar, but the quality of the tracks (momentum resolution and *Completeness*) is significantly higher for the Apollonius Triplet track finder. Here, the Apollonius Triplet track finder achieves a momentum resolution (*FWHM*) for secondaries with a *dPCA* of more than 3 cm of about 40 MeV/c, whereas the Hough track finder has a broad distribution with a *FWHM* of 180 MeV/c. In terms of *Completeness* the Apollonius Triplet track finder exceeds the Hough track finder with a *Completeness* of about 80 % compared to less than 50 % for the Hough Track finder.

6.1.4 Combination of Primary and Secondary Track Finders

To benefit from the advantages of the different track finders, the primary track finders are combined with the secondary track finder. Here, both combinations, Standard plus Apollonius Triplet track finder and Hough plus Apollonius Triplet track finder were investigated.

The efficiency for primary tracks is identical for both combinations and could be improved by 3 %-points in both cases, with a finding rate of about 93 %. For secondary tracks a significant improvement was achieved by combining the primary trackers with the secondary track finder. The combination of the Standard and Apollonius Triplet tracker improved the efficiency for secondaries from 45 % for the Standard tracker to 73 % for the combination of Standard and Apollonius Triplet track finder. The combination of Hough and Apollonius Triplet track finder achieved an even greater improvement to 79 % compared to the existing Standard tracker.

Adding a second algorithm was expected to increase the ghost and clone rates. However, the low ghost rate of the Hough track finder led to a reduction of the ghost rate for the combination of Hough and Apollonius Triplet track finder compared to the currently existing Standard tracker (16% for Hough + Apollonius Triplet track finder vs. 17% for the Standard tracker). To further reduce the ghost rate, a procedure to remove wrong tracks in the Standard tracker or a general clean-up procedure at the end of the combination of the algorithms is still missing. The clone rate is 19% for Hough and Apollonius Triplet track finder and 16% for Standard and Apollonius Triplet track finder. The reason for the higher clone rate for the combination of Hough and Apollonius Triplet tracker is the high efficiency of the Hough track finder to find secondary tracks. An improvement by either a subsequent merging procedure after combining the algorithms or by removing poorly reconstructed secondary tracks after the Hough track finder is pending.

6.2 Application to the reaction $\bar{p}p \rightarrow \Xi^-(1820)\Xi^+$

The final section of this thesis applied the tracking algorithms to a full event analysis of the reaction $\bar{p}p \rightarrow \Xi^+\Xi^-(1820)$. The first step towards a full event analysis is to apply a Kalman filter to the found tracks. However, first disadvantages of the track finders became apparent, which were not depicted by the efficiencies previously studied in the tracking analysis. The Hough track finder had a relatively high efficiency to find secondary tracks with a poor momentum resolution. However, it was not visible in the previous analysis that some of these tracks had no hits that provide z-information, but consisted nearly exclusively of *STT* hits from axial tubes. Consequently, there was information missing for the Kalman filter to work properly. These tracks were therefore removed. The correction mainly affected the poorly reconstructed secondary tracks found by the Hough track finder.

Nevertheless, a strong improvement was achieved for the full event analysis by developing a new primary track finder. A comparison of the reconstruction efficiencies when using only primary track finders showed that the final reconstruction efficiency could be improved by a factor of 2.5 compared to the Standard tracker, from 2.4% for the Standard tracker to 5.9% for the Hough tracker.

The combination of primary and secondary track finder significantly improved the reconstruction efficiency. The best result was achieved with the combination of the Standard and Apollonius Triplet track finder. Compared to the Standard track finder, the efficiency was improved by a factor of 4 from 2.4% to 9.9%. The combination of the Hough and Apollonius Triplet track finder also benefits from the additional secondary track finder. However, a slightly lower reconstruction efficiency of 8.2% was achieved, mostly originating from the missing z-component for the Kalman filter. It is promising to improve the overall efficiency of the combination of Hough and Apollonius Triplet track finder by optimizing the Hough track finder for highest finding rate for primary tracks rather than for highest overall finding rate (i.e. including secondaries), as is currently the case. Such an optimization would further increase the total efficiency when combining it with the secondary track finder. The efficiencies shown above do not include the detector acceptance. Including the detector acceptance a full event reconstruction efficiency times acceptance of 1.2% is achieved with the combination of Standard and Apollonius Triplet track finder.

6.3 Remarks & Outlook

The thesis showed that the best track finding performance can be achieved when combining algorithms specialized for specific conditions, such as primary and secondary track finding. For this reason, the combination of the Standard and Apollonius Triplet track finder currently shows the best reconstruction efficiency for a full event. However, this work has also shown, that the Hough Track finder is superior to the Standard tracker in some aspects such as the ghost rate. Currently, the Hough track finder is optimized for highest total efficiency including both primary and secondary tracks, although it is designed as a primary track finder. An optimization to find only primary tracks is therefore promising, if the algorithm is combined with a secondary track finder. In this case, the probability that the Hough tracker finds parts of the secondary tracks that are no longer available for the Apollonius Triplet track finder would be reduced. This could lead to an improvement of the total efficiency when combining the Hough and Apollonius Triplet track finders.

Another important topic is the online capability of the tracking algorithms. The online performance of the Hough track finder using GPUs has been investigated. The data handling and memory consumption are currently the most problematic part and require further research. Finally, an investigation of the Apollonius Triplet track finder is interesting to see if the data handling and memory consumption of the Apollonius Triplet track finder is better suited to be computed on a GPU.

The algorithms developed in this work are the basis to investigate the performance of PANDA to measure the channel $\bar{p}p \rightarrow \Xi^-(1820)\Xi^+$. The next steps are to combine these algorithms with the realistic p_z -finder that has been developed in the meantime for PANDA. With this step, the track finding in the target spectrometer becomes completely independent of the MC data and thus reflects the realistic track finding rate for the target spectrometer.

Using realistic trackers in the forward spectrometer and the already existing realistic PID, a fully realistic physics analysis is possible. In this way, the expected resolution and efficiency to measure reactions of interest can be determined, as well as the expected measurement time needed for the experiment to attain results of physical relevance.

Bibliography

- [1] Own work by uploader MissMJ, PBS NOVA, Fermilab, Office of Science, United States Department of Energy, Particle Data Group, “Particle content of the Standard Model.” visited on 22.06.2022; https://upload.wikimedia.org/wikipedia/commons/0/00/Standard_Model_of_Elementary_Particles.svg.
- [2] G. Aad *et al.*, “Observation of a new particle in the search for the Standard Model Higgs boson with the ATLAS detector at the LHC,” *Phys.Lett.*, B716, pp. 1–29, 2012. DOI: [10.1016/j.physletb.2012.08.020](https://doi.org/10.1016/j.physletb.2012.08.020).
- [3] Nobel Prize Outreach AB 2022, “The Nobel Prize in Physics 2013.” NobelPrize.org, 2022. <https://www.nobelprize.org/prizes/physics/2013/summary/>.
- [4] J. C. Maxwell, “A dynamical theory of the electromagnetic field,” *Philosophical Transactions of the Royal Society of London*, 155, pp. 459–513, 1865.
- [5] Nobel Prize Outreach AB 2022, “The Nobel Prize in Physics 1965.” NobelPrize.org, 2022. <https://www.nobelprize.org/prizes/physics/1965/summary/>.
- [6] P. Schleper, “Teilchenphysik für Fortgeschrittene.” Institut für Experimentalphysik, Universität Hamburg, 2011. https://www.desy.de/~schleper/lehre/TeilchenFortgeschrittene/WS_2010_11/TeilchenFortgeschrittene.pdf.
- [7] A. Ceccucci, Z. Ligeti and Y. Sakai, “Review of Particle Physics: CKM Quark-Mixing Matrix,” *PTEP*, 2020, pp. 261–270, 2020. DOI: [10.1093/ptep/ptaa104](https://doi.org/10.1093/ptep/ptaa104).
- [8] Nobel Prize Outreach AB 2022, “The Nobel Prize in Physics 1957.” NobelPrize.org, 2022. <https://www.nobelprize.org/prizes/physics/1957/summary/>.
- [9] Nobel Prize Outreach AB 2022, “The Nobel Prize in Physics 1980.” NobelPrize.org, 2022. <https://www.nobelprize.org/prizes/physics/1980/summary/>.
- [10] Nobel Prize Outreach AB 2022, “The Nobel Prize in Physics 1979.” NobelPrize.org, 2022. <https://www.nobelprize.org/prizes/physics/1979/summary/>.
- [11] Nobel Prize Outreach AB 2022, “The Nobel Prize in Physics 1969.” NobelPrize.org, 2022. <https://www.nobelprize.org/prizes/physics/1969/summary/>.

- [12] E. Accomando, “An Introduction to QED & QCD,” in *STFC HEP School 2019*, 2019. <https://conference.ippp.dur.ac.uk/event/785/attachments/3688/4138/QEDQCD-notes.pdf>.
- [13] V. M. Abazov *et al.* (D0 collaboration, TOTEM Collaboration), “Odderon Exchange from Elastic Scattering Differences between pp and $p\bar{p}$ Data at 1.96 TeV and from pp Forward Scattering Measurements,” *Phys. Rev. Lett.*, 127, p. 062003, 2021. DOI: [10.1103/PhysRevLett.127.062003](https://doi.org/10.1103/PhysRevLett.127.062003).
- [14] R. Alkofer and J. Greensite, “Quark confinement: the hard problem of hadron physics,” *J. Phys. G: Nuclear and Particle Physics*, 34, pp. S3–S21, 2007. DOI: [10.1088/0954-3899/34/7/s02](https://doi.org/10.1088/0954-3899/34/7/s02).
- [15] P. A. Zyla *et al.*, Revised August 2021 by J. Huston, K. Rabbertz and G. Zanderighi, “Review of Particle Physics: Quantum Chromodynamics,” *PTEP*, 2020, pp. 153–167, 2020. DOI: [10.1093/ptep/ptaa104](https://doi.org/10.1093/ptep/ptaa104).
- [16] Nobel Prize Outreach AB 2022, “The Nobel Prize in Physics 2004.” NobelPrize.org, 2022. <https://www.nobelprize.org/prizes/physics/2004/summary/>.
- [17] F. Halzen and A. D. Martin, *Quarks and leptons : an introductory course in modern particle physics*. New York, NY: Wiley, 1984.
- [18] K. G. Wilson, “Confinement of quarks,” *Phys. Rev. D*, 10, pp. 2445–2459, 1974. DOI: [10.1103/PhysRevD.10.2445](https://doi.org/10.1103/PhysRevD.10.2445).
- [19] K. G. Wilson, “The origins of lattice gauge theory,” *Nuclear Physics B - Proceedings Supplements*, 140, pp. 3–19, 2005. DOI: [10.1016/j.nuclphysbps.2004.11.271](https://doi.org/10.1016/j.nuclphysbps.2004.11.271).
- [20] S. Weinberg, “Phenomenological lagrangians,” *Physica A: Statistical Mechanics and its Applications*, 96, pp. 327–340, 1979. DOI: [https://doi.org/10.1016/0378-4371\(79\)90223-1](https://doi.org/10.1016/0378-4371(79)90223-1).
- [21] P. A. Zyla *et al.*, Revised August 2021 by S. Hashimoto and S. R. Sharpe, “Review of Particle Physics: Lattice Quantum Chromodynamics,” *PTEP*, 2020, pp. 333–346, 2020. DOI: [10.1093/ptep/ptaa104](https://doi.org/10.1093/ptep/ptaa104).
- [22] W. Heisenberg, “Über den Bau der Atomkerne,” *Zeitschrift für Physik* 77, p. 1–11, 1932. DOI: <https://doi.org/10.1007/BF01342433>.
- [23] G. D. Rochester and C. C. Butler, “Evidence for the existence of new unstable elementary particles,” *Nature*, 160, pp. 855–857, 1947. DOI: [10.1038/160855a0](https://doi.org/10.1038/160855a0).
- [24] M. Gell-Mann, “The eightfold way: A theory of strong interaction symmetry,” 1961. <https://resolver.caltech.edu/CaltechAUTHORS:20180910-145743377>.
- [25] S. Scherer, *Symmetrien und Gruppen in der Teilchenphysik*. Springer Spektrum, 2016. DOI: [10.1007/978-3-662-47734-2](https://doi.org/10.1007/978-3-662-47734-2).
- [26] Zyla, P. A. *et al.*, Revised August 2021 by J. Huston (Michigan State U.), K. Rabbertz (KIT) and G. Zanderighi (MPI Munich), “Review of Particle Physics: Quark Model,” *PTEP*, 2020, pp. 312–324, 2020. DOI: [10.1093/ptep/ptaa104](https://doi.org/10.1093/ptep/ptaa104).

- [27] Picture by user E2m at Wikimedia Commons, “The spin-0 nonet of mesons.” visited on 22.06.2022; https://commons.wikimedia.org/wiki/File:Meson_nonet_-_spin_0.svg.
- [28] Picture by user E2m at Wikimedia Commons, “The spin-1 nonet of mesons.” visited on 22.06.2022; https://commons.wikimedia.org/wiki/File:Meson_nonet_-_spin_1.svg.
- [29] Picture by user E2m at Wikimedia Commons, “Baryon Octet.” visited on 22.06.2022; https://commons.wikimedia.org/wiki/File:Baryon_octet.svg.
- [30] Picture by user E2m at Wikimedia Commons, “Baryon decuplet.” visited on 22.06.2022; https://commons.wikimedia.org/wiki/File:Baryon_decuplet.svg.
- [31] PANDA Collaboration, “Physics Performance Report for PANDA: Strong Interaction Studies with Antiprotons,” 2009. DOI: [10.15161/oar.it/1446204388.18](https://doi.org/10.15161/oar.it/1446204388.18).
- [32] T. Melde, W. Plessas and B. Sengl, “Quark-model identification of baryon ground and resonant states,” *Phys. Rev. D*, 77, 2008. DOI: [10.1103/physrevd.77.114002](https://doi.org/10.1103/physrevd.77.114002).
- [33] P. A. Zyla *et al.*, “Review of Particle Physics,” *PTEP*, 2020, p. 083C01, 2020. and 2021 update.
- [34] M. Gell-Mann, “A schematic model of baryons and mesons,” *Phys. Lett.*, 8, pp. 214–215, 1964. DOI: [https://doi.org/10.1016/S0031-9163\(64\)92001-3](https://doi.org/10.1016/S0031-9163(64)92001-3).
- [35] Belle Collaboration, “Observation of a narrow charmoniumlike state in exclusive $B^\pm \rightarrow K^\pm \pi^+ \pi^- j/\psi$ decays,” *Phys. Rev. Lett.*, 91, p. 262001, 2003. DOI: [10.1103/PhysRevLett.91.262001](https://doi.org/10.1103/PhysRevLett.91.262001).
- [36] BESIII Collaboration, “Observation of an isoscalar resonance with exotic $J^{PC} = 1^{-+}$ quantum numbers in $j/\psi \rightarrow \gamma \eta \eta'$,” *Phys. Rev. Lett.*, 129, p. 192002, Oct 2022. DOI: [10.1103/PhysRevLett.129.192002](https://doi.org/10.1103/PhysRevLett.129.192002).
- [37] B.-D. Wan, S.-Q. Zhang and C.-F. Qiao, “A possible structure of newly found exotic state $\eta_1(1855)$,” *Phys. Rev. D*, 106, p. 074003, 2022. DOI: <https://doi.org/10.1103/PhysRevD.106.074003>.
- [38] LHCb Collaboration, “Observation of an exotic narrow doubly charmed tetraquark,” *Nat. Phys.*, 18, p. 751–754, 2022. DOI: <https://doi.org/10.1038/s41567-022-01614-y>.
- [39] BESIII Collaboration, “Observation of a charged charmoniumlike structure in $e^+e^- \rightarrow \pi^+ \pi^- j/\psi$ @ $\sqrt{s} = 4.26$ GeV,” *Phys. Rev. Lett.*, 110, p. 252001, 2013. DOI: [10.1103/PhysRevLett.110.252001](https://doi.org/10.1103/PhysRevLett.110.252001).
- [40] Belle Collaboration, “Study of $e^+e^- \rightarrow \pi^+ \pi^- j\psi$ and observation of a charged charmoniumlike state at Belle,” *Phys. Rev. Lett.*, 110, 2013. DOI: [10.1103/physrevlett.110.252002](https://doi.org/10.1103/physrevlett.110.252002).

- [41] LHCb Collaboration, “Observation of $j/\psi p$ resonances consistent with pentaquark states in $\lambda_b^0 \rightarrow j/\psi k^- p$ decays,” *Phys. Rev. Lett.*, 115, 2015. DOI: [10.1103/physrevlett.115.072001](https://doi.org/10.1103/physrevlett.115.072001).
- [42] LHCb Collaboration, “Observation of a Narrow Pentaquark State, $P_c(4312)^+$ and of the Two-Peak Structure of the $P_c(4450)^+$,” *Phys. Rev. Lett.*, 122, 2019. DOI: [10.1103/physrevlett.122.222001](https://doi.org/10.1103/physrevlett.122.222001).
- [43] Belle Collaboration, “Observation of two charged bottomonium-like resonances in $\psi(5s)$ decays,” *Phys. Rev. Lett.*, 108, 2012. DOI: [10.1103/physrevlett.108.122001](https://doi.org/10.1103/physrevlett.108.122001).
- [44] M. Durante *et al.*, “All the fun of the FAIR: fundamental physics at the facility for antiproton and ion research,” *Physica Scripta*, 94, p. 14, 2019. DOI: [10.1088/1402-4896/aaf93f](https://doi.org/10.1088/1402-4896/aaf93f).
- [45] FAIR - Facility for Antiproton and Ion Research, “The accelerator facility.” FAIR Webpage: <https://fair-center.eu/overview/accelerator>. visited on 08.05.2022.
- [46] P. Spiller *et al.*, “The FAIR Heavy Ion Synchrotron SIS100,” *JINST*, 15, p. T12013, 2020. DOI: [10.1088/1748-0221/15/12/T12013](https://doi.org/10.1088/1748-0221/15/12/T12013).
- [47] “GSI-FAIR Scientific Report 2017,” Tech. Rep. GSI Report 2018-1, GSI Helmholtzzentrum für Schwerionenforschung, Darmstadt, 2018. DOI: [10.15120/GSI-2017-01856](https://doi.org/10.15120/GSI-2017-01856).
- [48] M. Vossberg *et al.*, “FAIR Control Centre (FCC) – Concepts and interim options for the existing GSI main control room,” in *IPAC2017: Proceedings of the 8th International Particle Accelerator Conference*, 2017. DOI: [10.18429/JACoW-IPAC2017-TUPIK047](https://doi.org/10.18429/JACoW-IPAC2017-TUPIK047).
- [49] P. Schütt, O. Geithner and P. Forck, “FAIR Operation Modes: Reference Modes for the Modularized Start Version (MSV),” 2016. https://indico.gsi.de/event/7647/contributions/33813/attachments/24507/30672/FAIR_Operation_Modes_V3-20160427.pdf.
- [50] K. Knie *et al.*, “Concept for the Antiproton Production Target at FAIR,” *Conf. Proc.*, C1205201, p. WEPPD030. 3 p, 2012. <https://cds.cern.ch/record/1558377>.
- [51] A. Dolinskii, “Collector Ring project at FAIR,” 2015. DOI: [10.13140/RG.2.1.3096.3042](https://doi.org/10.13140/RG.2.1.3096.3042).
- [52] FAIR - Facility for Antiproton and Ion Research, “Appa physics - atomic, plasma physics and applications.” FAIR Webpage: <https://fair-center.eu/user/experiments/appa>. visited on 08.05.2022.
- [53] T. Stöhlker *et al.*, “APPA at FAIR: From fundamental to applied research,” *Nucl. Instrum. Methods Phys. Res. Section B: Beam Interactions with Materials and Atoms*, 365, pp. 680–685, 2015. DOI: <https://doi.org/10.1016/j.nimb.2015.07.077>.
- [54] “GSI-FAIR Scientific Report 2020,” Tech. Rep. GSI Report 2021-1, GSI Helmholtzzentrum für Schwerionenforschung, Darmstadt, 2021. DOI: [10.15120/GSI-2021-01005](https://doi.org/10.15120/GSI-2021-01005).
- [55] C. P. Welsch and J. Ullrich, “FLAIR — a facility for low-energy antiproton and ion research,” in *TCP 2006* (J. Dilling, M. Comyn, J. Thompson, and G. Gwinner, eds.), (Berlin, Heidelberg), pp. 71–80, Springer Berlin Heidelberg, 2007.

- [56] P. Senger, “Status of the Compressed Baryonic Matter experiment at FAIR,” *International Journal of Modern Physics E*, 29, p. 2030001, 2020. DOI: [10.1142/s0218301320300015](https://doi.org/10.1142/s0218301320300015).
- [57] FAIR - Facility for Antiproton and Ion Research, “NUSTAR - Nuclear Structure, Astrophysics and Reactions.” FAIR Webpage: <https://fair-center.de/user/experiments/nustar>. visited on 08.05.2022.
- [58] Y. Zhou, H. Xu *et al.*, “The KOALA experiment for (anti)proton–proton elastic scattering,” *Nucl. Instrum. Methods Phys. Res. A: Accelerators, Spectrometers, Detectors and Associated Equipment*, 1019, p. 165849, 2021. DOI: <https://doi.org/10.1016/j.nima.2021.165849>.
- [59] M. Fritsch, “HESR schematic overview.” PANDA Webpage, 2019. https://panda.gsi.de/system/files/user_uploads/m.fritsch/material/HESR_Jun2017_2017%20Nov%2009_20190514180033.jpg visited on 15.05.2022.
- [60] A. Lehrach *et al.*, “Beam performance and luminosity limitations in the high-energy storage ring (HESR),” *Nucl. Instrum. Methods Phys. Res. Section A: Accelerators, Spectrometers, Detectors and Associated Equipment*, 561, pp. 289–296, 2006. DOI: <https://doi.org/10.1016/j.nima.2006.01.017>.
- [61] H. Stockhorst *et al.*, “Stochastic cooling developments for the HESR at FAIR,” *Conf. Proc. C*, 0806233, 2008. <https://accelconf.web.cern.ch/e08/papers/thpp055.pdf>.
- [62] K. Rathsman *et al.*, “Electron cooling force calculations for HESR,” *EPAC 2008 - Contributions to the Proceedings*, 2008.
- [63] G. Barucca *et al.* for the PANDA Collaboration, “PANDA phase one,” *The European Physical Journal A*, 57, 2021. DOI: [10.1140/epja/s10050-021-00475-y](https://doi.org/10.1140/epja/s10050-021-00475-y).
- [64] Z. Liu, “Four-quark matter—a new era of spectroscopy,” *AAPPS Bulletin*, 31, 2021. DOI: <https://doi.org/10.1007/s43673-021-00007-2>.
- [65] OBELIX Collaboration, “Study of the $k^+k^-\pi^+\pi^-\pi^0$ final state in antiproton annihilation at rest in gaseous hydrogen at NTP with the OBELIX spectrometer,” *Phys. Lett. B*, 545, pp. 261–271, 2002. DOI: [https://doi.org/10.1016/S0370-2693\(02\)02547-9](https://doi.org/10.1016/S0370-2693(02)02547-9).
- [66] G. Bardin *et al.*, “Determination of the electric and magnetic form factors of the proton in the time-like region,” *Nuclear Physics B*, 411, pp. 3–32, 1994. DOI: [https://doi.org/10.1016/0550-3213\(94\)90052-3](https://doi.org/10.1016/0550-3213(94)90052-3).
- [67] F. Anulli for the BABAR Collaboration, “Baryon Form Factors measurements in the time-like region at BaBar,” *Nuclear Physics B - Proceedings Supplements*, 225-227, pp. 205–210, 2012. DOI: <https://doi.org/10.1016/j.nuclphysbps.2012.02.043>.
- [68] BABAR Collaboration, “Measurement of the $e^+e^- \rightarrow p\bar{p}$ cross section in the energy range from 3.0 to 6.5 GeV,” *Physical Review D*, 88, 2013. DOI: [10.1103/physrevd.88.072009](https://doi.org/10.1103/physrevd.88.072009).
- [69] I. Zimmermann, *Feasibility studies for the measurement of the time-like electromagnetic proton form factors at the PANDA experiment*. PhD thesis, Mainz U., 2018. DOI: [10.25358/openscience-1173](https://doi.org/10.25358/openscience-1173).

- [70] U. Kurilla, “PANDA start setup.” PANDA Webpage. <https://panda.gsi.de/material/panda-start-setup-labeled-pdf> visited on 15.05.2022.
- [71] PANDA Collaboration, “Technical Design Report for the PANDA Internal Targets,” 2012. https://panda.gsi.de/system/files/user_uploads/u.kurilla/RE-TDR-2012-002.pdf.
- [72] A.-K. Hergemoeller *et al.*, “The cluster-jet target for PANDA,” *Verhandlungen der Deutschen Physikalischen Gesellschaft*, 45, 2013. https://inis.iaea.org/search/search.aspx?orig_q=RN:45081769.
- [73] E. Köhler, *Mass spectroscopy of hydrogen cluster jets and beam density optimisation studies*. [electronic ed.] ed., 2015. <https://nbn-resolving.de/urn:nbn:de:hbz:6-68209429504>.
- [74] A. Pysznik *et al.*, “A pellet tracking system for the PANDA experiment,” *Hyperfine Interactions*, 229, 2014. DOI: [10.1007/s10751-014-1052-5](https://doi.org/10.1007/s10751-014-1052-5).
- [75] PANDA Collaboration, “Technical Design Report for the PANDA Solenoid and Dipole Spectrometer Magnets,” 2009. DOI: <https://doi.org/10.48550/arXiv.0907.0169>.
- [76] PANDA Collaboration, “Technical Design Report for the: PANDA Micro Vertex Detector,” 2012. DOI: <https://doi.org/10.48550/arXiv.1207.6581>.
- [77] “PANDA Micro-Vertex-Detector (MVD).” MVD Webpage <https://panda-wiki.gsi.de/cgi-bin/view/Mvd/MvdPublic>. visited on 08.07.2022.
- [78] T. Stockmanns, “Private communication.” Forschungszentrum Jülich, 22.06.2022.
- [79] T. Stockmanns, “A high rate, low radiation length Micro-Vertex-Detector for the P⁻ANDA experiment,” *Nucl. Instrum. Methods Phys. Res. A: Accelerators, Spectrometers, Detectors and Associated Equipment*, 650, pp. 64–67, 2011. International Workshop on Semiconductor Pixel Detectors for Particles and Imaging 2010. DOI: <https://doi.org/10.1016/j.nima.2010.12.107>.
- [80] P. Gianotti, “Straw tube tracker.” PANDA Webpage: <https://panda.gsi.de/article/straw-tube-tracker>. visited on 12.05.2022.
- [81] Copyright: Peter Wintz (IKP, FZ Jülich), “Photograph of one STT hexagon sector.”
- [82] PANDA Collaboration, “Technical design report for the PANDA (AntiProton Annihilations at Darmstadt) Straw Tube Tracker,” *The European Physical Journal A*, 49, pp. 1–104, 2013. DOI: [10.1140/epja/i2013-13025-8](https://doi.org/10.1140/epja/i2013-13025-8).
- [83] P. Gianotti *et al.*, “The straw tube trackers of the PANDA experiment,” *2013 3rd International Conference on Advancements in Nuclear Instrumentation, Measurement Methods and their Applications (ANIMMA)*, 2013. DOI: [10.1109/animma.2013.6728039](https://doi.org/10.1109/animma.2013.6728039).
- [84] G. Perez Andrade *et al.*, “Private Communication, Callibration results from STS Callibration of the HADES FAIR Phase-0 experiment.” FAIRNESS 2022. https://indico.gsi.de/event/13960/contributions/62044/attachments/39760/54215/FAIRNESS_gpa_d2.pdf.

- [85] P. Wintz, "Private communication." Forschungszentrum Jülich, 5.12.2022.
- [86] L. Fabbietti for the GEM-TPC Collaboration, "The PANDA GEM-based TPC prototype," *Nucl. Instrum. Methods Phys. Res. Section A: Accelerators, Spectrometers, Detectors and Associated Equipment*, 628, pp. 204–208, 2011. DOI: [10.1016/j.nima.2010.06.317](https://doi.org/10.1016/j.nima.2010.06.317).
- [87] GEM-TPC Collaboration, "Technical Design Study for the PANDA Time Projection Chamber," 2012. DOI: [10.48550/ARXIV.1207.0013](https://doi.org/10.48550/ARXIV.1207.0013).
- [88] F. Sauli, "The gas electron multiplier (GEM): Operating principles and applications," *Nucl. Instrum. Methods Phys. Res. A: Accelerators, Spectrometers, Detectors and Associated Equipment*, 805, pp. 2–24, 2016. DOI: <https://doi.org/10.1016/j.nima.2015.07.060>.
- [89] J. Smyrski, "Forward tracker." PANDA Webpage. <https://panda.gsi.de/article/forward-tracker> visited on 08.05.2022.
- [90] PANDA Collaboration, "Technical design report for the PANDA Forward Tracker," 2018. https://panda.gsi.de/system/files/user_uploads/admin/RE-TDR-2017-001.pdf.
- [91] PANDA Collaboration, "Technical Design Report for the PANDA Barrel Time-of-Flight," 46, 2018. https://panda.gsi.de/system/files/user_uploads/ken.suzuki/RE-TDR-2016-003_0.pdf.
- [92] S. Zimmermann *et al.*, "The PANDA barrel-TOF detector at FAIR," *Nucl. Instrum. Methods Phys. Res. Section A: Accelerators, Spectrometers, Detectors and Associated Equipment*, 936, pp. 590–591, 2019. DOI: <https://doi.org/10.1016/j.nima.2018.10.100>.
- [93] PANDA Collaboration, "Technical Design Report for the PANDA Forward Time of Flight detector (FToF wall)," 2018. https://panda.gsi.de/system/files/user_uploads/admin/RE-TDR-2016-004.pdf.
- [94] B Singh *et al.*, "Technical design report for the PANDA Barrel DIRC detector," *J. Phys. G: Nucl. Part. Phys.*, 46, p. 045001, 2019. DOI: [10.1088/1361-6471/aade3d](https://doi.org/10.1088/1361-6471/aade3d).
- [95] PANDA Collaboration, "Technical Design Report for the PANDA Endcap Disc DIRC," 2019. DOI: [10.48550/ARXIV.1912.12638](https://doi.org/10.48550/ARXIV.1912.12638).
- [96] Z.-A. Liu, ed., *Endcap Disc DIRC for PANDA at FAIR*, (Singapore), Springer Singapore, 2018. DOI: [10.1007/978-981-13-1313-4_52](https://doi.org/10.1007/978-981-13-1313-4_52).
- [97] S. Kononov for the PANDA Collaboration, "Forward RICH detector for the PANDA experiment." INSTR2020, 2020. https://indico.inp.nsk.su/event/20/contributions/802/attachments/511/596/kononov_panda_frich_instr20.pdf.
- [98] PANDA Collaboration, "Technical Design Report for the PANDA Muon System," 2012. https://panda.gsi.de/system/files/user_uploads/u.kurilla/RE-TDR-2012-003.pdf.

- [99] PANDA Collaboration, “Technical Design Report for PANDA Electromagnetic Calorimeter (EMC),” 2008. DOI: [10.48550/ARXIV.0810.1216](https://doi.org/10.48550/ARXIV.0810.1216).
- [100] PANDA Collaboration, “Technical Design Report for the PANDA Forward Spectrometer Calorimeter,” 2017. DOI: [10.48550/ARXIV.1704.02713](https://doi.org/10.48550/ARXIV.1704.02713).
- [101] PANDA Collaboration, “Technical Design Report for the PANDA Luminosity Detector,” 2018. https://panda.gsi.de/system/files/user_uploads/m.fritsch/RE-TDR-2015-001_1.pdf.
- [102] H. Xu *et al.*, “Measurement of proton-proton elastic scattering into the Coulomb region at $P_{beam} = 2.5, 2.8$ and 3.2 GeV/c,” *Phys. Lett. B*, 812, p. 136022, 2021.
- [103] PANDA Collaboration, “Technical Design Report for the PANDA Data Acquisition and Event Filtering,” 2021. https://panda.gsi.de/system/files/user_uploads/l.schmitt/RE-TDR-2020-006.pdf.
- [104] I. Konorov *et al.*, “SODA: Time distribution system for the PANDA experiment,” in *2009 IEEE Nuclear Science Symposium Conference Record (NSS/MIC)*, pp. 1863–1865, 2009. DOI: [10.1109/NSSMIC.2009.5402172](https://doi.org/10.1109/NSSMIC.2009.5402172).
- [105] R. Brun and F. Rademakers, “ROOT: An object oriented data analysis framework,” *Nucl. Instrum. Meth. A*, 389, pp. 81–86, 1997. DOI: [10.1016/S0168-9002\(97\)00048-X](https://doi.org/10.1016/S0168-9002(97)00048-X).
- [106] M. Al-Turany *et al.*, “The FairRoot framework,” *J. Phys. Conf. Ser.*, 396, p. 022001, 2012. DOI: [10.1088/1742-6596/396/2/022001](https://doi.org/10.1088/1742-6596/396/2/022001).
- [107] S. Spataro for the PANDA Collaboration, “The PandaRoot framework for simulation, reconstruction and analysis,” *J. Phys.: Conf. Ser.*, 331, p. 032031, 2011. DOI: [10.1088/1742-6596/331/3/032031](https://doi.org/10.1088/1742-6596/331/3/032031).
- [108] A. Ryd *et al.*, “EvtGen: A Monte Carlo Generator for B-Physics,” 2005. <https://evtgen.hepforge.org/doc/EvtGenGuide.pdf>.
- [109] A. Capella, U. Sukhatme, C.-I. Tan and J. Tran Thanh Van, “Dual parton model,” *Physics Reports*, 236, pp. 225–329, 1994. DOI: [https://doi.org/10.1016/0370-1573\(94\)90064-7](https://doi.org/10.1016/0370-1573(94)90064-7).
- [110] B. Andersson, G. Gustafson and H. Pi, “The FRITIOF model for very high-energy hadronic collisions,” *Z. Phys. C*, 57, pp. 485–494, 1993. DOI: [10.1007/BF01474343](https://doi.org/10.1007/BF01474343).
- [111] T. T. Van, “Introduction to soft hadronic interactions: from hadron-hadron to heavy ion collisions,” 1988. <https://s3.cern.ch/inspire-prod-files-4/4454a5c9e0205da22bafedaca417378e>.
- [112] R. Brun *et al.*, “GEANT3,” 1987. <https://cds.cern.ch/record/1119728?ln=de>.
- [113] S. Agostinelli and J. Allison *et al.*, “GEANT4—a simulation toolkit,” *Nucl. Instrum. Methods Phys. Res. Section A: Accelerators, Spectrometers, Detectors and Associated Equipment*, 506, pp. 250–303, 2003. DOI: [https://doi.org/10.1016/S0168-9002\(03\)01368-8](https://doi.org/10.1016/S0168-9002(03)01368-8).

- [114] I. Hrivnacova *et al.*, “The virtual monte carlo,” *eConf C0303241:THJT006,2003*, 2003. DOI: [10.48550/ARXIV.CS/0306005](https://doi.org/10.48550/ARXIV.CS/0306005).
- [115] C. Höppner *et al.*, “A Novel Generic Framework for Track Fitting in Complex Detector Systems,” *Nucl. Instrum. Meth. A*, 620, pp. 518–525, 2010. DOI: [10.1016/j.nima.2010.03.136](https://doi.org/10.1016/j.nima.2010.03.136).
- [116] G. Schepers *et al.*, “Particle Identification at PANDA: Report of the PID TAG (March 2009),” 2009. <https://panda-wiki.gsi.de/foswiki/pub/Tagpid/WebHome/pid-tag-panda-note032009.pdf>.
- [117] M. Kunze, “Rho analysis framework.” online Sep. 2022: <https://github.com/marcelkunze/rhoframework>.
- [118] R. Karabowicz, “Global Track Finder for PANDA experiment.” GSI Scientific Report 2010, 2010. <http://citeseerx.ist.psu.edu/viewdoc/download?doi=10.1.1.231.1995&rep=rep1&type=pdf>.
- [119] A. Herten, *GPU-based Online Track Reconstruction for PANDA and Application to the Analysis of $D \rightarrow K\pi\pi$* . PhD thesis, Ruhr-Universität Bochum, Universitätsbibliothek, 2015.
- [120] W. A. M. Esmail, *Deep learning for track finding and the reconstruction of excited hyperons in proton induced reactions*. PhD thesis, Ruhr-Universität Bochum, Universitätsbibliothek, 2022. DOI: [10.13154/294-8563](https://doi.org/10.13154/294-8563).
- [121] J. Regina, *Time for Hyperons: Development of Software Tools for Reconstructing Hyperons at PANDA and HADES*. PhD thesis, Uppsala University: Faculty of Science and Technology, 2021.
- [122] A. Alicke, T. Stockmanns and J. Ritman, “Track Finding for the PANDA Detector Based on Hough Transformations,” *EPJ Web Conf. Volume 251, 25th International Conference on Computing in High Energy and Nuclear Physics (CHEP 2021)*, 2021. DOI: <https://doi.org/10.1051/epjconf/202125104002>.
- [123] J. Schumann, “Entwicklung eines schnellen Algorithmus zur Suche von Teilchenspuren im "StrawTube Tracker" des PANDA-Detektors,” Bachelorarbeit, FH Aachen, Campus Jülich, 2013.
- [124] P. V. C. Hough, “Method and means for recognizing complex patterns,” 1962. <https://www.osti.gov/doi/patents/biblio/4746348>.
- [125] W. Burger and M. J. Burge, *Digitale Bildverarbeitung : Eine Einführung mit Java und ImageJ*. Berlin, Heidelberg: Springer-Verlag, 2., überarbeitete auflage ed., 2005.
- [126] NVIDIA Corporation, “NVIDIA CUDA C Programming Guide.” https://developer.download.nvidia.com/compute/DevZone/docs/html/C/doc/CUDA_C_Programming_Guide.pdf, 2012. Version 4.2.
- [127] NVIDIA, P. Vingelmann and F. H. P. Fitzek, “Cuda, release: 10.2.89.” <https://developer.nvidia.com/cuda-toolkit>, 2020.

- [128] NVIDIA Corporation, “CUDA Samples.” <https://github.com/NVIDIA/cuda-samples> visited on 05.02.2023.
- [129] NVIDIA Corporation, “GeForce RTX 2060.” <https://www.nvidia.com/en-gb/geforce/news/gfecnt/nvidia-geforce-rtx-2060/> visited on 05.02.2023.
- [130] T. Hopp, “The sensitivity of three-point circle fitting,” 1994-09-01 1994. DOI: <https://doi.org/10.6028/NIST.IR.5501>.
- [131] J. I. Pütz, *Study of Excited Ξ Baryons in Anti-Proton Proton Collisions with the PANDA Detector*. PhD thesis, Rheinische Friedrich-Wilhelms-Universität Bonn, Feb. 2020. <https://hdl.handle.net/20.500.11811/8281>.
- [132] C. Höppner *et al.*, “A novel generic framework for track fitting in complex detector systems,” *Nucl. Instrum. Methods Phys. Res. A: Accelerators, Spectrometers, Detectors and Associated Equipment*, 620, pp. 518–525, 2010. DOI: <https://doi.org/10.1016/j.nima.2010.03.136>.
- [133] B. Musgrave *et al.*, “Study of $Y\bar{Y}$ Production in Two, Three, and Four Body Final States by 3.0, 3.6 and 4.0 GeV/c Antiprotons in Hydrogen,” *Nuovo Cim.*, 35, p. 735, 1965.

The Problem of Apollonius



Here the analytic solution of the classical Apollonius Problem for three circles (CCC) is shown, where the circles k_i with $i = 1, 2, 3$ are connected with the eight possible Apollonius circles. The circles k_i have centers (x_i, y_i) and radii r_i connected via the circle equation:

$$k_i : (x - x_i)^2 + (y - y_i)^2 - (r \pm r_i)^2 = 0 \quad (\text{A.1})$$

$$\Leftrightarrow x^2 + y^2 - r^2 - 2xx_i - 2yy_i \mp 2rr_i + x_i^2 + y_i^2 - r_i^2 = 0 \quad (\text{A.2})$$

The Apollonius circles can then be calculated by inserting the three equations into each other and solving them with the three parameters x , y and r .

$$k_i - k_j : 2x(x_j - x_i) + 2y(y_j - y_i) \pm 2r(r_j - r_i) + x_i^2 + y_i^2 - r_i^2 - x_j^2 - y_j^2 + r_j^2 = 0 \quad (\text{A.3})$$

Now new parameter definitions are introduced:

$$\begin{aligned} a &= 2(x_1 - x_2) & a' &= 2(x_1 - x_3) \\ b &= 2(y_1 - y_2) & b' &= 2(y_1 - y_3) \\ c &= 2(r_1 - r_2) & c' &= 2(r_1 - r_3) \\ d &= (x_1^2 + y_1^2 - r_1^2) - (x_2^2 + y_2^2 - r_2^2) & d' &= (x_1^2 + y_1^2 - r_1^2) - (x_3^2 + y_3^2 - r_3^2) \end{aligned}$$

leading to:

$$k_1 - k_2 : \quad -ax - by \mp cr + d = 0 \quad (\text{A.4})$$

$$k_1 - k_3 : \quad -a'x - b'y \mp c'r + d' = 0 \quad (\text{A.5})$$

Subtracting the equations lead to:

$$a'(k_1 - k_2) - a(k_1 - k_3) : \quad \underbrace{(-a'b + ab')}_N \cdot y \mp \underbrace{(a'c - ac')}_{D_y} \cdot r - \underbrace{(ad' - a'd)}_{C_y} = 0 \quad (\text{A.6})$$

$$b'(k_1 - k_2) - b(k_1 - k_3) : \quad -\underbrace{(ab' - a'b)}_N x \pm \underbrace{(bc' - b'c)}_{B_x} r + \underbrace{b'd - bd'}_{A_x} = 0 \quad (\text{A.7})$$

With the definitions

$$A_x = b'd - bd' \quad B_x = bc' - b'c \quad C_y = ad' - a'd \quad D_y = a'c - ac' \quad N = ab' - a'b$$

the equations in A.6 and A.7 are equivalent to

$$a'(k_1 - k_2) - a(k_1 - k_3) : \quad Ny \mp D_y r - C_y = 0 \quad (\text{A.8})$$

$$b'(k_1 - k_2) - b(k_1 - k_3) : \quad -Nx \pm B_x r + A_x = 0 \quad (\text{A.9})$$

Solving the equation for x and y results in:

$$x = \frac{A_x \mp B_x \cdot r}{N} \quad y = \frac{C_y + D_y \cdot r}{N} \quad (\text{A.10})$$

These equations can then be added to the circle equation A.1:

$$0 = \left(\frac{A_x \mp B_x \cdot r}{N} - x_i \right)^2 + \left(\frac{C_y + D_y \cdot r}{N} - y_i \right)^2 - (r \pm r_i)^2 \quad (\text{A.11})$$

$$\Leftrightarrow 0 = \left(\frac{A_x}{N} \mp \frac{B_x}{N} \cdot r - x_i \right)^2 + \left(\frac{C_y}{N} + \frac{D_y}{N} \cdot r - y_i \right)^2 - (r \pm r_i)^2 \quad (\text{A.12})$$

$$\Leftrightarrow 0 = r^2 \underbrace{\left(\frac{B_x^2}{N^2} + \frac{D_y^2}{N^2} - 1 \right)}_A + r \cdot \underbrace{\left(\mp \frac{2B_x}{N} \left(\frac{A_x}{N} - x_i \right) + \frac{2D_y}{N} \left(\frac{C_y}{N} - y_i \right) \pm 2r_i \right)}_B + \underbrace{\left(\frac{A_x}{N} - x_i \right)^2 + \left(\frac{C_y}{N} - y_i \right)^2 - r_i^2}_C \quad (\text{A.13})$$

with

$$A = \frac{B_x^2}{N^2} + \frac{D_y^2}{N^2} - 1$$

$$B = \frac{2 \cdot B_x}{N} \cdot \left(\frac{A_x}{N} - x_1 \right) + \frac{2 \cdot D_y}{N} \cdot \left(\frac{C_y}{N} - y_1 \right) \pm 2 \cdot r_1$$

$$C = \left(\frac{A_x}{N} - x_1 \right)^2 + \left(\frac{C_y}{N} - y_1 \right)^2 - (r_1)^2.$$

Finally, the radii of the Apollonius circles are computed as:

$$r = \frac{-B + \sqrt{D}}{2 \cdot A} \quad (\text{A.14})$$

with

$$D = B^2 - 4 \cdot A \cdot C.$$

Additional Figures for the Application to $p\bar{p} \rightarrow \Xi(1820)^-\Xi^+$

B

B.1 Final state Particles

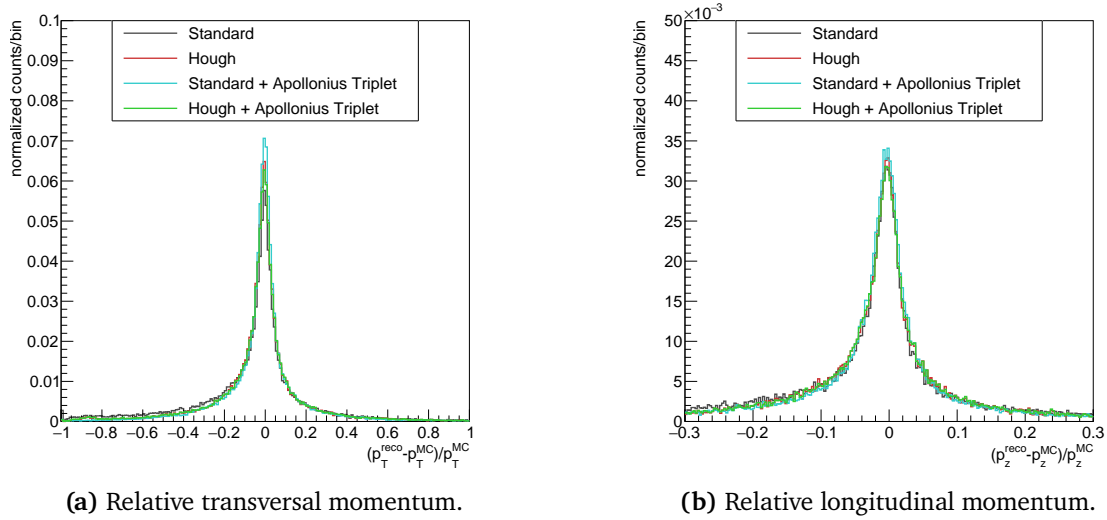
Table B.1: FWHM and RMS for the relative transversal momentum resolution of all final state particles for the different tracking algorithms.

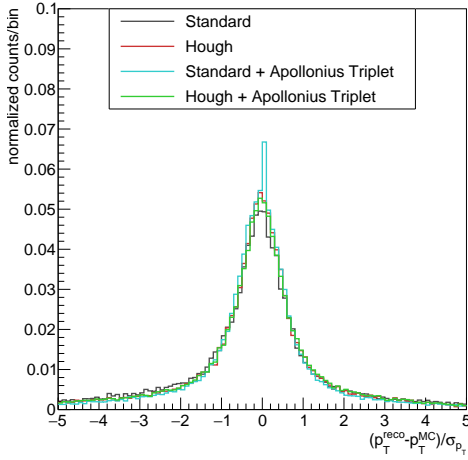
	Standard		Hough		Standard + Apollonius Triplet		Hough + Apollonius Triplet	
	FWHM [%]	RMS [%]	FWHM [%]	RMS [%]	FWHM [%]	RMS [%]	FWHM [%]	RMS [%]
K^-	6	25	6	16	5	14	7	17
P	6	27	8	22	6	20	8	23
π^-	11	36	10	28	9	27	10	28
$\pi^+(\Xi^+)$	11	34	8	26	9	25	8	26
\bar{P}	8	29	8	24	8	22	8	25
π^+	12	38	10	31	10	31	10	31

Table B.2: FWHM and RMS for the relative longitudinal momentum resolution of all final state particles for the different tracking algorithms.

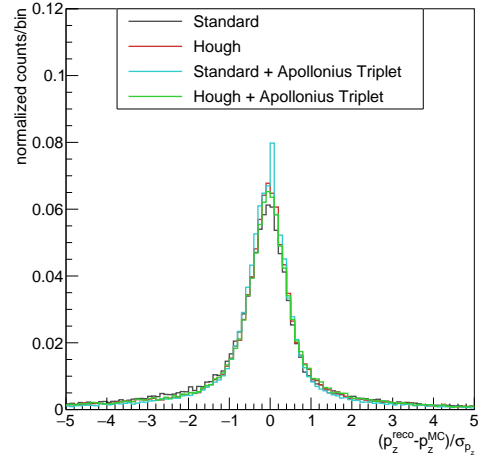
	Standard		Hough		Standard + Apollonius Triplet		Hough + Apollonius Triplet	
	FWHM [%]	RMS [%]	FWHM [%]	RMS [%]	FWHM [%]	RMS [%]	FWHM [%]	RMS [%]
K^-	5	10	6	9	5	8	6	9
P	4	10	4	10	4	9	5	10
π^-	6	11	6	11	5	10	5	11
$\pi^+(\Xi^+)$	5	11	6	10	5	10	6	11
\bar{P}	3	11	3	10	4	10	4	10
π^+	5	12	6	11	6	11	6	11

B.1.1 Proton

**Figure B.1:** Relative momentum distributions for the proton.

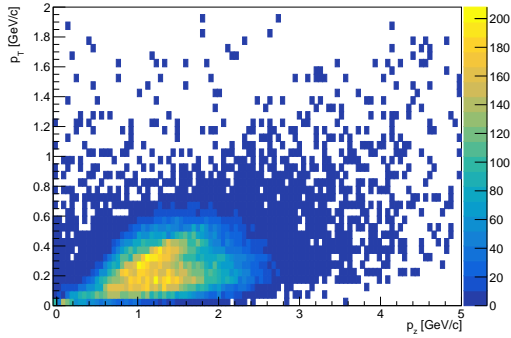


(a) Pull distribution for the transversal momentum.

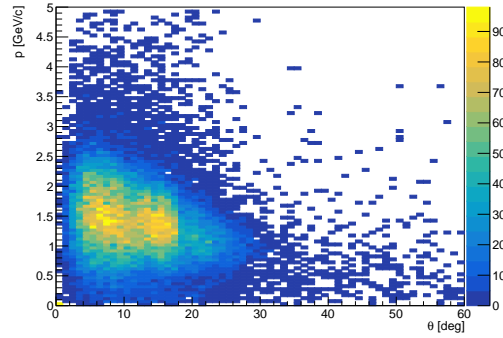


(b) Pull distribution for the longitudinal momentum.

Figure B.2: Pull distributions for the proton.

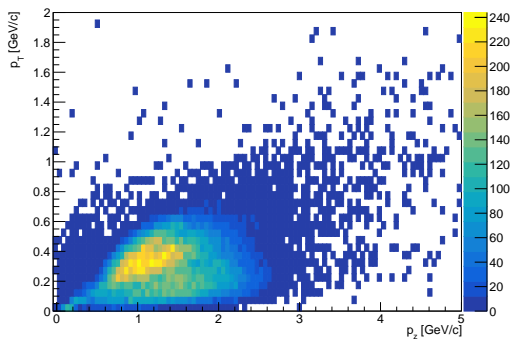


(a) Transverse vs. longitudinal momentum.

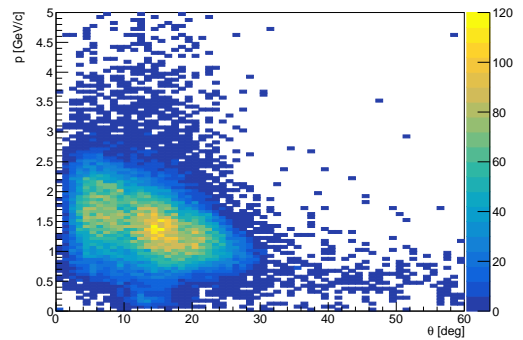


(b) Total momentum vs. polar angle.

Figure B.3: Distributions of p_T vs. p_z and p vs. θ for the proton found by the Standard track finder.



(a) Transverse vs. longitudinal momentum.



(b) Total momentum vs. polar angle.

Figure B.4: Distributions of p_T vs. p_z and p vs. θ for the proton found by the Hough track finder.

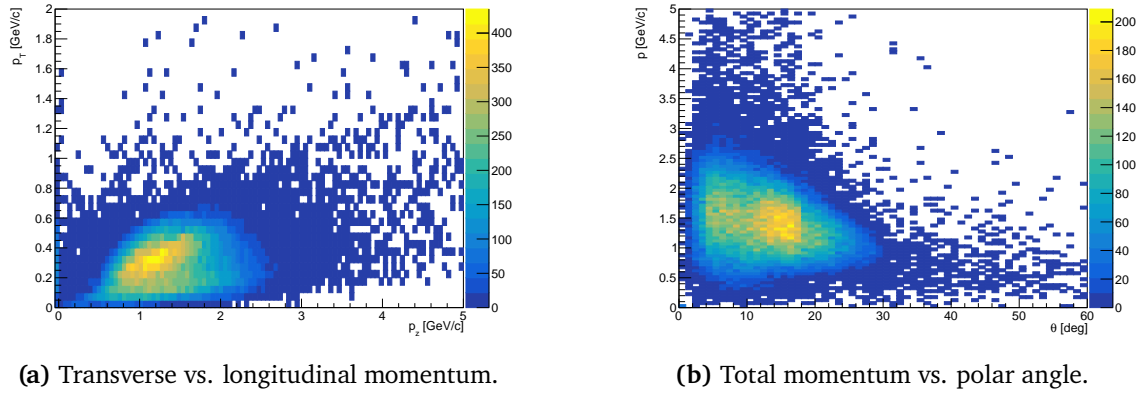


Figure B.5: Distributions of p_T vs. p_z and p vs. θ for the proton found by the Standard plus Apollonius Triplet track finder.

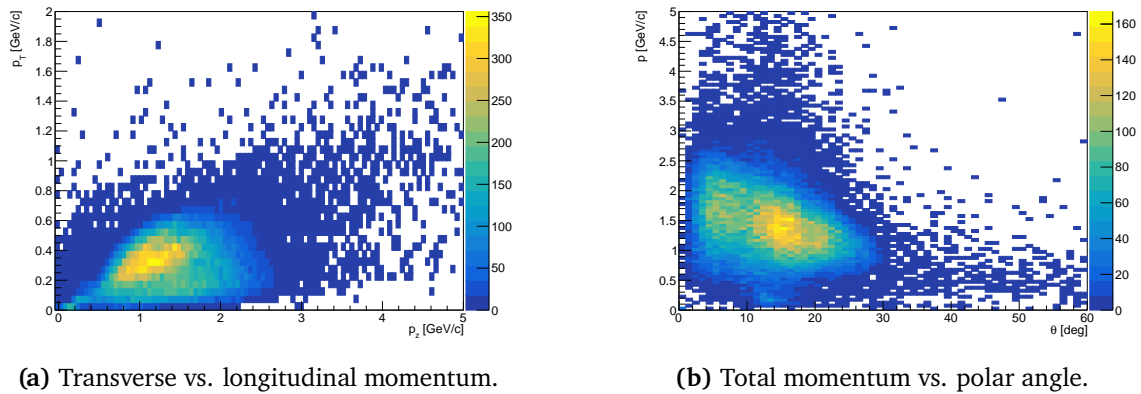
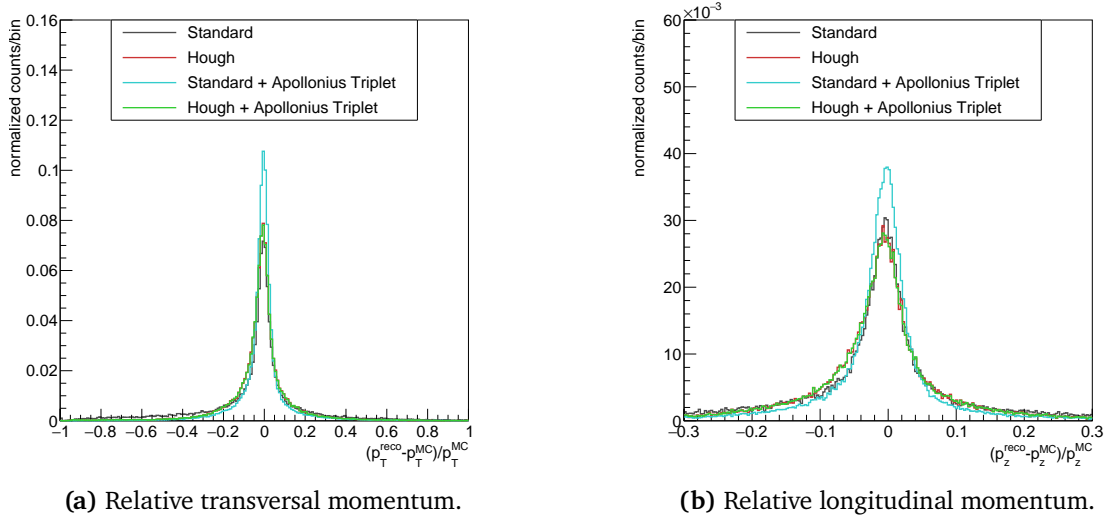
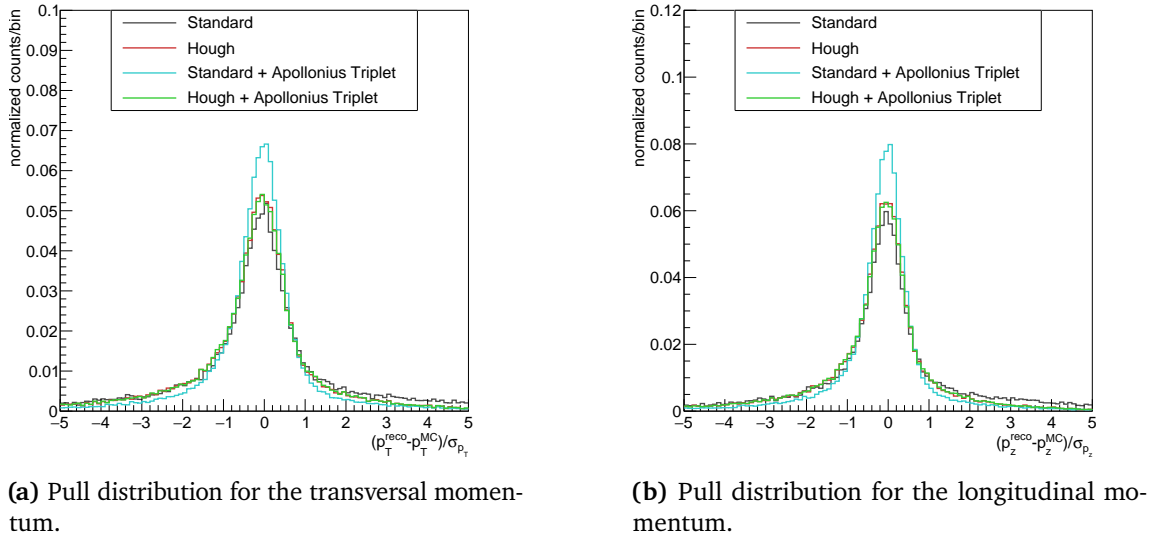
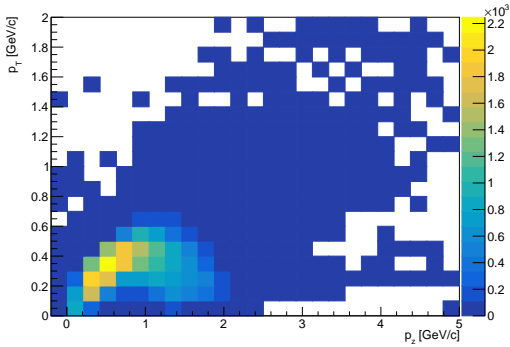


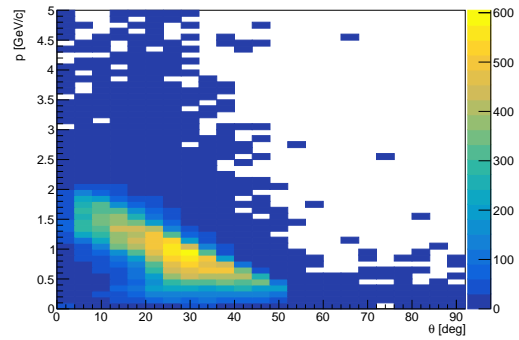
Figure B.6: Distributions of p_T vs. p_z and p vs. θ for the proton found by the Hough plus Apollonius Triplet track finder.

B.1.2 Kaon

Figure B.7: Relative momentum distributions for the K^- .Figure B.8: Pull distributions for the K^- .

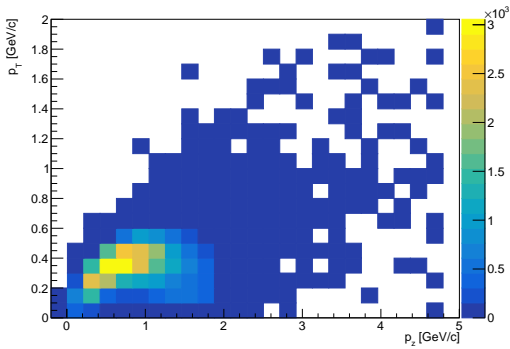


(a) Transverse vs. longitudinal momentum.

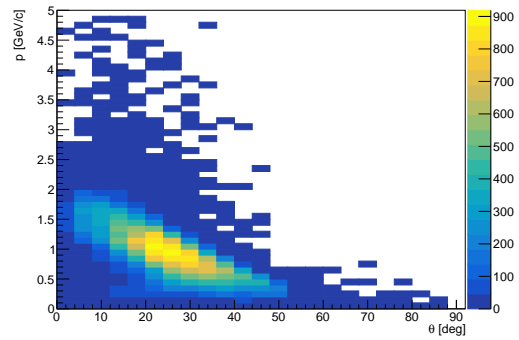


(b) Total momentum vs. polar angle.

Figure B.9: Distributions of p_T vs. p_z and p vs. θ for the K^- found by the Standard track finder.

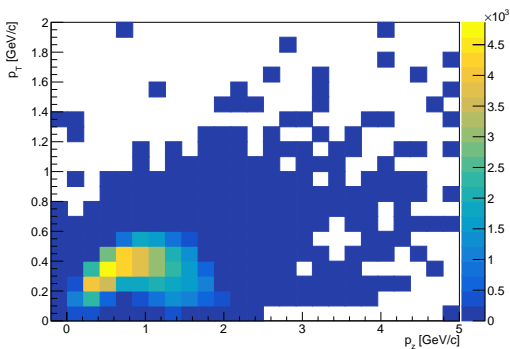


(a) Transverse vs. longitudinal momentum.

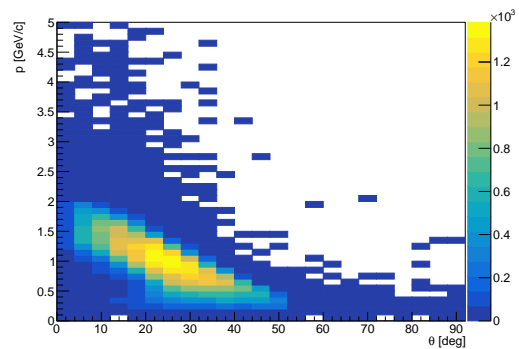


(b) Total momentum vs. polar angle.

Figure B.10: Distributions of p_T vs. p_z and p vs. θ for the K^- found by the Hough track finder.



(a) Transverse vs. longitudinal momentum.



(b) Total momentum vs. polar angle.

Figure B.11: Distributions of p_T vs. p_z and p vs. θ for the K^- found by the Standard plus Apollonius Triplet track finder.

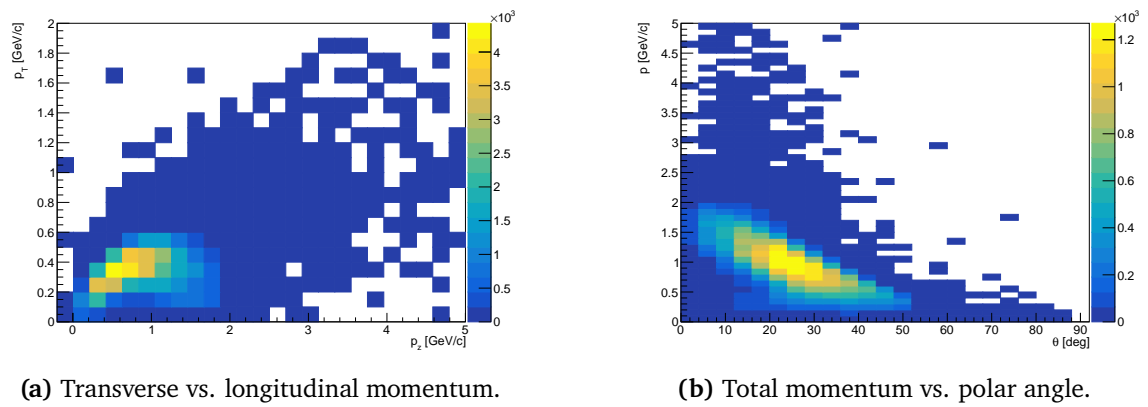


Figure B.12: Distributions of p_T vs. p_z and p vs. θ for the K^- found by the Hough plus Apollonius Triplet track finder.

B.1.3 Antiproton

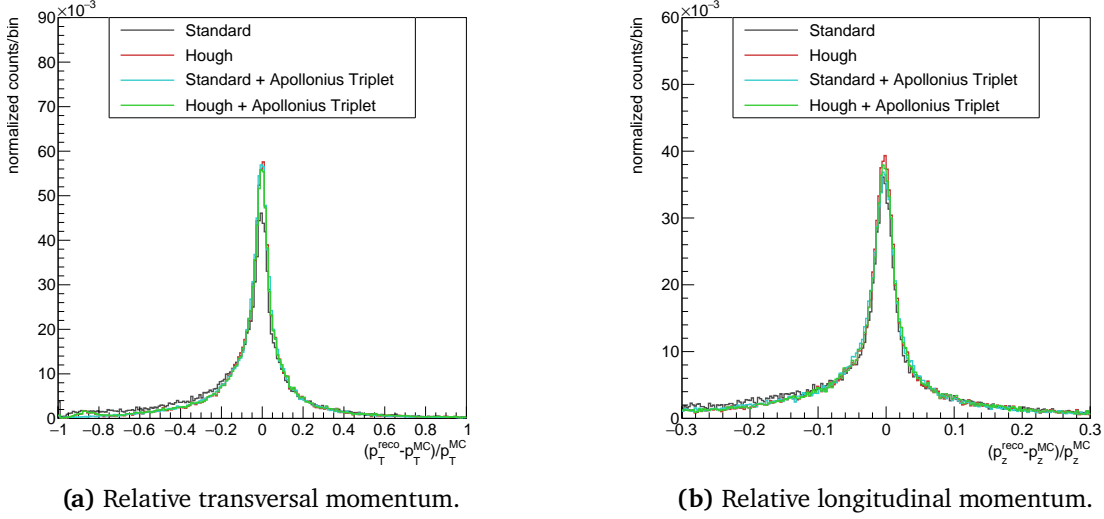


Figure B.13: Relative momentum distributions for the \bar{p} .

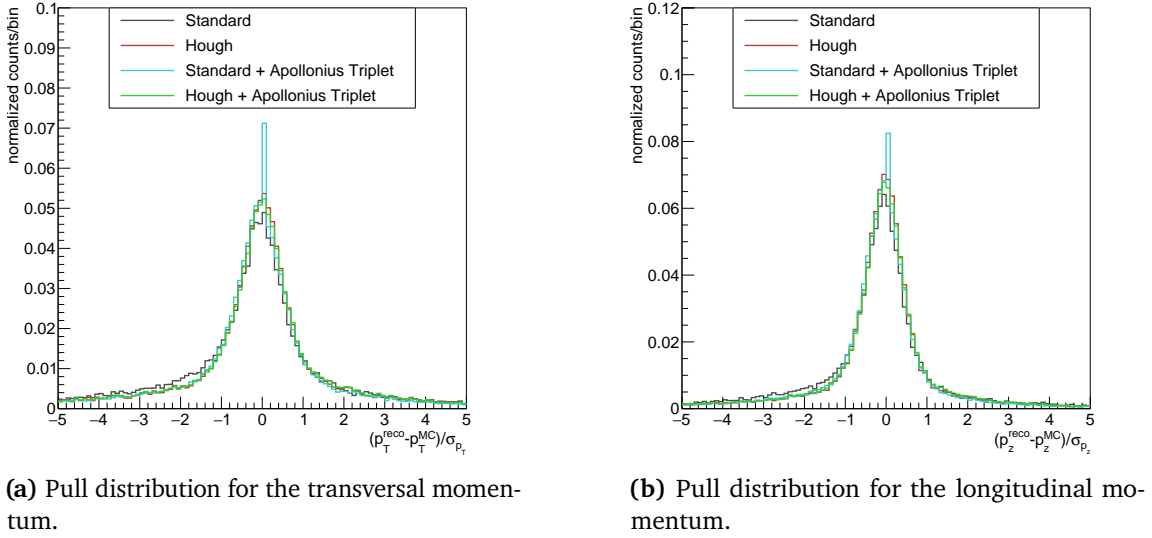


Figure B.14: Pull distributions for the \bar{p} .

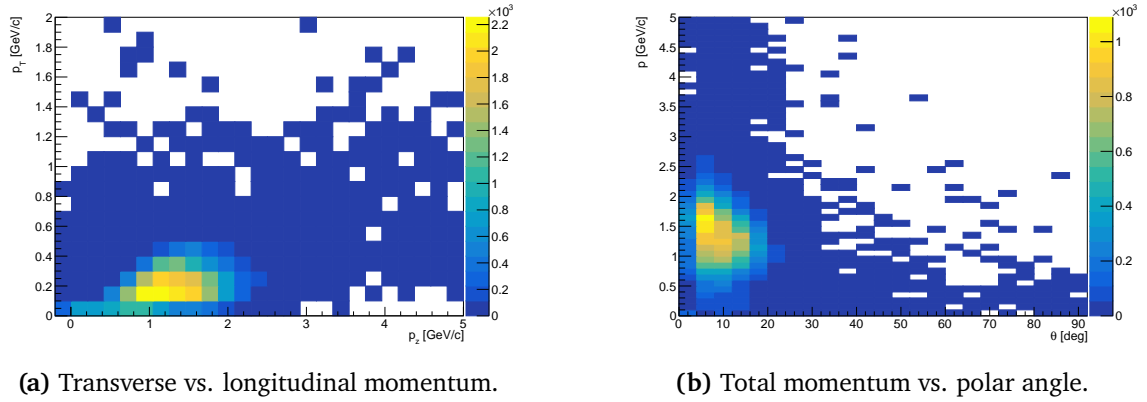


Figure B.15: Distributions of p_T vs. p_z and p vs. θ for the \bar{p} found by the Standard track finder.

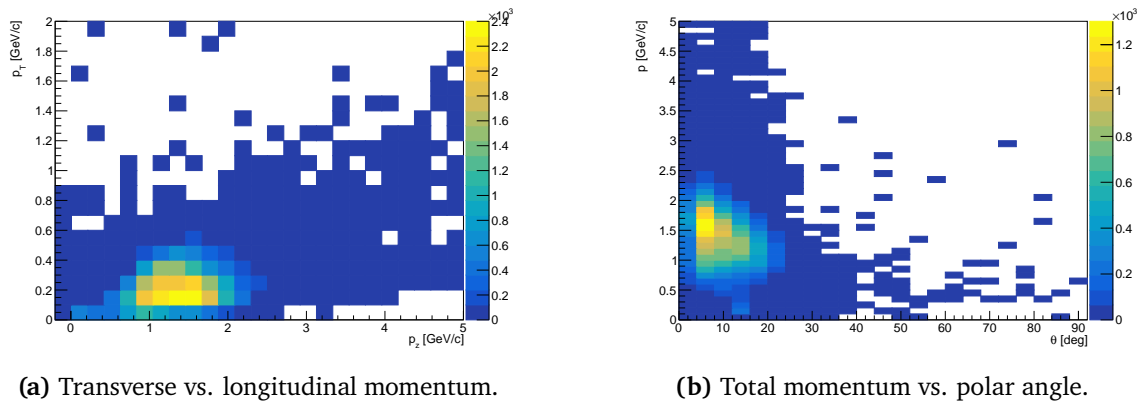


Figure B.16: Distributions of p_T vs. p_z and p vs. θ for the \bar{p} found by the Hough track finder.

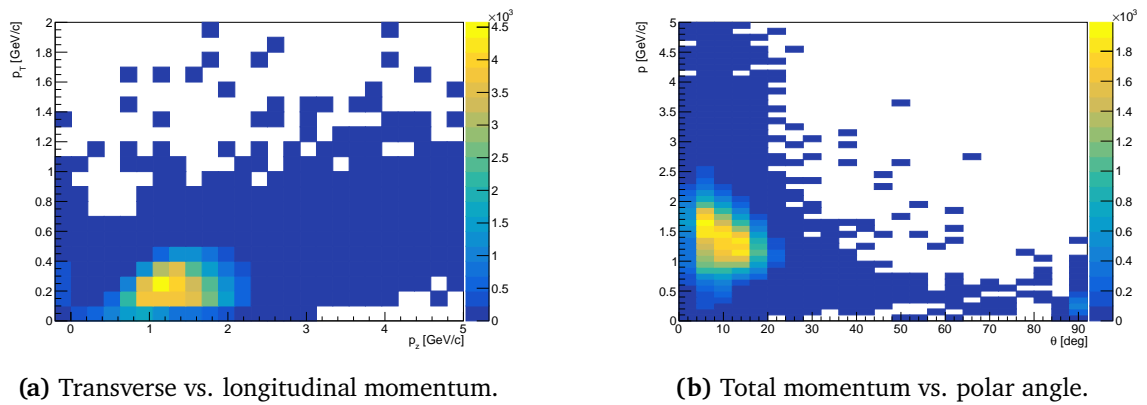


Figure B.17: Distributions of p_T vs. p_z and p vs. θ for the \bar{p} found by the Standard plus Apollonius Triplet track finder.

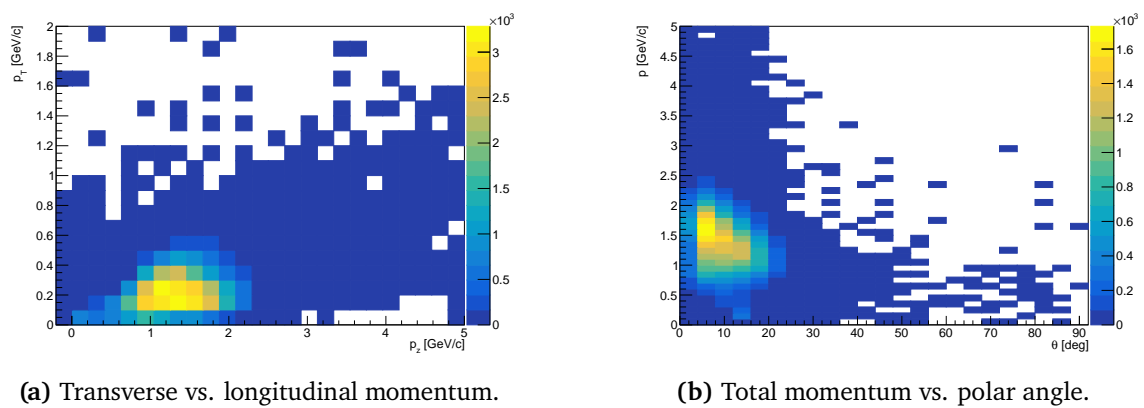
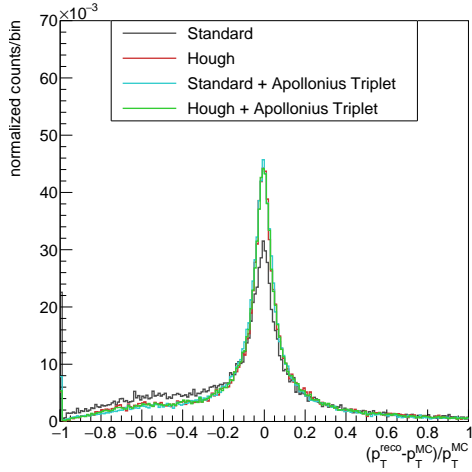
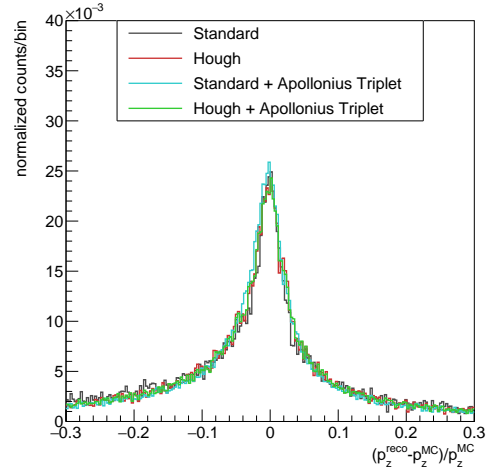


Figure B.18: Distributions of p_T vs. p_z and p vs. θ for the \bar{p} found by the Hough plus Apollonius Triplet track finder.

B.1.4 π^+

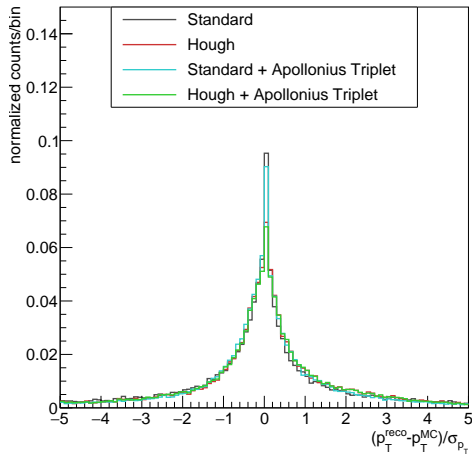


(a) Relative transversal momentum.

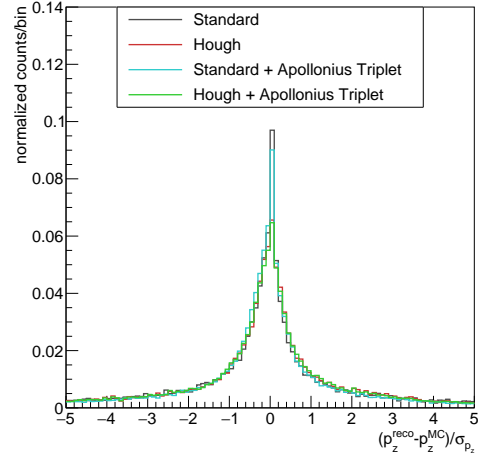


(b) Relative longitudinal momentum.

Figure B.19: Relative momentum distributions for the π^+ .

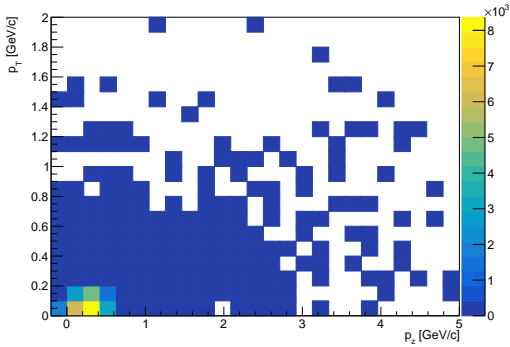


(a) Pull distribution for the transversal momentum.

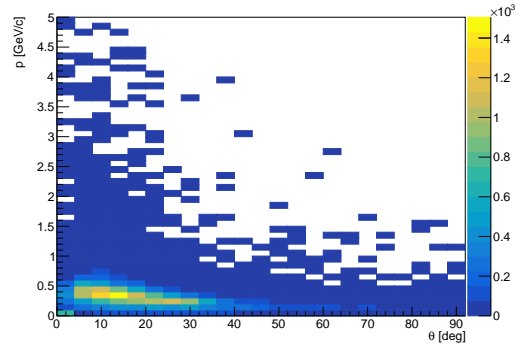


(b) Pull distribution for the longitudinal momentum.

Figure B.20: Pull distributions for the π^+ .

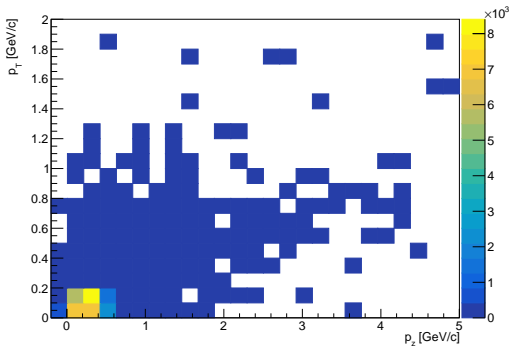


(a) Transverse vs. longitudinal momentum.

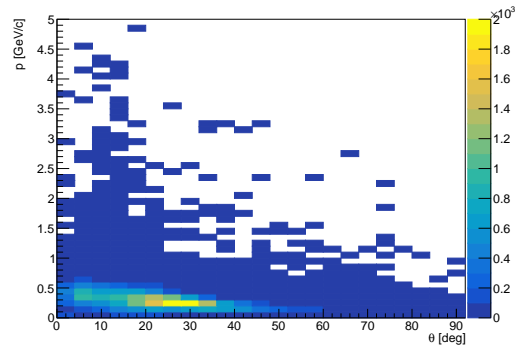


(b) Total momentum vs. polar angle.

Figure B.21: Distributions of p_T vs. p_z and p vs. θ for the π^+ found by the Standard track finder.

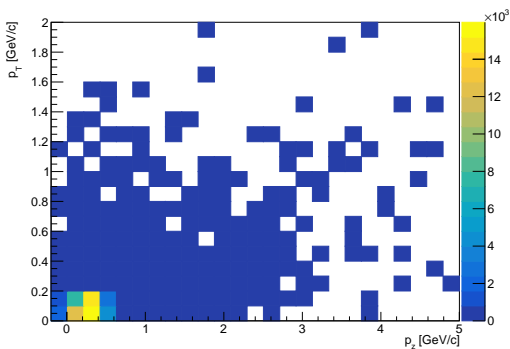


(a) Transverse vs. longitudinal momentum.

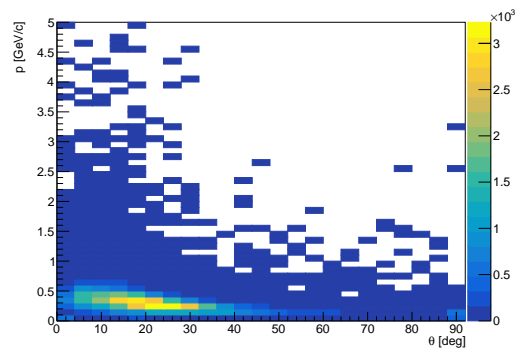


(b) Total momentum vs. polar angle.

Figure B.22: Distributions of p_T vs. p_z and p vs. θ for the π^+ found by the Hough track finder.

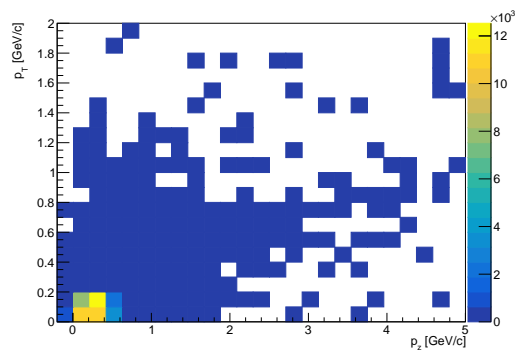


(a) Transverse vs. longitudinal momentum.

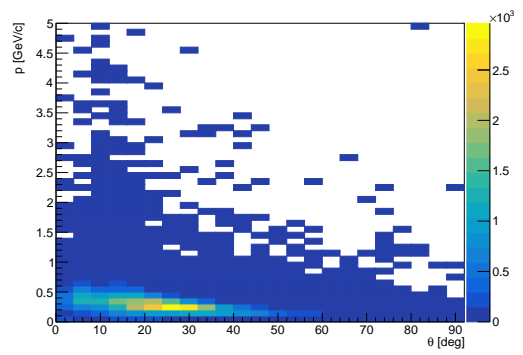


(b) Total momentum vs. polar angle.

Figure B.23: Distributions of p_T vs. p_z and p vs. θ for the π^+ found by the Standard plus Apollonius Triplet track finder.



(a) Transverse vs. longitudinal momentum.



(b) Total momentum vs. polar angle.

Figure B.24: Distributions of p_T vs. p_z and p vs. θ for the π^+ found by the Hough plus Apollonius Triplet track finder.

B.1.5 $\pi^+(\Xi^+)$

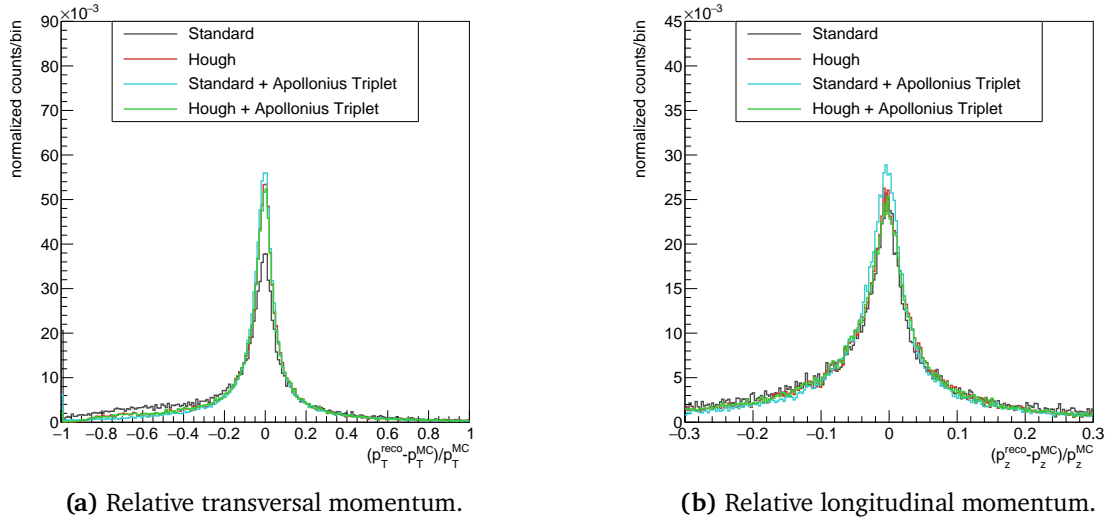


Figure B.25: Relative momentum distributions for the $\pi^+(\Xi^+)$.

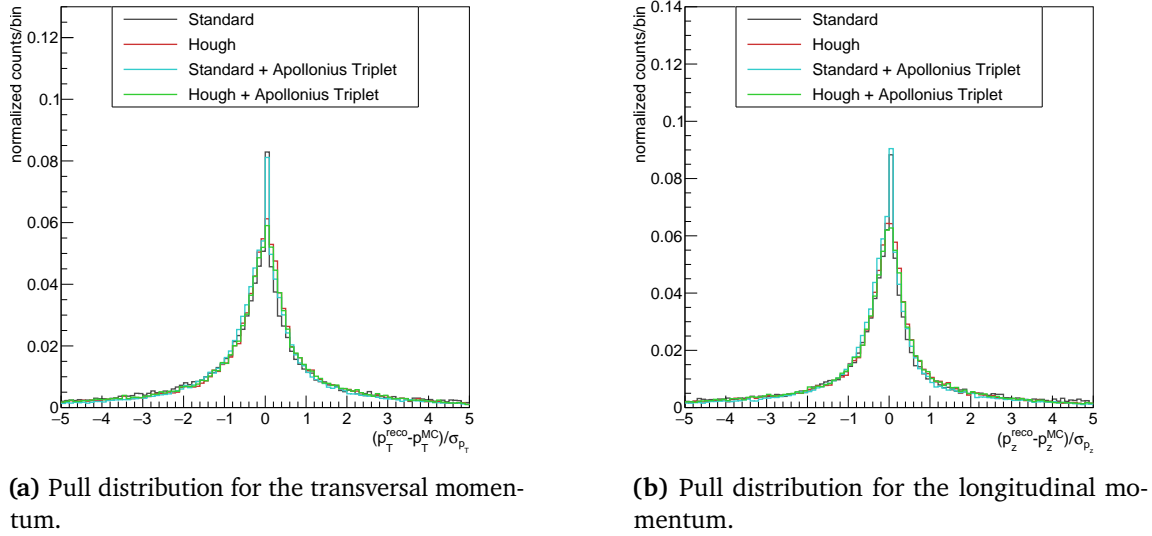
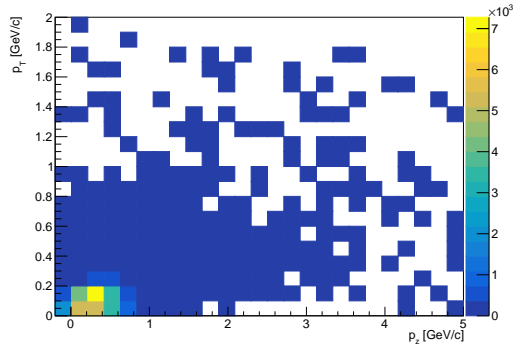
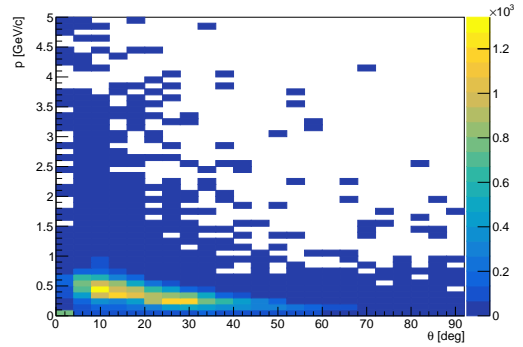


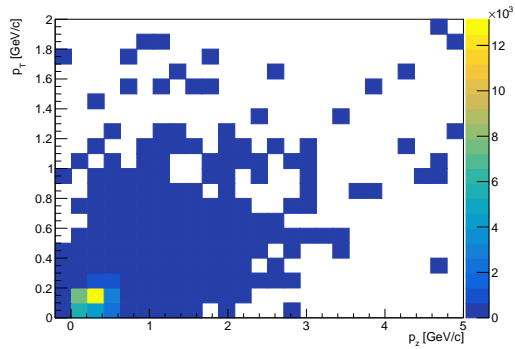
Figure B.26: Pull distributions for the $\pi^+(\Xi^+)$.



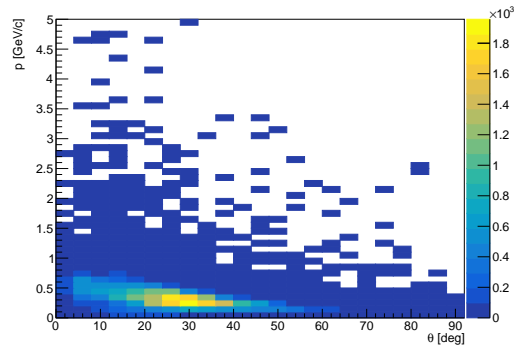
(a) Transverse vs. longitudinal momentum.



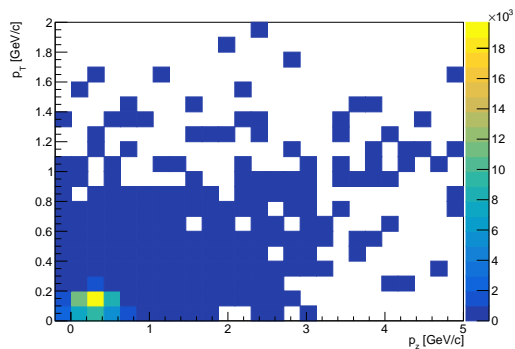
(b) Total momentum vs. polar angle.

Figure B.27: Distributions of p_T vs. p_z and p vs. θ for the $\pi^+(\Xi^+)$ found by the Standard track finder.

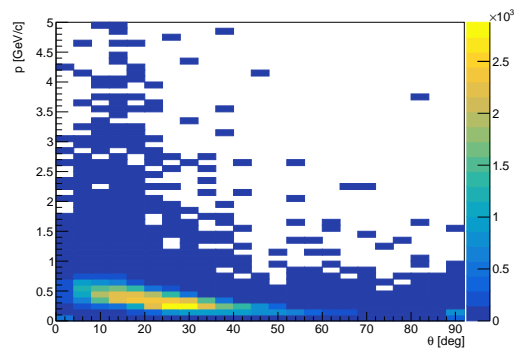
(a) Transverse vs. longitudinal momentum.



(b) Total momentum vs. polar angle.

Figure B.28: Distributions of p_T vs. p_z and p vs. θ for the $\pi^+(\Xi^+)$ found by the Hough track finder.

(a) Transverse vs. longitudinal momentum.



(b) Total momentum vs. polar angle.

Figure B.29: Distributions of p_T vs. p_z and p vs. θ for the $\pi^+(\Xi^+)$ found by the Standard plus Apollonius Triplet track finder.

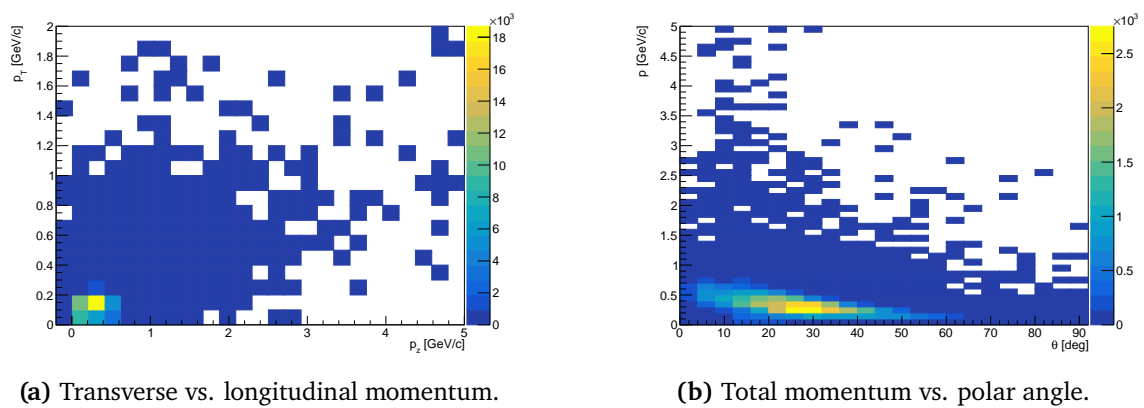


Figure B.30: Distributions of p_T vs. p_z and p vs. θ for the $\pi^+(\Xi^+)$ found by the Hough plus Apollonius Triplet track finder.

B.2 Λ Reconstruction

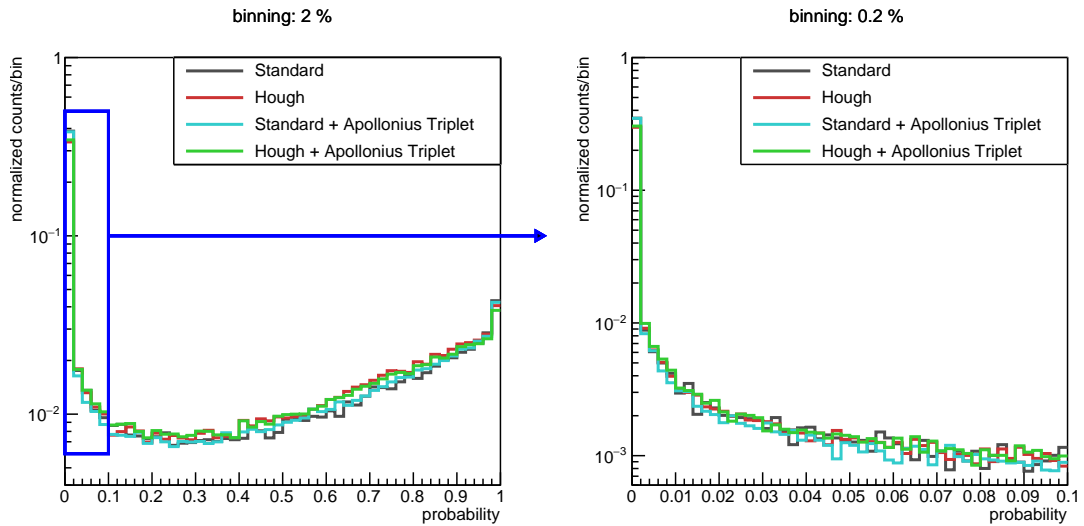


Figure B.31: Probability distribution for the vertex fit for the Λ candidates for various realistic track finders. A binning of 2% for probabilities in a range from 0 to 1 (left) and a finer binning of 0.2% in a range from 0 to 0.1.

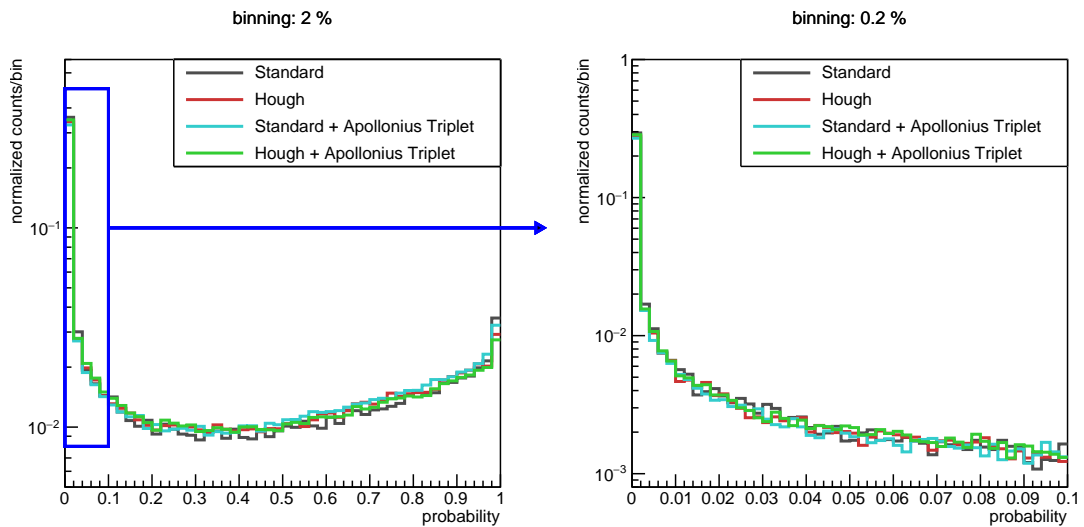


Figure B.32: Probability distribution for the mass constraint fit for the Λ candidates for various realistic track finders. A binning of 2% for probabilities in a range from 0 to 1 (left) and a finer binning of 0.2% in a range from 0 to 0.1.

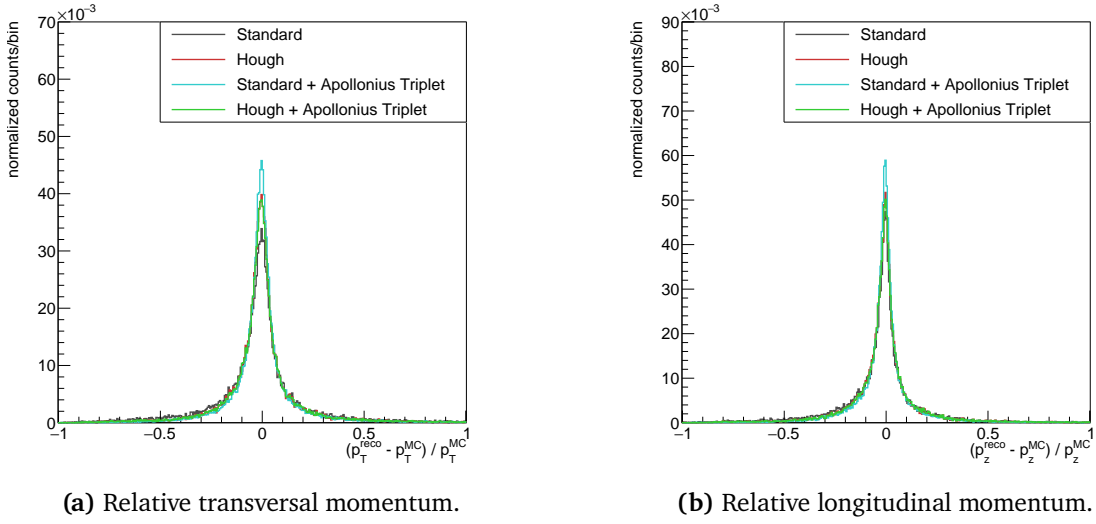


Figure B.33: Relative momentum distributions for the Λ for the different track finders.

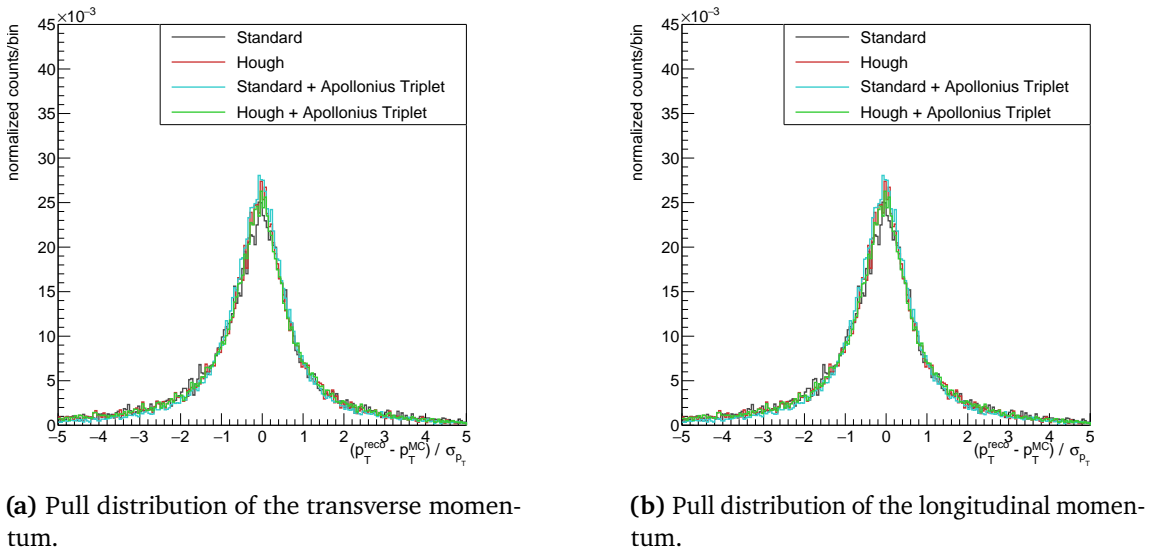


Figure B.34: Pull distributions for the Λ for the different track finders.

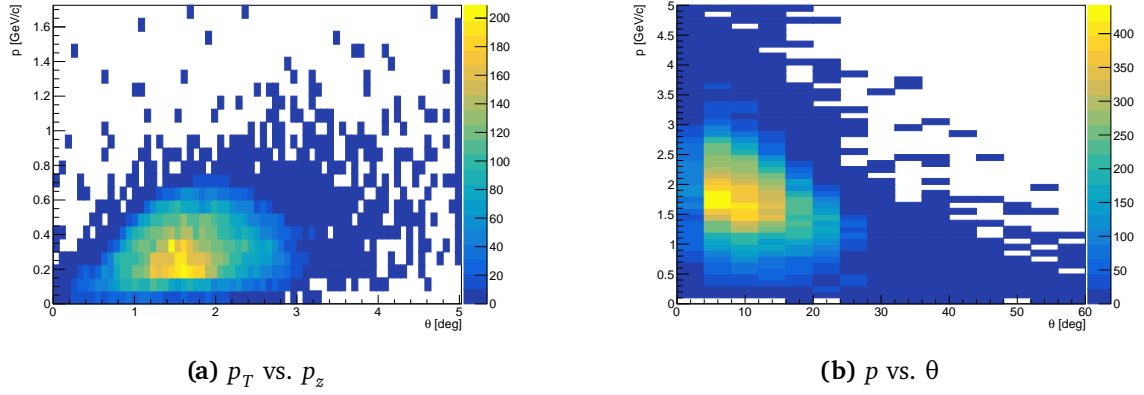


Figure B.35: Distributions of p_T vs. p_z and p vs. θ for the Λ using the Standard tracker.

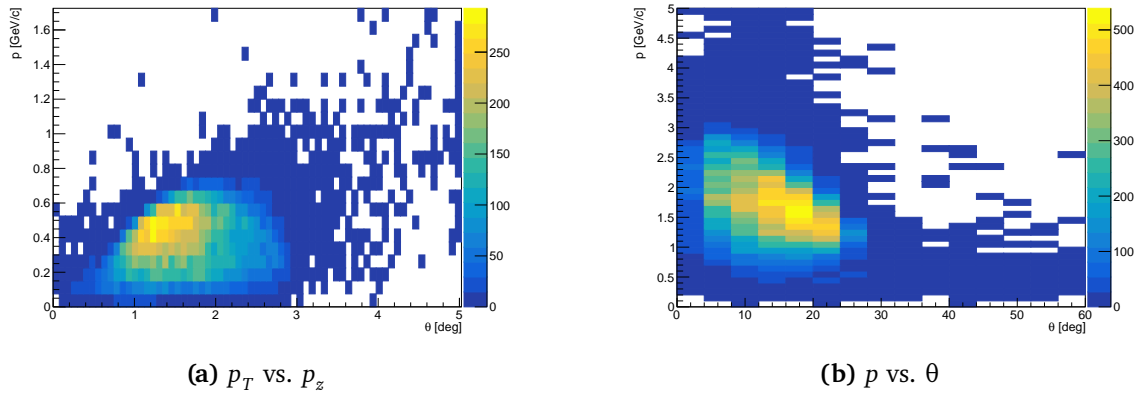


Figure B.36: Distributions of p_T vs. p_z and p vs. θ for the Λ using the Hough tracker.

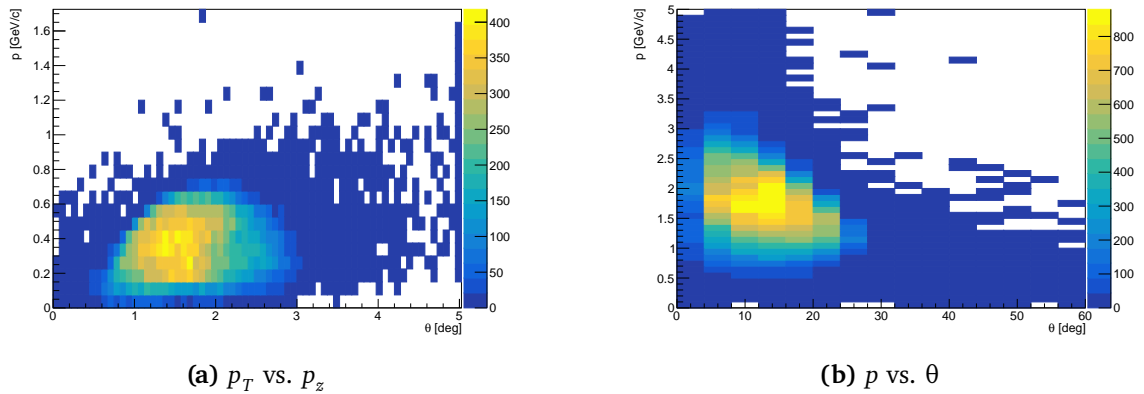


Figure B.37: Distributions of p_T vs. p_z and p vs. θ for the Λ using the Standard + Apollonius Triplet tracker.

B.3 $\bar{\Lambda}$ Reconstruction

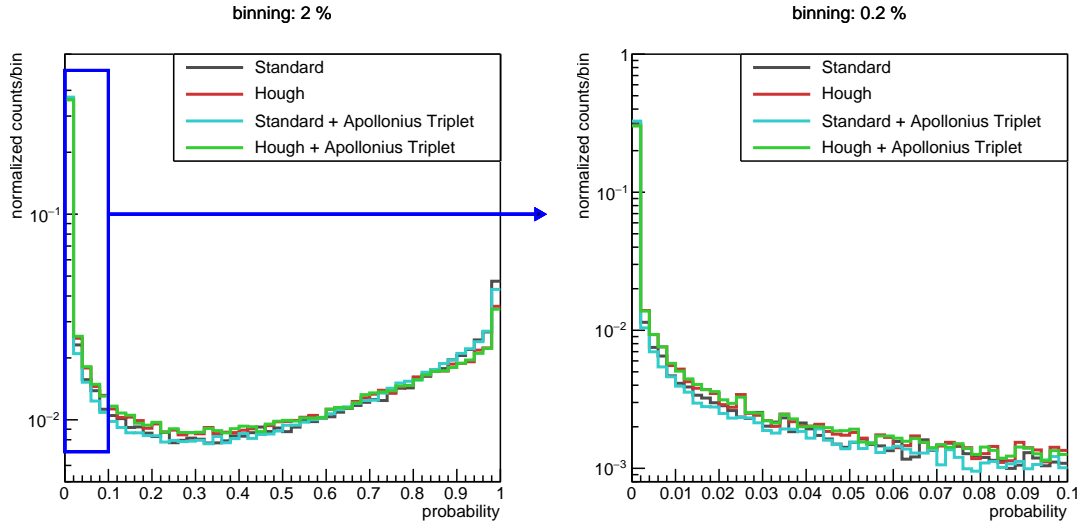


Figure B.38: Probability distribution for the vertex fit for the $\bar{\Lambda}$ candidates for various realistic track finders. A binning of 2% for probabilities in a range from 0 to 1 (left) and a finer binning of 0.2% in a range from 0 to 0.1.

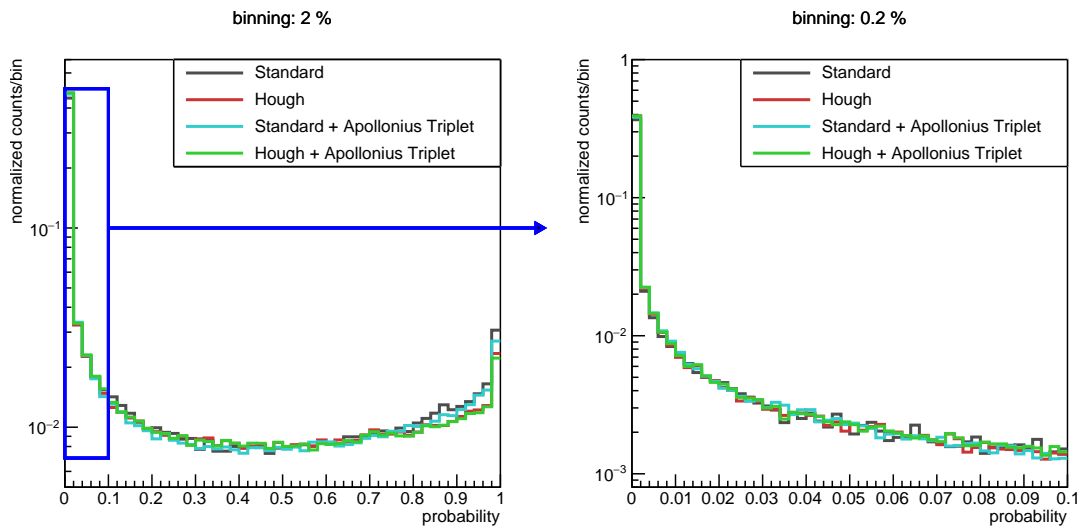


Figure B.39: Probability distribution for the mass constraint fit for the $\bar{\Lambda}$ candidates for various realistic track finders. A binning of 2% for probabilities in a range from 0 to 1 (left) and a finer binning of 0.2% in a range from 0 to 0.1.

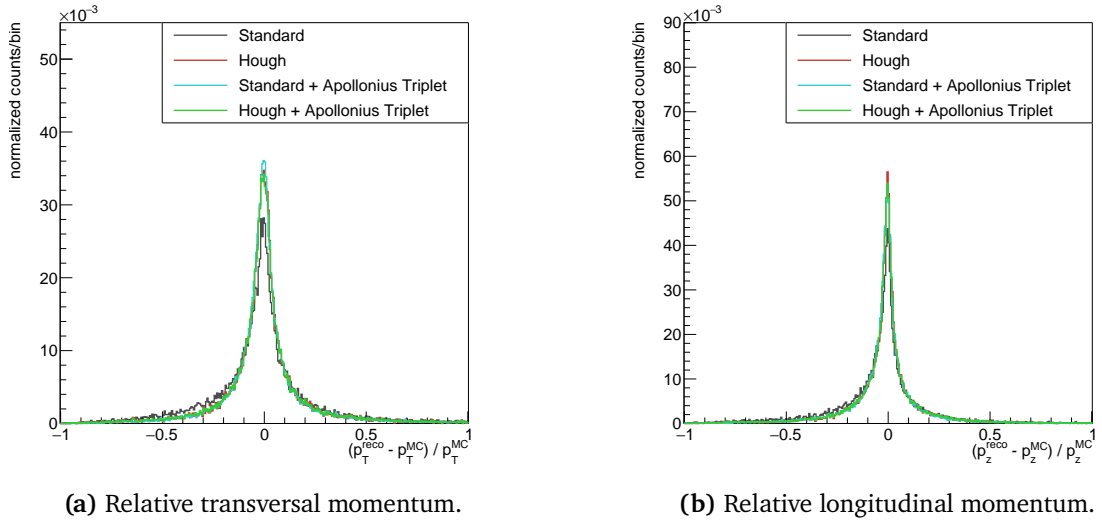


Figure B.40: Relative momentum distributions for the $\bar{\Lambda}$ for the different track finders.

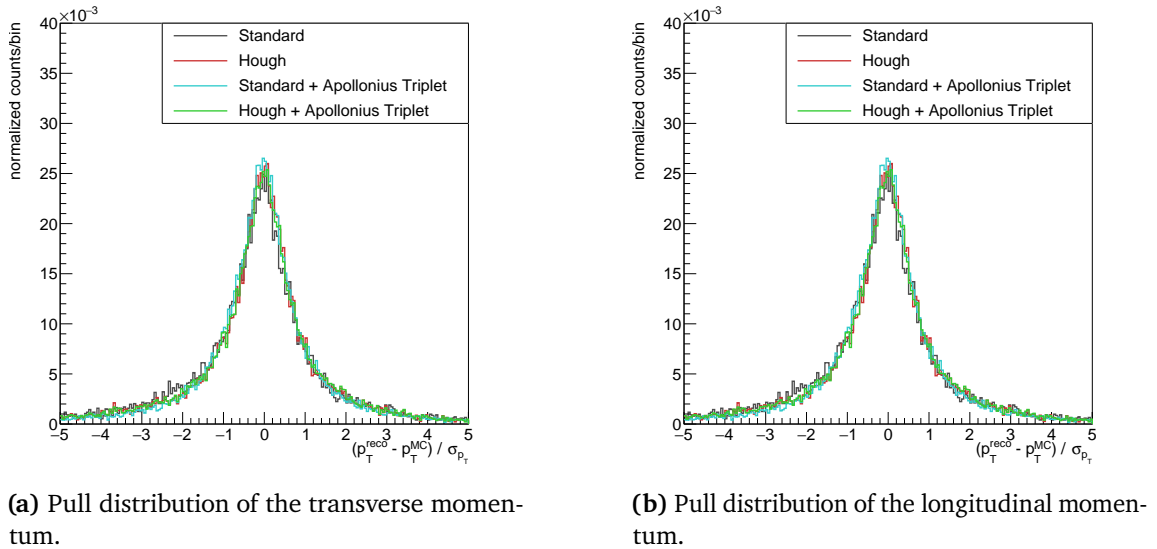
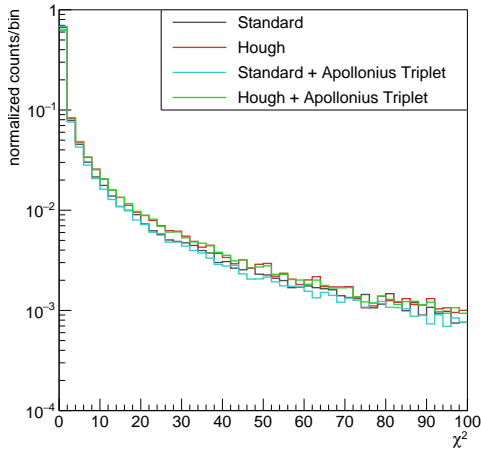
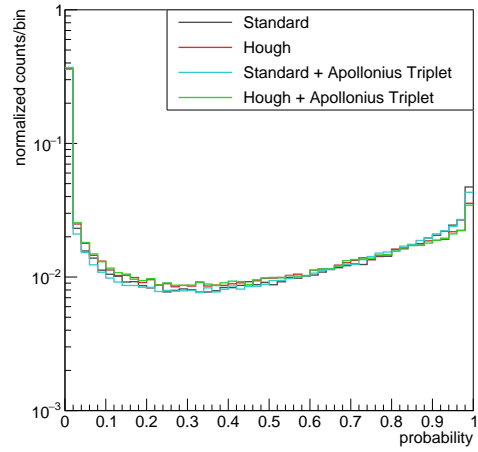


Figure B.41: Pull distributions for the $\bar{\Lambda}$ for the different track finders.

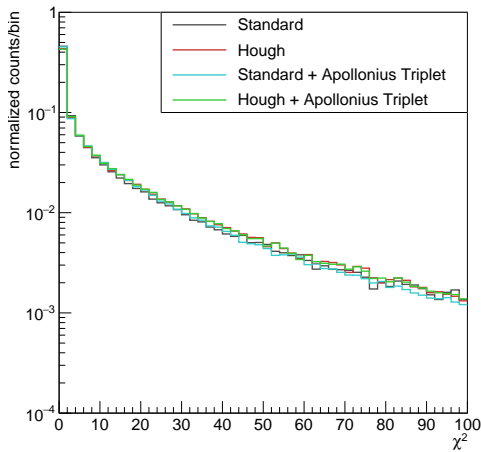


(a) χ^2 distribution for the $\bar{\Lambda}$ particle.

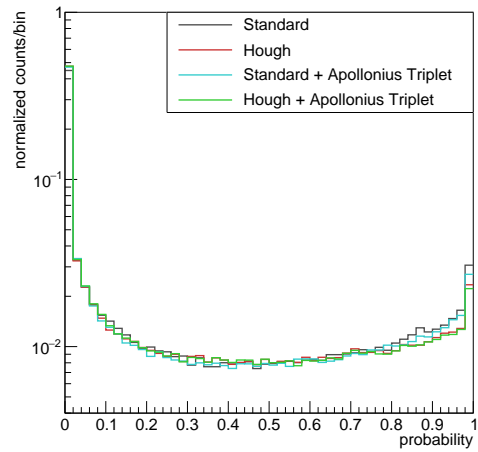


(b) Probability distribution for the $\bar{\Lambda}$ particle.

Figure B.42: χ^2 and probability distribution for the vertex fit for all realistic track finders.



(a) χ^2 distribution for the $\bar{\Lambda}$ particle.



(b) Probability distribution for the $\bar{\Lambda}$ particle.

Figure B.43: χ^2 and probability distribution for the mass constraint fit for all realistic track finders.

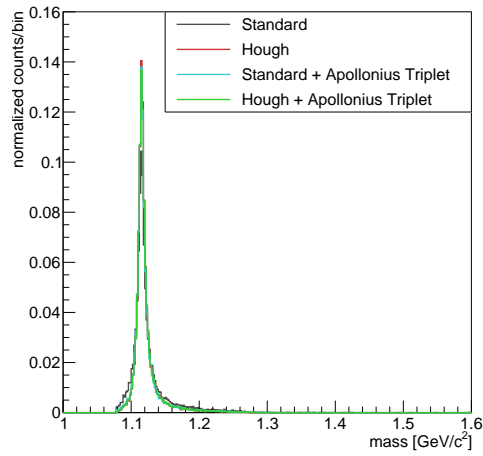


Figure B.44: Comparison of the mass distribution for the $\bar{\Lambda}$ for the different tracking algorithms.

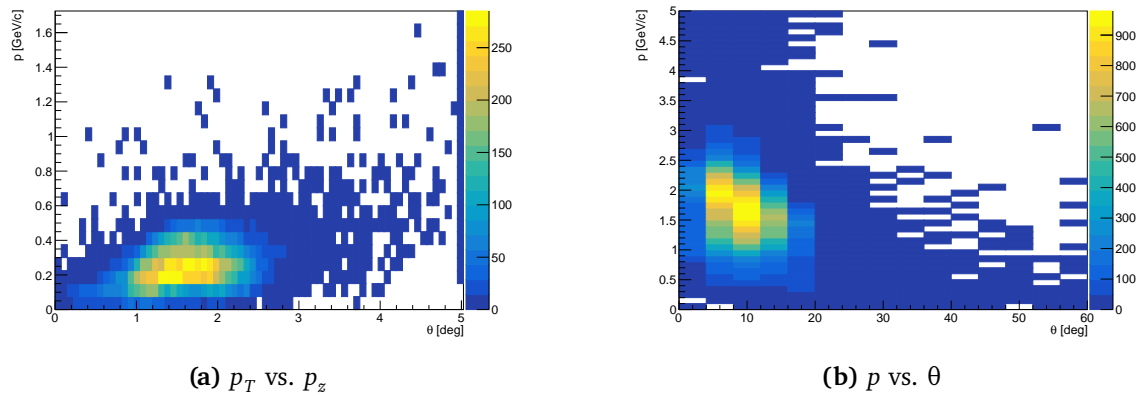


Figure B.45: Distributions of p_T vs. p_z and p vs. θ for the $\bar{\Lambda}$ using the Standard tracker.

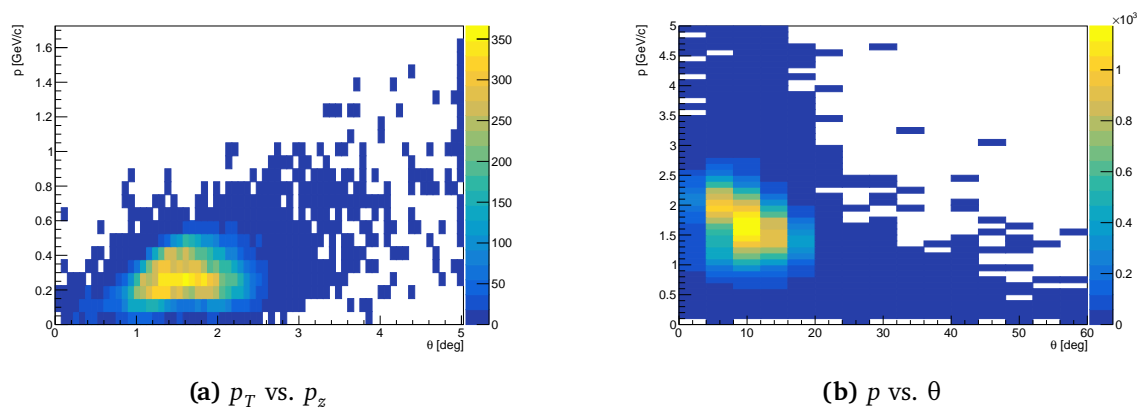


Figure B.46: Distributions of p_T vs. p_z and p vs. θ for the $\bar{\Lambda}$ using the Hough tracker.

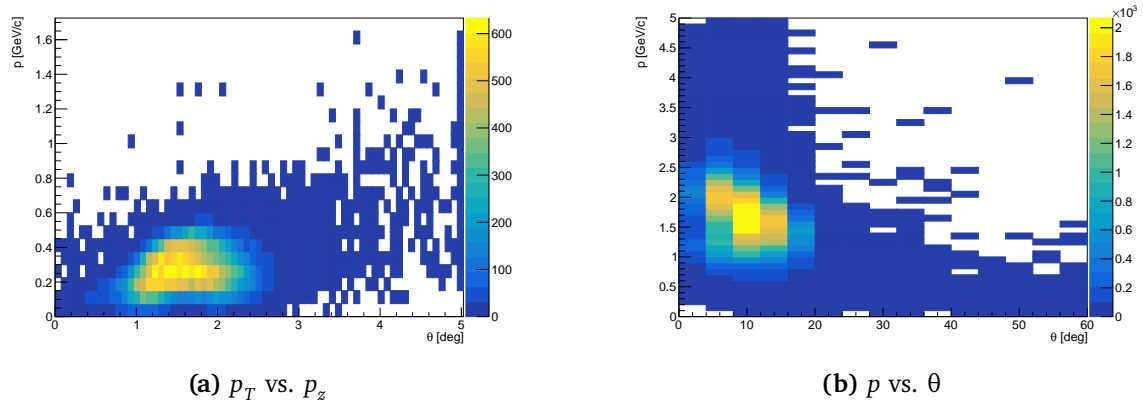


Figure B.47: Distributions of p_T vs. p_z and p vs. θ for the $\bar{\Lambda}$ using the Standard + Apollonius Triplet tracker.

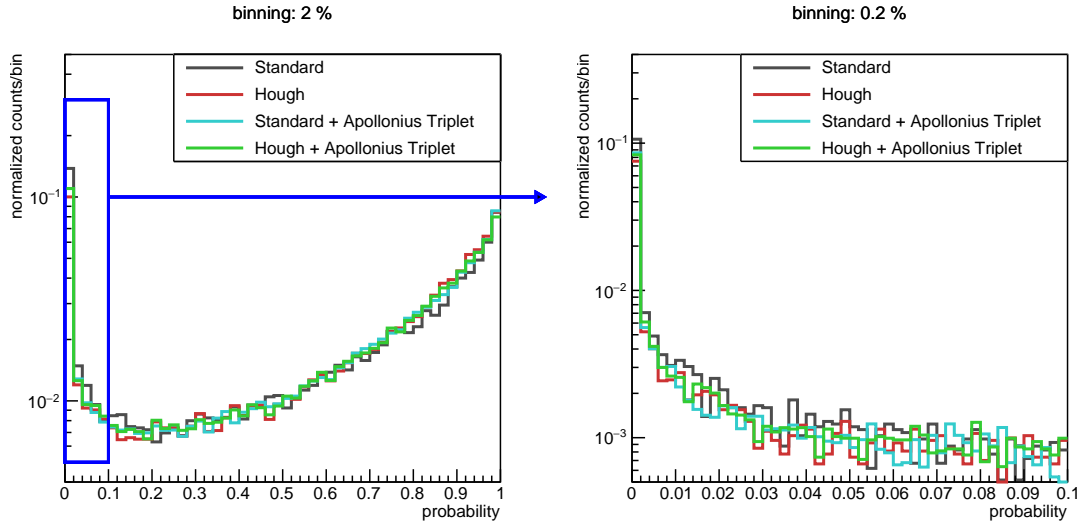
B.4 $\Xi(1820)^-$ Reconstruction

Figure B.48: Probability distribution for the vertex fit for the $\Xi(1820)^-$ candidates for various realistic track finders. A binning of 2% for probabilities in a range from 0 to 1 (left) and a finer binning of 0.2% in a range from 0 to 0.1.

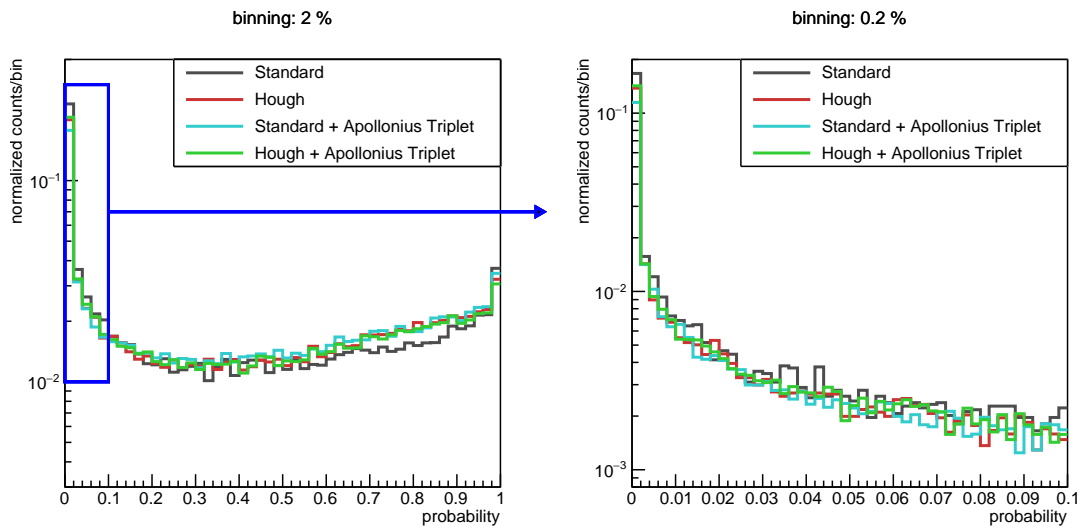


Figure B.49: Probability distribution for the mass constraint fit for the $\Xi(1820)^-$ candidates for various realistic track finders. A binning of 2% for probabilities in a range from 0 to 1 (left) and a finer binning of 0.2% in a range from 0 to 0.1.

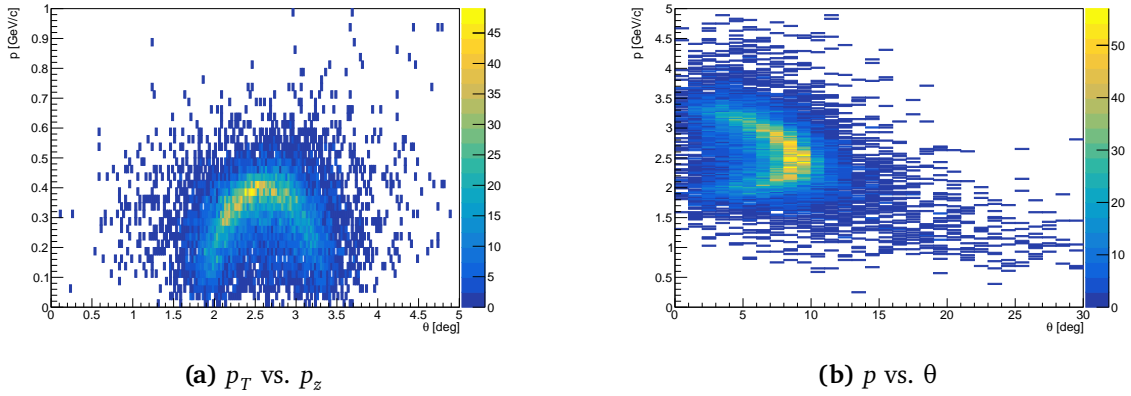


Figure B.50: Distributions of p_T vs. p_z and p vs. θ for the reconstructed $\Xi(1820)^-$ using the Standard tracker.

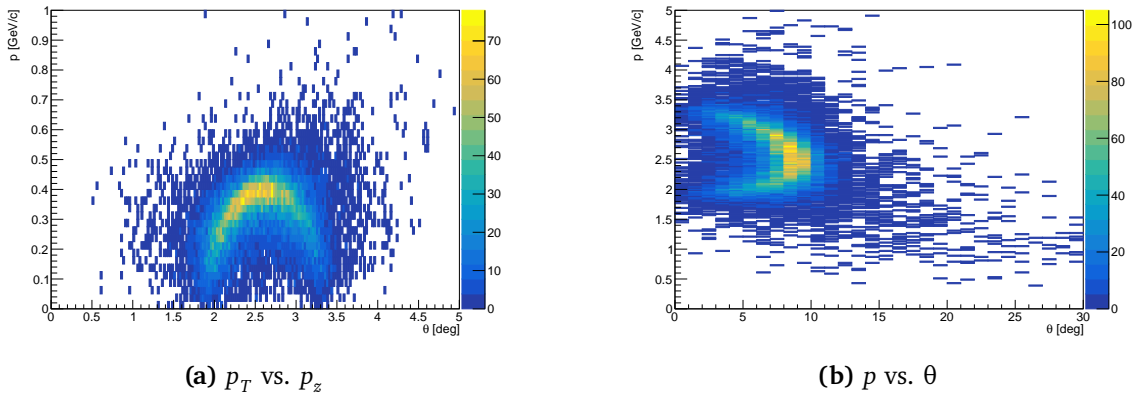


Figure B.51: Distributions of p_T vs. p_z and p vs. θ for the reconstructed $\Xi(1820)^-$ using the Hough tracker.

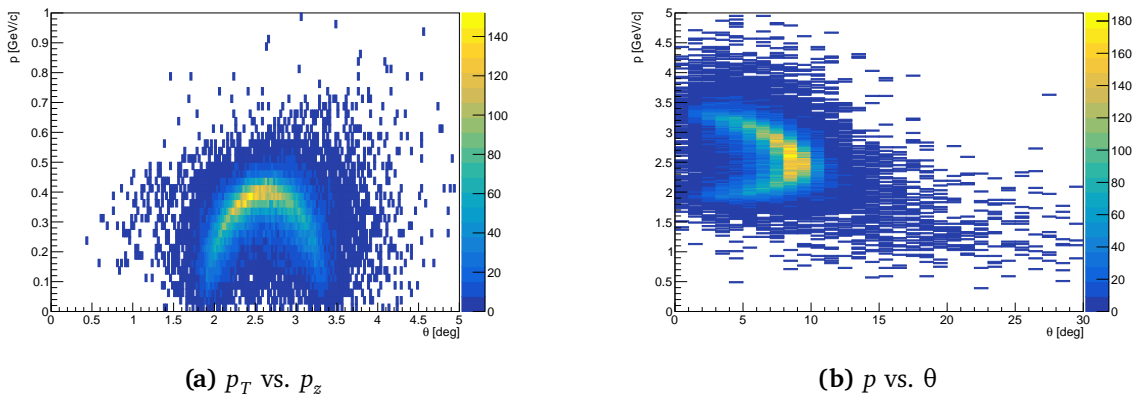


Figure B.52: Distributions of p_T vs. p_z and p vs. θ for the reconstructed $\Xi(1820)^-$ using the Standard + Apollonius Triplet tracker.

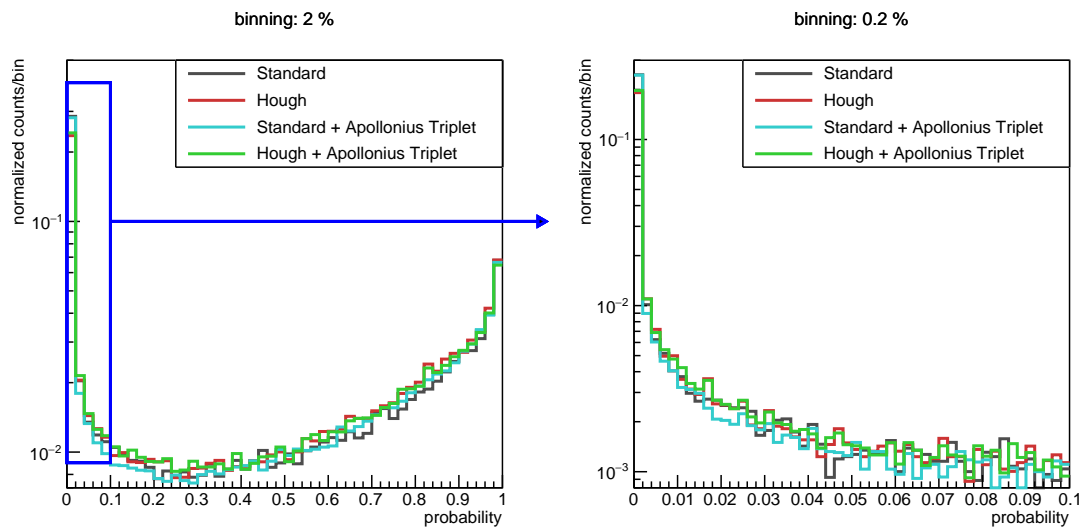
B.5 Ξ^+ Reconstruction

Figure B.53: Probability distribution for the vertex fit for the Ξ^+ candidates for various realistic track finders. A binning of 2% for probabilities in a range from 0 to 1 (left) and a finer binning of 0.2% in a range from 0 to 0.1.

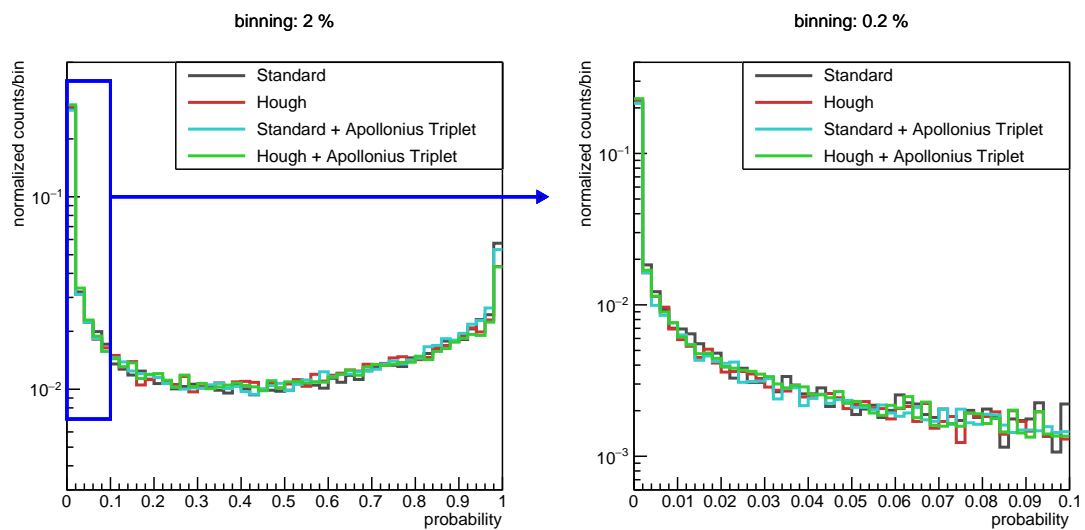
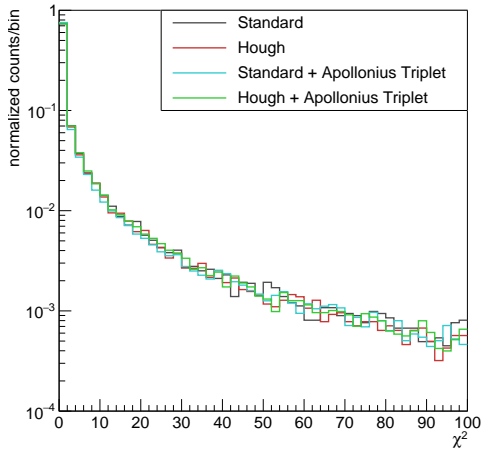
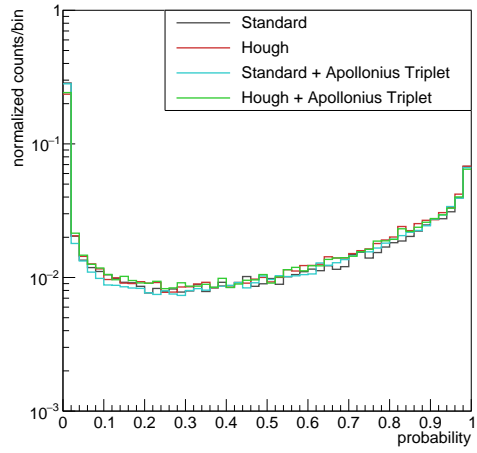


Figure B.54: Probability distribution for the mass constraint fit for the Ξ^+ candidates for various realistic track finders. A binning of 2% for probabilities in a range from 0 to 1 (left) and a finer binning of 0.2% in a range from 0 to 0.1.

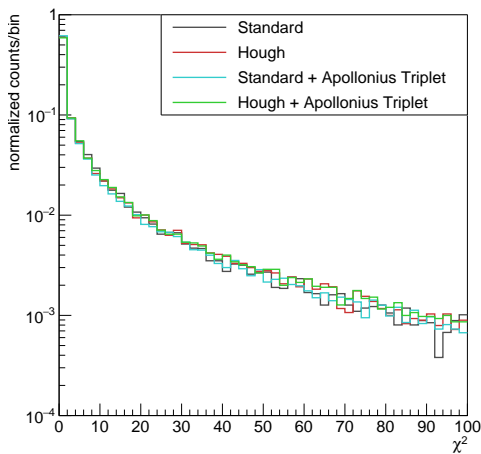


(a) χ^2 distribution of the vertex fit for the Ξ^+ resonance.

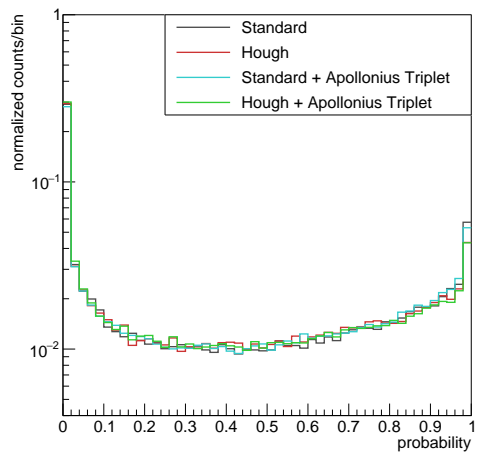


(b) Probability distribution of the vertex fit for the Ξ^+ resonance.

Figure B.55: χ^2 and probability distribution for the vertex fit for all track finders.



(a) χ^2 distribution of the mass constraint fit for the Ξ^+ resonance.



(b) Probability distribution of the mass constraint fit for the Ξ^+ resonance.

Figure B.56: χ^2 and probability distribution for the mass constraint fit for all track finders.

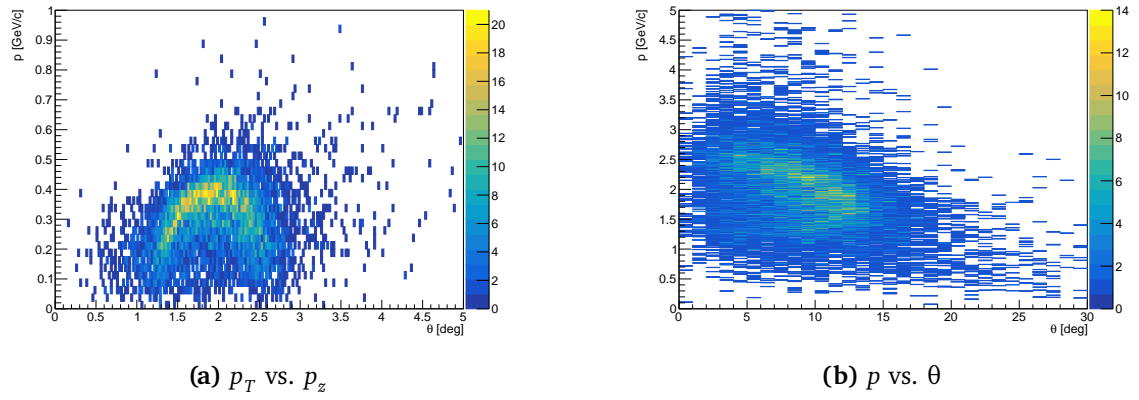


Figure B.57: Distributions of p_T vs. p_z and p vs. θ for the reconstructed Ξ^+ using the Standard tracker.

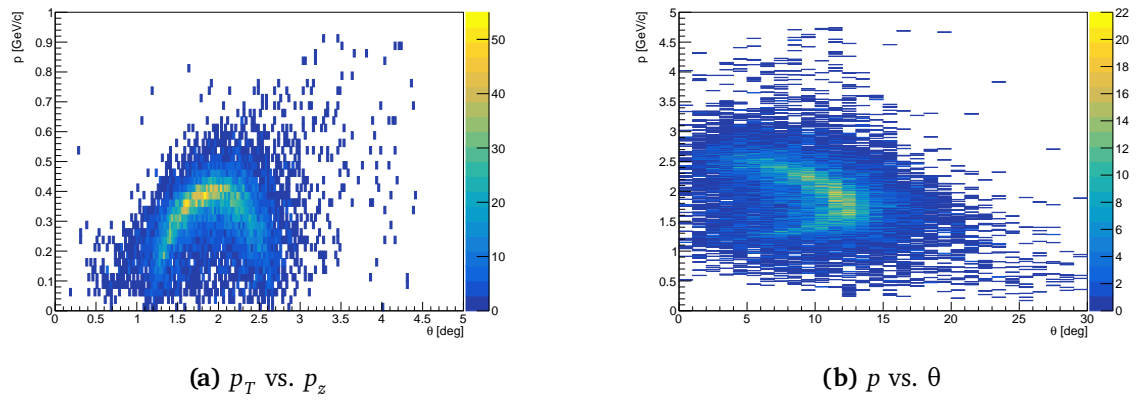


Figure B.58: Distributions of p_T vs. p_z and p vs. θ for the reconstructed Ξ^+ using the Hough tracker.

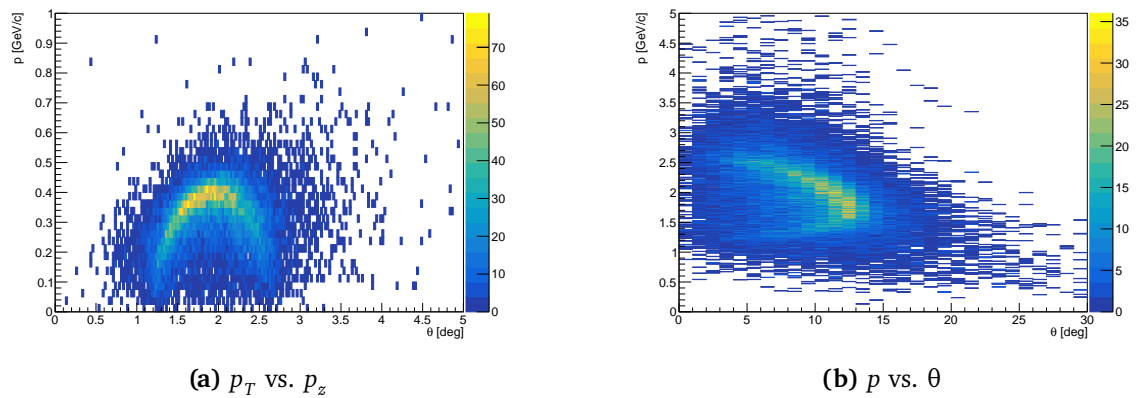


Figure B.59: Distributions of p_T vs. p_z and p vs. θ for the reconstructed Ξ^+ using the Standard + Apollonius Triplet tracker.

B.6 Full Event Reconstruction

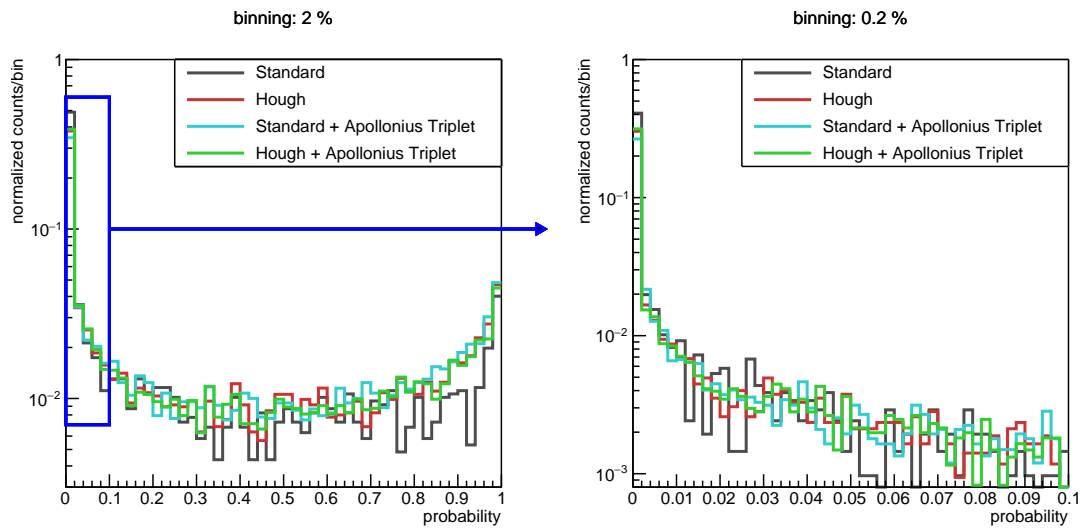
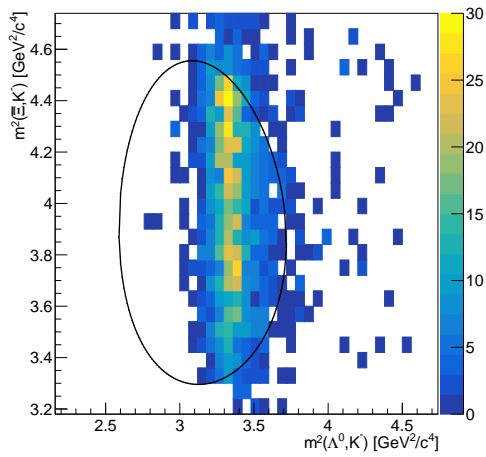
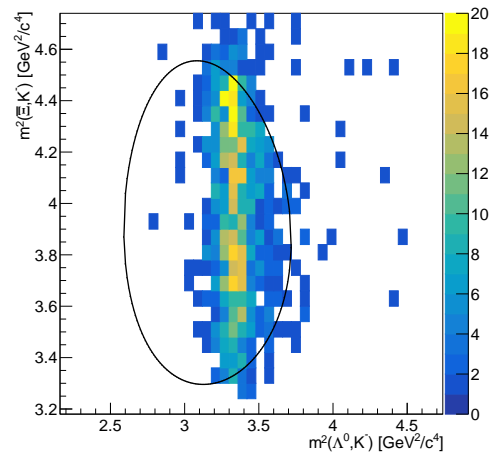


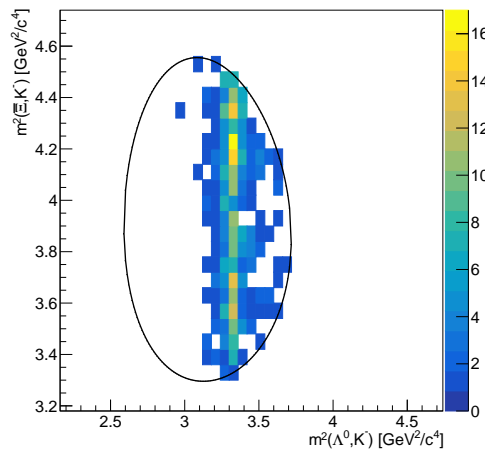
Figure B.60: Probability distribution for the kinematic fit with 4-momentum constraint for various realistic track finders. A binning of 2 % for probabilities in a range from 0 to 1 (left) and a finer binning of 0.2 % in a range from 0 to 0.1.



(a) All reconstructed events.

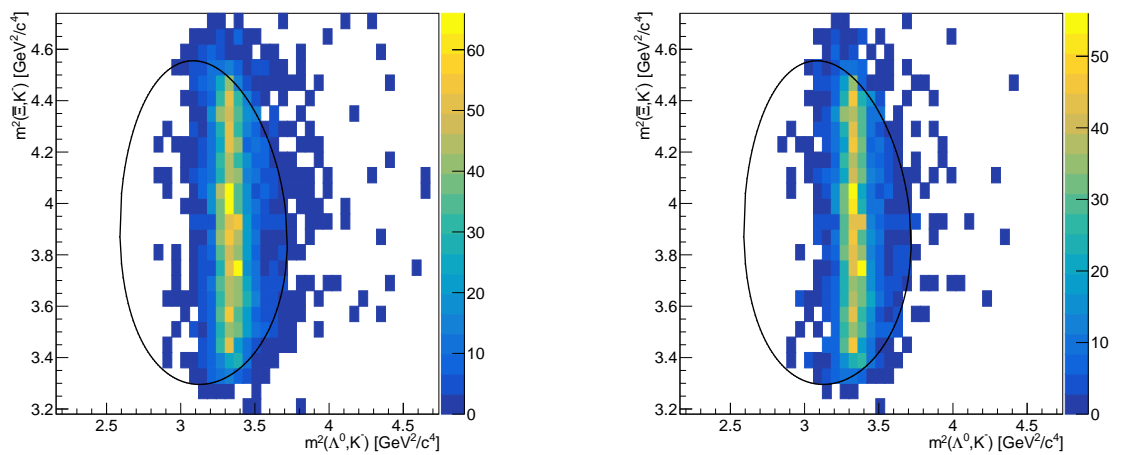


(b) All reconstructed events with MC-truth matching.



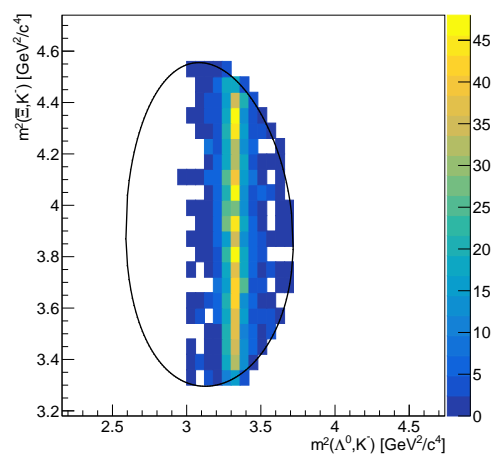
(c) All reconstructed events with MC-truth matching using the MC 4-momenta of the particles.

Figure B.61: Dalitz plot using the Standard tracker.



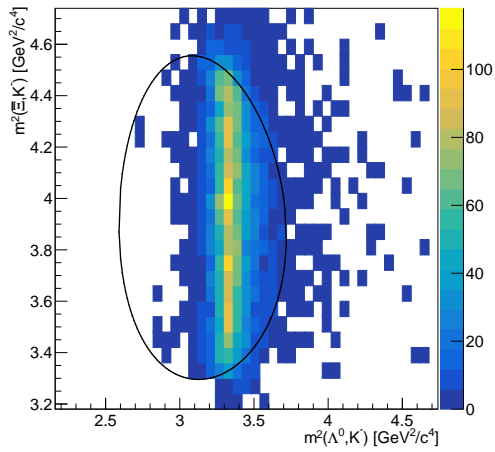
(a) All reconstructed events.

(b) All reconstructed events with MC-truth matching.

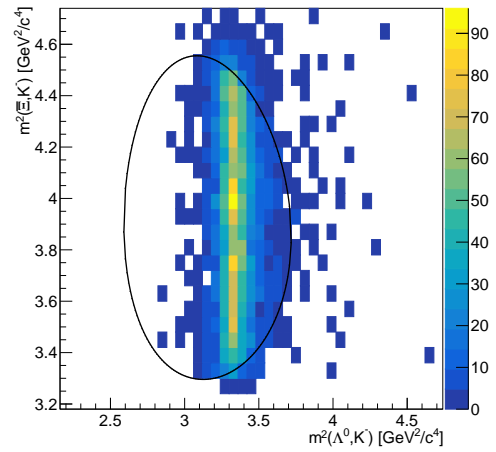


(c) All reconstructed events with MC-truth matching using the MC 4-momenta of the particles.

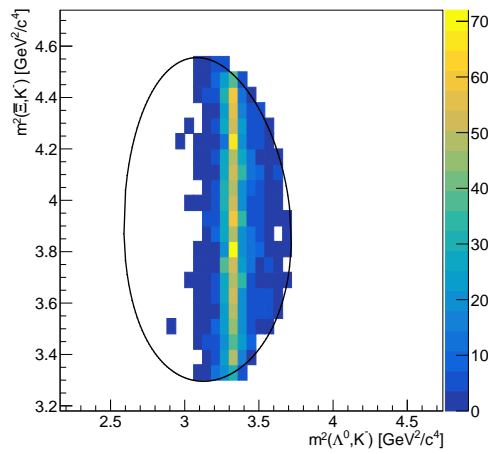
Figure B.62: Dalitz plot using the Hough tracker.



(a) All reconstructed events.



(b) All reconstructed events with MC-truth matching.



(c) All reconstructed events with MC-truth matching using the MC 4-momenta of the particles.

Figure B.63: Dalitz plot using the Standard + Apollonius Triplet tracker.

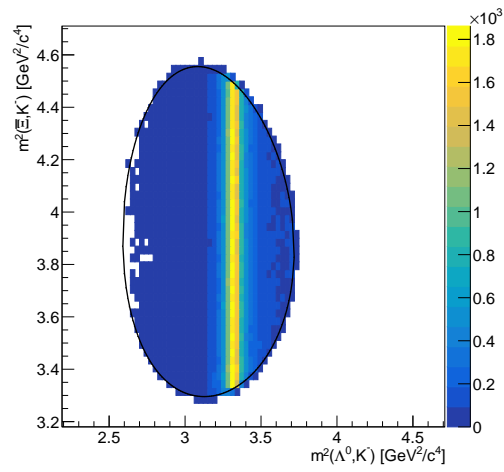


Figure B.64: MC generated Dalitz plot.

List of Figures

2.1	The Standard Model of Particle Physics.	6
2.2	Measurements of the strong coupling constant α_s as a function of the energy scale Q	11
2.3	Eightfold way for the mesonic states of the three lightest quarks.	12
2.4	Eightfold way for the baryonic states of the three lightest quarks.	13
2.5	Resonances for the lowest levels of Λ , Σ , Ξ and Ω	14
2.6	Full reaction chain $p\bar{p} \rightarrow \Xi^- \Xi^+$ studied in this thesis.	15
3.1	The Facility of Antiproton and Ion Research in Darmstadt (FAIR).	18
3.2	The High Energy Storage Ring HESR.	20
3.3	The research topics accessible with PANDA.	22
3.4	A comparison of theoretically determined charmonium excitations and measured data.	23
3.5	Schematic overview of the PANDA detector with labeled subdetectors.	26
3.6	The magnets of the PANDA detector [75].	28
3.7	Conceptual sketch of the Micro Vertex Detector (MVD).	30
3.8	Geometry of the different silicon sensors installed in the MVD.	31
3.9	A detailed view of the MVD showing the location of the different silicon sensors.	31
3.10	Half-section view of the basic structure of the Straw Tube Tracker.	32
3.11	Pictures of the STT construction.	33
3.12	Working principle of a single straw tube.	34
3.13	Drift time spectrum and calibration curve of a straw tube [84].	34
3.14	Structure of the GEM detector.	35
3.15	Picture of a GEM foil with high hole density and principle of a GEM foil.	36
3.16	Schematic illustration of a double layer of the FTS.	37
3.17	Design of the Time-of-Flight (ToF) detectors.	38
3.18	Schematic illustration of the Barrel DIRC detector.	39
3.19	Design of the Barrel DIRC detector.	40
3.20	Design of a quadrant of the disc DIRC.	41
3.21	Schematic Illustration of the Forward RICH detector.	41
3.22	Schematic images of the Electromagnetic Calorimeters.	43
3.23	The data acquisition chain of PANDA.	45
3.24	Simulation and analysis chain in PandaRoot.	47
4.1	A particle track passing the MVD, the STT and the GEM detector.	54
4.2	Working principle of the Cellular Automaton (CA).	61

4.3	Working principle of a linear Hough transformation for two points of a line.	62
4.4	Linear Hough transformation to find four lines in an image with noisy background.	63
4.5	The Problem of Apollonius for two circles and a point (CCP) on the left, and three circles (CCC) on the right.	64
4.6	The Hough space for a particle track in the x-y-plane.	66
4.7	The centers of the Apollonius circles are on two hyperbolas.	66
4.8	Hough transformation based on the Apollonius problem for one primary particle.	67
4.9	Efficiency as a function of the transverse momentum p_T for one track per event.	67
4.10	An example event of a primary track visualized in blue that was not found. The reason is, that the primary track decays into a secondary track shown in red with about the same momentum. Therefore the primary is defined as a ghost because too many hits of the daughter particle are included.	67
4.11	Hough transformation for an event with six tracks.	68
4.12	Preselection method by dividing the x-y projection of the detector hits into segments based on a φ histogram. Picture based on [122].	70
4.13	Example event for the merging procedure.	71
4.14	Optimization function for the merging procedure.	72
4.15	Tracks and Hough space for an example event as in Fig. 4.11.	72
4.16	Quality parameters versus the minimum number of hits required for a track to be considered within the fiducial volume.	73
4.17	Momentum distributions for primary and secondary tracks.	74
4.18	Momentum distributions for the different particle species.	75
4.19	Quality parameters for a simulated data sample of background events generated with the FTF generator at a beam momentum of 7 GeV/c.	76
4.20	Transverse momentum distributions for Standard, Hough and ideal track finder.	76
4.21	Finding rate vs. p_T for primary and secondary tracks.	77
4.22	Transverse momentum resolution for primary and secondary particles.	78
4.23	Relative transverse momentum resolution for primary and secondary particles.	78
4.24	Architecture of a CPU and a GPU.	80
4.25	Acceleration factor of the Apollonius calculation.	82
4.26	Acceleration factor of the Hough track finder with only Apollonius calculation on the GPU.	83
4.27	Acceleration factor of the Hough track finder on the GPU.	84
4.28	Illustration of the working principle of the Apollonius Triplet track finder.	86
4.29	Layer structure used for the Apollonius Triplet track finder.	87
4.30	Example of an event with a strongly curved, low momentum muon track.	88
4.31	Quality parameters of the Standard, Hough and the Apollonius Triplet track finder	90
4.32	Secondary tracks found by the Hough vs. Apollonius Triplet track finder.	91
4.33	Illustration of the distance of Point of Closest Approach (dPCA).	91
4.34	<i>Completeness</i> and momentum resolution for all secondary tracks with a dPCA > 3 cm.	92
4.35	Difference between number of MC generated hits minus the number of found hits vs. the MC generated number of hits in a track.	93
4.36	Relative reconstructed transverse momentum vs. generated transverse momentum for all found secondary particles.	93
4.37	Quality parameters of all investigated algorithms and combinations.	94
4.38	Transverse momentum resolution for primary and secondary particles.	95

4.39	Relative transverse momentum resolution for primary and secondary particles. . . .	96
5.1	Reaction chain of $p\bar{p} \rightarrow \Xi(1820)^-\Xi^+$	98
5.2	Momentum distribution of the six final state particles.	99
5.3	Angular distribution of the six final state particles.	100
5.4	Comparison of the relative momentum distributions for tracks with and without applying the Kalman filter.	102
5.5	Pull distributions for π^- originating from Λ	105
5.6	p_T vs. p_z and p vs. θ for proton for Hough + Apollonius Triplet tracker.	106
5.7	p_T vs. p_z and p vs. θ for π^- for Hough + Apollonius Triplet tracker.	107
5.8	χ^2 and probability distribution for the vertex fit.	108
5.9	χ^2 and probability distribution for the mass constraint fit.	109
5.10	Comparison of the mass distribution of Λ -candidates.	110
5.11	MC generated distributions of p_T vs. p_z and p vs. θ for Λ	112
5.12	p_T vs. p_z and p vs. θ for Λ for the Hough + Apollonius Triplet tracker.	112
5.13	MC generated distributions of p_T vs. p_z and p vs. θ for $\bar{\Lambda}$	112
5.14	p_T vs. p_z and p vs. θ for $\bar{\Lambda}$ for the Hough + Apollonius Triplet tracker.	113
5.15	χ^2 and probability distributions for the vertex fit for $\Xi(1820)$	113
5.16	χ^2 and probability distribution for the mass constraint fit for $\Xi(1820)$	114
5.17	Mass distribution for the reconstructed Ξ^+ and Ξ^- for the different track finders.	115
5.18	MC generated distributions of p_T vs. p_z (a) and p vs. θ (b) for $\Xi(1820)^-$	116
5.19	p_T vs. p_z and p vs. θ for $\Xi(1820)^-$ for the Hough + Apollonius Triplet tracker.	117
5.20	Fit results for the kinematic fit with 4-momentum constraint.	117
5.21	Dalitz plot for the Hough + Apollonius Triplet tracker. The black curve indicates the kinematically allowed region.	119
B.1	Relative momentum distributions for the proton.	140
B.2	Pull distributions for the proton.	141
B.3	p_T vs. p_z and p vs. θ for the proton (Standard tracker).	141
B.4	p_T vs. p_z and p vs. θ for the proton (Hough tracker).	141
B.5	p_T vs. p_z and p vs. θ for the proton (Standard + Apollonius Triplet tracker).	142
B.6	p_T vs. p_z and p vs. θ for the proton (Hough + Apollonius Triplet tracker).	142
B.7	Relative momentum distributions for the K^-	143
B.8	Pull distributions for the K^-	143
B.9	p_T vs. p_z and p vs. θ for the K^- (Standard tracker).	144
B.10	p_T vs. p_z and p vs. θ for the K^- (Hough tracker).	144
B.11	p_T vs. p_z and p vs. θ for the K^- (Standard + Apollonius Triplet tracker).	144
B.12	p_T vs. p_z and p vs. θ for the K^- (Hough + Apollonius Triplet tracker).	145
B.13	Relative momentum distributions for the \bar{p}	146
B.14	Pull distributions for the \bar{p}	146
B.15	p_T vs. p_z and p vs. θ for the \bar{p} (Standard tracker)	147
B.16	p_T vs. p_z and p vs. θ for the \bar{p} (Hough tracker)	147
B.17	p_T vs. p_z and p vs. θ for the \bar{p} (Standard + Apollonius Triplet tracker)	147
B.18	p_T vs. p_z and p vs. θ for the \bar{p} (Hough + Apollonius Triplet tracker)	148
B.19	Relative momentum distributions for the π^+	149
B.20	Pull distributions for the π^+	149

B.21	p_T vs. p_z and p vs. θ for the π^+ (Standard tracker)	150
B.22	p_T vs. p_z and p vs. θ for the π^+ (Hough tracker)	150
B.23	p_T vs. p_z and p vs. θ for the π^+ (Standard + Apollonius Triplet tracker)	150
B.24	p_T vs. p_z and p vs. θ for the π^+ (Hough + Apollonius Triplet tracker)	151
B.25	Relative momentum distributions for the $\pi^+(\Xi^+)$.	152
B.26	Pull distributions for the $\pi^+(\Xi^+)$.	152
B.27	p_T vs. p_z and p vs. θ for the $\pi^+(\Xi^+)$ (Standard tracker).	153
B.28	p_T vs. p_z and p vs. θ for the $\pi^+(\Xi^+)$ (Hough tracker).	153
B.29	p_T vs. p_z and p vs. θ for the $\pi^+(\Xi^+)$ (Standard + Apollonius Triplet tracker).	153
B.30	p_T vs. p_z and p vs. θ for the $\pi^+(\Xi^+)$ (Hough + Apollonius Triplet tracker).	154
B.31	Probability distribution for the vertex fit for the Λ candidates for various realistic track finders. A binning of 2% for probabilities in a range from 0 to 1 (left) and a finer binning of 0.2% in a range from 0 to 0.1.	155
B.32	Probability distribution for the mass constraint fit for the Λ candidates for various realistic track finders. A binning of 2% for probabilities in a range from 0 to 1 (left) and a finer binning of 0.2% in a range from 0 to 0.1.	155
B.33	Relative momentum distributions for the Λ for the different track finders.	156
B.34	Pull distributions for the Λ for the different track finders.	156
B.35	p_T vs. p_z and p vs. θ for the Λ (Standard tracker).	157
B.36	p_T vs. p_z and p vs. θ for the Λ (Hough tracker).	157
B.37	p_T vs. p_z and p vs. θ for the Λ (Standard + Apollonius Triplet tracker).	157
B.38	Probability distribution for the vertex fit for the $\bar{\Lambda}$ candidates for various realistic track finders. A binning of 2% for probabilities in a range from 0 to 1 (left) and a finer binning of 0.2% in a range from 0 to 0.1.	158
B.39	Probability distribution for the mass constraint fit for the $\bar{\Lambda}$ candidates for various realistic track finders. A binning of 2% for probabilities in a range from 0 to 1 (left) and a finer binning of 0.2% in a range from 0 to 0.1.	158
B.40	Relative momentum distributions for the $\bar{\Lambda}$ for the different track finders.	159
B.41	Pull distributions for the $\bar{\Lambda}$ for the different track finders.	159
B.42	χ^2 and probability distribution for the vertex fit for the $\bar{\Lambda}$.	160
B.43	χ^2 and probability distribution for the mass constraint fit for the $\bar{\Lambda}$.	160
B.44	Comparison of the mass distribution for the $\bar{\Lambda}$.	161
B.45	p_T vs. p_z and p vs. θ for the $\bar{\Lambda}$ (Standard tracker).	161
B.46	p_T vs. p_z and p vs. θ for the $\bar{\Lambda}$ (Hough tracker).	161
B.47	p_T vs. p_z and p vs. θ for the $\bar{\Lambda}$ (Standard + Apollonius Triplet tracker).	162
B.48	Probability distribution for the vertex fit for the $\Xi(1820)^-$ candidates for various realistic track finders. A binning of 2% for probabilities in a range from 0 to 1 (left) and a finer binning of 0.2% in a range from 0 to 0.1.	163
B.49	Probability distribution for the mass constraint fit for the $\Xi(1820)^-$ candidates for various realistic track finders. A binning of 2% for probabilities in a range from 0 to 1 (left) and a finer binning of 0.2% in a range from 0 to 0.1.	163
B.50	p_T vs. p_z and p vs. θ for the $\Xi(1820)^-$ (Standard tracker).	164
B.51	p_T vs. p_z and p vs. θ for the $\Xi(1820)^-$ (Hough tracker).	164
B.52	p_T vs. p_z and p vs. θ for the $\Xi(1820)^-$ (Standard + Apollonius Triplet tracker).	164

B.53	Probability distribution for the vertex fit for the Ξ^+ candidates for various realistic track finders. A binning of 2% for probabilities in a range from 0 to 1 (left) and a finer binning of 0.2% in a range from 0 to 0.1.	165
B.54	Probability distribution for the mass constraint fit for the Ξ^+ candidates for various realistic track finders. A binning of 2% for probabilities in a range from 0 to 1 (left) and a finer binning of 0.2% in a range from 0 to 0.1.	165
B.55	χ^2 and probability distribution for the vertex fit for the Ξ^+	166
B.56	χ^2 and probability distribution for the mass constraint fit for the Ξ^+	166
B.57	p_T vs. p_z and p vs. θ for the Ξ^+ (Standard tracker).	167
B.58	p_T vs. p_z and p vs. θ for the Ξ^+ (Hough tracker).	167
B.59	p_T vs. p_z and p vs. θ for the Ξ^+ (Standard + Apollonius Triplet tracker).	167
B.60	Probability distribution for the kinematic fit with 4-momentum constraint for various realistic track finders. A binning of 2% for probabilities in a range from 0 to 1 (left) and a finer binning of 0.2% in a range from 0 to 0.1.	168
B.61	Dalitz plot using the Standard tracker.	169
B.62	Dalitz plot using the Hough tracker.	170
B.63	Dalitz plot using the Standard + Apollonius Triplet tracker.	171
B.64	MC generated Dalitz plot.	172

List of Tables

2.1	Ξ resonances.	15
4.1	Summary of the distribution of generated particles in the data sample.	74
4.2	Summary of the FWHM and the RMS for the transverse momentum resolutions.	79
4.3	Properties of the GPU NVIDIA GeForce RTX 2060.	81
4.4	Summary of the FWHM and the RMS for the transverse momentum resolution for primary tracks.	96
4.5	Summary of the FWHM and the RMS for the transverse momentum resolution for secondary tracks.	96
5.1	Fraction of final state particles within the fiducial volume.	99
5.2	Fraction of the final state particles found by the ideal forward tracker.	101
5.3	Summary of the FWHM for the momentum resolutions with and without the Kalman filter.	103
5.4	ϵ_{Reco} (in %) of the final state particles before and after the Kalman filter.	104
5.5	Fraction (in %) of clone tracks for all final state particles.	105
5.6	FWHM and RMS for the pull distribution of p_T of all final state particles.	106
5.7	FWHM and RMS for the pull distribution of p_z of all final state particles.	106
5.8	Comparison of the rate to find all final state particles for events in which all final state particles are within the fiducial volume.	107
5.9	ϵ_{Reco} (MC-truth matched) and purity for Λ and $\bar{\Lambda}$	111
5.10	FWHM and RMS for the Λ and $\bar{\Lambda}$ mass.	111
5.11	ϵ_{Reco} (MC-truth matched) and purity and clone rate for $\Xi(1820)^-$ and Ξ^+	115
5.12	FWHM and RMS for the $\Xi(1820)^-$ and Ξ^+ mass.	116
5.13	ϵ_{Reco} (MC-truth matched) and purity for the full event reconstruction $\Xi^+\Xi(1820)^-$	118
5.14	Expected number of $\Xi^+\Xi(1820)^-$ events per day of data taking for the different track finding algorithms and the days of data taking needed for a reasonable partial wave analysis.	120
6.1	Efficiencies for the different track finders investigated in this thesis.	122
B.1	FWHM and RMS for the relative transversal momentum resolution of all final state particles.	139
B.2	FWHM and RMS for the relative longitudinal momentum resolution of all final state particles.	140

Acknowledgements

At this point I would like to thank everyone who made this work possible.

First, I thank my supervisor James Ritman for the interesting topic and the position at his institute. Jim, thank you for your valuable input and good and helpful guidance and support during the time of my PhD.

Another special thanks goes to Tobias Stockmanns, who was always there to help me with any questions I had about my daily work. The fact that you were right next door in the office made a lot of things easier and made it easier for me to get started with the topic as well as to find my way into the institute life. Even in Corona times, when we all worked in our home offices, you were always available and supported me with helpful answers and goal-oriented ideas.

I thank my colleagues, for the warm welcome in the IKP. In particular, I thank the other PhD students: Jenny, Gabi, Jakapt, Ashish, and Waleed, for making the last years as great as they were.

I would also like to thank the rest of my colleagues: Huagen, Jong, Frank, Peter, Rene, Artur and everybody I might have forgotten to mention. You were a great team in which I felt directly in good hands.

I would also like to thank the PandaRoot developers, especially Ralf and Jenny. The discussions with you about the further development of PandaRoot in C++ , about tracking and the physical analysis were very helpful and often showed me that the questions I asked myself were placed in the right spot.

Ein großen Dankeschön geht an meine Familie: meine Eltern und Geschwister. Danke, dass ihr mich auf meinem Weg immer unterstützt und gefördert habt. Ihr habt mir auch in schwierigen Zeiten immer den Rücken gestärkt und ward mir die größte moralische Unterstützung.

A last special thank you goes to my husband Pablo, who was always there for me. Thank you for always standing behind me and listening to me, no matter if it's about content issues or just everyday life.

Lebenslauf *Curriculum Vitae*

Persönliche Daten

Name: Anna Alicke, geb. Scholl
Geburtsdatum: 19.12.1991
Geburtsort: Euskirchen

Schulbildung

1998 - 2002 Grundschule Roetgen
2002 - 2011 Inda-Gymnasium, Aachen-Kornelimünster
Allgemeine Hochschulreife

Studium

2011-2015 Bachelorstudium Physik, RWTH Aachen University
Bachelorarbeit: "A method for charm quark identification in hadronic top quark decays with the CMS experiment"

2015-2017 Masterstudium Physik, RWTH Aachen University
Masterarbeit: "Erstellung von Wärmevervollständigungsszenarien für veränderliche Gebäudebestände – Anwendung am Beispiel des Forschungszentrum Jülich mit Hilfe evolutionärer Algorithmen"

Promotion

2018-2023 Promotion im Fach Physik an der Ruhr-Universität Bochum in Kooperation mit dem Institut für Kernphysik am Forschungszentrum Jülich
Doktorarbeit: "Development of fast track finding algorithms for densely packed straw tube trackers and its application to $\Xi(1820)$ hyperon reconstruction for the PANDA experiment"